

© 2010 by Rebecca Mae Lamb. All rights reserved.

THE BOER-MULDERS AND CAHN EFFECTS:
AZIMUTHAL MODULATIONS IN THE SPIN-INDEPENDENT SIDIS CROSS
SECTION AT HERMES

BY

REBECCA MAE LAMB

DISSERTATION

Submitted in partial fulfillment of the requirements
for the degree of Doctor of Philosophy in Physics
in the Graduate College of the
University of Illinois at Urbana-Champaign, 2010

Urbana, Illinois

Doctoral Committee:

Professor Matthias Grosse Perdekamp, Chair
Professor Naomi C. R. Makins, Director of Research
Professor Scott Willenbrock
Professor John Stack

Abstract

The $\cos\phi_h$ and $\cos 2\phi_h$ modulations of the spin independent semi-inclusive deep inelastic scattering cross section were measured at HERMES. These modulations are sensitive to the polarization and transverse motion of quarks within the nucleon. The *Cahn effect*, which contributes at subleading twist (twist-3) to $\cos\phi_h$ and twist-4 to $\cos 2\phi_h$, is sensitive to transverse motion of quarks. The *Boer-Mulders effect*, which contributes at subleading twist to $\cos\phi_h$ and leading twist to $\cos 2\phi_h$, requires non-zero transverse quark motion and is sensitive to quark polarization, effectively measuring the quark spin-orbit correlation.

These modulations were measured in a fully differential way, as a function of x , y , z , and $P_{h\perp}$ for positive and negative pions, kaons, and unidentified-hadrons produced from hydrogen and deuterium targets at HERMES. This is the the most complete measurement to date, for the first time granting access to the flavor dependent distribution and fragmentation functions that generate these moments.

These measurement would not have been possible without an improved hadron-type identification algorithm for the Ring Imaging Cherenkov (RICH) detector. The EVT event-level algorithm is presented and now is the primary method used at HERMES

To my family, who has always believed in me.

Acknowledgments

I could not have succeeded in completing my PhD without the help and support of so many amazing people. Thank you first to Naomi, for all of your guidance, support, advice, proofreading, cheerleading, and enthusiasm. From the first time we met I always knew I could ask any question, no matter how simple, and without this comfort I could never have learned so much.

An equal thanks goes to my parents for their love and support (financial and otherwise), to my sisters and brothers (all 6 of you!) for your love and support, and to my nieces and nephews (Brandon, Abigail, Genevieve, Myles, Cody and Darren) for bringing so much joy into our lives.

Thank you to my twin, Miranda, I could not have survived the trials of grad school and beyond without you on speed dial. Thank you also to Anne for always being there with advice and for keeping me grounded in reality.

Thank you to my research brothers: Alex, Josh and Sylvester. Thanks for teaching me everything about HERMES physics, HERMES people, and graduate school. And thanks for fixing my code when I couldn't figure it out. Special thanks to Josh for being the best travel buddy.

All my love to the entire HERMES collaboration and especially the HH crowd. Francesca, you have been the best teacher and partner I could have asked for and I hope to never talk to you again about physics. Beautiful Charlotte, you kept me sane, thank you. Achim, Caro, Yves, Eduard, Ami, thanks for all the Absacker. Marco, Elke, and Hal, thanks for all your input and help with my work. Many thanks to my colleagues at Tokyo Tech for their warm welcome and financial support during my visit in August of 2007.

Thank you to all those who have made the logistics simple, in particular Wendy Wimmer, Penny Sigler, and Sabine Krohn. You all make everyone's day brighter.

Thank you to my qual buddies, David and Rogan, I couldn't have passed without you. And thank you to the rest of the first year crew for all the fun times.

Thank you to all of the amazing teachers I have had over the years, especially Mr. Watkins, Mr. Monteith, and Prof. Peter Persans. You have all shaped my mind and my life, and I thank you for that.

Finally, thanks to my love, Voytek. The last year and a half would not have been nearly as joyous without

you. Thank you for listening, understanding, editing, advising, and loving me through everything. I am so blessed to have you in my life.

Table of Contents

| | | |
|------------------|--|-----------|
| Chapter 1 | Introduction: proton structure | 1 |
| 1.1 | Deep inelastic scattering | 2 |
| 1.2 | Semi-inclusive deep inelastic scattering | 4 |
| 1.2.1 | Non-collinear SIDIS | 7 |
| 1.2.2 | The Cahn and Boer-Mulders effects | 11 |
| 1.3 | Background processes | 12 |
| Chapter 2 | The HERMES experiment | 13 |
| 2.1 | HERA | 13 |
| 2.2 | Target | 13 |
| 2.3 | Spectrometer | 13 |
| 2.3.1 | Hodoscopes | 14 |
| 2.3.2 | Drift chambers | 14 |
| 2.3.3 | Particle identification detectors | 15 |
| 2.4 | Data taking | 17 |
| 2.4.1 | Trigger | 17 |
| 2.4.2 | Data acquisition | 18 |
| 2.5 | Offline data production | 18 |
| 2.5.1 | Decoding | 18 |
| 2.5.2 | Tracking | 18 |
| 2.5.3 | Slow control | 19 |
| 2.5.4 | μ DST production | 19 |
| 2.5.5 | Particle identification | 20 |
| 2.5.6 | Data quality | 22 |
| Chapter 3 | Improved particle identification with the RICH detector | 24 |
| 3.1 | Indirect Ray Tracing (IRT) | 24 |
| 3.1.1 | Further corrections: P-matrices | 25 |
| 3.2 | Direct Ray Tracing (DRT) | 28 |
| 3.3 | The RICH PID Scheduler and “BEST” | 28 |
| 3.4 | An event-level algorithm: EVT | 30 |
| 3.4.1 | Motivation | 30 |
| 3.4.2 | Implementation | 32 |
| 3.4.3 | Quality parameters | 33 |
| 3.4.4 | Backgrounds, dead tubes, and hot tubes | 34 |
| 3.4.5 | P-matrices | 37 |
| 3.4.6 | Results and comparisons between methods | 41 |

| | | |
|------------------|---|-----------|
| Chapter 4 | Data analysis procedure | 44 |
| 4.1 | Overview | 44 |
| 4.2 | Data | 45 |
| 4.2.1 | Data productions | 45 |
| 4.2.2 | Burst selection: data quality | 45 |
| 4.2.3 | Event and track selection | 46 |
| 4.2.4 | Charge symmetric background correction | 51 |
| 4.2.5 | RICH weights | 51 |
| 4.3 | Monte Carlo | 51 |
| 4.3.1 | MC for data normalization | 51 |
| 4.3.2 | Born MC | 52 |
| 4.3.3 | Reconstructed MC | 53 |
| 4.4 | 5-dimensional unfolding procedure | 54 |
| 4.4.1 | The smearing matrix and background vector | 54 |
| 4.4.2 | Linear regression | 56 |
| 4.4.3 | The Fold and Fit formalism | 58 |
| 4.4.4 | $\cos n\phi_h$ moments | 60 |
| 4.4.5 | Combining data sets | 61 |
| 4.4.6 | Integrated moments | 63 |
| 4.4.7 | Parameterization of the moments | 64 |
| Chapter 5 | Systematic studies | 66 |
| 5.1 | Cross-check of results | 66 |
| 5.2 | Detection effects | 67 |
| 5.2.1 | Track reconstruction | 67 |
| 5.2.2 | PID | 67 |
| 5.2.3 | Beam slopes | 69 |
| 5.2.4 | Detector misalignment | 69 |
| 5.3 | Systematic tests of the analysis procedure | 74 |
| 5.3.1 | DIS normalization | 74 |
| 5.3.2 | Binning tests | 74 |
| 5.3.3 | Additional azimuthal moments | 78 |
| 5.4 | MC model dependence tests | 85 |
| 5.4.1 | Model dependence of the smearing matrix | 85 |
| 5.4.2 | Model dependence of the background vector | 86 |
| 5.4.3 | Model dependence of the integration procedure | 86 |
| 5.5 | MC self-test of full extraction procedure | 87 |
| 5.6 | Time dependence of the data | 91 |
| 5.7 | Systematic errors | 94 |
| Chapter 6 | Results and interpretation | 97 |
| 6.1 | Pion results | 97 |
| 6.1.1 | Q^2 -dependence | 105 |
| 6.1.2 | $P_{h\perp}$ -dependence | 109 |
| 6.2 | Hadron results | 113 |
| 6.3 | Kaon results | 116 |
| 6.4 | Four-dimensional fits to the results | 121 |
| 6.4.1 | Inclusion in other HERMES analyses | 121 |

| | | |
|-------------------|---|------------|
| Chapter 7 | Comparison with other experimental results | 124 |
| 7.1 | Other $\cos \phi_h$ and $\cos 2\phi_h$ measurements | 124 |
| 7.1.1 | CLAS results | 126 |
| 7.1.2 | COMPASS results | 130 |
| 7.2 | The Collins fragmentation function | 133 |
| 7.3 | Drell-Yan results | 133 |
| Chapter 8 | Comparison to theory | 134 |
| 8.1 | $\cos \phi_h$ models | 134 |
| 8.1.1 | Anselmino et al. | 135 |
| 8.2 | $\cos 2\phi_h$ models | 136 |
| 8.2.1 | Gamberg et al. | 136 |
| 8.2.2 | Barone et al. | 137 |
| 8.2.3 | Zhang et al. | 141 |
| 8.2.4 | Evaluation of the model for a deuterium target | 142 |
| Chapter 9 | Conclusions | 144 |
| Chapter 10 | Poetry | 145 |
| References | | 146 |

Chapter 1

Introduction: proton structure

This thesis is primarily concerned with describing the theory, experimental procedure, and results of a measurement of the azimuthal modulation of the semi-inclusive deep inelastic scattering of leptons from nucleons. While this thesis assumes a basic knowledge of particle physics the following outline defines some terms such that a novice should be able to follow the remainder of the work, and in particular this chapter.

lepton - a class of elementary particles including (and in this thesis generally referring to) electrons and their antimatter counterpart, positrons. Leptons carry electromagnetic charge and can also interact via the weak and gravitational forces.

quark - a class of element particles that can interact via the strong, weak, electromagnetic and gravitational forces. Due to color confinement quarks are not found in isolation. Commonly found matter is made of up (u) and down (d) quarks. Strange (s) quarks are the next lightest and thus the next easiest quark flavor to produce.

hadron - a composite particle made of several quarks. These include 3-quark states (baryons) such as protons and quark-antiquark states (mesons) such as pions.

nucleon - one of the constituents of the atomic nucleus: a proton or neutron.

QED - Quantum ElectroDynamics, the quantum field theory describing the electromagnetic force.

QCD - Quantum Chromodynamics, the quantum field theory describing the strong force. Unlike QED many QCD elements cannot be calculated directly. Perturbative techniques enable calculations at high energies. Lattice techniques are making progress in some non-perturbative regimes but are computationally intensive.

1.1 Deep inelastic scattering

One way to study nucleon structure is to bombard protons with high energy electrons or positrons (hereafter referred to as leptons¹). If the leptons are of sufficiently high energy, *deep inelastic scattering* (DIS) occurs where the lepton (l), in the presence of the nucleon (N) target, emits a virtual photon or virtual Z^0 boson that interacts with a single quark in the nucleon, breaking up the nucleon into several final state hadrons (X): $l + N \rightarrow l' + X$. At HERMES the Z^0 boson mass, 91 GeV, is far above the beam energy of 27.6 GeV and thus their production is highly suppressed. Additionally, the formalism below assumes only a single virtual photon is exchanged. Multiple virtual photon exchange is expected to be small at HERMES and has in fact been measured to be compatible with zero at HERMES [1]. The 4-momentum of the virtual photon (\mathbf{q}) can be calculated from the 4-momenta of the incoming lepton (\mathbf{l}) and the scattered lepton (\mathbf{l}'). The squared 4-momentum of the virtual photon, because it is virtual and thus has imaginary mass, is negative. For convenience, the positive quantity Q^2 is defined as

$$-Q^2 \equiv \mathbf{q}^2 \equiv (\mathbf{l} - \mathbf{l}')^2. \quad (1.1)$$

The deep inelastic scattering region is defined by two kinematic requirements. First, $Q^2 > 1 \text{ GeV}^2$ is required to ensure a sufficiently high resolution virtual photon probe. This ensures that the virtual photon interacts with an individual quark or gluon in the nucleon and not the nucleon as a whole. High Q^2 also suppresses higher twist effects which include multiple interactions of the virtual photon with the target (see Section 1.2 for more details). In addition to the virtual photon invariant mass, the final state invariant mass should also be sufficiently large to ensure that the nucleon was broken apart and not merely excited to a resonance state. The latter would again imply that the virtual photon interacted with the nucleon as a whole, rather than a constituent, and thus is not a part of the deep inelastic scattering process described here. The final state invariant mass squared,

$$W^2 = (\mathbf{P} + \mathbf{q})^2 \quad (1.2)$$

depends only of the target 4-momentum (\mathbf{P}) and the virtual photon 4-momentum and thus can be calculated from the known initial state beam and target and the scattered lepton. To avoid the resonance region, $W^2 > 4 \text{ GeV}^2$ is sufficient although $W^2 > 10 \text{ GeV}^2$ is a more conservative cut sometimes used².

The cross section for DIS is given in terms of the leptonic tensor $L_{\mu\nu}$, which describes the lepton - virtual

¹ In general any lepton can be used in deep inelastic scattering. However, the HERMES experiment which is discussed in this text used only electrons and positrons.

²At HERMES kinematics there is very little data below $W^2 = 10 \text{ GeV}^2$ and so the more conservative cut is almost always used, without a significant loss of statistics.

photon interaction and can be calculated exactly in QED, and the hadronic tensor $W^{\mu\nu}$, which describes the non-perturbative structure of the hadronic target. In particular the unpolarized cross section with the scattered beam in a solid angle $d\Omega$ and energy interval $[E', E' + dE']$ is

$$\frac{d^2\sigma}{dE'd\Omega} = \frac{\alpha^2}{Q^4} \frac{E'}{E} L_{\mu\nu} W^{\mu\nu} \quad (1.3)$$

$$L_{\mu\nu} = 2 \cdot [l'_\mu l'_\nu + l'_\nu l'_\mu - g_{\mu\nu} (\mathbf{l}' \cdot \mathbf{l}' - m^2)] \quad (1.4)$$

$$W^{\mu\nu} = \left(-g_{\mu\nu} - \frac{q_\mu q_\nu}{Q^2} \right) \frac{F_1(x, Q^2)}{M} + \left(P_\mu + \frac{\mathbf{P} \cdot \mathbf{q}}{Q^2} q_\mu \right) \left(P_\nu + \frac{\mathbf{P} \cdot \mathbf{q}}{Q^2} q_\nu \right) \frac{F_2(x, Q^2)}{M(\mathbf{P} \cdot \mathbf{q})} \quad (1.5)$$

where $\alpha = e^2/4\pi$ is the fine structure constant, $g_{\mu\nu}$ is the Minkowski metric, and m (M) is the lepton (target) mass. The hadronic tensor is parameterized with the structure functions F_1 and F_2 , which have been measured in experiment. Summarizing and expressing the cross section in terms of the Lorentz invariant variables Björken x and Q^2 (see Table 1.1):

$$\frac{d^2\sigma}{dx dQ^2} = \frac{4\pi\alpha^2}{Q^4} \left[y^2 F_1(x, Q^2) + \left(1 - y - \frac{1}{4}\gamma^2 y^2 \right) \frac{F_2(x, Q^2)}{x} \right]. \quad (1.6)$$

In a frame where the nucleon moves quickly toward the virtual photon (the “infinite momentum frame”), x represents the fraction of the nucleon momentum carried by the struck quark.

Alternatively, defining the ratio of longitudinally polarized³ to transversely polarized virtual photon flux ϵ (see Table 1.1) the cross section can be written in terms of the longitudinal and transverse structure functions:

$$\frac{d^2\sigma}{dx dQ^2} = \frac{4\pi\alpha^2}{Q^4} \frac{y^2}{2x(1-\epsilon)} [F_T(x, Q^2) + \epsilon F_L(x, Q^2)]. \quad (1.7)$$

The longitudinal and transverse structure functions are related to F_1 and F_2 :

$$F_T(x, Q^2) = 2xF_1(x, Q^2), \quad (1.8)$$

$$F_L(x, Q^2) = (1 + \gamma^2)F_2(x, Q^2) - 2xF_1(x, Q^2). \quad (1.9)$$

³ For a massless spin 1 particle in vacuum only the spin +1 and -1 states are allowed, corresponding to right and left circularly polarized fields. Since the electric and magnetic fields in this case are perpendicular to the direction of motion of the wave these are referred to as *transversely polarized* photons. For a virtual photon, which has non-zero mass and only exists in the presence of a target field, the spin-0 state is also allowed. This state has component fields in the same direction as the photon momentum, and is thus referred to as a *longitudinally polarized* virtual photon.

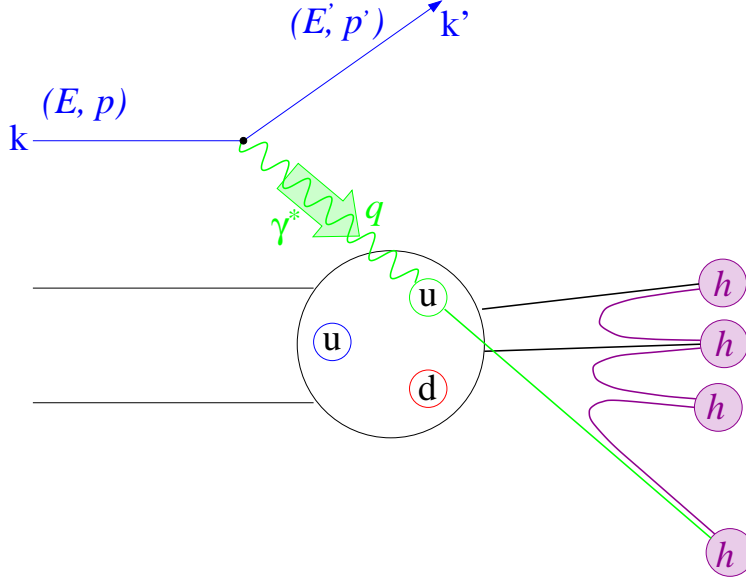


Figure 1.1: A schematic of the semi-inclusive deep inelastic scattering process.

1.2 Semi-inclusive deep inelastic scattering

Additional information about nucleon structure can be learned if, in addition to the scattered lepton, some or all other final state particles are observed. Observing the full final state — an *exclusive* measurement — is difficult and in general is only possible at HERMES when a single final state particle is produced. This thesis is instead based on a *semi-inclusive* measurement where some part of the hadronic final state is observed (in particular one hadron) in addition to scattered lepton. This process is depicted in Figure 1.1. The relevant kinematic variables for both DIS and semi-inclusive DIS (SIDIS) are summarized in Table 1.1

The observation of an additional hadron in the final state increases the number of kinematic variables on which the cross section can depend. Once the particle type (mass) is identified, each particle has three independent degrees of freedom ((p_x, p_y, p_z) , (p, θ, ϕ) , etc.), making 6 total degrees of freedom for the case of single-hadron SIDIS. However, the physics is independent of one overall azimuthal angle (physics is the same if the entire experiment is rotated by an arbitrary angle around the beam), reducing the total number of independent variables to 5. Typically, in addition to the inclusive variables x and Q^2 the semi-inclusive variables z , $P_{h\perp}$, and ϕ_h are used. In the laboratory frame, z represents the fraction of the virtual photon energy carried by the produced hadron while $P_{h\perp}$ represents the component of the hadron momentum transverse to the virtual photon direction. ϕ_h is the relative angle between the lepton plane, defined by \vec{k} , \vec{k}' and \vec{q} , and the hadron plane, defined by \vec{q} and \vec{P}_h , as shown in Figure 1.2.

Historically, the target quark has typically been approximated to be collinear with the nucleon and thus $P_{h\perp}$ is often neglected (integrated over). In this case there is also no ϕ_h -dependence in the unpolarized cross

Table 1.1: Definitions of kinematic variables

| DIS variables | |
|---|--|
| $\mathbf{P} \stackrel{lab}{=} (M, 0)$ | Target 4-momentum |
| $\mathbf{l}; \mathbf{l}' = (E, \vec{k}); (E', \vec{k}')$ | Incoming (outgoing) beam lepton 4-momenta |
| $\mathbf{q} = l - l' \stackrel{lab}{=} (\nu, \vec{q})$ | Virtual photon momentum |
| $Q^2 = -q^2 \stackrel{lab}{=} 4EE' \sin^2\left(\frac{\theta}{2}\right)$ | Negative squared four-momentum transfer |
| $\nu = \frac{\mathbf{P} \cdot \mathbf{q}}{M} \stackrel{lab}{=} E - E'$ | Energy transfer to the target |
| $y = \frac{\mathbf{P} \cdot \mathbf{q}}{\mathbf{P} \cdot \mathbf{l}} \stackrel{lab}{=} \frac{\nu}{E}$ | Fractional energy of the virtual photon |
| $x_B = \frac{Q^2}{2\mathbf{P} \cdot \mathbf{q}} \stackrel{lab}{=} \frac{Q^2}{2M\nu}$ | Björken scaling variable |
| $W^2 = (\mathbf{P} + \mathbf{q})^2 \stackrel{lab}{=} M^2 + 2M\nu - Q^2$ | Squared invariant mass of the final state |
| $\gamma = \frac{2Mx}{Q}$ | |
| $\epsilon = \frac{1 - y - \frac{1}{4}\gamma^2 y^2}{1 - y + \frac{1}{2}y^2 + \frac{1}{4}\gamma^2 y^2}$ | Ratio of longitudinal and transverse photon flux |
| SIDIS variables | |
| $\mathbf{P}_h = (E_h, \vec{P}_h)$ | Hadron momentum |
| $z = \frac{\mathbf{P} \cdot \mathbf{P}_h}{\mathbf{P} \cdot \mathbf{q}} \stackrel{lab}{=} \frac{E_h}{\nu}$ | Fractional energy of the final state hadron |
| $\phi_h = \arctan\left(\frac{\vec{P}_h \cdot (\hat{q} \times \hat{l})}{\vec{P}_h \cdot (\hat{q} \times \hat{l} \times \hat{q})}\right)$ | Azimuthal angle of the hadron with respect to the lepton scattering plane |
| $p_{CM}^{\parallel} = \vec{P}_h \cdot \hat{q}$ | Component of the hadron momentum parallel to the virtual photon in the virtual photon-nucleon center of mass frame |
| $x_F = \frac{p_{CM}^{\parallel}}{ \vec{q} } \stackrel{lab}{\simeq} \frac{2p_{CM}^{\parallel}}{W}$ | Feynman variable |

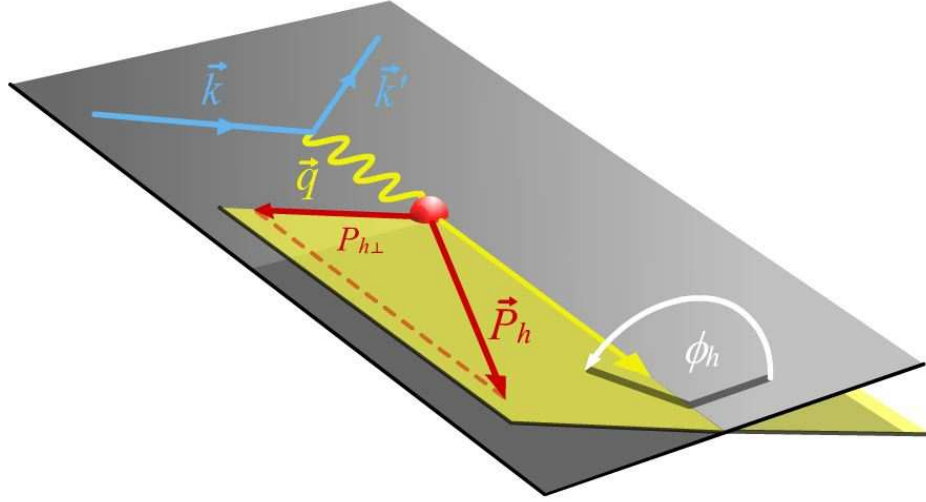


Figure 1.2: Definition of the azimuthal angle ϕ_h (white) with respect to the lepton scattering plane (gray) and the hadron production plane (yellow).

section and it can be written

$$\frac{d^3\sigma}{dx dQ^2 dz} = \frac{4\pi\alpha^2}{xQ^4} \frac{y^2}{2(1-\epsilon)} \left(1 + \frac{\gamma^2}{2x}\right) (F_{UU,T}(x, Q^2, z) + \epsilon F_{UU,L}(x, Q^2, z)) \quad (1.10)$$

where UU denotes unpolarized beam and target and L (T) denotes longitudinal (transverse) photon polarization. The structure functions F_{UU} are related to the inclusive structure functions via an integral over z and final state hadrons h :

$$F_T(x, Q^2) = \sum_h \int dz z F_{UU,T}^h(x, Q^2, z) \quad (1.11)$$

$$F_L(x, Q^2) = \sum_h \int dz z F_{UU,L}^h(x, Q^2, z) \quad (1.12)$$

$$(1.13)$$

It has been proven ([2, 3] and references therein) that in leading order QCD the x and z -dependence can be *factorized* such that the structure functions can be written

$$F_{UU,T}(x, Q^2, z) = x \sum_q e_q^2 f_1^q(x, Q^2) D_1^q(z, Q^2) \quad (1.14)$$

$$F_{UU,L}(x, Q^2, z) = 0 \quad (1.15)$$

where the sum is over quark and antiquark flavors q and e_q is the quark charge.

These functions can be interpreted physically. The *distribution functions* $f_1^q(x)$ describe the momentum distribution of the (anti)quark q in the target nucleon. The *fragmentation functions* D_1^q describe how the struck (anti)quark q forms into a final state hadron, as a function of the fractional momentum of the hadron. The distribution functions f_1^q provide more detailed information than the inclusive structure functions F_1 and F_2 since they are flavor dependent, however the two are simply related:

$$\begin{aligned}
 F_1(x, Q^2) &= \frac{1}{2} \sum_q e_q^2 f_1^q(x, Q^2), \\
 F_L(x, Q^2) &= 0 \\
 \Rightarrow F_2(x, Q^2) &= \frac{2x}{1 + \gamma^2} F_1(x, Q^2).
 \end{aligned}
 \tag{1.16}$$

The fragmentation functions provide information about the formation of final state particles. This cannot be learned from inclusive DIS where final state hadrons are not observed.

In addition to the spin-independent functions, two spin-dependent distribution functions $g_1^q(x, Q^2)$ ($h_1^q(x, Q^2)$) describe the distribution of longitudinally (transversely) polarized quarks in a longitudinally (transversely) polarized nucleon. The corresponding fragmentation functions $G_1^q(z)$ and $H_1^q(z)$ describe the fragmentation process for the same spin states. The spin dependent distribution functions are simply related to the spin-dependent structure functions $g_1(x, Q^2)$ and $g_2(x, Q^2)$ in a manner similar to Equation 1.16

All of the equations up to this point include only the leading term in an expansion in orders of the strong coupling constant α_s . This corresponds to diagrams with no strong force vertex, as in Figure 1.3a. Not included are next to leading order (NLO) processes such as the *QCD Compton* process shown in Figure 1.3b. In addition only leading twist terms are included. The *twist expansion* is an expansion in orders of $1/Q$, where leading-twist, twist-two, corresponds to $1/Q$. Physically this corresponds to a single interaction between the virtual photon probe and target (Figure 1.3a), while higher twist terms also account for re-interactions of the virtual photon with the target, the inclusion of quark masses, quark transverse momentum, and gluon interactions (Figure 1.3c). At the moderate Q^2 of the HERMES data ($\langle Q^2 \rangle_{\text{HERMES}} \sim 2.5 \text{ GeV}^2$) the contribution from higher twist terms can be significant, as discussed below.

1.2.1 Non-collinear SIDIS

In all of the above the quark momentum is taken to be a fraction of the nucleon momentum, x . However, in general the quark may also have momentum transverse to the nucleon momentum direction. Allowing for such non-collinear kinematics, many more distribution and fragmentation functions are possible. These are

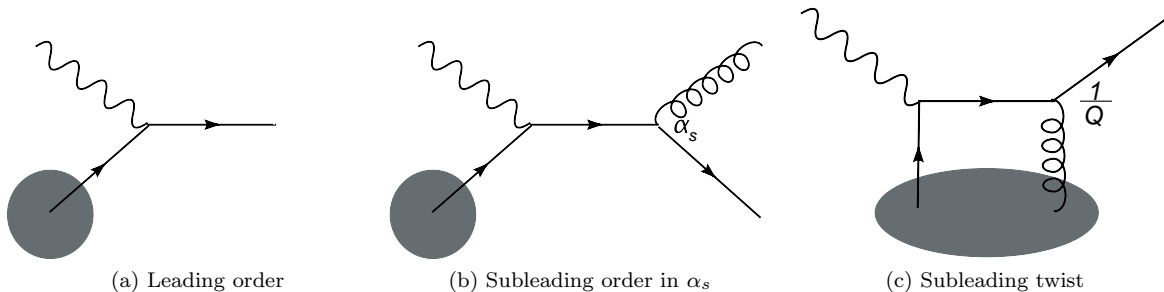


Figure 1.3: A few Feynman diagrams that contribution to the DIS cross section.

referred to as *transverse momentum dependent* functions (TMDs).

Factorization has also been proven for non-collinear SIDIS for low transverse momentum ($P_{h\perp}$) hadrons up to leading order in α_s and leading twist [4]. While reference [4] argues that factorization is valid to all orders of α_s , it is currently unknown if and how factorization can be extended to subleading twist. The limit on $P_{h\perp}$ is important to ensure that a single hard scale is present, namely Q^2 . When $Q^2 \sim P_{h\perp}$ factorization in this form no longer holds. For $P_{h\perp} \gg Q^2$ higher order perturbative QCD effects dominate and factorization can again be proven, but the TMDs defined above no longer provide a suitable description. In addition, factorization cannot be generalized to all processes, which leads to questions about the *universality* of the distribution functions. This topic is currently under intense theoretical study.

Like the non- $P_{h\perp}$ dependent (collinear) functions, the TMDs have simple probabilistic interpretations. All of the leading twist functions are summarized pictorially in Figure 1.4. The small blue circle represents the quark, which in some cases has an arrow attached to represent its spin directions. The larger yellow circles represent the target nucleon (or final state hadron in the case of the fragmentation functions), also with a spin vector attached. The spin vectors are relative to an incoming virtual photon from the left side of the page and the spin vectors at a 45° or 225° angle represent spin into or out of the page. The collinear functions discussed above, which survive an integration over transverse momentum, appear in the upper left portion of the figure.

The f_{1T}^\perp and h_1^\perp distribution functions and the D_{1T}^\perp and H_{1T}^\perp fragmentation functions shown in Figure 1.4 have the property of being odd under *naïve time reversal* (“T-odd”). This phrase denotes standard time reversal but without the interchange of the initial and final states. Since QCD amplitudes are T-even, T-odd functions can only exist as the interference of two amplitudes of different phases, one of which induces a spin-flip. T-odd fragmentation functions can arise due to potential final state interactions with the target remnant. Initially, leading twist T-odd distribution functions were thought to vanish since, by definition, it is only a single (forward scattering) amplitude and thus no interference could occur. However, experimental results

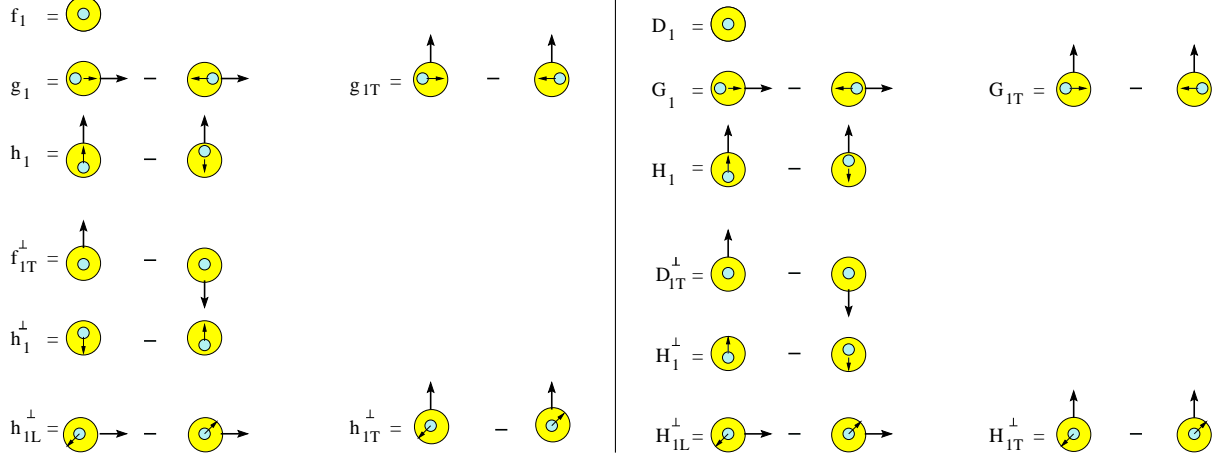


Figure 1.4: All leading twist distribution (lower case letters) and fragmentation (capital letters) functions, with their probabilistic interpretations, as described in the text.

[5, 6, 7] spurred further theoretical work. The initial proof of principle in by Brodsky, Hwang and Schmidt [8] found that the inclusion of gauge links in the definitions of the TMDs, which correspond to soft gluon exchange, can provide the necessary interference to produce T-odd distribution functions. The calculation requires wavefunctions with different orbital angular momentum. The T-odd distribution functions then describe a spin-orbit coupling within the nucleon and can provide access to the orbital angular momentum contribution to the nucleon spin.

Finally, using the formalism of Ref. [9], the cross section for unpolarized SIDIS at LO and subleading twist can be written as:

$$\begin{aligned}
 d\sigma &= \frac{d^5\sigma}{dx dy dz d\phi dP_{h\perp}^2} = \\
 &2\pi \frac{\alpha^2}{xyQ^2} \frac{y^2}{2(1-\epsilon)} \left(1 + \frac{\gamma^2}{2x}\right) \left[F_{UU,T} + \epsilon F_{UU,L} + \sqrt{2\epsilon(1+\epsilon)} \cos\phi_h F_{UU}^{\cos\phi_h} + \epsilon \cos 2\phi_h F_{UU}^{\cos 2\phi_h} \right] \quad (1.17)
 \end{aligned}$$

The structure functions F_{UU} are decomposed into individual distribution functions and fragmentation functions as follows:

$$F_{UU,T} = \mathcal{C}[f_1 D_1] \quad (1.18)$$

$$F_{UU,L} = 0 \quad (1.19)$$

$$F_{UU}^{\cos \phi_h} = \frac{2M}{Q} \mathcal{C} \left[-\frac{\hat{\mathbf{h}} \cdot \mathbf{k}_T}{M_h} \left(\frac{p_T^2}{M^2} h_1^\perp H_1^\perp + x \tilde{h} H_1^\perp + \frac{M_h}{M} f_1 \frac{\tilde{D}^\perp}{z} \right) - \frac{\hat{\mathbf{h}} \cdot \mathbf{p}_T}{M} \left(f_1 D_1 + x \tilde{f}^\perp D_1 + \frac{M_h}{M} h_1^\perp \frac{\tilde{H}}{z} \right) \right] \quad (1.20)$$

$$F_{UU}^{\cos 2\phi_h} = \mathcal{C} \left[-\frac{2(\hat{\mathbf{h}} \cdot \mathbf{k}_T)(\hat{\mathbf{h}} \cdot \mathbf{p}_T) - \mathbf{k}_T \cdot \mathbf{p}_T}{MM_h} h_1^\perp H_1^\perp \right]. \quad (1.21)$$

Here, $\hat{\mathbf{h}}$ is the unit vector in the $\mathbf{P}_{h\perp}$ direction and M_h is the mass of the detected final-state hadron. \mathbf{p}_T is the transverse vector component of the quark in the target hadron. \mathbf{k}_T is the transverse momentum of the final state hadron, with respect to the momentum of the struck quark. The functions with a “ \sim ” over them are the subleading twist distribution and fragmentation functions, which do not have simple probabilistic interpretation such as those in Figure 1.4. The terms with only leading twist functions are highlighted in green. The convolution integral $\mathcal{C}[w f D]$ is defined as follows:

$$\mathcal{C}[w f D] = x \sum_q e_q^2 \int d^2 \mathbf{p}_T d^2 \mathbf{k}_T \delta^2(\mathbf{p}_T - \mathbf{k}_T - P_{h\perp}/z) w(\mathbf{p}_T, \mathbf{k}_T) f^q(x, \mathbf{p}_T^2) D^q(z, \mathbf{k}_T^2) \quad (1.22)$$

In this thesis measurements of the $F_{UU}^{\cos \phi_h}$ and $F_{UU}^{\cos 2\phi_h}$ structure functions (relative to the unpolarized structure functions $F_{UU,T}$) will be made. The angular dependence of these terms is fortuitous as it provides access to higher twist functions which would otherwise be overwhelmed by lower twist components of the cross section which do not suffer from kinematic suppression. The leading twist contributions to each Fourier moment are of particular interest and are discussed below. The higher twist functions have not been independently measured but are expected to have a small contribution to the moments and are thus generally neglected in the interpretation.

At $P_{h\perp} < 1$ GeV NLO effects are not expected to contribute significantly [10]. While most of the results presented will fall within this kinematic range an effort is made to present a result in the highest $P_{h\perp}$ bin, 1.0 – 1.3 GeV in order to test this supposition. One additional $P_{h\perp}$ bin was also explored but was eliminated both due to low statistics and because in this region of HERMES kinematics $P_{h\perp} \sim Q^2$ which makes the result difficult to interpret.

1.2.2 The Cahn and Boer-Mulders effects

The $\cos \phi_h$ moment

The $\cos \phi_h$ moment of the SIDIS cross section contains several contributions. The *Cahn effect* is proportional to the unpolarized distribution and fragmentation functions, $f_1 D_1$; it is a $\cos \phi_h$ modulation arising solely from the inclusion of non-zero transverse quark momentum in the nucleon (\mathbf{p}_T) and was first discussed by Cahn [11, 12]. Since a non-zero quark transverse momentum is required by the Cahn effect, observations of the Cahn effect can provide information on the quarks' intrinsic transverse momentum distribution, potentially including flavor dependence. Cahn's original calculations found the $\cos \phi_h$ modulation to be:

$$\langle \cos \phi_h \rangle_{Cahn} = -\frac{2p_T}{Q} \frac{(2-y)\sqrt{1-y}}{1+(1-y)^2}, \quad (1.23)$$

producing a negative moment proportional to \mathbf{p}_T . Below $P_{h\perp} \sim 1$ GeV NLO QCD sources of transverse momentum are expected to be small, so $P_{h\perp} \sim \mathbf{p}_T$, and thus the Cahn contribution to $\cos \phi_h$ is expected to be proportional to $P_{h\perp}$.

A second leading-twist contribution to $\cos \phi_h$ is the *Boer-Mulders effect*, which is a convolution of the Boer-Mulders distribution function h_1^\perp and the Collins fragmentation function H_1^\perp . The sign and magnitude of $h_{1,q}^\perp$ reflects the correlation between the spin \vec{S}_q and orbital angular momentum \vec{L}_q of a quark of flavor q within the nucleon. Reference [13] predicts the Boer-Mulders function to be roughly similar to the Sivers function, which from recent fits [14] is found to be positive for u quarks and negative for d quarks.

Additionally, terms which involve a higher-twist distribution or fragmentation function contribute to the $\cos \phi_h$ moment but they are expected to be small.

The $\cos 2\phi_h$ moment

Including only up to twist three terms the $\cos 2\phi_h$ modulation arises solely from the Boer-Mulders effect, providing direct access to h_1^\perp . However, at twist-4 the Cahn effect also appears, as calculated by Cahn in his original calculations [11]:

$$\langle \cos 2\phi_h \rangle_{Cahn} = \frac{2p_T^2}{Q^2} \frac{(1-y)}{1+(1-y)^2}, \quad (1.24)$$

A review of previous measurements of the Cahn and Boer-Mulders effects can be found in Chapter 7.

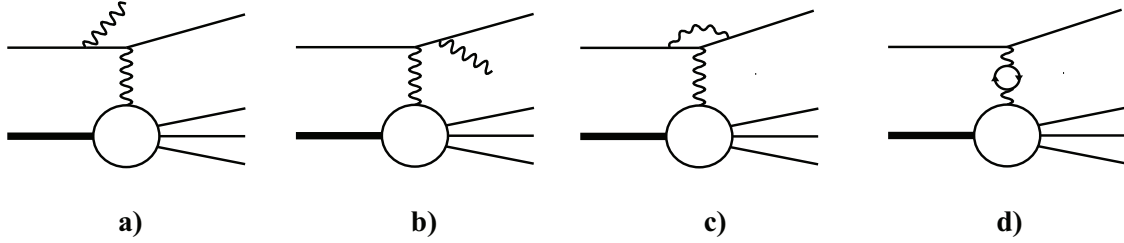


Figure 1.5: Radiative effects: the lepton (—) emits a real photon (\sim) as well as a virtual photon (\sim) which interacts with the target (\circ)

1.3 Background processes

Some processes can mimic SIDIS and contribute a background to the interpretation of the measured moments.

Higher order QED processes, generally termed *radiative effects*, are present in the measured SIDIS cross section; they are corrected for via an unfolding procedure (Section 4.4). Some contributing diagrams are shown in Figure 1.5 where the lepton emits a real photon. The largest contributions come from initial state radiation (Figure 1.5a) and final state radiation (Figure 1.5b).

The decay products of exclusively produced vector mesons also contribute to the measured yields, with the dominant contribution arising from $\rho^0 \rightarrow \pi^+\pi^-$. Since most ρ^0 s produced at HERMES cannot be reconstructed due to one of the decay products falling outside the acceptance, no model-independent correction can be made for this contribution.

The elastic Bethe-Heitler process, where the virtual photon interacts elastically with the target while emitting a photon, does not contribute to the SIDIS cross section since there is no fragmentation and no final state hadrons, but it does contribute to the inclusive DIS cross section where only the scattered lepton is observed. The inclusive DIS cross section is used in this work as a normalization factor and so, when normalizing data relative to Monte Carlo (MC) simulation, it is important that the MC generator includes the Bethe-Heitler process as such events cannot be excluded from the measured inclusive DIS cross section.

Chapter 2

The HERMES experiment

2.1 HERA

The HERMES experiment made use of the HERA 27.6 GeV electron/positron beam. The HERA proton beam, used by the collider experiments, passed through the center of the experiment, dividing it into upper and lower halves.

2.2 Target

The HERMES target was internal to the HERA lepton storage ring and consisted of an open ended cell that was filled with longitudinally and transversely polarized hydrogen and deuterium and unpolarized hydrogen, deuterium, helium, nitrogen, krypton, neon, and xenon. Only data from the hydrogen and deuterium targets is used in this work. A 40 cm long storage cell was used from 1995 to 2005. In 2006 a recoil detector was installed in the target region which required a shorter target cell of 15 cm which was shifted forward (toward the spectrometer) with respect to the old target cell.

2.3 Spectrometer

Figure 2.1 shows a schematic of the HERMES spectrometer where the lepton beam enters from the left and passes through the target (yellow), tracking chambers (red) and a 1.5 T·m magnet (blue) for momentum measurements, hodoscopes (black) for triggering, and a Transition Radiation Detector (TRD), Ring Imaging Cherenkov (RICH), preshower, and calorimeter (green) for particle identification. Each subsystem is described in detail in the following subsections.

The overall angular coverage of HERMES was $|\theta_x| < 180$ mrad and 40 mrad $< |\theta_x| < 140$ mrad where the vertical (y) coverage was limited at low angles by the septum plate, a steel plate which shielded the beams from the magnetic field.

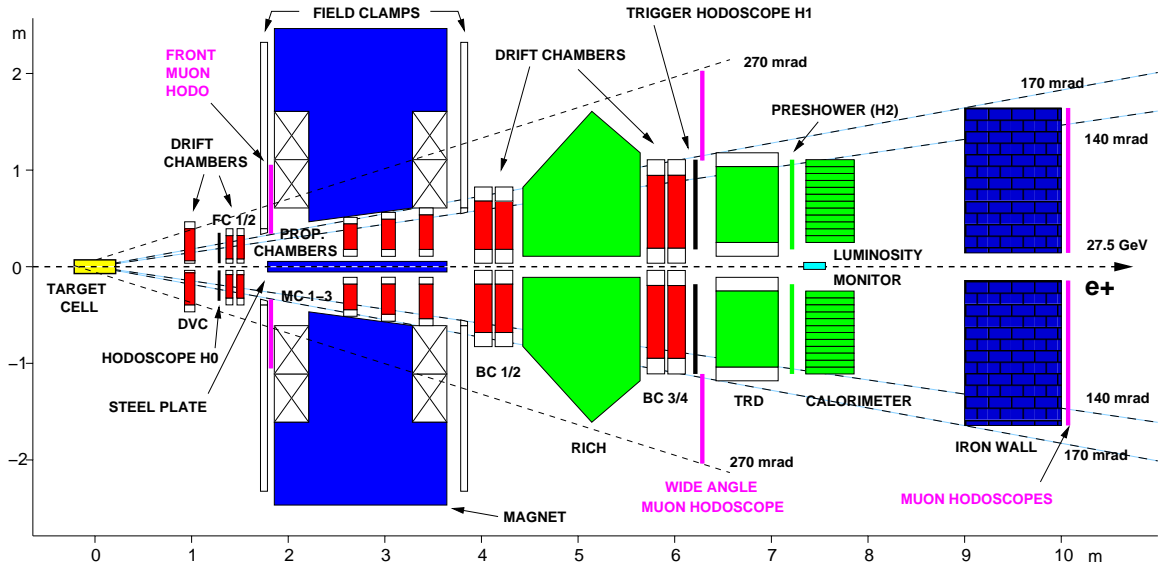


Figure 2.1: A side view of the HERMES detector. See text for details.

2.3.1 Hodoscopes

Hodoscopes, shown in black in Figure 2.1, were positioned before (H0) and after (H1) the spectrometer magnet, as well as in front of the Calorimeter (H2, the Preshower detector, see section 2.3.3). These hodoscopes were made from plastic scintillator material that fluoresces when charged particles pass through. They were coupled with photomultiplier tubes which collected and measured the pulse of light. H0 consisted of a single sheet of scintillator while H1 and H2 were composed of 42 vertical strips (per detector half) of scintillator, each with independent readout. The hodoscopes were used for triggering, as described in section 2.4.1.

2.3.2 Drift chambers

Several drift chambers were positioned before (DVC, FC1/2), within (MC1, 2, and 3), and after (BC 1/2, 3/4) the spectrometer magnet. Each chamber layer was made of alternating anode wires, held at ground potential, and cathode wires, held at negative high voltage. The wires were held in a gas mixture of Ar (90%), CO₂ (5%) and CF₄ (5%). Charged particles passing through the detector ionized the gas and the free electron then accelerated toward the anode, further ionizing the gas along the way, creating an avalanche. The time delay of the avalanche hitting the wire allowed for a precise determination of the charged track position with respect to the anode wire.

Each chamber was composed of six planes, whose wires were either vertical (X) or positioned at $\pm 30^\circ$ with respect to the vertical (U, V). Each chamber was arranged with its six planes ordered as follows:

(DVCs and FCs) $XX'UU'VV'$ or (BCs) $UU'XX'VV'$ where the primed layers were offset by half a cell size to resolve the left-right ambiguity. The six planes allowed for a precise $x - y$ position determination within each chamber. The spacial resolution achieved was $220\mu\text{m}$ in the DVCs, $225\mu\text{m}$ in the FCs, $250\mu\text{m}$ in BC 1/2, and $275\mu\text{m}$ in BC 3/4. The drift chambers were used for particle tracking, as described in section 2.5.2.

2.3.3 Particle identification detectors

Several detectors were used to determine particle type and are explained below.

The Transition Radiation Detector (TRD)

The transition radiation detector (TRD) was composed of six modules, each with polypropylene fibers in a 6.35 cm thick sheet surrounded by Xe (90%) and CH_4 (10%) gas that was positioned in front of a Multi-Wire Proportional Chamber (MWPC) made of vertical wires separated by 1.27 cm. Particles passing through the fibers passed through approximately 267 transition between the dielectric of the fibers and the gas. At each transition there was a chance for the particle to radiate to compensate for the electric field difference of the particle in the two mediums. This radiation was then detected in the MWPC. As the radiation probability is small, many transitions were needed to produce a sizable signal. The TRD detector had six fiber+MWPC chambers. The total energy emitted depended linearly on the particle's Lorentz factor γ and thus electrons emitted significantly larger signals than hadrons or muons, allowing for particle identification as described in section 2.5.5.

The preshower detector

The Preshower detector, as mentioned in section 2.3.1, was a hodoscope, but unlike the other hodoscopes the Preshower was preceded by a curtain of 11 mm of lead sandwiched in layers of 1.3 mm of steel. In the presence of large nuclei, leptons (due to their small mass) are deflected and emit Bremsstrahlung radiation. These high energy photons then pair-produce, generating more leptons, which in turn Bremsstrahlung, producing photons which pair-produce, etc. The result is a particle shower which carried through the lead curtain and was detected by the H2 hodoscope. In contrast, heavier particles such as pions do not Bremsstrahlung and only deposit energy by ionizing the material, creating a minimum ionizing pulse. The difference in the energy deposited by leptons and hadrons was used for particle identification, as described in section 2.5.5.

The calorimeter

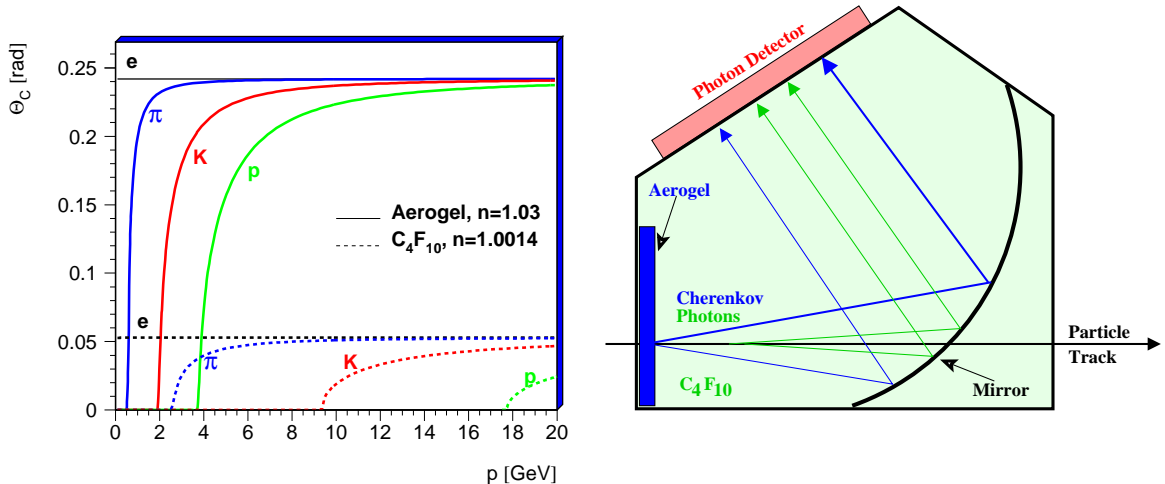
The calorimeter was a 42x10 array (in each detector half) of 9x9x50 cm³ lead-glass crystals, each coupled to a photomultiplier tube. Charged leptons passing through the crystal were accelerated in the presence of large lead nuclei and emitted Bremsstrahlung radiation in the forward direction, again initiating a particle shower as in the Preshower detector. The 50 cm length of the calorimeter crystals corresponded to 18 radiation lengths of material; thus electrons lost nearly all of their energy in the detector. Cherenkov radiation from the electromagnetic shower was collected by the photomultiplier tubes positioned at the back of each crystal; the size of the resulting signal was proportional to the energy of the electron that caused it. In addition, photons entering the calorimeter could also pair-produce, generate a shower, and be detected. The calorimeter's ability to detect photons was particularly important for HERMES measurements involving real photons (such as the Deeply Virtual Compton Scattering process) and neutral pions ($\pi^0 \rightarrow \gamma\gamma$). Hadrons passing through the calorimeter only emitted a minimum ionizing pulse (as in the preshower). For this reason the calorimeter was also used for particle identification, as described in section 2.5.5. In addition, the calorimeter formed a part of the trigger, signaling when a lepton was present in the event, as described in section 2.4.1

The Ring Imaging Cherenkov detector (RICH)

The Ring Imaging Cherenkov was installed in the HERMES spectrometer in 1998, replacing the Threshold Cherenkov detector. The RICH detector was based on the principle that Cherenkov radiation, emitted by charged particles moving faster than the speed of light in the medium, is emitted in a cone at the angle

$$\cos(\theta) = \frac{1}{\beta n} \quad (2.1)$$

where $\beta = \frac{v}{c}$ is the speed of the particle and n is the index of refraction of the material. This angle is shown in Figure 2.2a as a function of the momentum of particles of different mass, for both of the radiator materials used in the HERMES RICH. The RICH radiators were constructed from two materials with different indices of refraction: C₄F₁₀ gas — gas with the highest refractive index ($n = 1.001$) — and aerogel — the solid with the lowest refractive index ($n = 1.03$). The aerogel was arranged as a wall of tiles in front of the large gas volume. Behind the gas was a spherical mirror which reflected the Cherenkov cones into rings focused on the array of 1934 photomultiplier tubes (PMTs) positioned above. This design is shown in Figure 2.2b. Since the probability of multiple Cherenkov photons hitting a single PMT was small, the readout was digitized, recoding a *hit* whenever the pulse exceeded a threshold of 0.1 photoelectrons.



(a) Opening angle of Cherenkov photons from electrons, pions, kaons, and protons generated in the two HERMES radiators.

(b) Design of the RICH detector, including the aerogel and C_4F_{10} radiators, the spherical mirror, and photomultiplier tube array (photon detector) as well as two example Cherenkov photon paths.

Figure 2.2: Details of the RICH detector.

Given that the momentum of a particle was known from tracking (see Section 2.5.2) and the particle velocity was determined from the opening angle of Cherenkov photons in the RICH, the particle mass and therefore particle type could be determined. This allowed for hadron identification as described in Chapter 3 and also helped with lepton-hadron discrimination, as described in section 2.5.5.

2.4 Data taking

2.4.1 Trigger

Electron bunches passed through the HERMES target at a rate of 10 MHz. This rate was too fast for the Data Acquisition (DAQ) system and thus only those events of most interest were recorded. Most analyses at HERMES are inclusive (only the scattered lepton was detected) or semi-inclusive (the scattered lepton and an additional hadron were detected), and thus the main signature of an interesting HERMES event is the presence of a high energy lepton. The main HERMES trigger, trigger 21, was thus a coincidence of signals in all three hodoscopes (H0, H1, and H2) along with a large deposit (> 3.5 GeV in two adjacent blocks combined) of energy in the calorimeter, all in one detector half. A deposit of only 1.4 GeV was required during polarized data taking (with lower gas densities), but this data was not used in this thesis.

2.4.2 Data acquisition

Raw signals from the detector were recorded. In addition, every ~ 10 seconds additional information (“slow control” data) was recorded such as detector high voltage levels, luminosity and beam/target polarization measurements, prescalers (limits on particular triggers), tracking efficiencies, and status, calibration, and data quality information. This 10 second time frame defines one *burst*. All of this recorded data was then processed offline in the data production chain.

2.5 Offline data production

The offline data production chain converted the raw detector data to physical track information used by analyzers.

2.5.1 Decoding

The first step in the offline data production was to map the raw data into physically meaningful quantities; this was done by the HERMES DeCoder (HDC). HDC maps software channels back to hardware channels. Using calibration information provided by detector groups ADC (Analog to Digital Converter) detector signals were converted to energy measurements and TDC (Time to Digital Converter) detector signals were converted to drifts times and distances. The detector geometry, which includes the physical position of wires, was then used to determine hit positions in the HERMES coordinate system.

2.5.2 Tracking

The next step was to convert hits in the drift chambers into particle tracks. From the particle trajectory through the spectrometer magnet the particle charge and momentum could be determined. This information was then used in further analyzing the track.

HRC

The HERMES ReConstruction code (HRC) used a tree-search pattern recognition algorithm to search a database of track trajectories with increasing resolution. Straight tracks were reconstructed separately in the front (DVSs, FCs) and back (BCs) region and then combined with the MCs to produce the full track.

HTC

Recently (in 2009) the HERMES Tracking Code (HTC) was appended to HRC to further improve the tracking. This code begins from the tracks reconstructed by HRC and reparameterizes them, taking into account measured detector misalignment, beam positions and magnetic fields coming from both the target magnet (during polarized data taking in 2002-2005 and recoil data taking in 2006-2007) and the spectrometer magnet. HTC also allows for a track parameterization at any z (along the beamline) position. In practice parameterizations at a few z positions were produced. An additional user-code allows for multi-track vertices to be determined. This was particularly vital for the reconstruction of decayed particles such as the Λ but can also be used to ensure that both scattered beam lepton and observed hadrons originate from the beam in the center of the target (as was done in this analysis). At the time of writing the 2002-2007 data has been reprocessed with HTC. Data from 2000 and previous years is in the process of being processed by HTC.

2.5.3 Slow control

The slow control data mentioned above also undergoes processing. Detector experts check for data quality and a smoothing (over time) was done for the luminosity and polarization measurements. Data quality was checked and information such as the best polarimeter (the Longitudinal Polarimeter near the HERMES experimental area or the Transverse Polarimeter on the opposite side of the HERA ring) to use for a given burst was added. Additional information such as the beam spin for each running period was added by hand. All this data was merged together with time stamp information and put in the proper format to be read in by the μ DST production.

2.5.4 μ DST production

The final output of the data production process, and the input for analyzers, are the μ DST (micro Data Summary Tape) files. This file format merges together information from the HRC/HTC and slow productions and includes only information used by analyzers; information such as raw detector hits were not included, making these files substantially smaller than their HRC counterparts (hence the “micro” designation). For each production the μ DST production was run at least twice: once to compile the relevant information needed for the particle identification algorithm (see the next section) and a second time to include the results of the particle identification software.

2.5.5 Particle identification

Lepton / hadron identification

The HERMES particle identification (PID) scheme is based on Bayes' Theorem which, stated mathematically, is

$$P(A|B) = \frac{P(B|A)P(A)}{P(B)}. \quad (2.2)$$

Here $P(x|y)$ is the probability of x given y , and $P(x)$ is the overall probability of x .

The quantity of interest for PID is the probability $P(T_{l(h)}|\mathcal{R}, p)$ that the track is a lepton (hadron), $T_{l(h)}$, given the observed detector response (\mathcal{R}) recorded by the PID detectors and momentum (p) determined by the tracking system. From Bayes' theorem, for a fixed momentum (or one bin in momentum) this is given by

$$P(T_{l(h)}|\mathcal{R}) = \frac{P(\mathcal{R}|T_{l(h)})P(T_{l(h)})}{P(\mathcal{R})} \quad (2.3)$$

or, generalizing to include momentum,

$$P(T_{l(h)}|\mathcal{R}, p) = \frac{P(\mathcal{R}|T_{l(h)}, p)P(T_{l(h)}|p)}{P(\mathcal{R}|p)} \quad (2.4)$$

$P(\mathcal{R}|p)$, the probability that any track of momentum p will induce a response \mathcal{R} in the detector is just the sum of the probabilities that each particle type (lepton, hadron) will both have momentum p and will create response \mathcal{R} , so that Equation 2.4 can be written

$$P(T_{l(h)}|\mathcal{R}, p) = \frac{P(\mathcal{R}|T_{l(h)}, p)P(T_{l(h)}|p)}{\sum_{i=l,h} P(\mathcal{R}|T_i, p)P(T_i|p)} \quad (2.5)$$

The quantities $P(\mathcal{R}|T_{l(h)}, p)$ are in fact the overall probability due to all PID detectors (d).

$$P(\mathcal{R}|T_{l(h)}, p) = \prod_d P_d(\mathcal{R}|T_{l(h)}, p) \quad (2.6)$$

These ‘‘parent distributions’’ $P_d(\mathcal{R}|T_{l(h)}, p)$ describe the detector response \mathcal{R} (typically an energy deposit in the detector) to a lepton (hadron) of momentum p . $P(T_{l(h)}|p)$ are the ‘‘flux factors’’ and describe the flux of leptons (hadrons) at momentum p .

The PID value of a track is evaluated by comparing the lepton and hadron probabilities for the track:

$$PID = \log_{10} \frac{P(T_l|\mathcal{R}, p)}{P(T_h|\mathcal{R}, p)}. \quad (2.7)$$

Including the log allows for simple definition of leptons ($PID > 0$) and hadrons ($PID < 0$). In addition it turns the products into sum so that the total PID can be written

$$PID = \sum_d \log_{10} \frac{P_d(\mathcal{R}|T_l, p)}{P_d(\mathcal{R}|T_h, p)} - \log_{10} \frac{P(T_l|p)}{P(T_h|p)} \quad (2.8)$$

$$PID_{detector} = \log_{10} \frac{P_d(\mathcal{R}|T_l, p)}{P_d(\mathcal{R}|T_h, p)} \quad (2.9)$$

$$\Phi = \log_{10} \frac{P(T_l|p)}{P(T_h|p)} \quad (2.10)$$

where the “flux factor” Φ has been defined.

Both the parent distributions and the flux factors were extracted from data. To construct the parent distributions the particle identity was determined by making hard cuts on the other PID detector responses. This created a clean sample of each particle type from which the precise detector response could be observed. The particles fluxes catalog how many particles of each type were produced, which requires accurate particle identification. Thus, to produce the fluxes an iterative approach was used. Initially the lepton and hadron fluxes were assumed to be equal (making $\Phi = 0$) and the PID value of each track was determined. From these rough PID values fluxes were calculated. Then, the PID was recalculated, including the newly produced flux factors, which allowed for the fluxes to be re-determined. This cycle was repeated until the flux values converge, which typically took 2-3 iterations.

Both parent distributions and flux factors were recalculated for each data production from the μ DST files. The μ DST production had to be rerun after the PID input was calculated to include the PID values in the μ DST tables. The μ DST tables include variables PID2, PID3, and PID5, defined as:

$$PID2 = PID_{Preshower} + PID_{Calorimeter} \quad (2.11)$$

$$PID3 = PID_{Preshower} + PID_{Calorimeter} + PID_{RICH} \quad (2.12)$$

$$PID5 = PID_{TRD} \quad (2.13)$$

such that PID3+PID5 makes use of all the PID detector information. When a detector could not determine a PID value for a track for any reason, a PID_d value of -999 was returned as an error flag and used in the calculation of $PID2$, $PID3$ and $PID5$.

Unfortunately, the information stored in the μ DST files does not allow access to the individual detector PID values. This was typically not a problem, however, it does unnecessarily exclude some tracks where a single detector fails (giving the value -999) while the other three detector are operating fine and a reliable

PID value could be calculated from these three detectors. This situation was particularly common when two particle tracks were very close together. This could result in confusion for the detector and not allow for a PID value to be calculated by that detector. In the analysis presented here, these events are vital as they correspond to small ϕ_h values and their exclusion could result in the measurement of false $\cos n\phi_h$ modulations. Luckily, there is a simple solution; the PID code can also be run by directly by analyzers. It provides the PID values calculated by each detector individually and thus allows analyzers to carefully choose which detectors to include. The effect of this careful choosing of PID can be seen in Figure 2.3 where a comparison is shown between the hadron events selected when all PID detector are taken (the standard PID3+PID5) and when events where any single PID detectors is disregarded if it returned an error code of -999. In addition, since this plot was made from Monte Carlo data, all true hadrons are also shown. The comparison is made separately for positive and negative hadrons, both when the hadron is alone in the detector half and when it is accompanied by the scattered beam lepton. The distributions are shown versus the x-distance between the hadron and lepton, as calculated at the front of the calorimeter. There is no inefficiency when hadrons are alone in the detector half but a clear inefficiency is seen when both tracks are in the same detector half. Using the scheme outlined above, this inefficiency is corrected for almost perfectly.

Hadron-type identification

As the author has done extensive work on this subject, the next chapter, Chapter 3, is devoted to the explanation of hadron-type identification with the RICH detector.

2.5.6 Data quality

One additional input was used by analyzers: the data quality burst list. Here, a 32-bit hexadecimal number, provided by the “data cops” team, encodes such information as the reliability of target state and detector performance, reasonable measurements for deadtime and luminosity, and information recorded in the logbook while data taking. By carefully masking off the bits not relevant for a given analysis analyzers can then select only bursts where the data taken was of sufficiently high quality to be included in analysis.

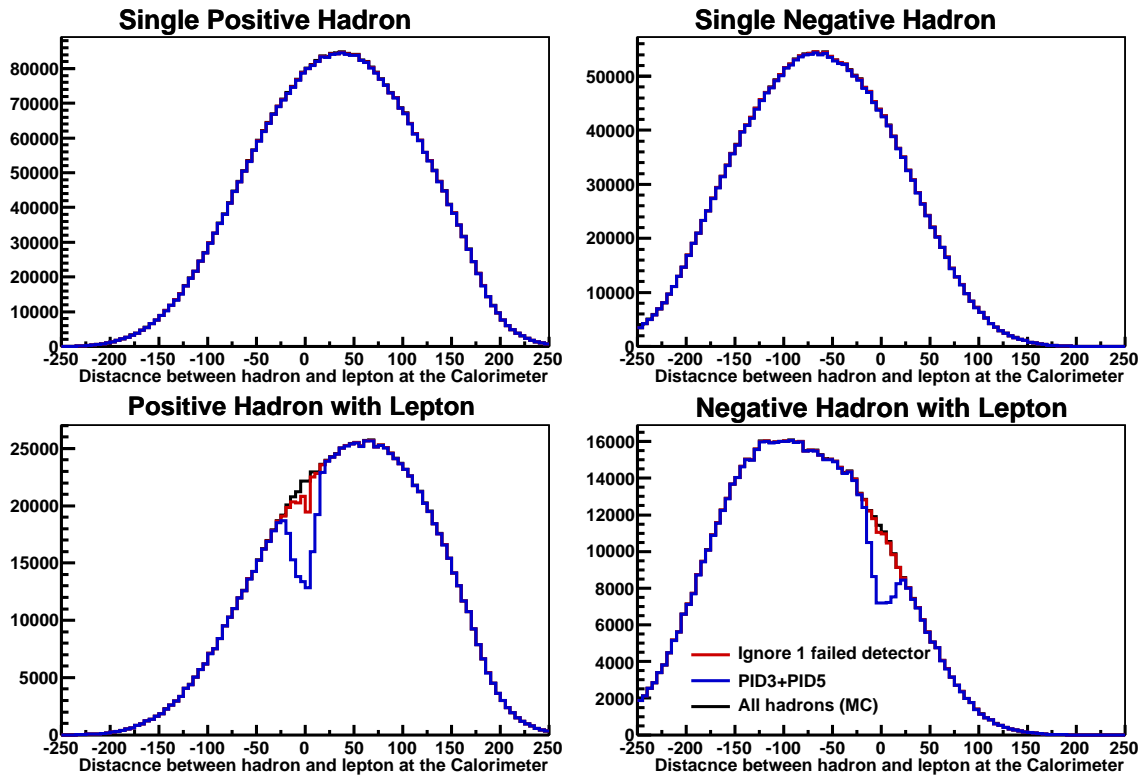


Figure 2.3: Comparison of different particle identification schemes for MC events. The x-distance (observed at the front of the calorimeter) between a hadron and the scattered beam lepton for positive (left) and negative (right) hadrons are shown when the lepton and hadron are in opposite (top) or the same (bottom) detector half. When the two particles are in the same half PID3+PID5 (blue) shows an inefficiency compared to perfect PID (black). This inefficiency is mostly recovered if the modified PID value described in the text (red) is used.

Chapter 3

Improved particle identification with the RICH detector

The HERMES Ring Imaging Cherenkov (RICH) detector (described in section 2.3.3) recorded Cherenkov light “hits” on the PMT matrix. Translating this information into a particle type is the work of software and the subject of this chapter.

Over the history of HERMES there have been several increasingly better algorithms for the RICH particle identification. These are summarized here, with the work of the author, EVT, discussed in the greatest detail in the last sections of the chapter.

3.1 Indirect Ray Tracing (IRT)

The Indirect Ray Tracing (IRT) algorithm was the first attempt to reconstruct particle type from the RICH detector readout and is describe in detail in [15]. The basic idea is that, given tracking information and RICH PMT hits, the Cherenkov-photon emission angle can be reconstructed. The distribution of observed photon angles is compared to the expected angle for each particle type and the most likely particle type is determined.

The overall algorithm is depicted schematically in Figure 3.1 and proceeds as follows:

- loop (all tracks in this detector half)
 - loop (aerogel / gas radiator)
 - * loop (PMT hits)
 - Assume emission point is along the particle track, in the center of the radiator
 - Use known information (center of spherical mirror, location of PMT in array, track momentum) to calculate the emission angle θ of this photon
 - * make a histogram of angles for all PMT hits (Figure 3.1 top)
 - * loop ($h = \pi, K, p$)

- From track momentum and assumed particle type h calculate expected theoretical radiation angle θ_h^{th}
 - Compute the average angle $\langle\theta\rangle_h$ from the distribution of observed angles within a 4σ window around θ_h^{th} , (Figure 3.1 bottom). This window minimizes the inclusion of photons from other tracks while allowing for a moderate spread in angles due to detector effects.
 - Calculate the likelihood $L_h^{radiator} = \exp\left[-\frac{(\theta_h^{th}-\langle\theta\rangle_h)^2}{2\sigma_{\langle\theta\rangle}^2}\right]$ that particle type h would produce this average angle $\langle\theta\rangle_h$, taking into account the average angle resolution $\sigma_{\langle\theta\rangle}$
 - If the particle is below threshold (i.e. where no hits should have been produced) and θ_h^{th} is undefined, or above threshold but no hits are detected, a predefined likelihood is assigned which smoothly connects with the likelihood behavior in well defined regions.
- Determine the total probability $L_h^{tot} = L_h^{aerogel} L_h^{C_4F_{10}}$ for each possible particle type h
 - Choose most likely particle type for this track; if two particle types are equally likely the track is unidentified (type “X”)
 - Compute the RICH Quality Parameter $rQp = L_{2^{nd}}^{tot}/L_{1^{st}}^{tot}$ as the ratio of the likelihoods for the most likely particle type and the 2^{nd} most likely particle type.

The advantage to the IRT method is that it is fast and not computationally intensive. However, it has the lowest accuracy of the methods discussed in this chapter. Only a single radiation point is chosen at the center of each radiator from which to reconstruct the emission angle. In addition, there is no differentiation between PMT hits coming from different tracks or different radiators: all PMT hits are assumed to be from every track and every radiator.

3.1.1 Further corrections: P-matrices

While IRT did a fairly good job identifying particle type, it had known inefficiencies. These inefficiencies could be corrected for, on average, by performing an *unfolding*. A matrix is constructed, $P(r, t)$ where r is the reconstructed particle type ($r = \text{pion, kaon, proton, X}$) including unidentified particles (X) and t is the true particle type ($t = \text{pion, kaon, proton}$). This matrix describes the inefficiency and contamination of the RICH particle identification such that the measured yields R of type r are related to the true yields T of type t in this way:

$$R(r) = P(r, t)T(t) \tag{3.1}$$

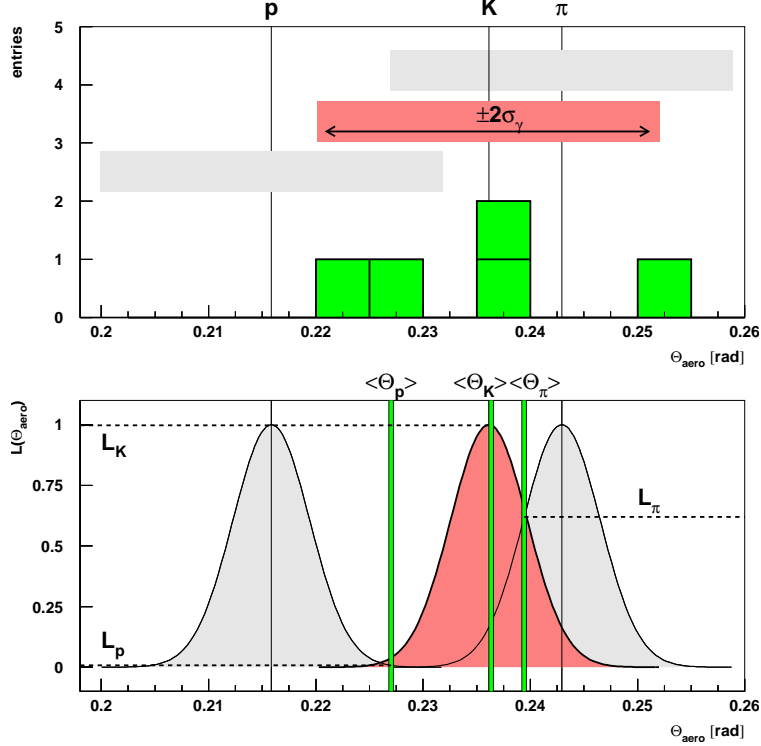


Figure 3.1: Schematic of the IRT algorithm, as described in the text

Thus to recover the true yields from those measured, given a known P-matrix, one can truncate the X row from the P-matrix ($P \rightarrow P'$), invert, and apply to the measured yields:

$$T'(t) = P'^{-1}(t, r)R(r) \quad (3.2)$$

To further refine this correction separate matrices can be made for different kinematic conditions that effect the performance of RICH. In particular, matrices were generated in 1 GeV bins of hadron momentum and for different topologies (tracks per detector half = 1, 2, 3 or more). This P-matrix unfolding can then be performed on a track-by-track level, giving each hadron track a pion, kaon, and proton weight.

Such P-matrices were constructed at HERMES from Monte Carlo (MC) simulations of the spectrometer, as described in detail in [16]. Earlier attempts were made to determine P-matrices entirely from data: data was analyzed to reconstruct decay particles of known mass using all hadrons, thus giving the true identity of the particles in the peak. However, the limited kinematics and statistics of this method did not allow for a full P-matrix to be computed directly. Instead, a MC was tuned to the decay particle yields by adjusting the mirror roughness parameter in the RICH simulation. In addition, the MC was alternatively tuned to produce the correct electron yields, leading to a different mirror roughness parameter. Finally, the

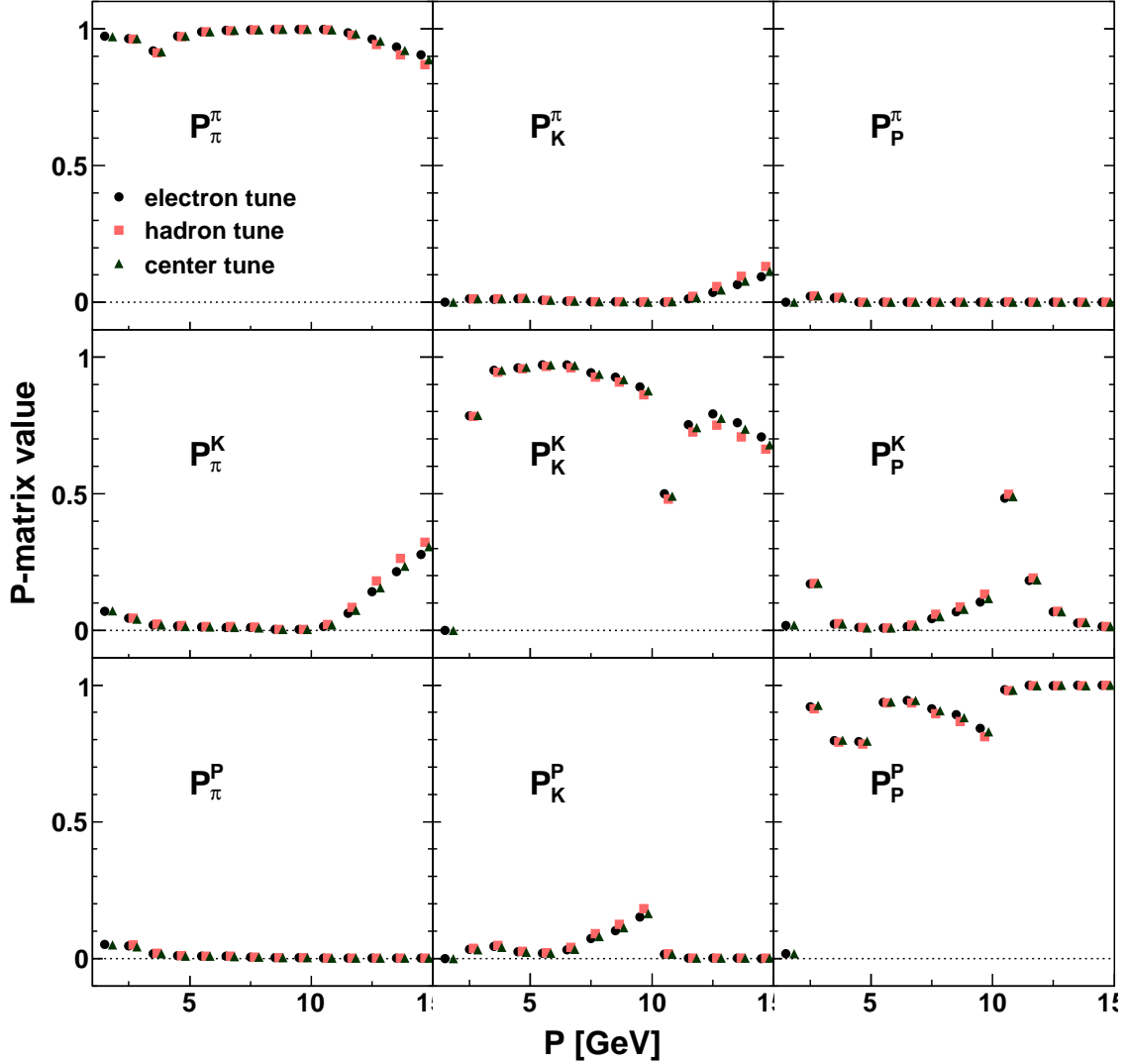


Figure 3.2: IRT P-matrices for a single track in the detector half. P_i^t is the probability that a hadron of type t is identified as type i , as a function of the hadron momentum P . Diagonal panels show the identification efficiency while off-diagonal panels show contamination.

two mirror roughness parameters were averaged and P matrices were produced from MCs run with each of the three mirror roughness parameters, resulting in three P-matrices: the “hadron-tune”, “electron-tune”, and “center-tune” P-matrices. The center-tune P-matrix was used for physics analysis while the other two provided alternatives which produced a systematic error on the RICH hadron identification correction. The comparison between the different tunes for the case of a single track can be seen in Figure 3.2

3.2 Direct Ray Tracing (DRT)

The Direct Ray Tracing (DRT) algorithm simulates a PMT hit pattern $N^{(h,t,r)}(i)$ based on the track (t) kinematics and a particle type hypothesis (h) in the radiator r . In the aerogel 360 photons are generated at two vertex positions, while for the larger gas volume 10 vertex positions are used to generate 360 photons. Hit patterns are generated for each particle type hypothesis ($h = \pi, K, p$) and the likelihood of this hypothesis is calculated by comparing the simulated hit pattern to the actual hit pattern recorded (Ref. [17]):

$$L^{(h,t)} = \sum_i \log[P_{PMT}^{(h,t)}(i)C_{PMT}(i) + \bar{P}_{PMT}^{(h,t)}(i)(1 - C_{PMT}(i))]. \quad (3.3)$$

Here $C_{PMT}(i)$ is the hit pattern from data, stating if PMT i is hit (1) or not hit (0), and $P_{PMT}^{(h,t)}(i)$ is the probability of a hit given the kinematics of track t and hypothesis h:

$$P_{PMT}^{(h,t)}(i) = 1 - \exp\left(-\sum_r \left[\frac{N^{(h,t,r)}(i)}{\sum_i N^{(h,t,r)}(i)} * n^{(h,t,r)}\right] - B(i)\right) \quad (3.4)$$

This expression contains a sum over the hits from both radiators (r), which is weighted with the total number of expected PMT hits due to a track of the given hypothesis and kinematics on radiator r ($n^{(h,t,r)}$)¹. The probability of no hit is simply $\bar{P}_{PMT}^{(h,t)}(i) = 1 - P_{PMT}^{(h,t)}(i)$. The $B(i)$ “background” term was added to take into account the probability of a random PMT firing due to electronic noise and was given a constant value of 0.0001.

The most likely particle type is evaluated and, as in IRT, the rQp is calculated as the ratio of the second to the first most likely choice.

3.3 The RICH PID Scheduler and “BEST”

The RICH PID Scheduler (RPS) [18] is not a separate RICH method but rather a way to optimize the use of existing methods. Since DRT is more computationally expensive and time consuming than IRT, when it was created it was not possible to run DRT on each event.

The flow of the RPS is diagramed in Figure 3.3. First a track is put into a bin in momentum (1 GeV bins from 0-30 GeV), track multiplicity (1, 2, 3, > 3 tracks in the detector half), and for 2-track events, the track topology, as parameterized by an overlap parameter, which evaluates the amount the rings from

¹ The total number of photons generated ($\sum_i N^{(h,t,r)}(i) = 360$) is much larger than would be expected physically ($n^{(h,t,r)} \sim 0 - 10$), so the probability function contains the simulated hit pattern ($N^{(h,t,r)}(i)$) scaled by the ratio of expected to generated photons ($n^{(h,t,r)}/\sum_i N^{(h,t,r)}(i)$).

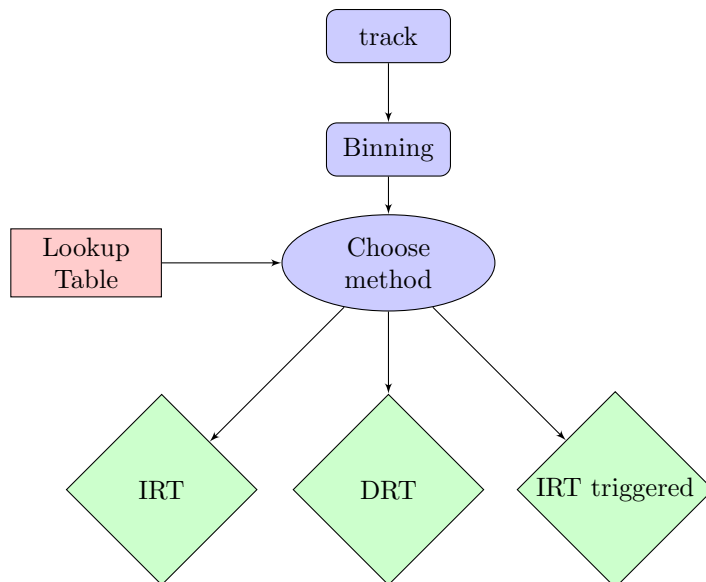


Figure 3.3: RICH PID Scheduler (RPS) structure

the tracks should overlap on a 0-1 scale. Once the multi-parameter bin is determined for the track a lookup table is consulted to decide which method to run: IRT, DRT, or potentially both with the *IRT triggered* method. The lookup table is constructed from MC by evaluating the accuracy of each method in each bin.

The *IRT triggered* method is shown schematically in Figure 3.4. First the IRT method is run and the resulting rQ_p is compared to a normalization number in this bin taken from a lookup table that is again constructed from MC. If the quality of the IRT identification is sufficient, the IRT result is taken. If not, DRT is also run and the better of the two methods (as determined by comparing the normalized rQ_p from each method) is taken as the best result.

In the μ DST tables, the $g1Track$ table links to the $smRICH$ table via the links IRT, DRT, BEST, and EVT (explained below). IRT and DRT point to the corresponding rows in the $smRICH$ table with the results from each method; if a given method was not run the link is set to NULL. BEST point to either IRT or DRT. If only one of the two methods was run, BEST point to this method, otherwise BEST points to the better method, as indicated by the IRT triggered method (Figure 3.4).

It should also be noted here that although significant work went into generating the IRT P-matrices, P-matrices for DRT and BEST were never constructed. Use of the IRT P-matrices for DRT or BEST, although it has often been done in the history of HERMES, is fundamentally wrong. The P-matrices, as described in section 3.1.1, describe the inefficiency of the method. DRT and BEST have different (generally better) efficiencies, so using the IRT P-matrix over corrects the observed yields in some regions. The result is pure nonsense. Further, the electron-, hadron- and center- tunes come from MC tuned to the IRT results.

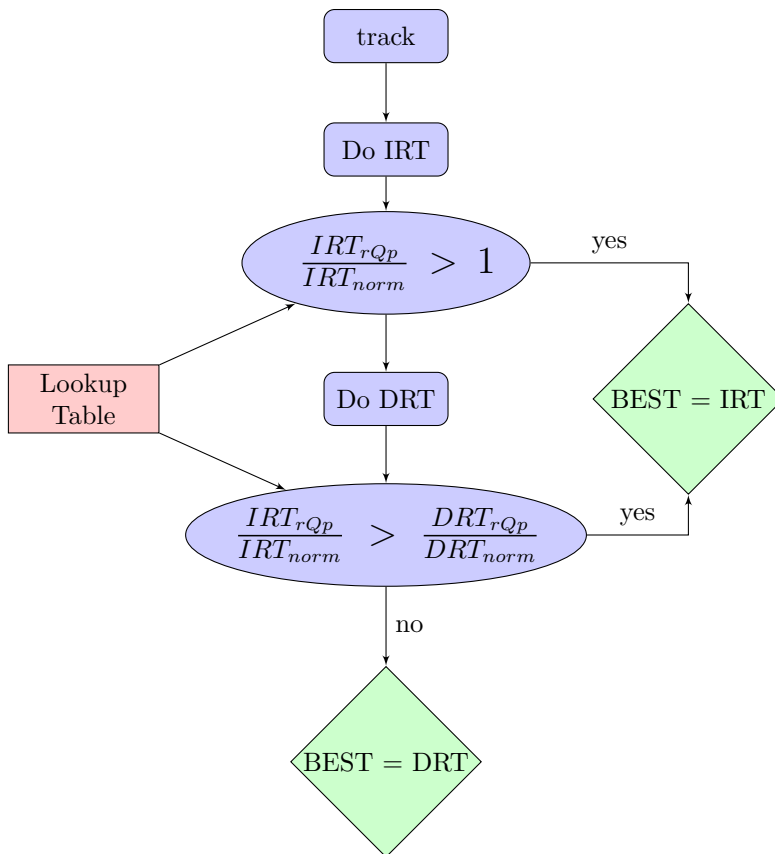


Figure 3.4: The IRT triggered algorithm

Tuning to DRT or BEST would presumably also change this tuning and although it may not affect the central values could have an effect on the systematic error derived from using the three alternate tunes.

3.4 An event-level algorithm: EVT

More refined analyses at HERMES, and in particular the $\cos n\phi_h$ analysis, demand more precise RICH particle identification. A new method, EVT, was implemented by the author and is described here.

3.4.1 Motivation

As with electron/hadron PID (see section 2.5.5) hadron identification is difficult when two tracks are close together, and in particular when the scattered lepton is near the hadron. This is because the large rings (see Figure 2.2a) from the lepton can overlap and overwhelm the smaller, fainter (or non-existent) rings from the hadron. This is depicted schematically in Figure 3.5. Here a proton (blue x) that is below threshold for both radiators enters the RICH very close to a lepton (black x) which produces rings in both radiators.

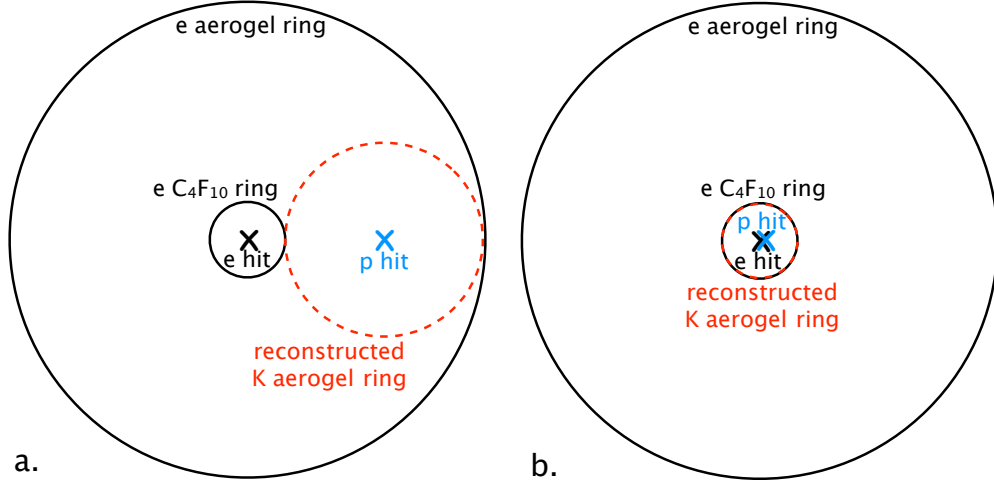


Figure 3.5: Schematic of how a proton (blue x) can be misidentified as a kaon (red ring) when it enters the RICH close to an electron (black x and ring)

The PMT hits from the lepton are considered when determining the identity of the hadron with both the IRT and DRT methods. These PMT hits can “fake” the correct angle for a kaon ring and lead to the misidentification of the proton. From Figure 3.5 it is clear that such a misidentification can occur not only when the two tracks are very close (Figure 3.5b) but also when the proton is somewhat offset from the lepton track, as in Figure 3.5a. This behavior is also seen in the data. In Figures 3.6 and 3.7 the distance between the two tracks is shown for the cases that the two tracks are in the same (top row) or opposite (center row) detector halves. The overall shift to the right (left) for positive (negative) hadrons is due to the bending in the spectrometer magnet. Both the lepton and hadron tracks are bent but as the hadron is generally lower momentum it tends to be bent more. When the two tracks are in the same detector half the distributions show some inefficiency near zero (where the tracks are close together). The center-right plot for (anti)protons shows a strange triple-peaked distribution which suggests that the schematic of Figure 3.5 holds some truth.

In the bottom rows of Figures 3.6 and 3.7 the same-half distributions are shown after RICH unfolding. Since the unfolding is not binned in track separation it is unable to correct for the inefficiency. However, worse than this, the (anti)protons in the lower right plots actually acquire unphysical negative yields in some regions of Δx_{RICH} . This is due to hadrons that are erroneously identified as kaons (and pions) and contribute negative weights to the proton yield. This plot provides definitive evidence that in these regions of Δx_{RICH} an unusually high (not accounted for in the P-matrices) number of protons are misidentified as kaons and pions.

While these results are not good, in most analyses the distance between the lepton and hadron is not a

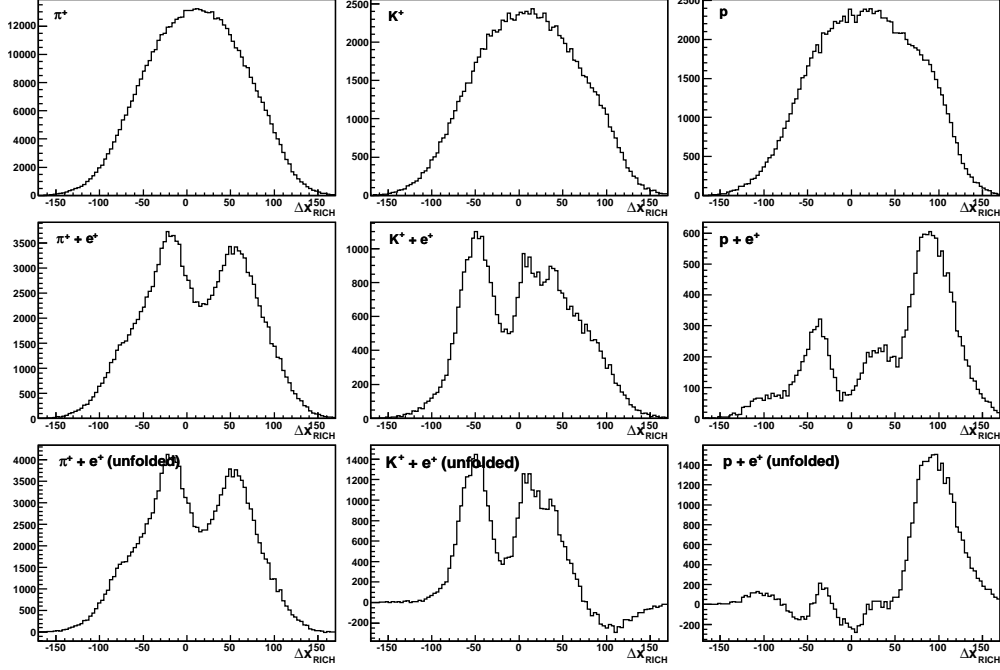


Figure 3.6: Distance between hadrons and the scattered beam lepton at the front of the RICH detector (Δx_{RICH}) for positive pions (left), kaons (center), and protons (right) identified with IRT when the lepton is in the opposite detector half (top) or the lepton is in the same half (center). The distributions after RICH unfolding for the same-half case (center row) is shown in the bottom row.

relevant variable and Δx_{RICH} is integrated over. In this case the P-matrices are able to correct, on average, the overall yields. However, as indicated previously, the $\cos n\phi_h$ analysis is sensitive to Δx_{RICH} in that an inefficiency at small Δx_{RICH} can induce a $\cos n\phi_h$ modulation. To combat this inefficiency a new RICH method was developed that simultaneously considers all tracks in the detector half.

3.4.2 Implementation

The new EVent level algorithm, EVT, builds upon the existing DRT algorithm. The improvement is to look at each event as a whole rather than individual tracks. Since the measured hit pattern in data is for all tracks together it make sense to compare this to the simulated hit pattern for the entire event. To do this Equations 3.3 and 3.4 are modified to read:

$$L^H = \sum_i \log[P_{PMT}^H(i)C_{PMT}(i) + \bar{P}_{PMT}^H(i)(1 - C_{PMT}(i))] \quad (3.5)$$

$$P_{PMT}^H(i) = 1 - \exp\left(-\sum_{r,t} \left[\frac{N^{(H_t,t,r)}(i)}{\sum_i N^{(H_t,t,r)}(i)} * n^{(H_t,t,r)} \right] - B(i)\right) \quad (3.6)$$

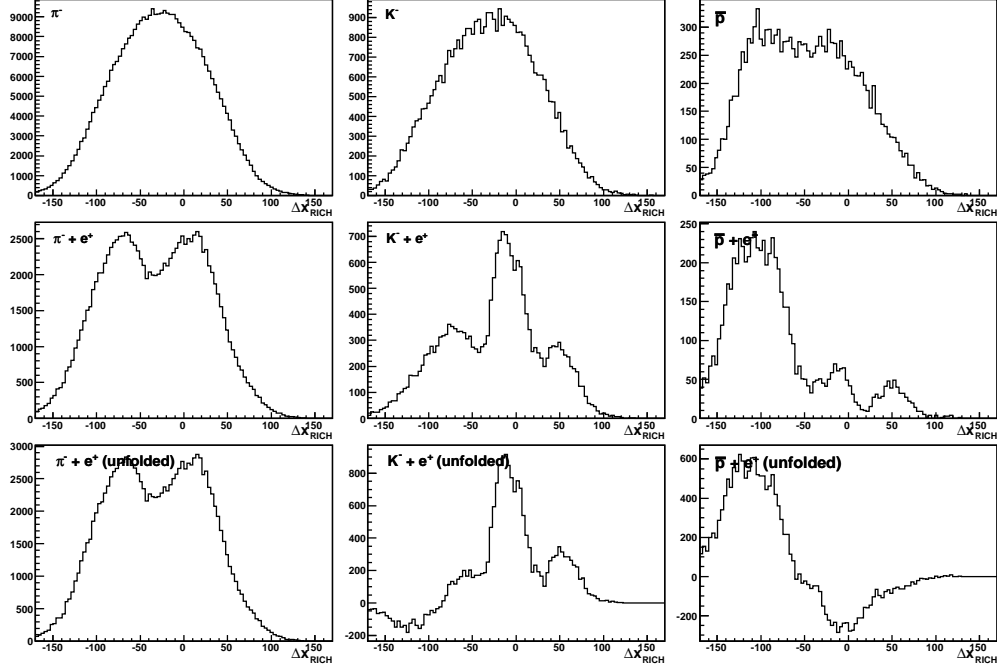


Figure 3.7: As Figure 3.6 but for negative hadrons.

Where now the probability has an additional sum over all the tracks t in the event. H is a combined particle type hypothesis, that is, a set of particle type hypotheses, one for each track in the event. Given t tracks, each with h ($=3$, pions, kaons, proton) possible hypothesis, there are a total of h^t combined particle type hypothesis H . H_t gives the hypothesis for track t given the combined particle type hypothesis H .

The computationally intensive part of the DRT algorithm is the calculation of the simulated hit patterns $N^{(h,t,r)}(i)$. Once this is done the EVT algorithm uses negligible additional time to compute the sums of these hit patterns. For a single track in the detector half EVT simply reduces to DRT and no additional computations are done. Once the likelihoods L^H are computed the most likely is chosen and the particle type of each track in the event is recorded in the μ DST files.

While the track multiplicity per event in the HERMES spectrometer rarely exceeds 3, a safety feature is implemented in the code that limits the number of tracks to 5, such that the maximum number of combined particle type hypotheses is $3^5 = 243$. Events with more than five tracks in one detector half are not analyzed by EVT and the DRT or IRT results must be used.

3.4.3 Quality parameters

The IRT and DRT algorithms each returns a quality parameter $rQp = L_{2^{nd}}/L_{1^{st}}$ given by the ratio of the likelihoods for the 2nd and 1st most likely particle type hypothesis. Because EVT does not compute

individual track particle hypotheses but rather combined track hypotheses this definition of rQp cannot be applied. Instead, the most likely combined particle type hypothesis L_{H^1} is compared to the next most likely combined particle type hypothesis that has track t identified as a different particle type, that is:

$$rQp_{EVT} = \max \left(\frac{L_{H^2}}{L_{H^1}} \right) \quad \text{with } H_t^2 \neq H_t^1 \quad (3.7)$$

Additional parameters, such as the ratio of the 1st and 2nd ($G(1,2)$) and the 1st and 3rd ($G(1,3)$) combined particle type hypothesis likelihoods were suggested in [19] where the EVT method was first conceived. In that work it was demonstrated that cuts on these parameters could clean the event sample to 98% purity (2% misidentification) while maintaining 90% of the sample. However, in this study a momentum cut of 2 GeV was made on all hadrons, which corresponds to the kaon threshold in the aerogel (Figure 2.2a). Only when all tracks in the event meet this criterion can the results in [19] be achieved. (If tracks below 2 GeV are included H^1 and H^2 may only differ in identifying a below threshold hadron as a kaon or proton, and thus $L_{2^{nd}}$ and $L_{1^{st}}$ would be identical.) However, in data most events contain low momentum particles, in particular 1 – 2 GeV pions which produce rings and can be well identified. Eliminating events with tracks less than 2 GeV is not an option, while ignoring these tracks undermines the EVT procedure as the tracks may be pions or electrons which produce hits in the RICH. Thus, after investigation, these additional quality parameters were abandoned.

3.4.4 Backgrounds, dead tubes, and hot tubes

In the course of upgrading the RICH algorithm, the background term $B(i)$ in Equation 3.6 was also investigated. $B(i)$ was evaluated from data by counting the average number of hits in each PMT when there is no track in that detector half. Background values of ~ 0.005 on average were observed in the data with a structure that shows the highest values nearest the beam, indicating that the origin was not merely electronic noise. An example can be seen in Figure 3.8 for the polarized 2000 data. Here the x-axis refers to the PMT number from 1 to 1934. The numbering of the PMTs is from top to bottom, left to right, such that the periodic spikes every ~ 26 PMTs correspond to those PMTs closest to the beam where the most particles are seen. The overall growth in the center corresponds to the left-right center of the detector, again where more particles are concentrated. These “background” events where PMT hits are seen with no corresponding tracks can be viewed with the HERMES RICH Event display (HeRE), as shown in Figure 3.9. It is clear from this figure that these are not random noise hits but in fact form a ring. Both the background structure of Figure 3.8 and trackless rings in the HeRE display also appear in MC, confirming that this “background”

PMT background levels

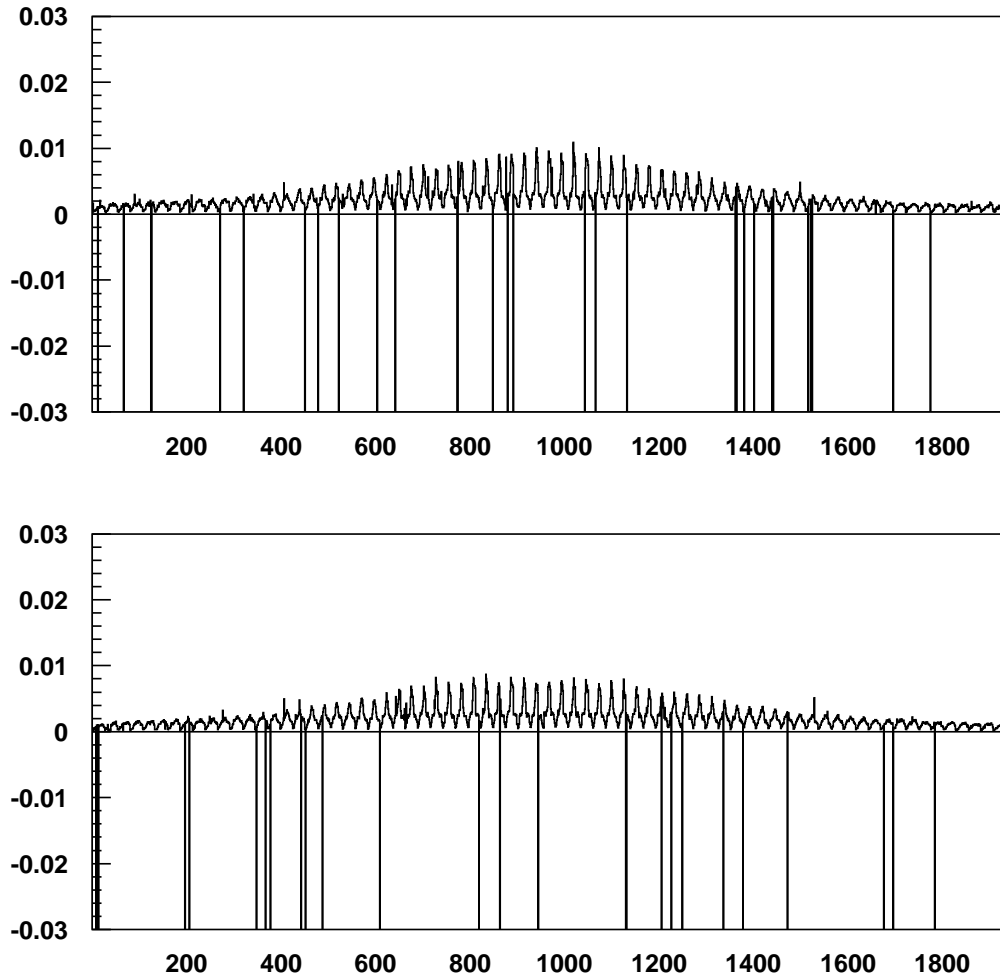
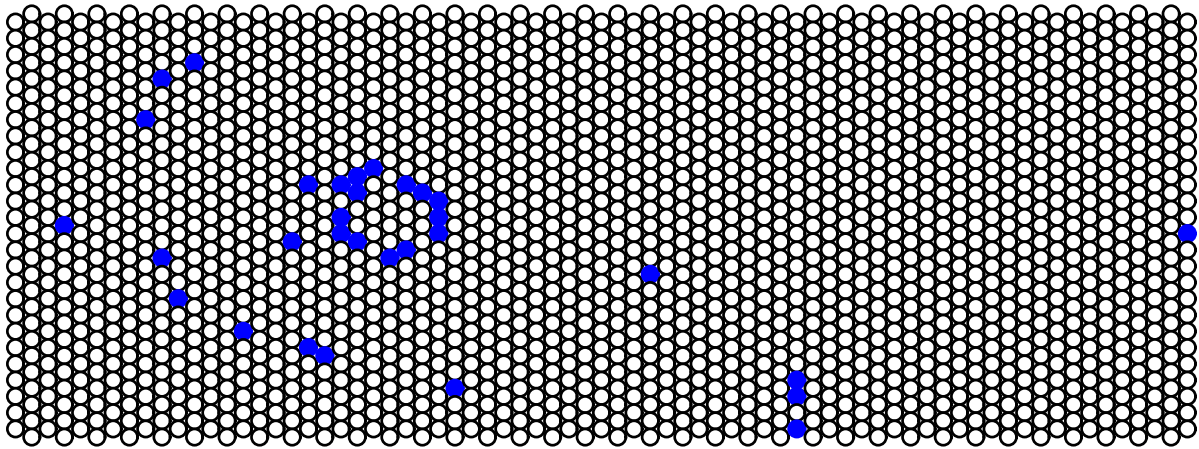
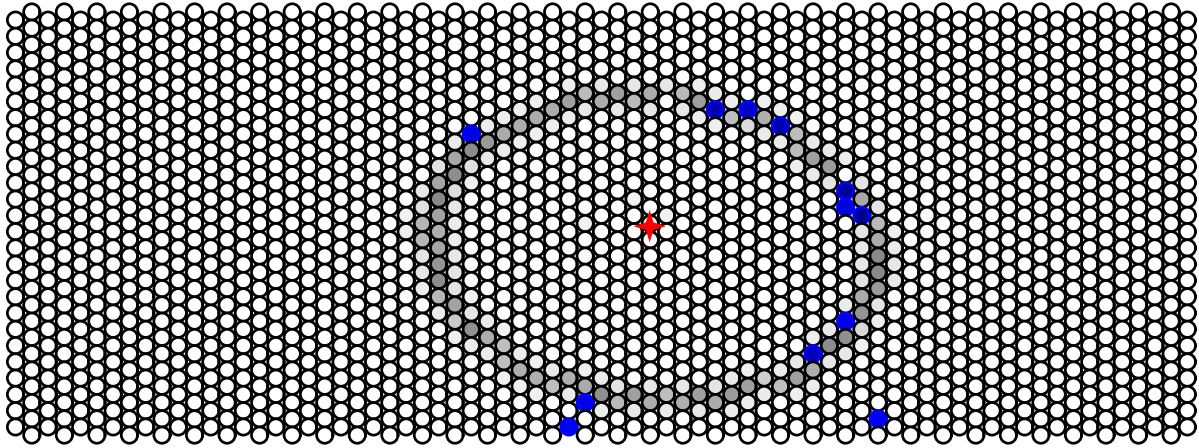


Figure 3.8: Backgrounds $B(i)$ for the top (upper plot) and bottom (lower plot) detector from the polarized 2000 data. Negative values indicate a “hot” or “dead” PMT.

is from physical particles not tracked by the spectrometer. MC studies indicate that the primary source is $\pi^0 \rightarrow \gamma\gamma$ decays, generating photons which pair-produce near the RICH.

While the $B(i)$ term can only provide an average treatment (i.e., averaged over many events) of such untracked rings it is the simplest way to take this physical background into account using the existing algorithm. MC tests using $B(i)$ determined from data showed that it gave superior particle identification to using the constant 0.0001 value previously used.

Extracting $B(i)$ from different subsets of the data showed that while $B(i)$ is relatively insensitive to the type of target gas it is affected by the gas density, showing higher values with a higher density target. When applied to MC a larger $B(i)$ favors (anti)protons while a smaller $B(i)$ favors kaons. In each case there is a trade-off between efficiency and contamination. Since the overall flux of pions is largest, it is relatively



Run: 12345

Event: 57596322

Figure 3.9: Background event from the 2005 data. The RICH top half (upper panel) has one track (red star) and several PMT hits (blue) which are reconstructed into a ring (gray), while the lower half (lower panel) also has several PMT hits (blue) which seem to form a ring structure, but there is no associated track.

unaffected by changing the background while the very small antiproton flux shows relatively large changes when using a different $B(i)$. Section 3.4.5 discusses how this can be treated as a systematic error.

$B(i)$ was extracted from the standard-density target data (i.e. polarized target data for 1998-2005 and normal running for 2006-2007; not the high-density target end-of-fill data) for each data year and used for the RICH algorithm applied to all of the data from that year.² This scheme is used for both simplicity of producing the data and for consistency in the data. Using a background file for the high-density target

² The 2007 data is an exception: the background is extracted from all of the data, including the high density target data. This increases the background values by about 20%. The 2007 background is different for historical reasons and in principle should be recalculated with only the regular density target data for consistency. However, at the time of writing no reproduction of the 2007 data is scheduled.

data which is extracted from the high-density target data itself would change the RICH PID but would *not* “correct” for the different background present in high-density target data. Said another way, using the same background file or different background files for the normal and high-density target data both lead to somewhat different RICH PID (due to the differing conditions) but the latter adds an additional complication and additional work for the production team. Ideally, both methods could be executed and the two productions could be used in systematic studies, however there is no plan to do this at the time of writing.

3.4.5 P-matrices

P-matrices for EVT were extracted from MC with both Pythia and disNG generators, tuned to HERMES kinematics. When applying the RICH algorithm to the MC productions a choice can be made for $B(i)$, including: $B(i)$ extracted from the MC production itself, that extracted from the other MC generator, or that extracted from any set of real data. Since it was observed that $B(i)$ from Pythia and disNG differ from each other and from both high and low density data, a series of P-matrices was computed using all of these possible $B(i)$'s.

In addition, the electron-, hadron- and center-tune mirror roughness parameters extracted previously for IRT were used to produce P-matrices. However, it was found that the variation in these P-matrices is smaller than that seen when the background is varied.

Finally, the shorter target cell (section 2.2) used during 2006 and 2007 data taking affects the acceptance of the spectrometer and changes the background $B(i)$ and the P-matrices. So, for the determination of the systematic error on the RICH four alternative matrices were produced from MC for each data taking period, “99” (1998-2005) and “06” (2006-2007):

center = disNG_ownBkg A disNG MC sample, with RICH identification including $B(i)$ extracted from the sample itself (“own”).

disNG_dataBkg The same disNG MC sample with RICH identification including $B(i)$ extracted from the 2000 (2006) data.

disNG_pythiaBkg The same disNG MC sample with RICH identification including $B(i)$ extracted from the Pythia MC sample.

pythia_disnkBkg A pythia MC sample with RICH identification including $B(i)$ extracted from the disNG sample.

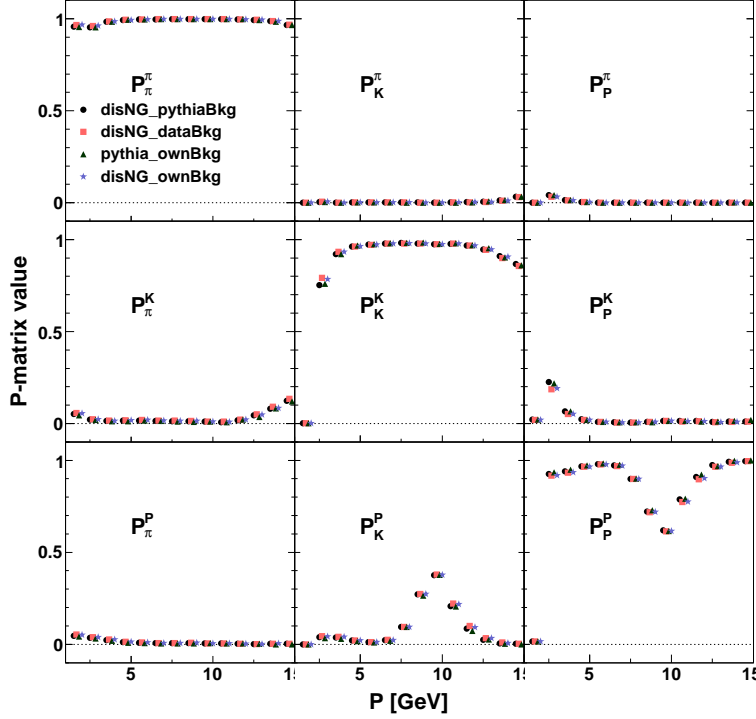


Figure 3.10: P-matrices for the EVT method for single tracks (which is simply DRT) for the 1999 geometry. Description of the four different versions can be found in the text. P_i^t is the probability that a hadron of type t is identified as type i , as a function of the hadron momentum P . Diagonal plots show the identification efficiency while off-diagonal plots show contamination.

These four P-matrices, each run through a detector simulation with the 1999 (2006) geometry, can be used by analyzers to provide a systematic uncertainty on the RICH unfolding. The 1999 P-matrices for 1, 2, and 3+ tracks are shown in Figures 3.10 to 3.12. While in most bins the different P-matrices give very similar results, differences can be seen, particularly in the lowest statistics bins for 3+ tracks at high momentum. When comparing the different P-matrices it should be noted that the disNG P-matrices come from the same statistical sample and thus differences in their central values are significant even in the presence of sizable statistical errors. The Pythia production is statistically independent from the disNG productions and so the statistical error bars should be taken into account when comparing these P-matrices.

Charge-dependent P-matrices were previously investigated for IRT, and though a small dependence was found, they were never used by analyzers. Charge dependence was investigated again with the introduction of EVT and it was quickly realized that not only the hadron charge but also, for two or more tracks in the detector half, the lepton charge is an important quantity. This points to the same problem that instigated the implementation of EVT: misidentification when two tracks are close together, which is more likely for two tracks that are of the same charge and thus bend the same way in the magnet. This can be seen clearly in the $\pi + e^+$ plots in Figures 3.6 and 3.7 where the dip near zero is more pronounced for the π^+ case.

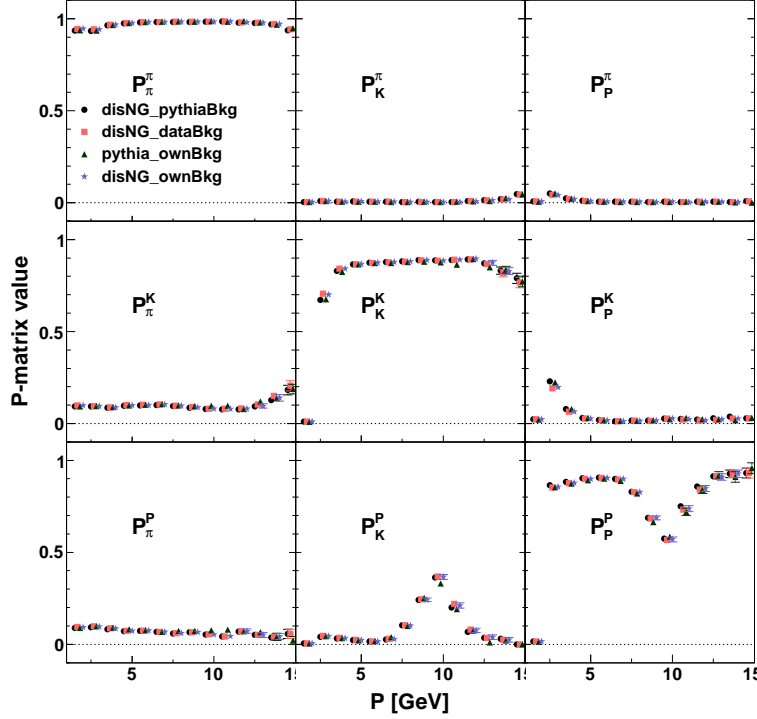


Figure 3.11: P-matrices for the EVT method for two tracks in the detector half. See Figure 3.10 for details.

To avoid producing different P-matrices for different beam charges (which would also necessitate running more MC productions) and to avoid the ambiguity of how to define charge-dependent 3+ track P-matrices, “charge-likeness” matrices were devised. They were defined as follows:

like = the track in question is accompanied by at least one like-charged track in the detector half

unlike = the track in question is the only track of this charge in the detector half

With this definition the charge of the beam becomes irrelevant since only the relative charge of tracks is considered. To be explicit, the following combinations, where the first sign is the track in question, are described as like / unlike:

like: (++) (--) (+-) (-+) (+++) (---)

unlike: (+) (-) (+-) (-+) (+--) (-++)

It was found that, while the IRT P-matrices show a clear dependence on charge-likeness, the EVT P-matrices are nearly independent of the charge-likeness. This is another confirmation that EVT is able to clearly identify tracks that are close together as well as tracks that are well separated. To keep things simple for analyzers only the traditional charge-combined P-matrices are provided.

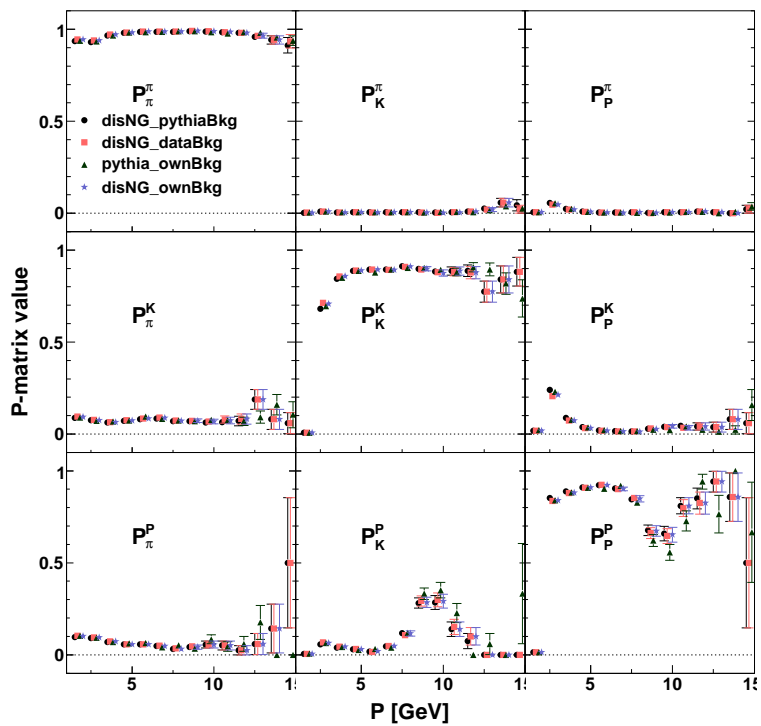


Figure 3.12: P-matrices for the EVT method for 3 or more tracks in the detector half. See Figure 3.10 for details.

3.4.6 Results and comparisons between methods

The EVT P-matrices look promising, showing improved identification compared to IRT. A comparison between IRT and EVT P-matrices, both extracted from the same MC sample, is shown in Figures 3.13 to 3.15. With the exception of 8 - 12 GeV protons (near the kaon C_4F_{10} threshold, see Figure 2.2a), which are rare at HERMES, EVT has better efficiency and lower contamination in all bins. Even if the IRT P-matrices could perfectly correct for the method's inefficiencies, the superior performance of EVT is an advantage because the weights introduced in the unfolding inflate the statistical errors of the measured yields. However, the primary motivation for EVT was the position dependence seen in IRT in Figures 3.6 and 3.7. The same quantity is shown in Figures 3.16 and 3.17 for both IRT and EVT. As hoped, the low efficiency at small Δx_{RICH} values is much less pronounced in the EVT results and the EVT yields never become negative after unfolding. As indicated by the P-matrices, the higher accuracy of EVT means that fewer events are moved between hadron types and so the “raw” (2nd row) and unfolded (bottom row) results for EVT are very similar to each other. Overall, EVT is a clear improvement over IRT and enables the extraction of observables which are sensitive to relative track position.

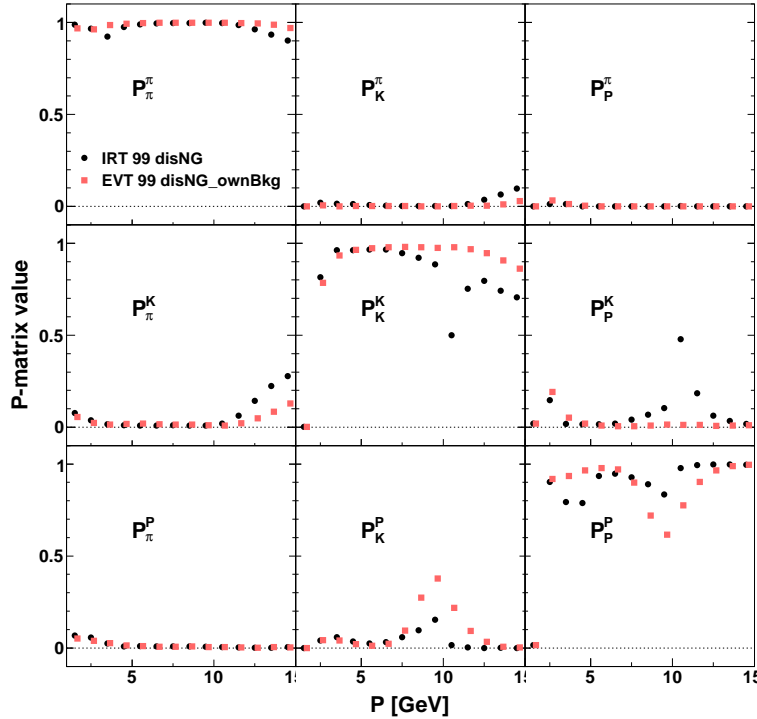


Figure 3.13: P-matrices for the IRT and EVT (DRT) methods for a single track in the detector half. See Figure 3.10 for details.

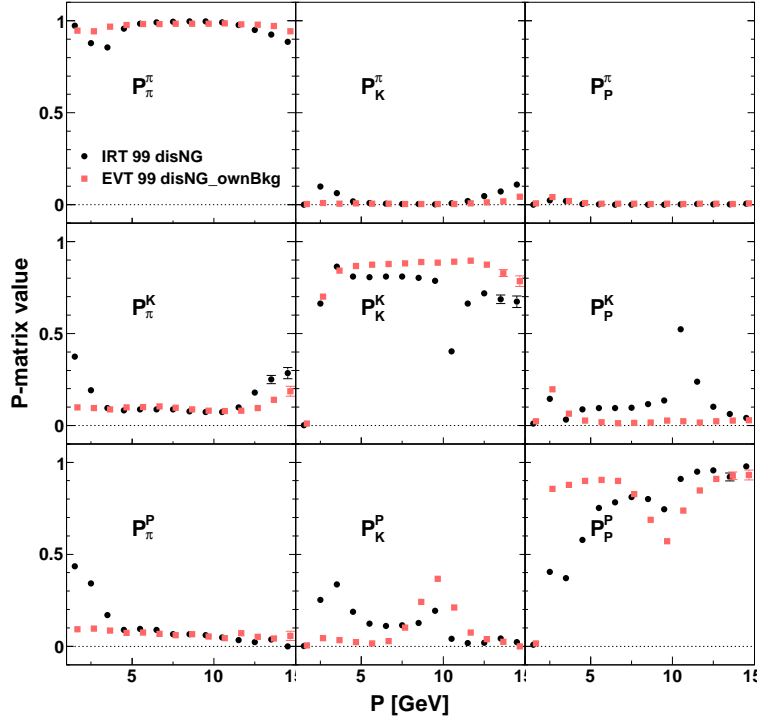


Figure 3.14: P-matrices for the IRT and EVT methods for a two tracks in the detector half. See Figure 3.10 for details.

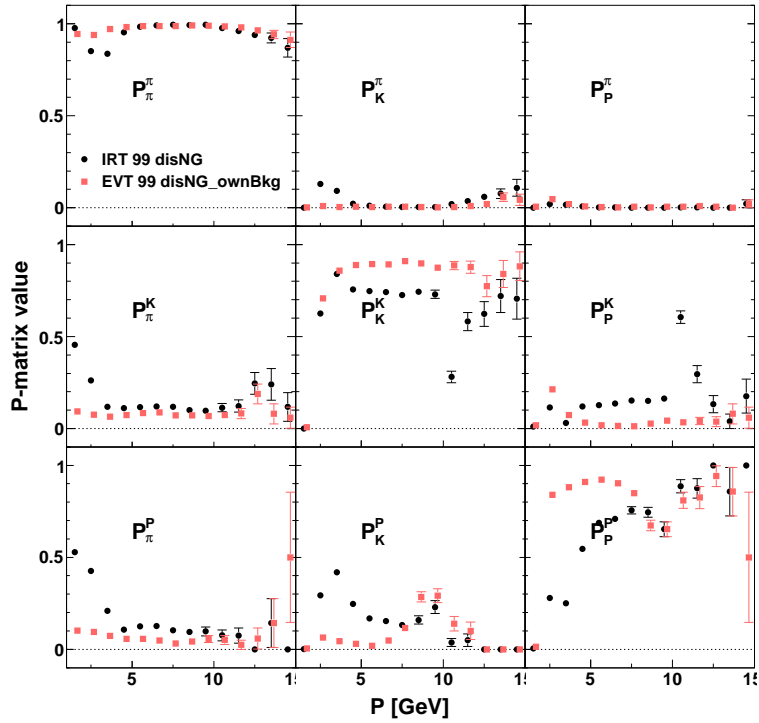


Figure 3.15: P-matrices for the IRT and EVT methods for a three or more tracks in the detector half. See Figure 3.10 for details.

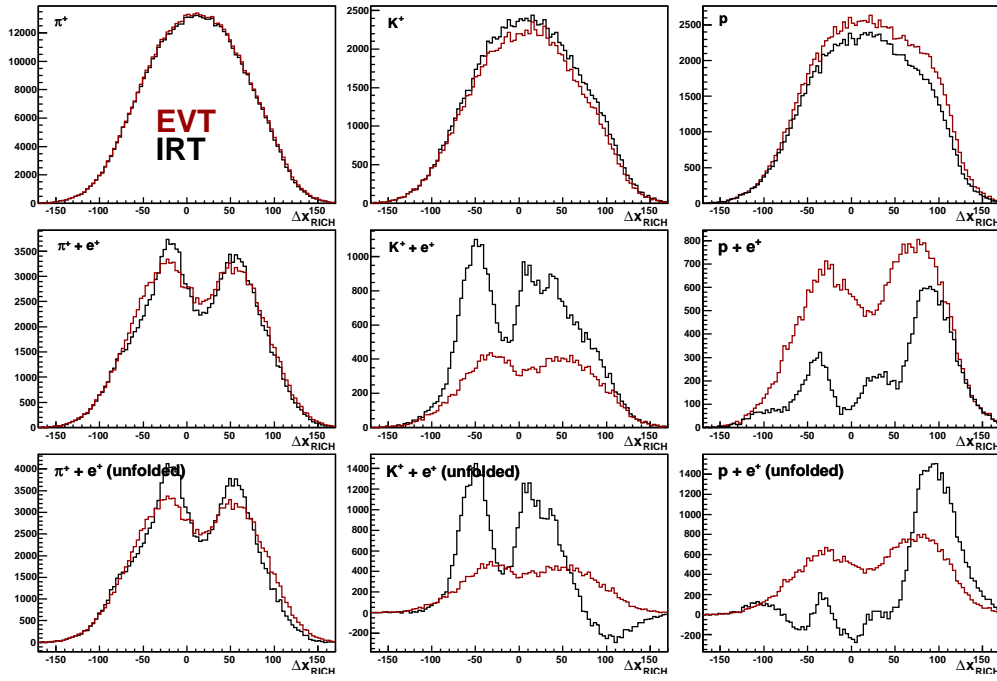


Figure 3.16: As Figure 3.6 but for both the IRT (black) and EVT (red) methods.

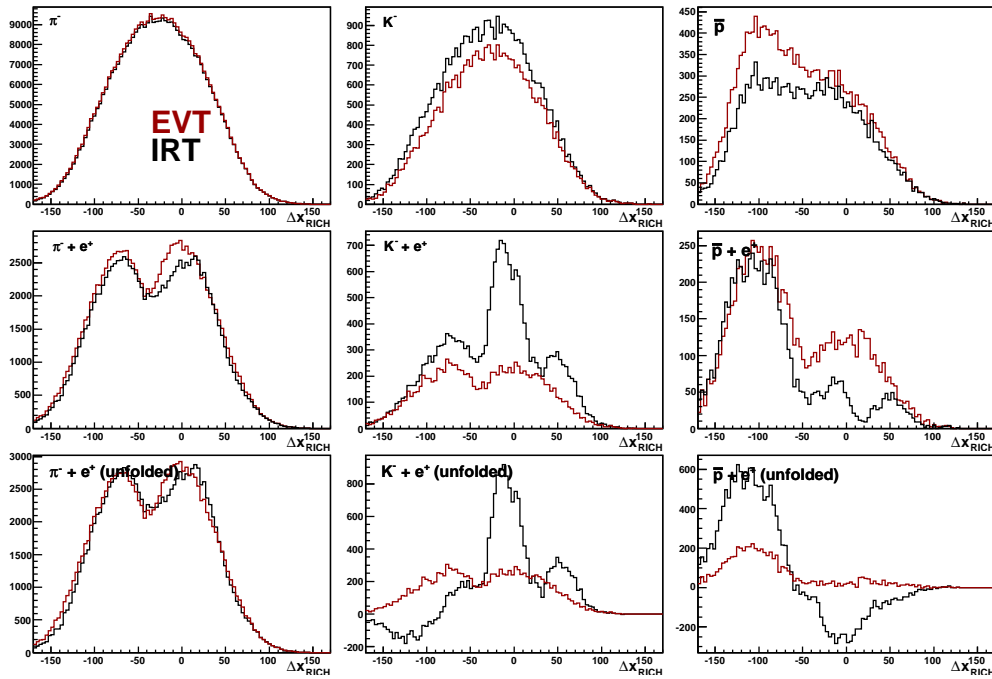


Figure 3.17: As Figure 3.16 but for negative hadrons.

Chapter 4

Data analysis procedure

This chapter explains how HERMES data was analyzed to extract the $\cos n\phi_h$ moments described in Section 1.2.2.

4.1 Overview

The analysis procedure is complex and an outline is provided here so that the reader does not get lost in the details presented later in the chapter.

Data selection Data is selected based on quality criteria, constraints from the detector and DIS kinematics.

It is then binned in a 5-dimensional vector in the variables x , y , z , $P_{h\perp}$, and ϕ_h , and normalized to the total DIS yield.

MC productions The Pythia MC generator is used to produce events at the Born-level, which are binned in the same way as the data. Another Pythia production includes radiative corrections and a full detector simulation; these events are reconstructed with the production chain used for data.

Smearing matrix A matrix is constructed from the reconstructed MC that describes the migration of events between bins; this is then normalized with the Born-level MC.

Unfolding and Fitting Typically, the next step is to invert the smearing matrix and multiply it by the data vector to obtain the Born-level yields. As this analysis also requires fitting the Born-yields to a linear function of the form $A + B \cos \phi_h + C \cos 2\phi_h$, these two linear operations are performed simultaneously by use of linear regression.

Calculate moments The fit parameters above are used to calculate the moments:

$$\begin{aligned} 2\langle \cos \phi_h \rangle_{UU} &= \frac{B}{A} \\ 2\langle \cos 2\phi_h \rangle_{UU} &= \frac{C}{A} \end{aligned}$$

Combine data sets Data taken during the years 2000, 2005, 2006 and 2007 are included in this analysis and, due to different running conditions in different years, each must be unfolded independently. In this final step the data from all years is statistically averaged to produce the final observed moments.

Integrate moments Although the full results are obtained in the previous step, for interpretation it is advantageous to view the moments integrated over all but one variable.

Parameterization The fully differential moments are also fit to a 4-dimensional function so that they can be used as input in MC and other analysis procedures.

4.2 Data

The data is subject to quality checks, kinematic constraints, normalization and event-by-event corrections, all described below.

4.2.1 Data productions

The data productions used in this analysis are summarized in Table 4.1, along with the DQ mask (see Section 4.2.2) used and the DIS statistics of each production. The first two digits of the production name represent the data taking year while the second two represent the data production version. In all cases the latest production is used. In the case of the 2000 production, a new production is in progress at the time of writing which will include, for the first time, HTC tracking (Section 2.5.2) in the 2000 data. All other data years used in this analysis already contain HTC tracking.

During 2000 and 2005 data taking the target was polarized for most of the fill. Only during the final hour of data taking, when the beam current dropped below ~ 14 mA, was the target filled with high density unpolarized gas. Only the data taken with the unpolarized target is used here. The most substantial contribution to the hydrogen data set (and nearly half of the deuterium data set) comes from the final years of data taking — 2006 and the first half of 2007 — before the shutdown of the HERA facility. During this time the recoil detector was installed and, due to space constraints, the target was unpolarized. The target was primarily hydrogen but every 6th fill a deuterium target was used.

4.2.2 Burst selection: data quality

As described in Section 2.5.6 each burst is assigned a 32-bit quality parameter. The definition of these bits varied some from year to year. In each year of data taking the following parameters were checked, which correspond to the DQ Masks listed in Table 4.1:

Table 4.1: Data Productions used

| Production | Beam | DQ Mask | Statistics |
|-------------------------|------|------------|------------|
| Hydrogen target | | | |
| 00d2 | e+ | 0xc27c03dc | 6.4M DIS |
| 06e1 | e- | 0x467e03dc | 6.7M DIS |
| 06e1 | e+ | 0x467e03dc | 18.9M DIS |
| 07c2 | e+ | 0x467e03dc | 20.5M DIS |
| Deuterium target | | | |
| 00d2 | e+ | 0xc27c03dc | 8.1M DIS |
| 05c2 | e- | 0x427e03dc | 5.2M DIS |
| 06e1 | e+ | 0x467e03dc | 4.6M DIS |
| 07c2 | e+ | 0x467e03dc | 5.4M DIS |

Running conditions

- select reasonable dead time
- select reasonable burst length
- select reasonable beam current
- eliminate first burst in a run
- select runs indicated as “analyzable” by the shift crew in the logbook

Detector performance

- eliminate bad NOVC tracking efficiency
- eliminate high voltage trips
- eliminate runs during which RICH revealed problems
- eliminate dead blocks in calo
- eliminate dead blocks in H2 or Lumi
- eliminate bad TRD
- eliminate bad RICH

Data processing

- eliminate bad uDST records
- eliminate no PID

Each burst was checked by calculating a logical AND between the DQ Mask and the bit pattern assigned to each burst. A non-zero result indicates that a relevant bit was flagged as having a problem; these bursts are not used in the analysis.

4.2.3 Event and track selection

To be considered in this analysis, each event must have produced a *trigger 21*. Considering only trigger 21 events allows for the trigger efficiency to be corrected for (considering all events would not allow a correction for the unknown all-trigger efficiency).

DIS event selection

The total number of DIS events in the data sample is needed for normalization (see Section 4.3.1). To obtain this number, each track in an event is considered with HTC parameters calculated in the 1-track-to-beam scenario. Each track must meet the HTC track probability and fiducial *Track cuts*, the momentum and PID *Lepton cuts*, as well as the Q^2 , W^2 and HTC vertex probability *Event cuts* listed in Table 4.2. The HTC vertex cut ensures that the track and beam have a common vertex. The HTC track cuts remove tracks where the track fitting quality is poor. The fiducial volume cuts ensure that the track passed through the active region of the detector, avoiding inefficiencies at the edges. The PID cut identifies the track as a lepton while the momentum cut tries to eliminate low energy non-beam leptons. Finally, the Q^2 and W^2 cuts ensure that this is a lepton from a deep inelastic scattering event while the high y cut excludes the region where events with initial or final state QED radiation collect. The high y cut can be understood from the definition of y (Table 1.1).

$$y \stackrel{lab}{=} \frac{\nu}{E} = \frac{E_{in} - E_{out}}{E_{in}}$$

The incoming lepton energy (E_{in}) is *overestimated* in the case of initial state radiation (Figure 1.5a) and the outgoing lepton energy (E_{out}) is *underestimated* in the case of final state radiation (Figure 1.5b). In both cases y is reconstructed to be larger than it should be. Events with very large y , where the virtual photon carries nearly all of the incoming lepton's energy, are kinematically suppressed, and thus, events reconstructed at high y are dominated by events that are truly at lower y but where the lepton radiated a real photon. The unfolding procedure described below can corrected for this in an average way. However, with such a large correction in this region it is preferable to eliminate these events where it is highly probable that the event kinematics were incorrectly reconstructed.

In the 2000 data where HTC is not yet available the HRC track parameters were used and no HTC probability cuts were made.

SIDIS event selection

To construct the semi-inclusive event sample a lepton and a hadron track should be found in coincidence, originating from the target. HTC allows for the reconstruction of track kinematics from the vertex (point of closest approach) of two tracks plus the beam. Since the track kinematics can change slightly depending on the other track considered in the vertex, each pair of tracks in an event must be considered. Thus, for every event, including those where a DIS lepton was not found, a vertex is constructed and track parameters

are calculated for each pair of tracks. If this two-track pair contains a lepton and a hadron within the fiducial volume, meets DIS cuts, and meets SIDIS cuts, i.e., meets all the cuts listed in Table 4.2, then it is included in the event sample. In addition to the DIS cuts described in the previous section the hadron cuts ensure a clean SIDIS sample. The x_F cut approximately distinguishes the current region, where hadrons are produced in the fragmentation of the struck quark, in contrast to the target region, where hadrons are produced predominately from the target remnant. θ_{γ^*h} is the angle between the virtual photon and the hadron. At small θ_{γ^*h} a small miscalculation in the virtual photon or hadron kinematics can shift the hadron to the opposite side of the virtual photon, shifting ϕ_h between $\sim 0^\circ$ and $\sim 180^\circ$, which can influence the $\cos n\phi_h$ modulations. Thus, events with θ_{γ^*h} below the resolution for this angle were discarded. This has the effect of limiting the minimum $P_{h\perp}$ to ~ 0.05 GeV. For the unidentified-hadron event sample the pion mass is used to calculate z and x_F while for the pion (kaon) event sample the pion (kaon) mass is used.

Such a procedure can result in double counting of a single hadron track if an event contains multiple leptons. This is rare but is corrected for by the charge symmetric background correction described in Section 4.2.4

Events meeting these criteria were binned in five parameters, x , y , z , $P_{h\perp}$, and ϕ_h . The binning is shown in Table 4.3. The range of the binning is defined by the kinematically accessible region in data given by the cuts described above. The bin edges were selected so that each bin has approximately the same statistical significance.

The binning can be seen graphically in Figure 4.1. These plots highlight that kinematic edges correspond to the edge of the accessible range at HERMES. The decision to use y rather than the more physically relevant Q^2 was motivated by the strong correlation between x and Q^2 . This correlation can be seen in Figure 4.2; it is obvious that a square binning in x and Q^2 would have most bins unfilled. On the other hand, a square grid in x and y has nearly every bin filled and allows for an easy distribution of the statistics.¹

Of note is that this binning does not exclude the high z region where exclusive hadron production dominates. While this region is difficult to interpret it was not ignored in the analysis. The highest z bin, from $0.75 - 1$ isolates the exclusive region from the traditional SIDIS region. For the integrated results discussed below the highest z bin is not included so that the interpretation and comparison to theory and other experiments is clear. However, the fully differential results include this region.

¹An x - Q^2 binning was attempted, however it was found that the average x in a single x bin varied more in a Q^2 -binning than in a y -binning.

Table 4.2: Event and track cuts

| Track cuts (lepton & hadron) | | | |
|---|----------------------|------------------|---|
| $0.01 <$ | HTC_{prob} | | ensure good tracking |
| | $vert_d$ | $< 0.8\text{cm}$ | vertex inside the target in the x-y plane (transverse to the beam) |
| $-18\text{cm} <$ | $vert_z$ | $< 18\text{cm}$ | vertex inside the target in z direction |
| $5\text{cm} <$ | | $< 20\text{cm}$ | |
| Fiducial Volume Cuts | | | |
| | x_{FFC} | $< 31\text{cm}$ | avoid front field clamp |
| $7\text{cm} <$ | y_{SP} | | avoid septum plate |
| | y_{RFC} | $< 54\text{cm}$ | avoid rear field clamp |
| | x_{IRFC} | $< 100\text{cm}$ | long track avoid rear field clamp |
| | y_{IRFC} | $< 54\text{cm}$ | long track avoid rear field clamp |
| | x_{CALO} | $< 175\text{cm}$ | avoid edge of the calorimeter |
| $30\text{cm} <$ | y_{CALO} | $< 108\text{cm}$ | avoid edge of the calorimeter |
| Lepton cuts | | | |
| $1 <$ | PID | | identify a lepton |
| $4\text{GeV} <$ | p | | ensure this is the scatter beam lepton |
| Event cuts | | | |
| $0.01 <$ | HTC_{prob} | | ensure both tracks and beam have the same origin |
| $1\text{GeV}^2 <$ | Q^2 | | DIS regime |
| $10\text{GeV}^2 <$ | W^2 | | avoid resonance region |
| | y | < 0.85 | avoid region with large radiative effects |
| Hadron cuts | | | |
| $-100 <$ | PID | < 0 | identify a hadron |
| $0.2 <$ | x_F | | select current region |
| $0.02\text{rad} <$ | θ_{γ^*h} | | avoid region where ϕ_h smearing is large |
| $1\text{GeV} <$ | p | $< 15\text{GeV}$ | allow for good RICH PID |

Table 4.3: Binning

| | | | | | | |
|----------------|---------|-------|-------|-------|------|---------|
| $x =$ | 0.023 | 0.042 | 0.078 | 0.145 | 0.27 | 0.6 |
| $y =$ | 0.2 | 0.3 | 0.45 | 0.6 | 0.7 | 0.85 |
| $z =$ | 0.2 | 0.3 | 0.4 | 0.5 | 0.6 | 0.75 1 |
| $P_{h\perp} =$ | 0.05 | 0.2 | 0.35 | 0.5 | 0.7 | 1.0 1.3 |
| $\phi_h =$ | 12 bins | | | | | |

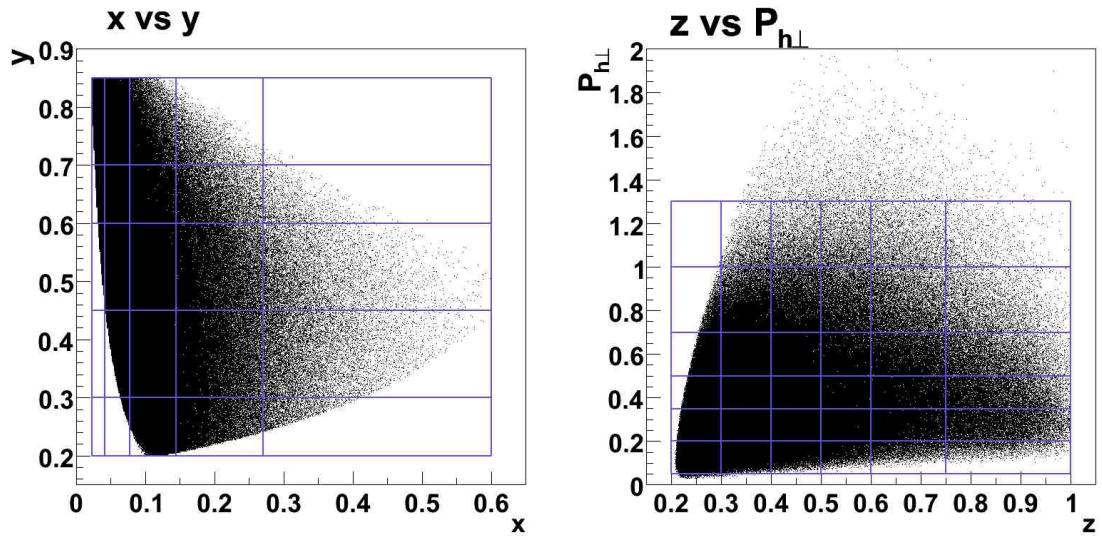


Figure 4.1: Scatter plots showing the distribution of data statistics in x and y (left) and z and $P_{h\perp}$ (right). Blue lines denote bin edges.

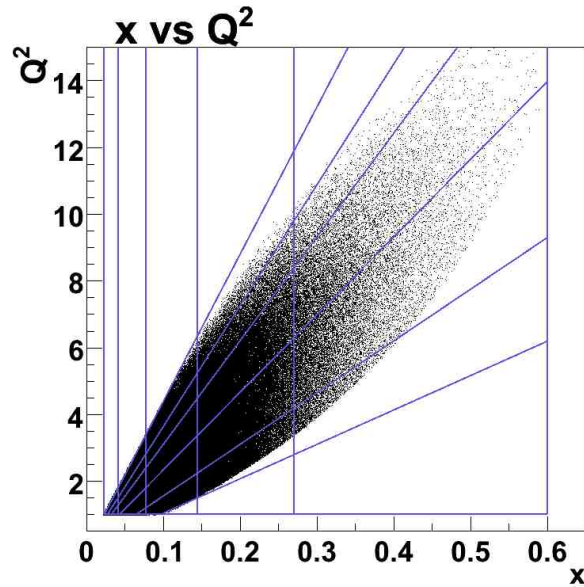


Figure 4.2: Scatter plot showing data statistics in x and Q^2 , blue lines denote x and y bin edges.

4.2.4 Charge symmetric background correction

In the event level cuts in Table 4.2 the lepton charge is not constrained. This is done to allow for a *charge symmetric background* correction. Events with a lepton charge opposite to the beam are given a negative weight, so as to subtract the symmetric events where the lepton charge was correct but the lepton selected was not in fact the scattered beam lepton. This subtraction is effective because the few sources of non-beam leptons are symmetric in charge. The dominant sources of non-beam leptons corrected for by this procedure originate from lepton-pair production in detector materials ($\gamma \rightarrow e^+e^-$) or meson Dalitz decay ($\pi^0/\eta \rightarrow \gamma e^+e^-$).

4.2.5 RICH weights

In the case that pions (kaons) are identified, each event is given a pion (kaon) weight from the inverted P-matrix with the appropriate number of tracks in the detector half and hadron momentum, according to the RICH identification type, as described by Equation 3.2. The EVT method along with the center-tune P-matrices described in Section 3.4.5 were used.

4.3 Monte Carlo

The unfolding procedure described below requires two MC samples: “Born MC” without any radiative effects, and “Reconstructed MC”, which includes radiative effects as well as a full detector simulation. In both cases the Pythia [20] generator, which provides a good description of SIDIS cross section, is used. In addition, the normalization of the data requires the total DIS yield from a third, small MC production. This was generated with disNG [21] which provides the most accurate simulation of the inclusive cross section. Deuterium target productions (for both generators) were formed from statistically balanced proton and neutron productions. The MC productions used in this analysis are described in detail in the next sections.

4.3.1 MC for data normalization

The data and MC must be relatively normalized to properly subtract the background (extracted from MC, see Section 4.4.1) from the data. This is accomplished by comparing the total number of inclusive DIS events seen in the data and in a MC production generated by disNG. disNG is based on the LEPTO [21] generator and includes the RADGEN [22] package to simulate QED radiation. disNG is used because of its accurate description of the inclusive cross section: unlike Pythia, it includes the radiative tail of elastic eN events. Generated events are run through a GEANT [23] simulation of the HERMES detector and then analyzed by

the standard data production chain (HRC/HTC, μ DST). The MC events are then analyzed exactly as the data to identify inclusive DIS events. disNG provides event weights, and the sum of these weights for all DIS events is tallied. Normalizing this number by the number of generated events, which is provided by disNG as the *IEVGEN* variable, gives the total inclusive DIS cross section, $\frac{DIS_{MC}}{IEVGEN} = \sigma_{DIS,total}[\mu\text{barns}]$ within the cuts stated above. The data can then be normalized in this way:

$$\sigma_{data} = \frac{N_{data}}{DIS_{data}} \sigma_{DIS,total} = \frac{N_{data}}{IEVGEN \frac{DIS_{data}}{DIS_{MC}}} \quad (4.1)$$

where σ_{data} are the normalized yields, N_{data} are the unnormalized yields, and DIS_s is the total number of DIS from source s ($s = data, MC$). In this way it is clear that the data is normalized as if it were MC.

Productions were run for each data set, varying the detector set-up and beam charge to match that of the data. The productions, along with their statistics, are summarized in Table 4.4. Since the 2006 positron and 2007 data taking period have identical beam and detector settings a single production is used for both years.

Table 4.4: Statistic of disNG MC production used for data normalization

| disNG MC | Inclusive DIS Statistics |
|------------------|--------------------------|
| 00H | 2.9M |
| 06H(e $-$) | 2.9M |
| 06H(e $+$), 07H | 2.9M |
| 00D | 2.6M |
| 05D | 2.4M |
| 06D(e $+$), 07D | 2.6M |

4.3.2 Born MC

Born MC productions from Pythia were generated for proton and neutron targets. Test productions with different beam charges showed no dependence on the beam charge and so all productions were done with positron beam.

The true scattered beam lepton and event kinematics were used (as opposed to the reconstructed or radiatively distorted values) and cuts on Q^2 , W^2 and x_F as in Table 4.2 were applied to ensure that only DIS events were selected. True pions, kaons, and protons were selected for the unidentified-hadron event sample while only true pions (kaons) were used for the pion (kaon) event sample. In all cases the proper hadron mass for the identified particle was used to calculate the (correct) z and x_F for the track. All other cuts in Table 4.2 were ignored as they pertain only to contamination seen in data where the true kinematics are unknown. The MC events were then binned like the data (Table 4.3).

Pythia does not generate event-by-event weights but rather produces an overall weight *extraweight* representing the total cross section within generator limits as calculated at the end of each Pythia run. The Pythia event sample is normalized as follows:

$$\sigma_{Born} = \frac{N_{Born} \text{ extraweight}}{IEVGEN} \quad (4.2)$$

where σ_{Born} is the normalized Born vector, N_{Born} is the unnormalized Born vector, *extraweight* is the overall weight computed by Pythia, and *IEVGEN* is the total number of generated events. The term “vector” here is shorthand for any quantity binned in the 5-dimensional $x, y, z, P_{h\perp}, \phi_h$ binning described above.

4.3.3 Reconstructed MC

Reconstructed MC was generated with Pythia, including radiative effects simulated with RADGEN [22], and a GEANT [23] detector simulation. Separate productions were made for each year including the proper beam charge, target (p for Hydrogen, p+n for deuterium) and detector configuration, where again the 2006 positron and 2007 years have identical configurations and use the same MC sample.

The productions and statistics are summarized in Table 4.5. Large event samples were needed to fill the migration matrix described below. The 2006 positron and 2007 productions have ~ 3 times the statistics of the others to mimic the larger statistics collected during these periods.

Table 4.5: Statistic of Pythia MC productions used

| Reconstructed Pythia MC | Inclusive DIS Statistics |
|---------------------------|--------------------------|
| 00H | 98M |
| 06H(e ⁻) | 112M |
| 06H(e ⁺), 07H | 310M |
| 00D | 98M |
| 05D | 99M |
| 06D(e ⁺), 07D | 102M |

The reconstructed MC events are binned in a *migration matrix* that correlates the true with the observed (reconstructed) kinematics. The reconstructed bin i is determined by treating the event in the same way as the data. Each pair of tracks in the event is considered. If a true lepton (of any charge) is identified along with a track meeting the PID cuts for a hadron, plus all of the other cuts in Table 4.2 are met the event is retained. As in data the pion mass is used for the unidentified-hadron event sample to calculate z and x_F while for the pion (kaon) event sample the pion (kaon) mass is used. Events with lepton charge opposite to the beam, as in data, are given a negative weight to account for the charge symmetric background. The only

differences from the data treatment are that the trigger is not simulated and the hadron-type identification is done with the true type (rather than the RICH type and a P-matrix weight).

The sample of good reconstructed events is then given a second index, the Born bin j . This is determined from the true kinematics as with the Born event sample, using the true lepton and hadron kinematics and only making the cuts made on the Born event sample: Q^2 , W^2 , and x_F . Again, the proper hadron mass is used to calculate z and x_F . If the true kinematics of this event fall outside the Born-level cuts the event is given the Born index $j = 0$. These events will be used later as a background subtraction.

The reconstructed event sample is normalized in exactly the same way as the Born event sample, as described in Section 4.3.2

4.4 5-dimensional unfolding procedure

4.4.1 The smearing matrix and background vector

The zero-bin of the migration matrix represents the “background” of events that smear into the event sample from outside of the measured region. When the zero bin is properly normalized ($m(i, 0)$), this vector can be used to correct the normalized data $\sigma_{data}(i)$ for such events:

$$\sigma'_{data}(i) \equiv \sigma_{data}(i) - m(i, 0). \quad (4.3)$$

To form the smearing matrix $S'(i, j)$ the normalized migration matrix with the zero bin truncated $m'(i, j)$ is divided by the normalized Born vector $b(j)$:

$$S'(i, j) = \frac{m'(i, j)}{b(j)}. \quad (4.4)$$

This matrix describes both the migration of events between bins and the fraction of events that are observed in each bin (i.e., the acceptance). The migration may be due to mis-reconstructed track kinematics due to radiative effects (Section 1.3), multiple scattering in the target or detector material, or external Bremsstrahlung. The correction for radiative effects is particularly important as initial and final state radiation both smear events in the same direction and can produce a $\cos n\phi_h$ modulation. Detection inefficiency is due predominantly to the spectrometer acceptance, as well as track reconstruction and PID inefficiencies. HTC track and vertex probability distributions in reconstructed MC appear similar to the data (though not identical) thus the elimination of these events from data is corrected for by the smearing matrix. PID inefficiencies such as the loss of tracks when two tracks are close together as described in Section 2.5.5, are

also observed in reconstructed MC, so these are taken into account as well.

In order to correct for the imperfections in the data which are catalogued in the smearing matrix, the inverted smearing matrix can be applied to the data:

$$\sigma'_{data}{}^{Born}(j) = S'^{-1}(j, i)\sigma'_{data}(i). \quad (4.5)$$

Statistical errors

The covariance on the un-smearred yields originates from the input yields, the zero bin, and the statistical uncertainty of the smearing matrix:

$$C_{\sigma'_{data}{}^{Born}} = \left(\frac{\partial \sigma'_{data}{}^{Born}}{\partial \sigma_{data}} \right)^2 (\delta \sigma_{data})^2 + \left(\frac{\partial \sigma'_{data}{}^{Born}}{\partial m(i, 0)} \right)^2 (\delta m(i, 0))^2 + \left(\frac{\partial \sigma'_{data}{}^{Born}}{\partial S'} \right)^2 (\delta S')^2 \quad (4.6)$$

Data

From Equation 4.5 and Equation 4.3 the partial $\frac{\partial \sigma'_{data}{}^{Born}}{\partial \sigma_{data}}$ is simply S'^{-1} . The covariance of the data itself, $(\delta \sigma_{data})^2 = C_{\sigma_{data}}$, is the sum of the squared event weights, which for unidentified-hadrons are just the normalization factor and for pions and kaons are the RICH inverted P-matrix weights times the normalization factor. As the weights are squared, charge-symmetric background events contribute positively to the error. As the errors between bins are uncorrelated $C_{\sigma_{data}}$ is diagonal.

Background subtraction

Again from Equation 4.5 and Equation 4.3 the partial $\frac{\partial \sigma'_{data}{}^{Born}}{\partial m(i, 0)}$ is S'^{-1} . The covariance of the background subtraction, $(\delta m(i, 0))^2 = C_{m(i, 0)}$, is the sum of the squared weights. As the Pythia events themselves are unweighed this is just the number of events in the bin times the squared normalization factor. Again the errors are uncorrelated and $C_{m(i, 0)}$ is diagonal.

Smearing matrix

The error due to the statistical uncertainty in the smearing matrix is a bit more complicated. The partial $\frac{\partial \sigma'_{data}{}^{Born}}{\partial S'}$ can be found from Equation 4.5 in the form $\sigma'_{data}(i) = S'(i, j)\sigma'_{data}{}^{Born}(j)$:²

$$\begin{aligned} \frac{\partial \sigma'_{data}(i)}{\partial \sigma'_{data}{}^{Born}(j)} \frac{\partial \sigma'_{data}{}^{Born}(j)}{\partial S'(a, b)} &= \frac{\partial \sigma'_{data}(i)}{\partial S'(a, b)} \\ S'(i, j) \frac{\partial \sigma'_{data}{}^{Born}(j)}{\partial S'(a, b)} &= \sigma'_{data}{}^{Born}(b) \\ \frac{\partial \sigma'_{data}{}^{Born}(j)}{\partial S'(a, b)} &= S'^{-1}(j, a)\sigma'_{data}{}^{Born}(b) \end{aligned} \quad (4.7)$$

² in the first to the second line the identity $i = a$ has been made, changing the indices of S' in the last line

The covariance of the smearing matrix due to the statistics of the migration matrix and the Born vector are given by:

$$S(i, j) = \frac{n_m m'(i, j)}{n_b b(j)} \quad (4.8)$$

$$\begin{aligned} (\delta S(i, j))^2 = C_{S'} &= \left(\frac{\partial S(i, j)}{\partial m'(i, j)} \right)^2 (\delta m'(i, j))^2 + \left(\frac{\partial S(i, j)}{\partial b(j)} \right)^2 (\delta b(j))^2 \\ &= \left(\frac{n_m}{n_b b(j)} \right)^2 m'(i, j) + \left(\frac{-n_m m'(i, j)}{n_b b(j)^2} \right)^2 b(j) \end{aligned} \quad (4.9)$$

where the normalization factors for the migration matrix n_m and the Born vector n_b are included explicitly for clarity. This calculation assumes that there is no correlation between smearing matrix bins since these correlations are unknown. Thus the result is a matrix, rather than a 4-dimensional hypermatrix (i.e., $\delta^2 S(a, b, c, d) = \delta^2 S(a, b) \delta_{ac} \delta_{bd}$). The contribution to the covariance from the smearing matrix term is then

$$\begin{aligned} \left(\frac{\partial \sigma'_{data}{}^{Born}}{\partial S'} \right)^2 (\delta S')^2 &= S^{-1}(i, a) \sigma'_{data}{}^{Born}(b) \delta^2 S(a, b, c, d) S^{-1}(j, c) \sigma'_{data}{}^{Born}(d) \\ &= S^{-1}(i, a) \sigma'_{data}{}^{Born}(b) \delta^2 S(a, b) S^{-1}(j, a) \sigma'_{data}{}^{Born}(b) \\ &= S^{-1}(i, a) \left[\sum_b \sigma'_{data}{}^{Born}(b) \delta^2 S(a, b) \sigma'_{data}{}^{Born}(b) \right] S^{-1T}(a, j) \end{aligned} \quad (4.10)$$

The quantity in square brackets is, after the sum over b , only a function of the bin a and thus a diagonal matrix.

Finally, the full covariance can be rewritten³:

$$C_{\sigma'_{data}{}^{Born}} = S'^{-1} C_{\sigma_{data}} S'^{-1T} + S'^{-1} C_{m(i,0)} S'^{-1T} + S'^{-1} \sigma'_{data}{}^{Born} C_{S'} \sigma'_{data}{}^{BornT} S'^{-1T} \quad (4.11)$$

$$= S'^{-1} \left(C_{\sigma_{data}} + C_{m(i,0)} + \sigma'_{data}{}^{Born} C_{S'} \sigma'_{data}{}^{BornT} \right) S'^{-1T} \quad (4.12)$$

4.4.2 Linear regression

As it will be used in the next section, linear regression and some variables are defined here. To fit an N -element vector σ to the linear function

$$A + B \cos \phi_h + C \cos 2\phi_h \quad (4.13)$$

³ The covariance is now rewritten to look more like the form of Equation 4.19 given below. Notice that the two derivations give identical results for the data and zero bin terms, however, the formulation below does not give a clear derivation for the propagation of the smearing matrix covariance.

a χ^2 parameter can be defined

$$\chi^2 = (\sigma - X\beta)^T C_\sigma^{-1} (\sigma - X\beta) \quad (4.14)$$

where C_σ is the $N \times N$ covariance matrix of the vector σ , β is the M -vector of fit parameters A_i , B_i and C_i , and X is the design matrix that describes the fit function:

$$\begin{pmatrix} 1 & \cos(\phi_1) & \cos(2\phi_1) & 0 & 0 & 0 & \dots & 0 & 0 & 0 \\ 1 & \cos(\phi_2) & \cos(2\phi_2) & 0 & 0 & 0 & \dots & 0 & 0 & 0 \\ \dots & & & & & & & & & \\ 1 & \cos(\phi_n) & \cos(2\phi_n) & 0 & 0 & 0 & \dots & 0 & 0 & 0 \\ 0 & 0 & 0 & 1 & \cos(\phi_1) & \cos(2\phi_1) & \dots & 0 & 0 & 0 \\ 0 & 0 & 0 & 1 & \cos(\phi_2) & \cos(2\phi_2) & \dots & 0 & 0 & 0 \\ \dots & & & & & & & & & \\ 0 & 0 & 0 & 1 & \cos(\phi_n) & \cos(2\phi_n) & \dots & 0 & 0 & 0 \\ \dots & & & & & & & & & \\ 0 & 0 & 0 & 0 & 0 & 0 & \dots & 1 & \cos(\phi_n) & \cos(2\phi_n) \end{pmatrix}. \quad (4.15)$$

X has dimensionality $M \times N$ where $M = 3\frac{N}{n}$ for 3 parameters (A , B , and C) and n ϕ_h bins (for this analysis $n = 12$). Minimizing χ^2 immediately produces the desired fit parameters β :

$$\beta = (X^T C_\sigma^{-1} X)^{-1} X^T C_\sigma^{-1} \sigma \quad (4.16)$$

In general the covariance C_η of a function $\eta(\theta)$ is obtained from the covariance of θ (C_θ) by

$$A_{ij} = \frac{\partial \eta_i(\theta)}{\partial \theta_j} \quad (4.17)$$

$$C_\eta = A C_\theta A^T. \quad (4.18)$$

For a linear function η , A is just the transformation matrix M itself:

$$\begin{aligned} \eta(\theta) &= M\theta \\ C_\eta &= M C_\theta M^T \end{aligned} \quad (4.19)$$

The covariance of the fit parameters β is then:

$$\begin{aligned}
C_\beta &= ((X^T C_\sigma^{-1} X)^{-1} X^T C_\sigma^{-1}) C_\sigma ((X^T C_\sigma^{-1} X)^{-1} X^T C_\sigma^{-1})^T \\
&= (X^T C_\sigma^{-1} X)^{-1} X^T (C_\sigma^{-1} C_\sigma) C_\sigma^{-1T} X (X^T C_\sigma^{-1} X)^{-1T} \\
&= (X^T C_\sigma^{-1} X)^{-1} (X^T C_\sigma^{-1} X)^T (X^T C_\sigma^{-1} X)^{-1T} \\
&= (X^T C_\sigma^{-1} X)^{-1}.
\end{aligned} \tag{4.20}$$

4.4.3 The Fold and Fit formalism

The smearing-unfolding of Equation 4.5 and linear regression as defined in Equation 4.14 can be performed simultaneously. The parameters β that satisfy the relation

$$\sigma'_{data}{}^{Born} = S'^{-1} \sigma'_{data} = X\beta \tag{4.21}$$

must be determined. Here the prime indicates data normalized to MC and background subtracted (see Equation 4.3). This expression is equivalent to

$$\sigma'_{data} = S' X \beta, \tag{4.22}$$

in which case the χ^2 function to minimize is:

$$\chi^2 = (\sigma'_{data} - S' X \beta)^T C_{\sigma'_{data}}^{-1} (\sigma'_{data} - S' X \beta) \tag{4.23}$$

where $C_{\sigma'_{data}}$ is the covariance matrix of the data, discussed in detail below. Simple matrix manipulations show that this is exactly equivalent to using the unfolded yields $\sigma'_{data}{}^{Born}$

$$\begin{aligned}
\chi^2 &= ((S' S'^{-1}) \sigma'_{data} - S' X \beta)^T C_{\sigma'_{data}}^{-1} ((S' S'^{-1}) \sigma'_{data} - S' X \beta) \\
&= (S'^{-1} \sigma'_{data} - X \beta)^T S'^T C_{\sigma'_{data}}^{-1} S' (S'^{-1} \sigma'_{data} - X \beta) \\
&= (S'^{-1} \sigma'_{data} - X \beta)^T (S'^{-1} C_{\sigma'_{data}} S'^{-1T})^{-1} (S'^{-1} \sigma'_{data} - X \beta) \\
&= (S'^{-1} \sigma'_{data} - X \beta)^T (C_{\sigma'_{data}{}^{Born}})^{-1} (S'^{-1} \sigma'_{data} - X \beta)
\end{aligned} \tag{4.24}$$

The parameter vector β and its covariances in this method are:

$$\beta = (X^T S'^T C_{\sigma'_{data}}^{-1} S' X)^{-1} X^T S'^T C_{\sigma'_{data}}^{-1} \sigma'_{data} \quad (4.25)$$

$$C_\beta = (X^T S'^T C_{\sigma'_{data}}^{-1} S' X)^{-1} \quad (4.26)$$

These two equations define the ‘‘Fold and Fit’’ method used for this analysis. The computational advantage of this method then becomes clear: the S' matrix need not be inverted and neither does $C_{\sigma'_{data}^{Born}}$, the covariance of the unfolded yields.

Statistical errors

The covariance of the data $C_{\sigma'_{data}}$ should include the covariance of the data itself and the covariance due to the zero bin. However, in Equation 4.24 the substitution has been made:

$$C_{\sigma'_{data}^{Born}} = S'^{-1} C_{\sigma'_{data}} S'^{-1T} \quad (4.27)$$

which leaves out the smearing matrix contribution to the covariance of the born yields. Thus, to include the smearing matrix statistical uncertainty in the Fold and Fit method it can be artificially inserted into the definition of the not-unfolded data covariance. From Equation 4.12 this can be written as

$$C_{\sigma'_{data}} \equiv C_{\sigma_{data}} + C_{m(i,0)} + \sigma_{data}^{Born} C_{S'} \sigma_{data}^{BornT}, \quad (4.28)$$

where these quantities are defined in Section 4.4.1. Since all the covariances are diagonal (see Equation 4.10 and the text thereafter for a note on diagonal nature of the smearing matrix term) the inversion of $C_{\sigma'_{data}}$ is trivial, another advantage to the Fold and Fit method.

Dealing with empty bins

Inevitably some kinematic bins are poorly populated or even entirely empty. For example, the lowest x - y bin, in the lower left corner of Figuer 4.1, is empty due to kinematic constraints:

$$y_{min}(x_{bin1}) = \frac{\nu_{min}(x_{bin1})}{E_{max}} = \frac{Q_{min}^2}{2Mx_{bin1}} \frac{1}{E_{max}} = \frac{1\text{GeV}^2}{2(1\text{GeV})(0.042)} \frac{1}{27.6\text{GeV}^2} = 0.43$$

So the minimum y at the upper edge of the lowest x bin is constrained by the minimum Q^2 cut to be in the third y bin. The matrix inversion involved in Fold and Fit procedure (Equations 4.25 and 4.26) cannot

be computed if there is a zero on the diagonal. Thus, several steps are taken to remove unfilled or sparsely filled bins. Bins where the data vector, Born vector, or the diagonal of the migration matrix are zero are removed from all vectors (σ'_{data} , $b(j)$) and matrices ($C_{\sigma'_{data}}$, $m'(i, j)$, X). For the $C_{\sigma'_{data}}$ and $m'(i, j)$ matrices the corresponding row and column are removed; for the X matrix only the corresponding row is removed. Then, each kinematics bin, comprised of 12 ϕ_h bins, is considered as a whole. Sufficient statistics should be distributed throughout the bin to ensure a reasonable fit. The following criteria are applied

$$\frac{\delta y}{y} = 1 \text{ for removed } \phi_h \text{ bins} \quad (4.29)$$

$$N_1 = \sum_{\phi_h \in 0 - \frac{\pi}{2}, \frac{3\pi}{2} - 2\pi} \frac{\delta y}{y} \quad (4.30)$$

$$N_2 = \sum_{\phi_h \in \frac{\pi}{2} - \frac{3\pi}{2}} \frac{\delta y}{y} \quad (4.31)$$

$$N = \frac{\sqrt{(N_1)^2 + (N_2)^2}}{12} < 0.4 \quad (4.32)$$

Kinematic bins that have $N > 0.4$ are eliminated; every ϕ_h bin is removed from all vectors and matrices as above. For the X matrix 3 column sets are removed for each kinematic bin that is removed.

4.4.4 $\cos n\phi_h$ moments

Experimentally, the unpolarized cross section azimuthal modulations can be accessed via the $\langle \cos n\phi_h \rangle_{UU}$ moments ($n = 1, 2$), defined as

$$\langle \cos n\phi_h \rangle_{UU} = \frac{\int \cos n\phi_h d\sigma d\phi_h}{\int d\sigma d\phi_h} \quad (4.33)$$

where $d\sigma$ is the differential cross section defined in Equation 1.17 and modeled with the fit function of Equation 4.13. Plugging in Equation 4.13 yields:

$$\langle \cos \phi_h \rangle_{UU} = \frac{B}{2A} \quad (4.34)$$

$$\langle \cos 2\phi_h \rangle_{UU} = \frac{C}{2A} \quad (4.35)$$

where the factor of 2 comes from the trigonometric functions:

$$\int_0^{2\pi} \cos n\phi_h d\phi_h = \int_0^{2\pi} \cos \phi_h \cos 2\phi_h d\phi_h = 0 \quad (4.36)$$

$$\int_0^{2\pi} \cos^2 n\phi_h d\phi_h = \pi \quad (4.37)$$

$$\int_0^{2\pi} 1 = 2\pi \quad (4.38)$$

(i.e. from the ratio of Equations 4.37 and 4.38, which enter into the calculation of the numerator and denominator respectively of Equations 4.34 and 4.35).

Statistical errors for the moments can be calculated from Equation 4.18 where the A matrix is given by Equation 4.17 and describes the formulas $\eta_i(\cos n\phi_h)$ to calculate the $\cos n\phi_h$ moments from the parameters β :

$$\eta_i(\cos n\phi_h) = \frac{\beta_{3i+n}}{\beta_{3i}} \quad (4.39)$$

$$A_{ij} = \frac{\partial \eta_i}{\partial \beta_j}, \quad (4.40)$$

where the 3 in the composite index $3i + n$ is due to the 3 fit parameters for each kinematic bin i .

The moments are related to the structure functions of Section 1.2.1 via the azimuthal-independent part of the cross section:

$$F_{UU}^{\cos \phi_h} = \frac{2\langle \mathbf{cos} \phi_h \rangle_{UU}}{\sqrt{2\epsilon(1+\epsilon)}} F_{UU,T} = \frac{2\langle \mathbf{cos} \phi_h \rangle_{UU} (1-y + \frac{1}{2}y^2 + \frac{1}{4}\gamma^2 y^2)}{(2-y)\sqrt{1-y - \frac{1}{4}\gamma^2 y^2}} F_{UU,T} \quad (4.41)$$

$$F_{UU}^{\cos 2\phi_h} = \frac{2\langle \mathbf{cos} 2\phi_h \rangle_{UU}}{\epsilon} F_{UU,T} = \frac{2\langle \mathbf{cos} 2\phi_h \rangle_{UU} (1-y + \frac{1}{2}y^2 + \frac{1}{4}\gamma^2 y^2)}{(1-y - \frac{1}{4}\gamma^2 y^2)} F_{UU,T} \quad (4.42)$$

where it is assumed that $F_{UU,L}$ is negligible [9]. The definition of ϵ (Table 1.1) has been substituted in the expressions on the far right for the reader's convenience.

4.4.5 Combining data sets

The smearing matrix described in Section 4.4.1 must accurately replicate the data to properly correct for detector effects. Consequently, the MC used for each data set differs to coincide with the measurement conditions: the target cell length and position, known misalignment of the tracking chambers, beam charge, and target gas. As a consequence, the Fold and Fit method must be applied to each data set (see Table 4.1) independently. To get an overall result the results from each data set must be averaged in some way. Two

options were investigated and both are presented below.

The most straightforward option is to statistically average the moments. Using the same tools as in the previous sections, the problem can be written as a χ^2 -minimization task:

$$\chi^2 = \left(\begin{pmatrix} m_1 \\ \vdots \\ m_n \end{pmatrix} - \begin{pmatrix} I \\ \vdots \\ I \end{pmatrix} m \right)^T \begin{pmatrix} C_{m,1}^{-1} & 0 & 0 \\ 0 & \dots & 0 \\ 0 & 0 & C_{m,n}^{-1} \end{pmatrix} \left(\begin{pmatrix} m_1 \\ \vdots \\ m_n \end{pmatrix} - \begin{pmatrix} I \\ \vdots \\ I \end{pmatrix} m \right) \quad (4.43)$$

$$m = \left(\sum_{y=1}^n C_{m,y}^{-1} \right)^{-1} \left(\sum_{y=1}^n C_{m,y}^{-1} m_y \right) \quad (4.44)$$

$$C_m = \left(\sum_{y=1}^n C_{m,y}^{-1} \right)^{-1} \quad (4.45)$$

where m_y is the vector of moments from year y , m is the averaged vector of moments, $C_{m,y}$ is the covariance of the moments from year y , and C_m is the covariance of the averaged moments.

While this is a satisfactory method, a second option, to perform a fit for the A_i , B_i , and C_i parameters over all data sets simultaneously, was explored. To simultaneously fit all data years the Fold and Fit formalism was extended to use a “super matrix” which contains as block-diagonal elements the matrices from each year:

$$\chi^2 = \left(\begin{pmatrix} \sigma'_{data,1} \\ \vdots \\ \sigma'_{data,n} \end{pmatrix} - \begin{pmatrix} S'_1 \\ \vdots \\ S'_n \end{pmatrix} X\beta \right)^T \begin{pmatrix} C_{data,1}^{-1} & 0 & 0 \\ 0 & \dots & 0 \\ 0 & 0 & C_{data,n}^{-1} \end{pmatrix} \left(\begin{pmatrix} \sigma'_{data,1} \\ \vdots \\ \sigma'_{data,n} \end{pmatrix} - \begin{pmatrix} S'_1 \\ \vdots \\ S'_n \end{pmatrix} X\beta \right) \quad (4.46)$$

$$\beta = \left(X^T \left(\sum_{y=1}^n S_y'^T C_{data,y}^{-1} S_y' \right) X \right)^{-1} X^T \left(\sum_{y=1}^n S_y'^T C_{data,y}^{-1} \sigma'_{data,y} \right) \quad (4.47)$$

This is identical to the statistically-weighted average of the parameters $\beta = \{A_1, B_i, C_i\}$ (as opposed to

the moments $\frac{B_i}{A_i}$ and $\frac{C_i}{A_i}$ that are averaged in the first method):

$$\chi^2 = \left(\begin{pmatrix} \beta_1 \\ \vdots \\ \beta_n \end{pmatrix} - \begin{pmatrix} I \\ \vdots \\ I \end{pmatrix} \beta \right)^T \begin{pmatrix} C_{\beta,1} & 0 & 0 \\ 0 & \ddots & 0 \\ 0 & 0 & C_{\beta,n} \end{pmatrix} \left(\begin{pmatrix} \beta_1 \\ \vdots \\ \beta_n \end{pmatrix} - \begin{pmatrix} I \\ \vdots \\ I \end{pmatrix} \beta \right)$$

$$\beta = \left(\sum_{y=1}^n C_{\beta,y}^{-1} \right)^{-1} \left(\sum_{y=1}^n C_{\beta,y}^{-1} \beta_y \right) = \left(\sum_{y=1}^n X^T S_y'^T C_{\sigma'_{data,y}}^{-1} S_y' X \right)^{-1} \left(\sum_{y=1}^n X^T S_y'^T C_{\sigma'_{data,y}}^{-1} S_y' X \beta_y \right) \quad (4.48)$$

$$C_\beta = \left(\sum_{y=1}^n X^T S_y'^T C_{\sigma'_{data,y}}^{-1} S_y' X \right)^{-1} \quad (4.49)$$

In reality the desired result is to have the same effect as having one single year with all the statistics and a single smearing matrix. However, even assuming that the smearing matrices are all the same in Equations 4.46 and 4.47, the calculation reduces to

$$\beta = \left(X^T S'^T \left(\sum_{y=1}^n C_{data,y}^{-1} \right) S' X \right)^{-1} X^T S'^T \left(\sum_{y=1}^n C_{data,y}^{-1} \sigma'_{data,y} \right) \quad (4.50)$$

$$C_\beta = \left(X^T S'^T \left(\sum_{y=1}^n C_{data,y}^{-1} \right) S' X \right)^{-1} \quad (4.51)$$

which is not equivalent to simply combining the statistics from the beginning since $\sum_{y=1}^n (C_{data,y}^{-1}) \neq (C_{data,all})^{-1}$ and $\sum_{y=1}^n (C_{data,y}^{-1} \sigma'_{data,y}) \neq (C_{data,all})^{-1} (\sum_{y=1}^n \sigma'_{data,y})$. However, averaging the moments is even further from the desired result since $2\langle \mathbf{cos} \phi_{\mathbf{h}} \rangle_{UU}(\text{AverageMoments}) = \text{avg}(\frac{B}{A})$ while $2\langle \mathbf{cos} \phi_{\mathbf{h}} \rangle_{UU}(\text{AverageParameters}) = \frac{\text{avg}(B)}{\text{avg}(A)}$. The simultaneous fit / averaging parameters method is chosen as the best allowable way to combine the data sets.

4.4.6 Integrated moments

The final results of the analysis are the year-averaged fully differential moments. However, to compare the results with theory and other experiments, and to gain a qualitative picture of the behavior of the $\langle \mathbf{cos} \mathbf{n} \phi_{\mathbf{h}} \rangle_{UU}$ moments, an integration can be done over three variables, highlighting the dependence of the moments on the fourth variable. Importantly, an *integral*, not a statistically weighted average, should be done. To do this the $\phi_{\mathbf{h}}$ -independent cross section is needed to “weight” the moments. This is taken from the Born-level Pythia production discussed in Section 4.3.2. The statistical error can again be propagated with Equations 4.17 and 4.18.

When performing such an integral care must be taken in selecting the integration range as a measurement

cannot be made in some bins (see Section 4.4.3). In addition to the bins eliminated before fitting, some bins have very large errors due to a poor fit. If these bins with large error coincide with a high cross section the error of the integrated result may be large. In addition, some bins have unphysically large moments as well as large errors. These bins clearly mark a region where there are insufficient statistics to make a meaningful measurement. Therefore, bins with an error greater than 1 are eliminated, both from the fully differential results and the integrated result.

4.4.7 Parameterization of the moments

The fully differential final results are also fit to a four-dimensional function. This allows for the measured modulations to be simulated in MC. The parameterization is used in this analysis to perform systematic tests with MC that include $\cos n\phi_h$ moments similar to the data (see Sections 5.4.1, 5.4.2, 5.5), and for the $\cos n\phi_h$ moments to be included at generator level in MC productions, such as for `gmCTRANS` (see Section 5.4.3). In addition these parameterizations can be used by other analyzers within the HERMES collaboration who seek to remove or evaluate the effect of the $\cos n\phi_h$ on their analysis; for examples see Section 6.4.1.

The primary fit function used has 38 parameters, 19 for $\cos \phi_h$ and 19 for $\cos 2\phi_h$, each with the functional form:

$$\begin{aligned}
 f = & A_1 + A_2x + A_3y + A_4z + A_5P_{h\perp} \\
 & + A_6x^2 + A_7z^2 + A_8P_{h\perp}^2 + A_9xz \\
 & + A_{10}xP_{h\perp} + A_{11}zP_{h\perp} + A_{12}yP_{h\perp} \\
 & + A_{13}yx + A_{14}yz + A_{15}y^2 \\
 & + A_{16}x^3 + A_{17}z^3 + A_{18}P_{h\perp}^3 + A_{19}y^3
 \end{aligned}$$

In addition, several other parameterizations were tested, including:

- 34 parameters:

$$\begin{aligned}
 f = & A_1 + A_2x + A_3y + A_4z + A_5P_{h\perp} \\
 & + A_6x^2 + A_7z^2 + A_8P_{h\perp}^2 + A_9xz \\
 & + A_{10}xP_{h\perp} + A_{11}zP_{h\perp} + A_{12}yP_{h\perp} \\
 & + A_{13}yx + A_{14}yz + A_{15}y^2 \\
 & + A_{16}z^3 + A_{17}P_{h\perp}^3
 \end{aligned}$$

- 42 parameters:

$$\begin{aligned}
f = & A_1 + A_2x + A_3y + A_4z + A_5P_{h\perp} \\
& + A_6x^2 + A_7z^2 + A_8P_{h\perp}^2 + A_9xz \\
& + A_{10}xP_{h\perp} + A_{11}zP_{h\perp} + A_{12}yP_{h\perp} \\
& + A_{13}yx + A_{14}yz + A_{15}y^2 \\
& + A_{16}x^3 + A_{17}z^3 + A_{18}P_{h\perp}^3 + A_{19}y^3 \\
& + A_{20}z^2P_{h\perp} + A_{21}P_{h\perp}^2z
\end{aligned}$$

- 50 parameters:

$$\begin{aligned}
f = & A_1 + A_2x + A_3y + A_4z + A_5P_{h\perp} \\
& + A_6x^2 + A_7z^2 + A_8P_{h\perp}^2 + A_9xz \\
& + A_{10}xP_{h\perp} + A_{11}zP_{h\perp} + A_{12}yP_{h\perp} \\
& + A_{13}yx + A_{14}yz + A_{15}y^2 \\
& + A_{16}x^3 + A_{17}z^3 + A_{18}P_{h\perp}^3 + A_{19}y^3 \\
& + A_{20}x^2z + A_{21}x^2P_{h\perp} + A_{22}y^2z + A_{23}y^2P_{h\perp} \\
& + A_{24}z^2P_{h\perp} + A_{25}P_{h\perp}^2z
\end{aligned}$$

Chapter 5

Systematic studies

While the analysis procedure presented in the previous chapter makes every effort to accurately extract the $\langle \cos n\phi_h \rangle_{UU}$ moments there are many places where missed corrections and mis-corrections can alter the extracted results from the true physics. In an effort to identify and account for such potential inaccuracies many studies have been performed.

In Sections 5.2 to 5.6 sources of systematic error are identified and explored. Most have no significant influence on the extracted moments and are taken as proof of the robust nature of the results. The sources of uncertainty discussed in Sections 5.2 and 5.3 that can be simulated were absorbed into an all-in-one error evaluated with the MC self-test described in Section 5.5. The systematic studies of Sections 5.4 to 5.6 contribute to the final systematic uncertainty. The calculation of the final systematic is presented in Section 5.7

5.1 Cross-check of results

All the results presented in this thesis have been meticulously verified by two independent analyzers, Dr. Francesca Giordano (Ph.D March 2008) and the author. This ensures that bugs present in the analysis code are rooted out. In addition it presents an opportunity to scrutinize each analyzer's methodology and debate the choice of technique when some ambiguity is present. For example, when identifying a DIS lepton, should the highest momentum lepton be identified and then fiducial volume cuts be applied (potentially throwing out the DIS event) or should the highest momentum lepton that passes the fiducial volume cut be chosen? Such questions are easy to overlook when one is focused on the logic of writing a computer code, but come under scrutiny when two analyzers use different approaches that must be reconciled. While it is always possible that the same errors have been committed by both analyzers, it is the author's firm opinion that the data presented in this thesis has been properly analyzed in as far as it is possible with the tools (MC, tracking, etc.) available.

5.2 Detection effects

Several potential sources of error come from particle detection and reconstruction and are discussed in this section.

5.2.1 Track reconstruction

Two tracking methods, HTC and HRC (Section 2.5.2) are used to convert the detector hits into track position and momentum information. Inefficiencies that depend on variables in which the data are binned and the overall normalization are irrelevant since they cancel in the 4-dimensionally binned ratio of the fit terms used to extract the moments (Section 4.4.4). However, other inefficiencies, such as sensitivity to multi-track topology, could influence the moments if they are not accurately simulated in the MC.

Since HTC provides parameters which indicate the quality of the track or vertex reconstruction, this can be used as a tool to estimate the influence of poor tracking on the moments. The moments were extracted with various cuts on the vertex and track probabilities and the results are shown in Figure 5.1. Some fluctuation is expected when changing the probability cut since the statistic of the data sample is changing. However, the moments are stable within uncertainties and this is taken as evidence that the 0.01 cut sufficiently removes poorly tracked events.

The poorly tracked events in HRC, or any potential problems with HTC are accounted for when the 2000 data, analyzed with HRC, is compared to the 2005-2007 data, analyzed with HTC (Section 5.6). In addition, the MC self-test (Section 5.5) that compares the model input in the MC to the results extracted after running the MC through the detector simulation and tracking should also account for any influence the tracking has on the results.

5.2.2 PID

As discussed in Section 2.5.5 and Section 3.4.1 particle-type identification is difficult when two tracks are close together. Significant work went into discovering that using only three of the four PID detectors when one failed greatly improves the lepton/hadron separation for close tracks. Even more time was spent developing and testing the EVT method of RICH hadron-type identification. While these both offer great improvements over the previous options they are still not perfect.

In the reconstructed MC used for the unfolding procedure (Section 4.4.1) the PID detectors used for electron/hadron separation are simulated in detail. From Figure 2.3 it is clear that the MC accurately reproduced the inefficiencies of the data. Therefore, the unfolding procedure, by correcting to the Born-level

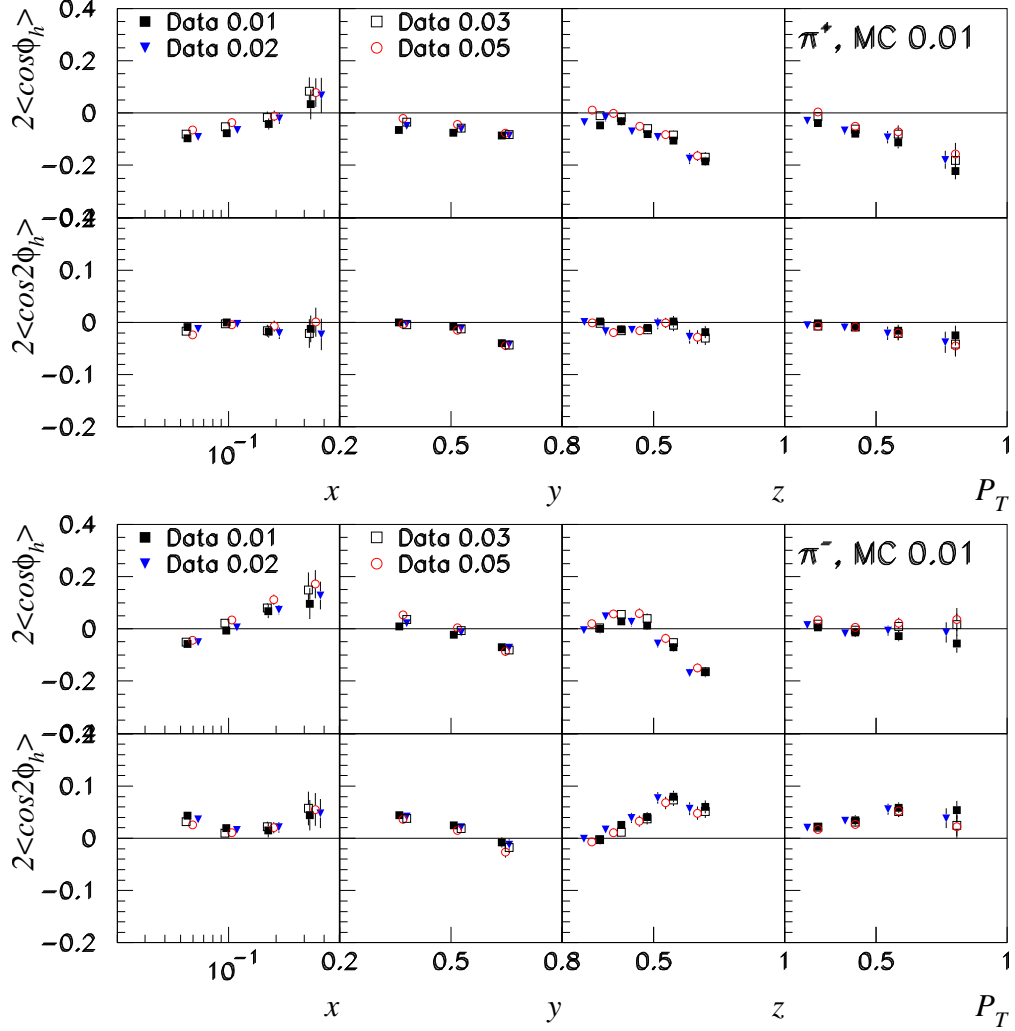


Figure 5.1: Moments extracted with various HTC vertex and track probability cuts on the data for π^+ (upper plot) and π^- (lower plot)

where true particle identification was used, corrects for inefficiencies in electron/hadron discrimination.

Inefficiencies in the identification of hadrons with the RICH are corrected for with the RICH inverted P-matrix weights. In addition, RICH hadron-type identification is used in the MC self-test described below (Section 5.5) and was thus included in the resultant systematic error.

5.2.3 Beam slopes

While HTC tracking corrects for all known detector misalignments and variations in beam position, beam slopes are not accounted for. Beam slopes are provided by HERA; however only a relative slope is known. Alexander Kisselev created a “beam finder” code which traces out the beam line by finding the common line from which giant samples of single tracks most closely originate. With this code the beam slope from the data is estimated to be up to 200 μrad vertically and up to 300-500 μrad horizontally. In analyzing the data a beam slope has the effect of shifting the lepton scattering plane, which changes ϕ_h . Several tests were done by reanalyzing the 2007 hydrogen data with an assumed x and y slope of the beam chosen within the extreme ranges found by the beam finder. The slopes used are described in Table 5.1. The results for cases 1, 2 and 3 are shown in Figure 5.2. Clearly, the beam slope has no significant effect on the moments. The other cases (not shown) have the same negligible effect.

Table 5.1: Beam slope parameters used

| Case | Horizontal beam slope | Vertical beam slope |
|------|----------------------------------|---------------------------------|
| 1 | 300 μrad | 200 μrad |
| 2 | -300 μrad | 200 μrad |
| 3 | 300 μrad | 100 μrad |
| 4 | 200 μrad | 100 μrad |
| 5 | relative values from HERA | |
| 6 | 100 μrad | 100 μrad |
| 7 | 100+(HERA value) μrad | 50+(HERA value) μrad |
| 8 | 500 μrad | 300 μrad |

5.2.4 Detector misalignment

Survey measurements and careful analysis of the data [24] revealed that the spectrometer components differed from their prescribed locations by up to ~ 1 mm, and these offsets changed between data taking periods when major shutdowns occurred. During these shutdowns major construction was done in some areas and detectors could have been slightly displaced. The known misalignments are corrected for in the HTC tracking, but some unknown misalignment may remain.

Top / bottom studies

To try to quantify any remaining detector misalignment that is not accounted for in the tracking, the moments were extracted from the 2007 hydrogen data separately for events with the lepton in the top half or the bottom half of the detector. A similar test constrained the hadron position to only the top half or only the bottom half. The top and bottom detector halves should be completely symmetric and so these

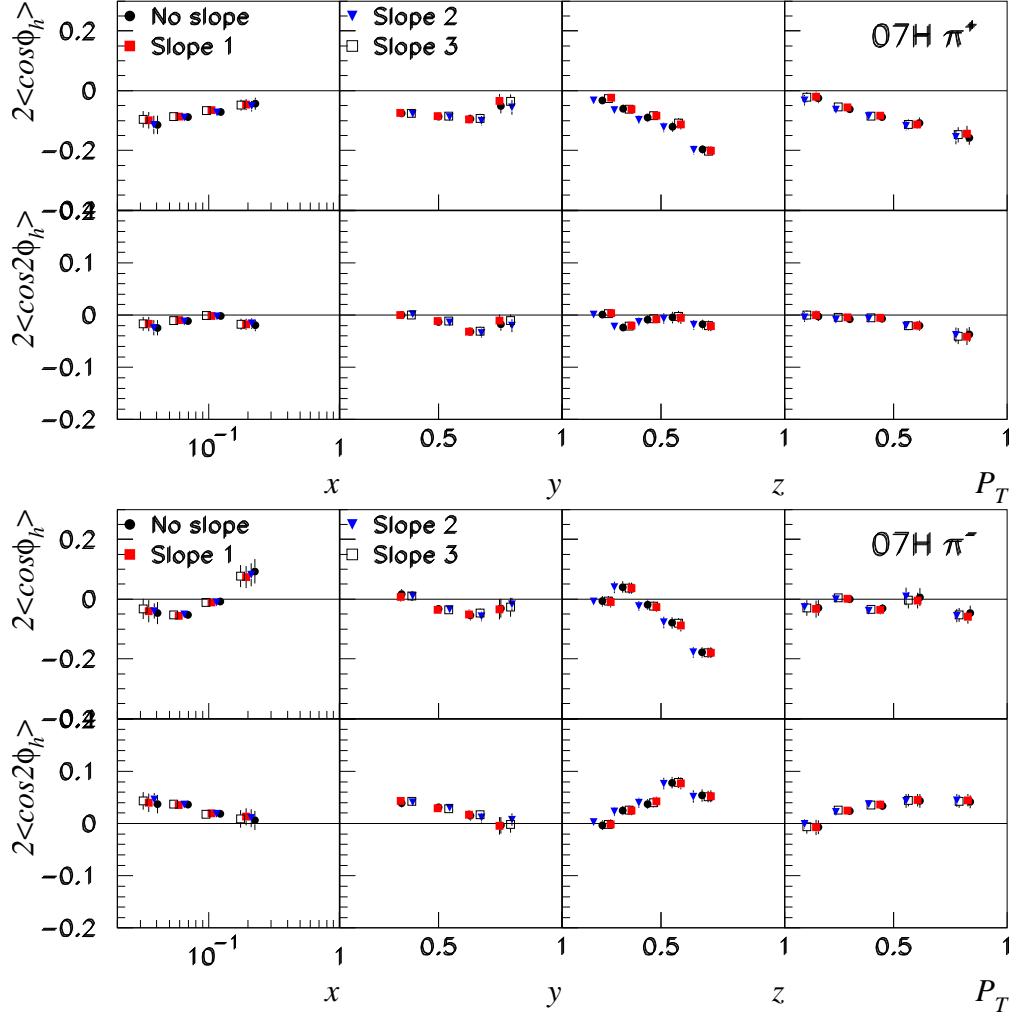


Figure 5.2: 2007 hydrogen target π^+ (upper plot) and π^- (lower plot) moments extracted with different beam slope assumptions. Labels refer to Table 5.1

different subsets of the data ought to be the same. However, both tests showed some dependence on the position of the lepton or hadron, as can be seen in Figures 5.3 and 5.4. This is evidence of some asymmetry between the upper and lower detector. Further investigation showed that the difference between the moments extracted from the top and bottom is sensitive to beam slopes (described in Section 5.2.3), as seen in Figure 5.5 (but again note from Section 5.2.3 that the full moments with top and bottom detector halves together is independent of the beam slope). This again points to a top/bottom detector asymmetry but makes it difficult to quantify since the true beam slopes are not known and thus the true difference between the moments extracted from the top and bottom cannot be determined. However, this result is irrelevant: a true separation of the $\cos n\phi_h$ measurements into “top” and “bottom” cannot be done since *two* tracks must be observed in each event, the lepton and the hadron. The detector-half constraint can only be placed on

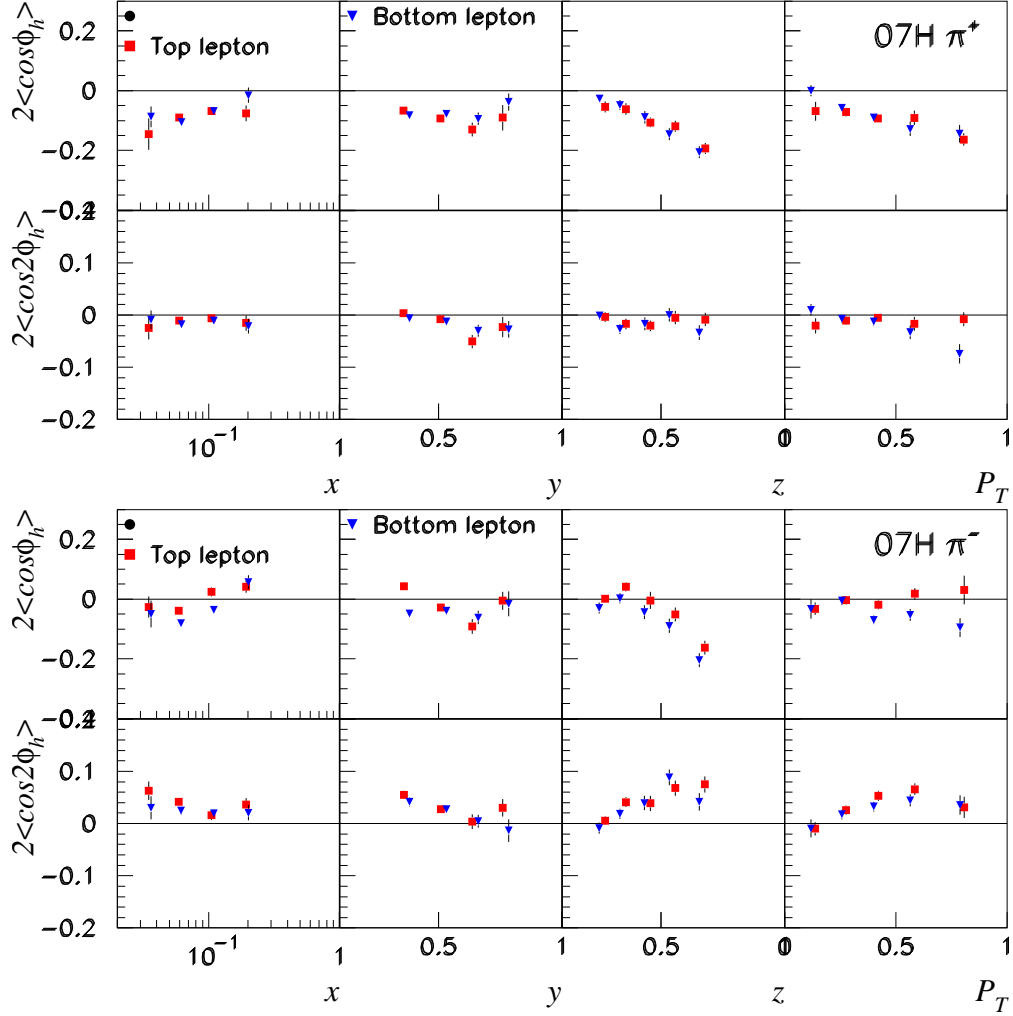


Figure 5.3: π^+ (upper plot) and π^- (lower plot) moments from the 2007 hydrogen target data set with the lepton restricted to the top (red) or bottom (blue) detector half.

one track; constraining both tracks to be in one detector half does not allow for full coverage in ϕ_h . Hence, both “top” and “bottom” moments are some convolution of data from the top and bottom detector halves. In summary, it is clear that this test is not a useful measure of the detector misalignment.

Since the misalignment is difficult to estimate directly the difference between results from different data periods, where the alignment also differed, was taken into account in the systematic error, as described in Section 5.6

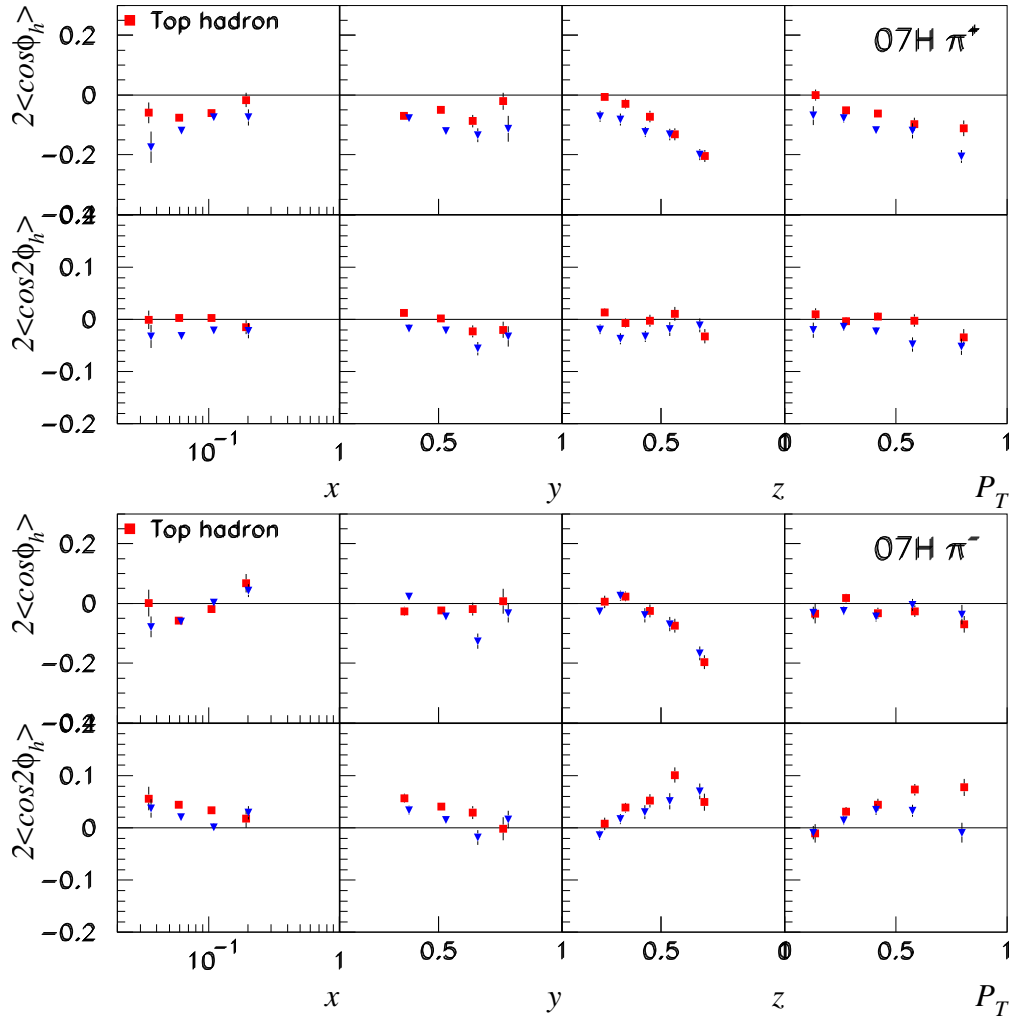


Figure 5.4: π^+ (upper plot) and π^- (lower plot) moments from the 2007 hydrogen target data set with the hadron restricted to the top (red) or bottom (blue) detector half.

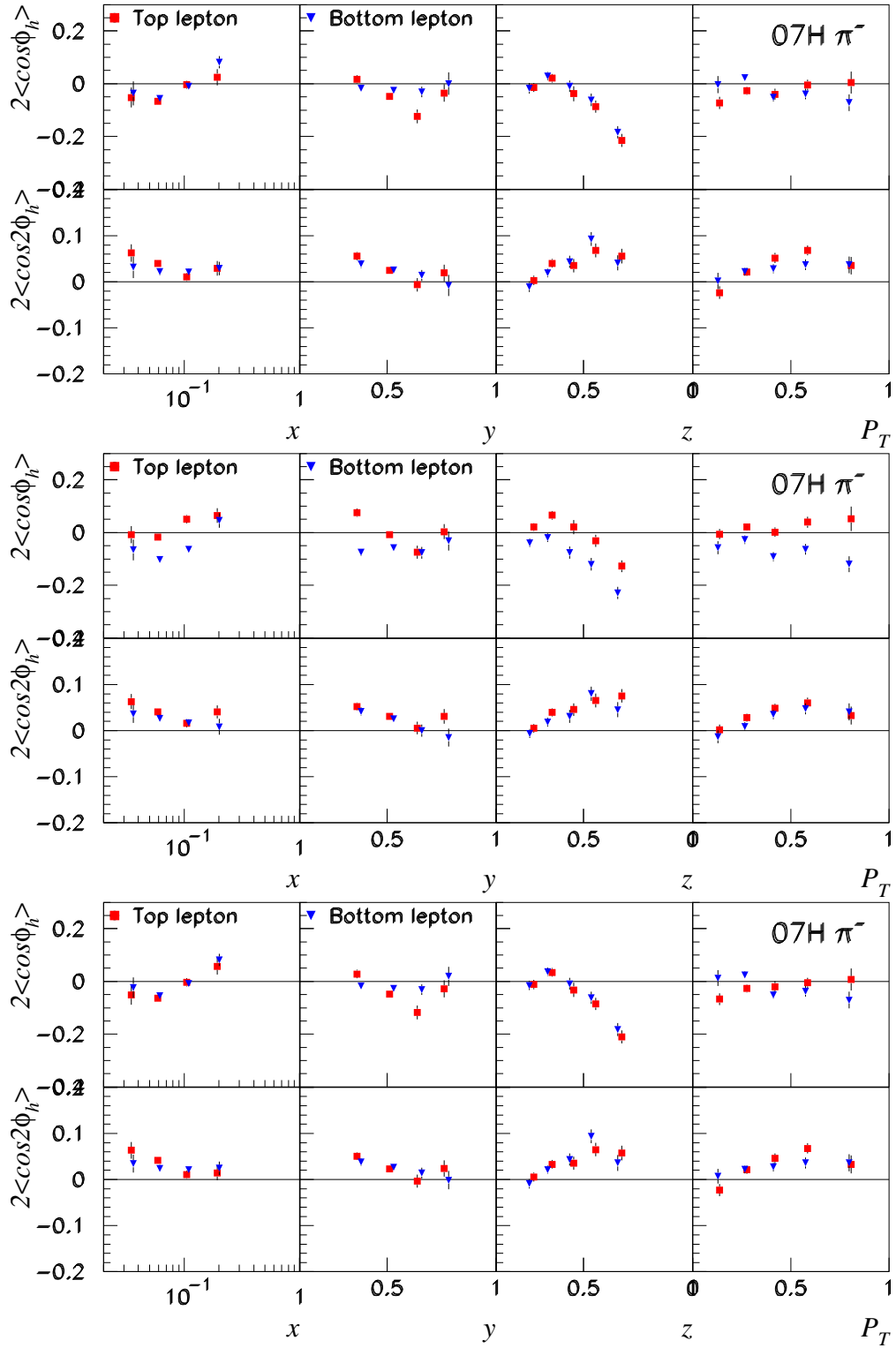


Figure 5.5: π^- moments from the 2007 hydrogen target data set with the lepton restricted to the top (red) or bottom (blue) detector half and correcting for a beam slope of case 1 (top plot), 2 (middle plot) or 3 (bottom plot) as described by Table 5.1

5.3 Systematic tests of the analysis procedure

The analysis procedure described in Section 4.4 can potentially introduce a bias in the results. Possible effects are evaluated here.

5.3.1 DIS normalization

The total number of DIS events in the data sample is used to normalize the data relative to the MC (Section 4.3.1). Since a ratio of the fit parameters is used to calculate the moments (Section 4.4.4) this normalization affects only the background vector relative to the data. In Figure 5.6 the effect of multiplying or dividing the DIS normalization by a factor of 2 is shown for the 2000 hydrogen π^+ data. Since this weight is applied to the data, dividing the weight by a factor of two effectively doubles the background that is subtracted. This has some effect on the data (though moderate), while decreasing the background relative to the data has only a small effect. This is an extreme test which shows that the results are relatively insensitive to even large changes in the normalization.

One alternative to using the total number of DIS events for MC-data normalization is to use the total number of SIDIS events. This gives a normalization factor that is within $\sim 10\%$ of that from DIS and so should produce identical results. No systematic uncertainty is explicitly included for the normalization: the tests described here show that its influence is very small, and further, its model dependence is evaluated in Section 5.4.2 and shown to be equally negligible.

5.3.2 Binning tests

ϕ_h binning

To test that the number of bins in ϕ_h is sufficient the number of ϕ_h bins was increased and decreased from the standard 12 bins. The results of extracting the moments from the 2007 hydrogen π^+ data with 8, 10, 11, 12, or 13 ϕ_h bins are shown in Figure 5.7. While some fluctuations are present, the moments are generally stable. A systematic error due to the ϕ_h binning is included in the MC self-test (Section 5.5).

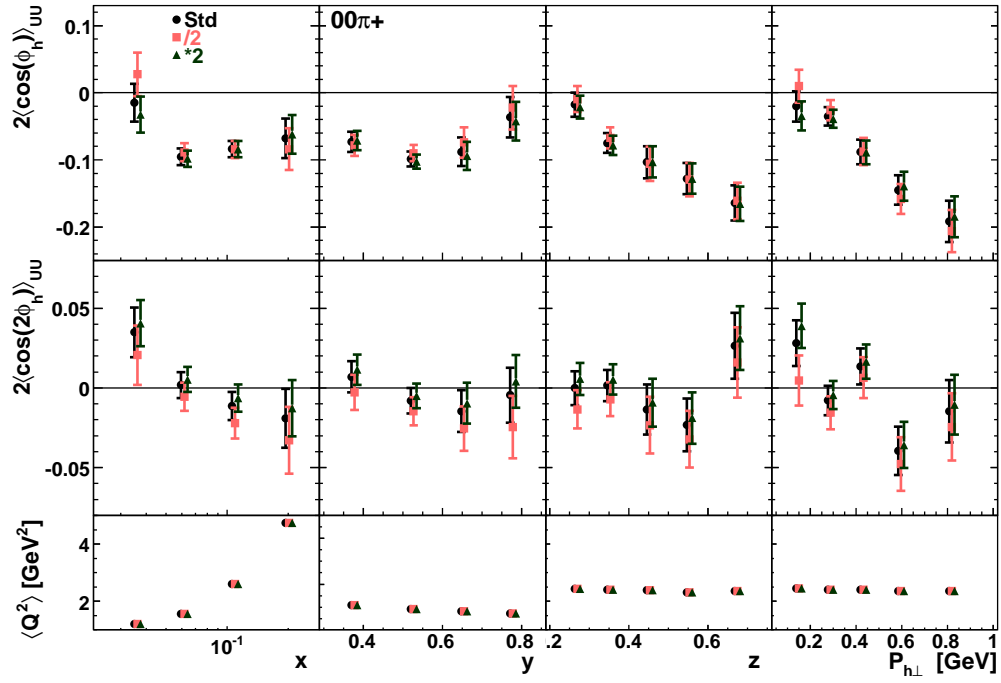


Figure 5.6: Effect of multiplying/dividing the DIS normalization by a factor of 2

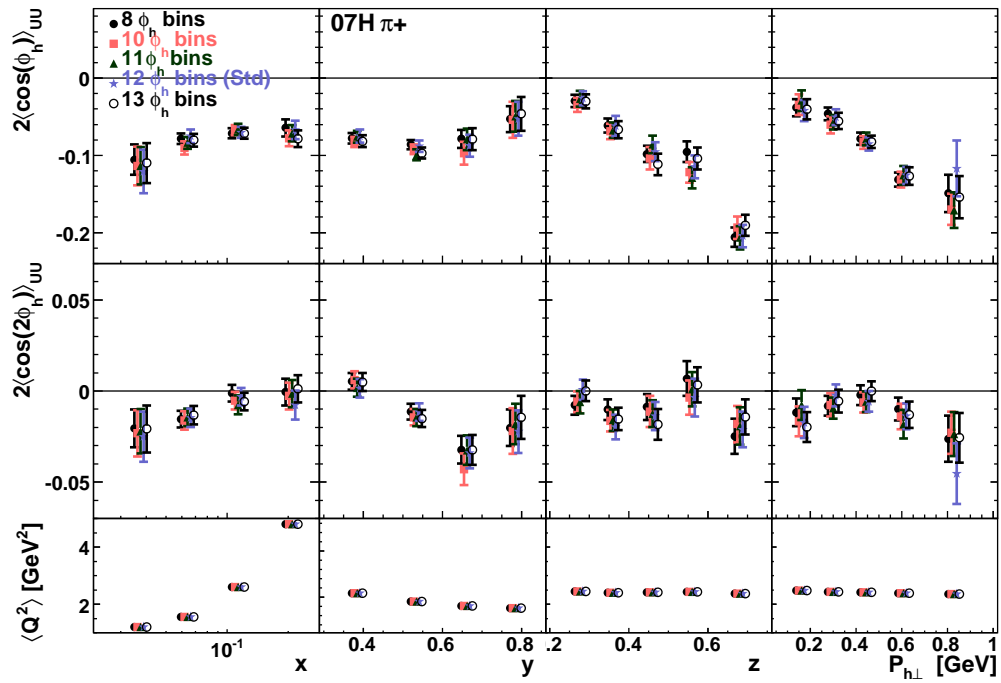


Figure 5.7: Effect of changing the number of bins in ϕ_h

Table 5.2: Kinematic regions used in binning test

| Test Variable | Variable | Kinematic Range | | Number of Bins (± 1) |
|---------------|--------------|-----------------|--------|----------------------------|
| x | y | 0.3 | - 0.7 | 3 |
| | z | 0.3 | - 0.75 | 4 |
| | $P_{h\perp}$ | 0.2 | - 0.7 | 3 |
| y | x | 0.023 | - 0.27 | 4 |
| | z | 0.3 | - 0.6 | 3 |
| | $P_{h\perp}$ | 0.2 | - 1.0 | 4 |
| z | x | 0.023 | - 0.27 | 4 |
| | y | 0.3 | - 0.7 | 3 |
| | $P_{h\perp}$ | 0.2 | - 0.7 | 3 |
| $P_{h\perp}$ | x | 0.023 | - 0.27 | 4 |
| | y | 0.3 | - 0.7 | 3 |
| | z | 0.3 | - 0.75 | 4 |

Kinematic binning

Care must be taken when testing the effect of the kinematic binning to avoid changing the kinematic region under study. Accordingly tests were performed separately for x , y , z , and $P_{h\perp}$. For the x test, the x binning was kept fixed, as were the y , z , and $P_{h\perp}$ ranges, while the number of bins in y , z , and $P_{h\perp}$ was increased or decreased by one. The tests for the other kinematic variables were the same: the variable under study and the kinematic range were fixed and the number of bins was increased or decreased by one in the other three variables. This test is problematic if the statistics are low, as increasing the number of bins can lead to bins with too few events to make a meaningful fit to the $\cos n\phi_h$ moments. To avoid this, a limited kinematic region with high statistics was chosen within which to perform each test. The region and number of bins used for each variable are described in Table 5.2. The results of the test are shown in Figure 5.8. The moments are generally stable although some effect is seen, especially when the number of bins is decreased. However, with fewer bins the bins sizes increase and the smearing matrix becomes more model dependent. A systematic error due to the kinematic binning is included in the MC self-test (Section 5.5).

Cut on poorly populated kinematic bins

The variable N defined in Equation 4.32 from Section 4.4.3 is one of the key variables used to exclude “bad bins” that give unstable fits. The cut on N was tested by applying cuts of 0.3, 0.4 (the standard cut used in this analysis), 0.5, 0.6, 0.7 and 0.8 to the 2007 hydrogen data. A cut of 0.8 includes all bins since the maximum value of N (when all ϕ_h bins are empty) is $\sqrt{(6^2 + 6^2)}/12 = 0.71$. Relaxing the standard cut of 0.4 to include more bins in the fit was found to have no significant effect on the the fit of the bins already included with the standard cut, while strengthening the cut to 0.3 produced unphysically large moments, indicating that this value is too strict. The question is then only of the quality of the fit in the additional

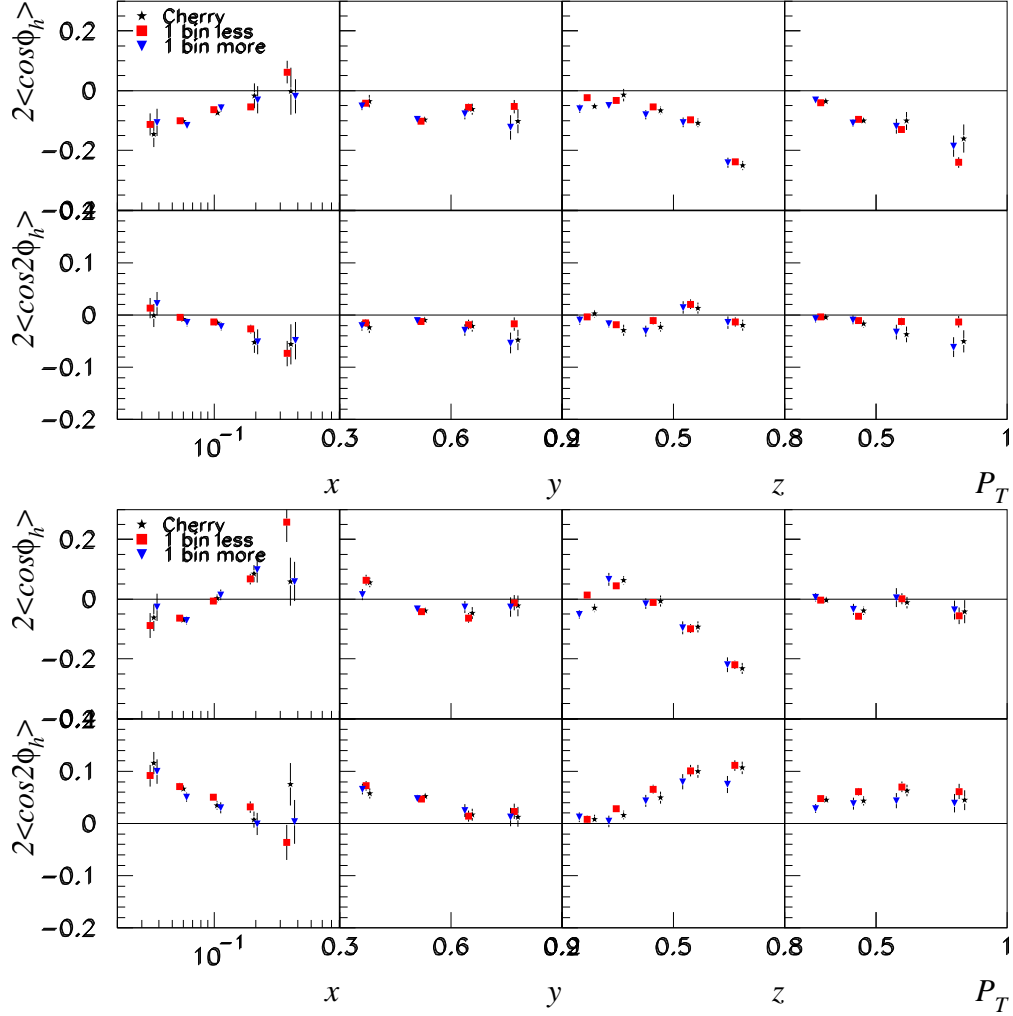


Figure 5.8: Kinematic binning tests as described in the text for π^+ (upper plot) and π^- (lower plot). Increasing the number of bins in the integrated variables by 1 (blue triangle), or decreasing by 1 (red squares), is compared to the standard binning (black stars).

bins added by the relaxed cut values. Relaxing the cut from 0.4 to 0.5 added ~ 35 additional bins where a fit could be performed. Of these bins, three are found to “fail” positivity: the absolute value of the moment minus the statistical error was larger than one. This is not necessarily a true violation of positivity since the systematic error is not taken into account and, due to the other cosine moments, the maximum amplitude is not strictly 1. However such a large moment is not expected physically and is vastly different from the moments observed in other kinematic regions where the statistics are better. When the Born-level yields (Equation 4.5) are compared to the fit function obtained for this kinematic bin the sense that the moments extracted from this fit are untrustworthy appears to be well founded. Such a bin is shown in Figure 5.9a. When the other bins added by relaxing the cut are viewed in a similar manner most appear to have equally untrustworthy fits, as can be seen in the example in Figure 5.9b. These are in contrast to Figure 5.10 where

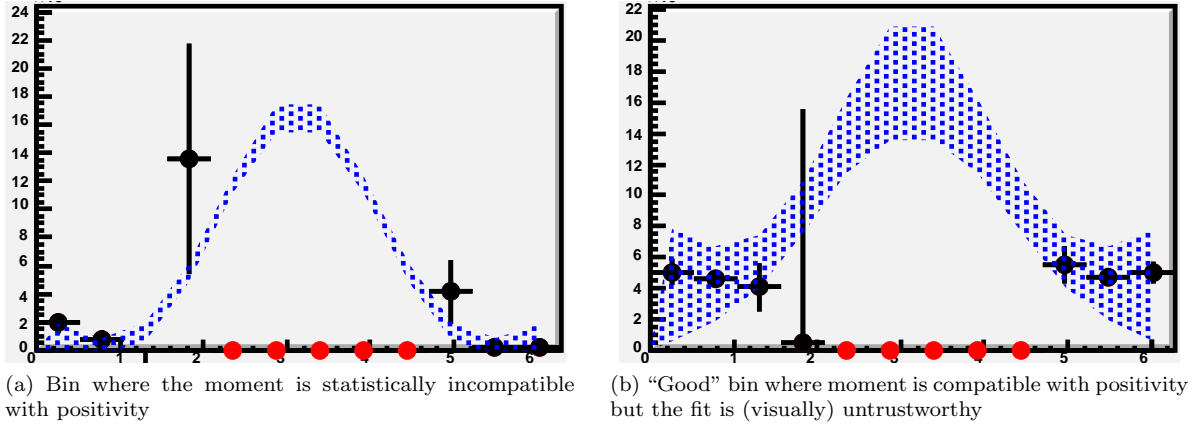


Figure 5.9: Two bins added when the cut is relaxed from 0.4 to 0.5. The black points are the unfolded data, the red points note an empty bin, and the blue band shows the fit.

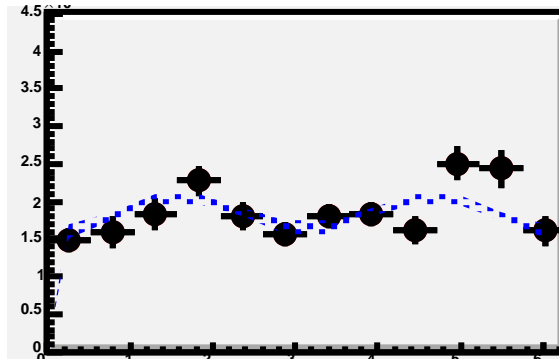


Figure 5.10: A typical bin with unfolded data points (black) and a more realistic fit (blue).

a more typical bin with high statistics in each ϕ_h bin is shown along with its fit. From these studies it is clear that the standard cut of 0.4 is optimal.

A systematic error stemming from bins eliminated from the integration region, as well as from bins with poor quality fits that are still included in the 0.4 cut, is included in the MC self-test described in Section 5.5.

5.3.3 Additional azimuthal moments

Theoretically the unpolarized cross section in the one-photon approximation, up to leading order in α_s and sub-leading twist (Equation 1.17), is not expected to have any sine terms or any cosine terms higher than $\cos 2\phi_h$. The acceptance of the spectrometer, however, may include higher-order Fourier terms. In Figure 5.11 the moments extracted from the raw data (without unfolding) are shown, compared to the same quantities extracted from the Pythia MC. It is clear that a $\cos 3\phi_h$ modulation, which is known to be zero in Pythia and expected to be zero in the data, can arise from the spectrometer acceptance. Thus, as an

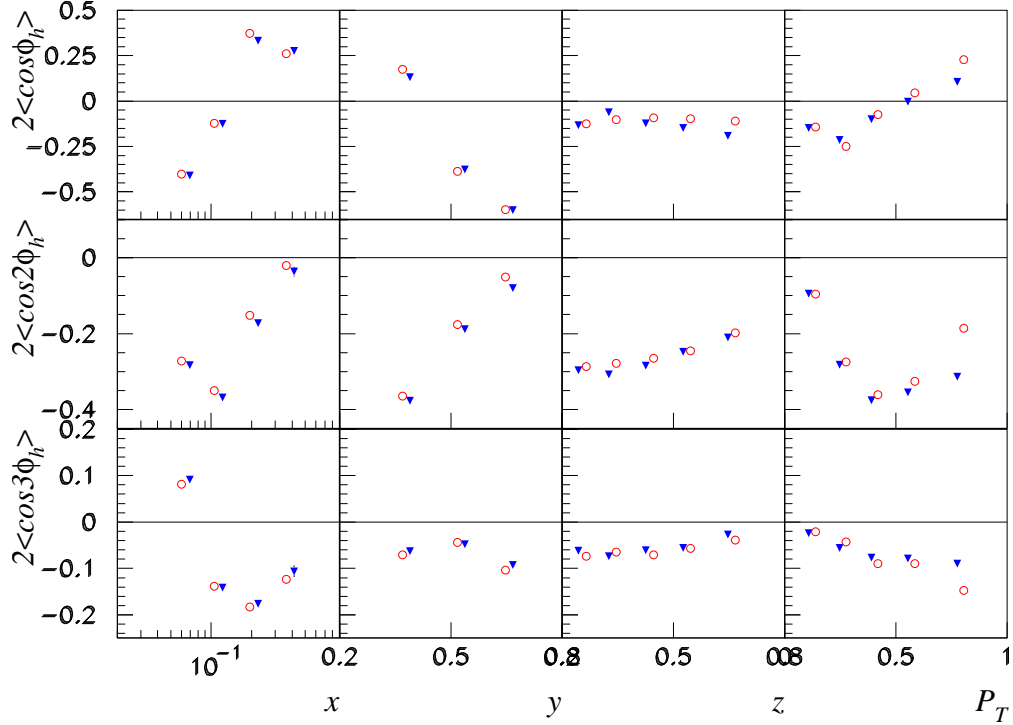


Figure 5.11: Acceptance Moments: $\cos \phi_h$ (top), $\cos 2\phi_h$ (middle) and $\cos 3\phi_h$ (bottom) moments extracted from raw (not unfolded) 2007 hydrogen data (blue triangles) and Pythia MC (red circles).

additional test of the unfolding procedure, additional Fourier moments can be extracted from the data.

The Fold and Fit procedure was extended to include one additional moment: $\cos 3\phi_h$, $\cos 4\phi_h$, or $\sin \phi_h$. The results of the test including $\cos 3\phi_h$ are shown in Figures 5.12 to 5.15. The $\cos \phi_h$ and $\cos 2\phi_h$ moments are stable with respect to including or not the additional fit term. The $\cos 3\phi_h$ moments are near zero. When a systematic error is calculated for the $\cos 3\phi_h$ moments (using the same procedure as described in this chapter for $\cos \phi_h$ and $\cos 2\phi_h$) they are consistent with zero, as shown in Figure 5.16.

The results of including $\cos 4\phi_h$ in the fit are shown in Figures 5.17 and 5.18 while the results of including $\sin \phi_h$ in the fit are shown in Figures 5.19 and 5.20, all for the hydrogen target. In both cases, the $\cos \phi_h$ and $\cos 2\phi_h$ moments are stable with respect to including or not the additional fit term. The $\cos 4\phi_h$ and $\sin \phi_h$ moments are consistent with zero. The deuterium target shows similar results.

These tests show that the Fold and Fit procedure is able to properly account for the acceptance of the spectrometer and remove any additional Fourier moments induced by the acceptance.

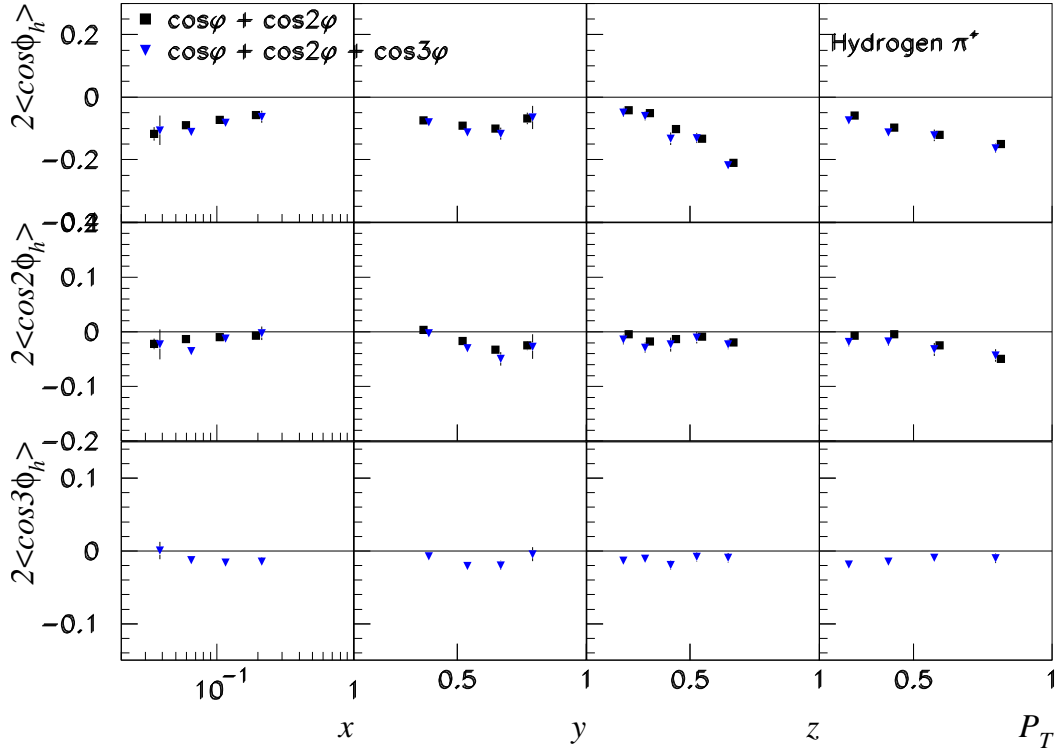


Figure 5.12: 2007 hydrogen target π^+ moments extracted with the standard fit function (black) compared to a fit including $\cos 3\phi_h$ (blue).

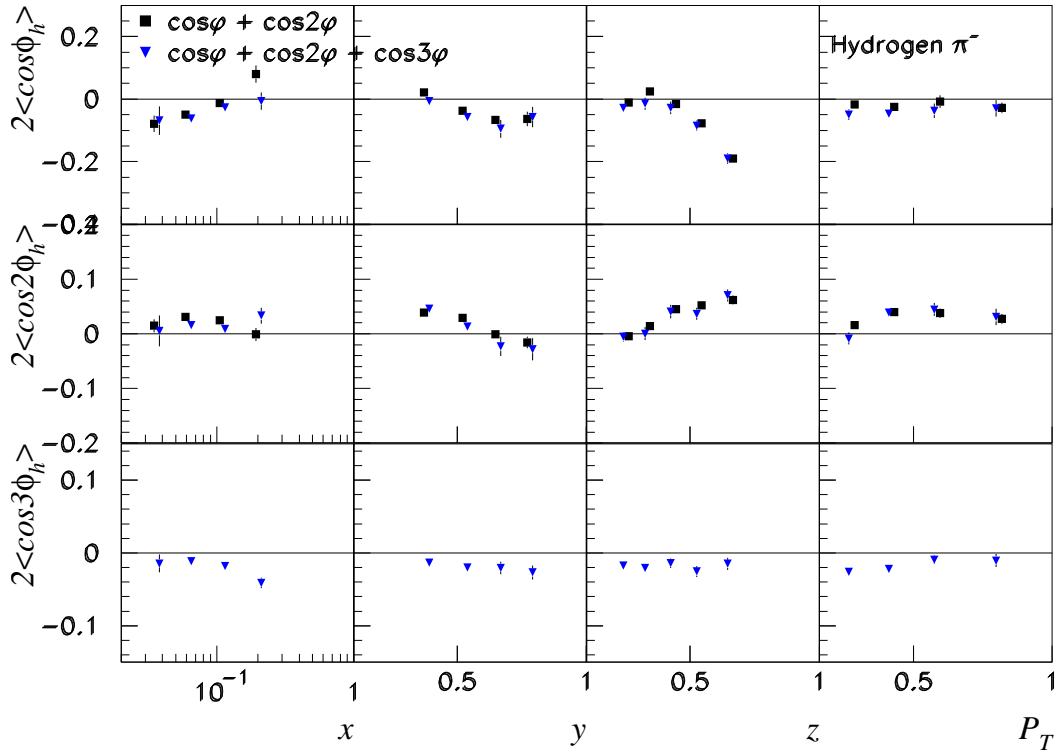


Figure 5.13: Like Figure 5.12 but for π^-

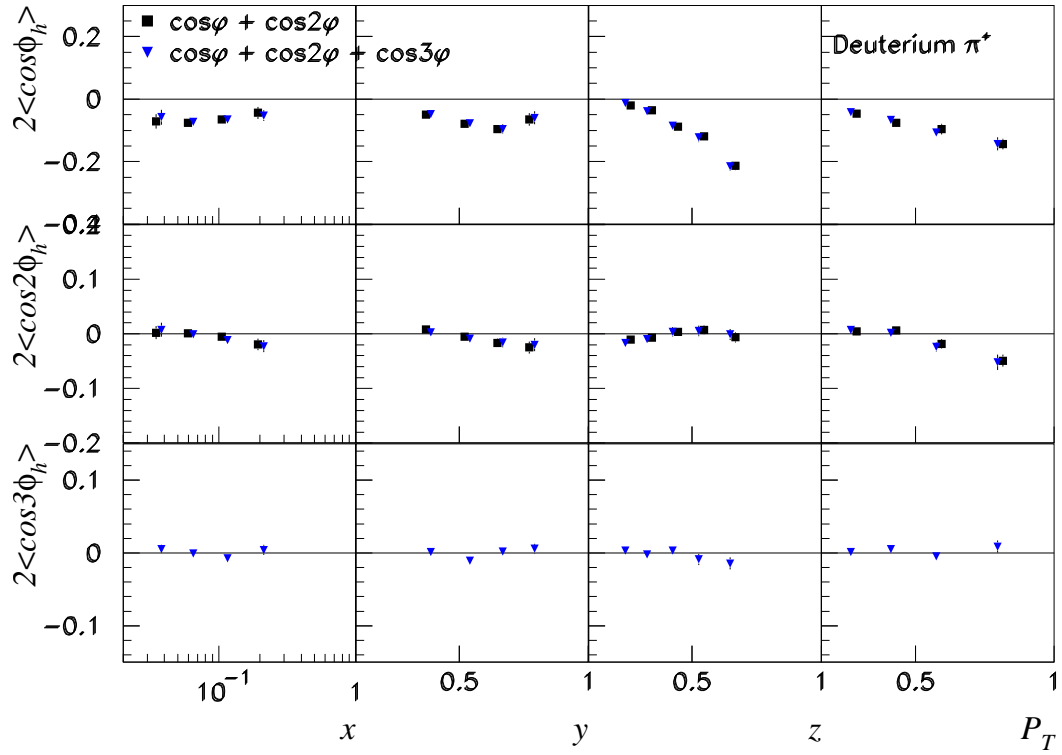


Figure 5.14: Like Figure 5.12 but for a deuterium target

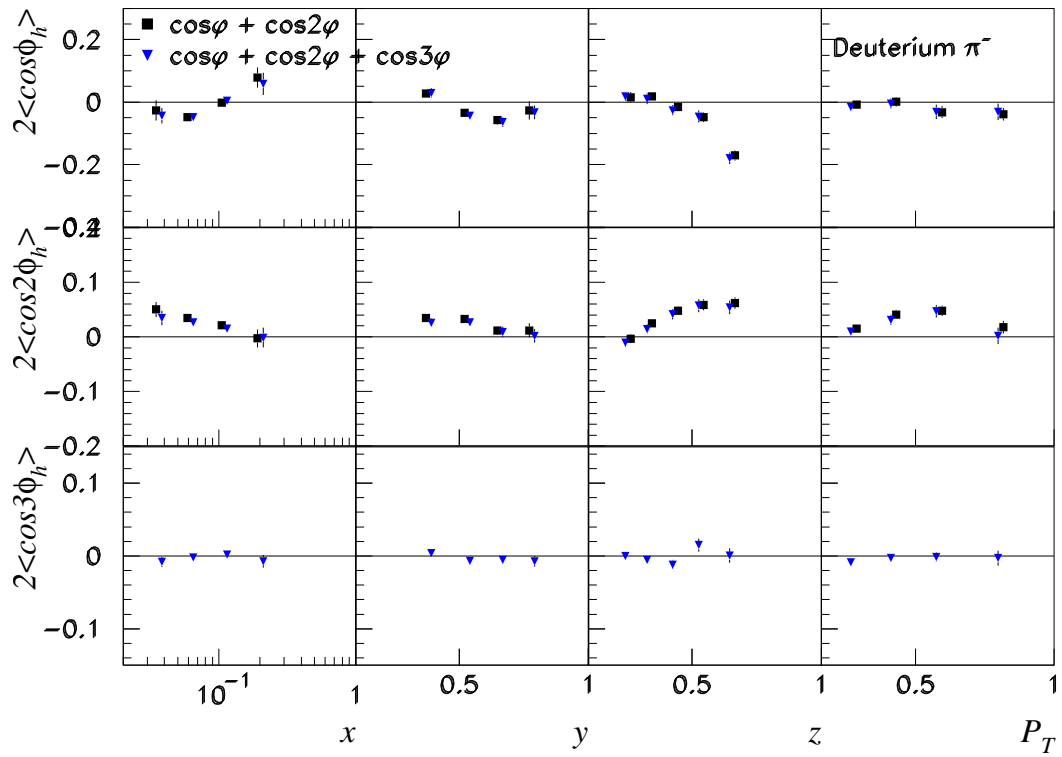


Figure 5.15: Like Figure 5.12 but for π^- on a deuterium target

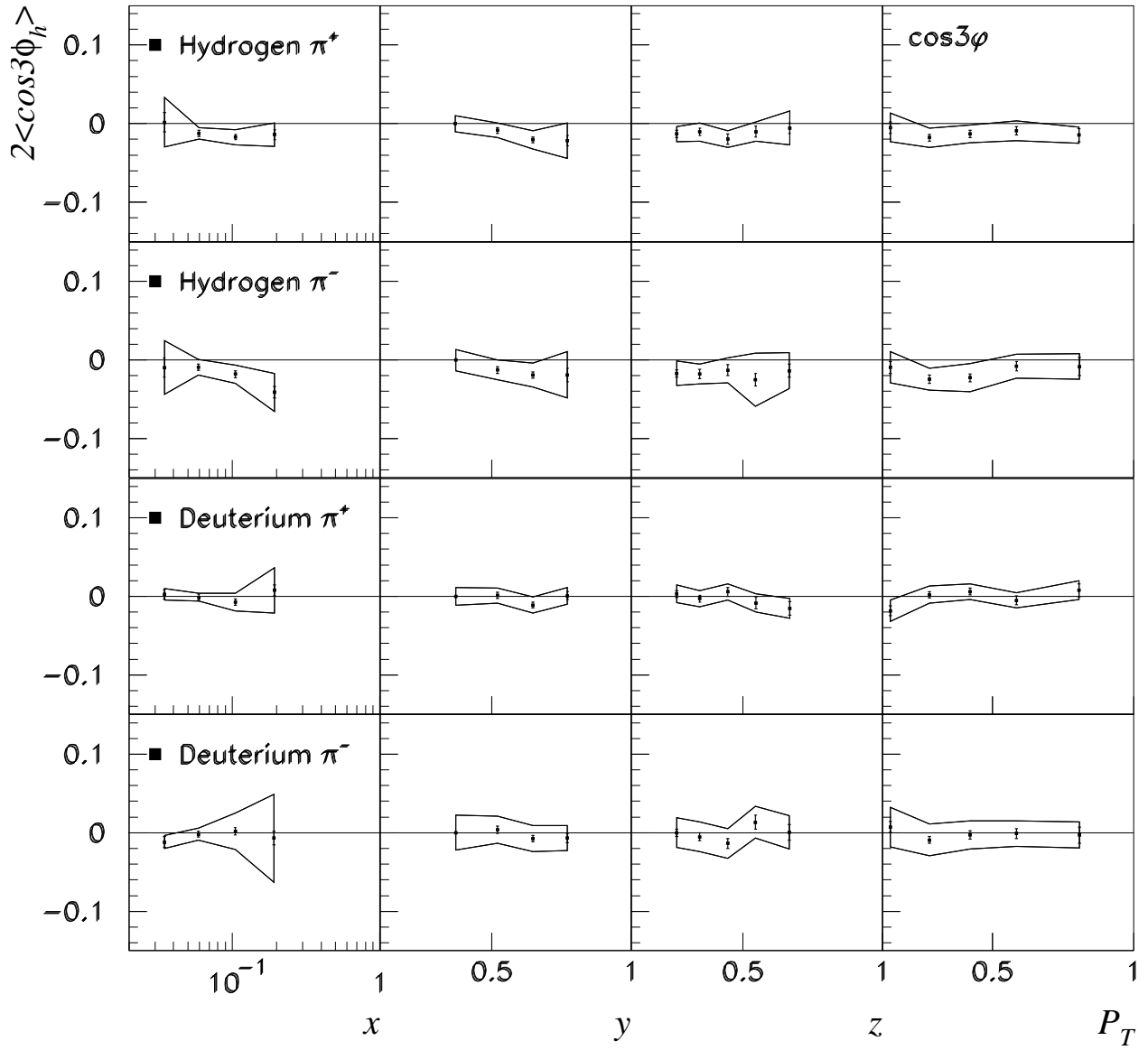


Figure 5.16: The $\cos 3\phi_h$ moments from Figures 5.12 to 5.15 with a systematic error band.

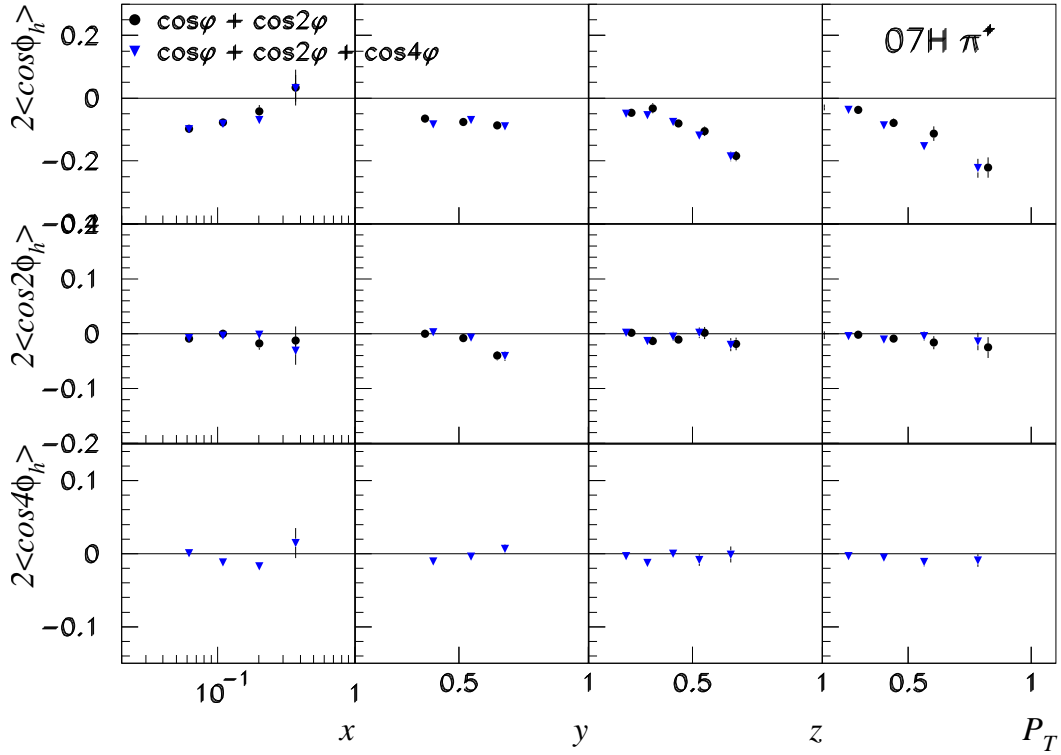


Figure 5.17: 2007 hydrogen target π^+ moments extracted with the standard fit function (black) compared to a fit including $\cos 4\phi_h$ (blue).

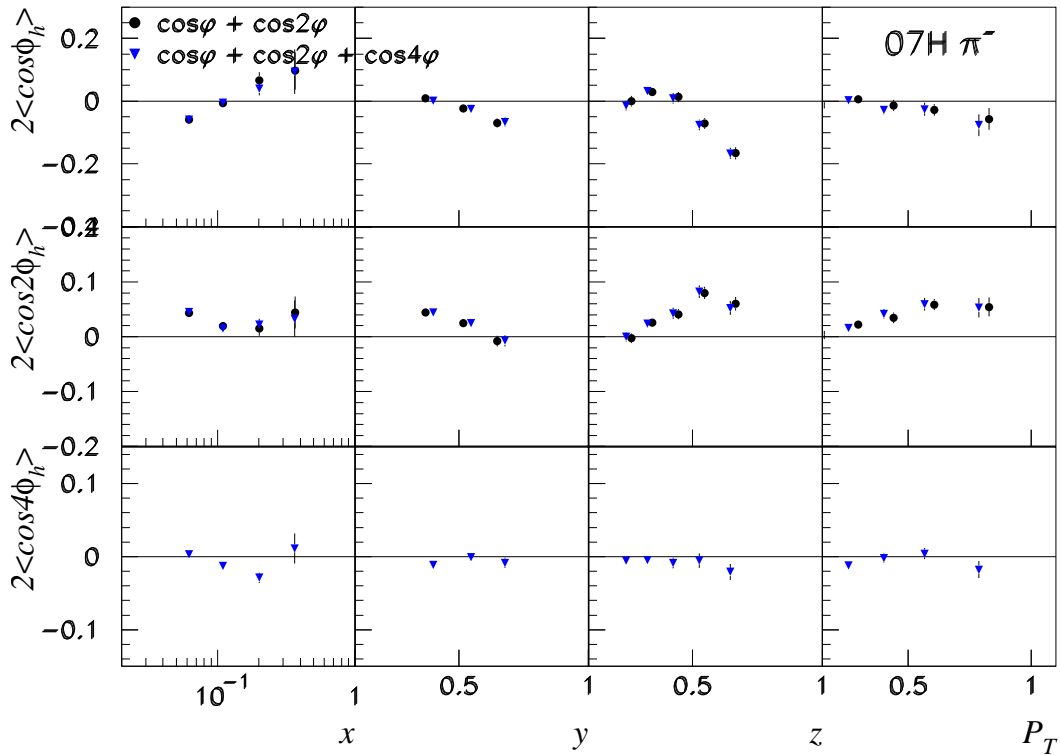


Figure 5.18: Like Figure 5.17 but for π^-

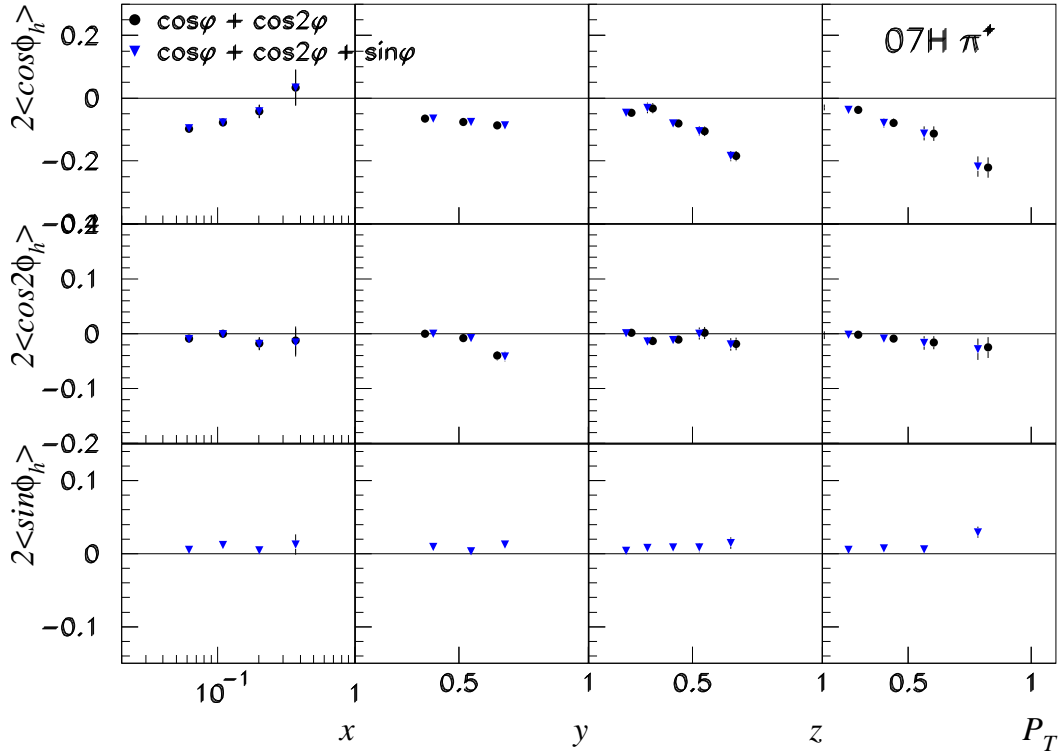


Figure 5.19: 2007 hydrogen target π^+ moments extracted with the standard fit function (black) compared to a fit including $\sin \phi_h$ (blue).

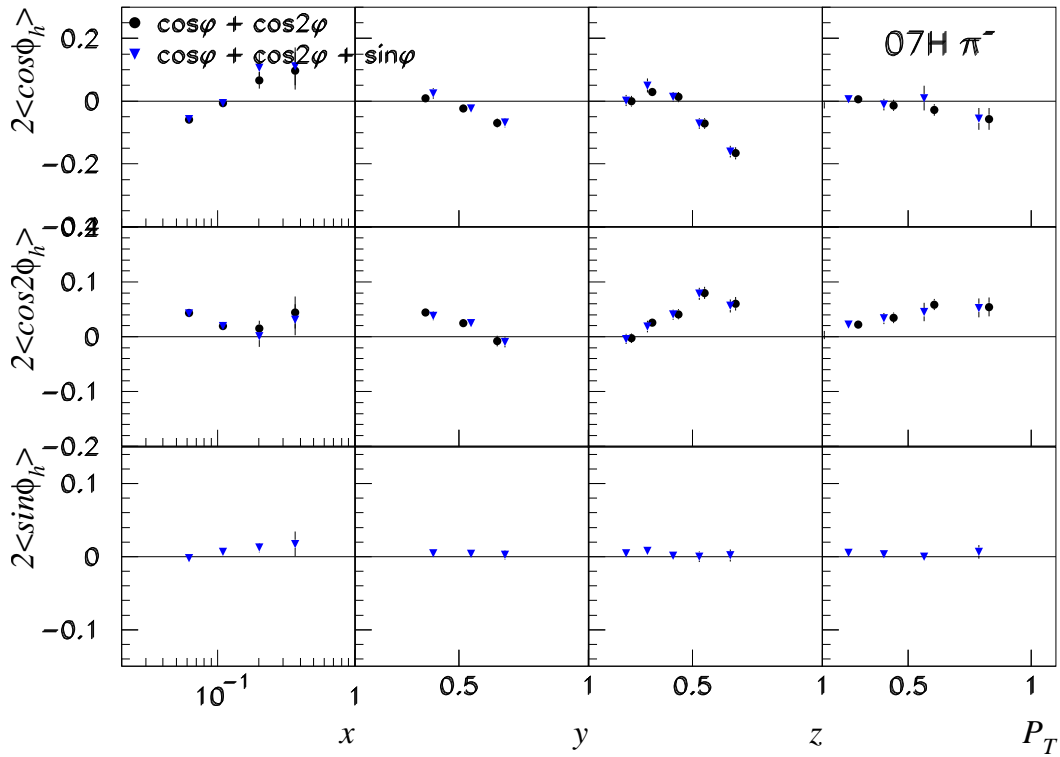


Figure 5.20: Like Figure 5.19 but for π^-

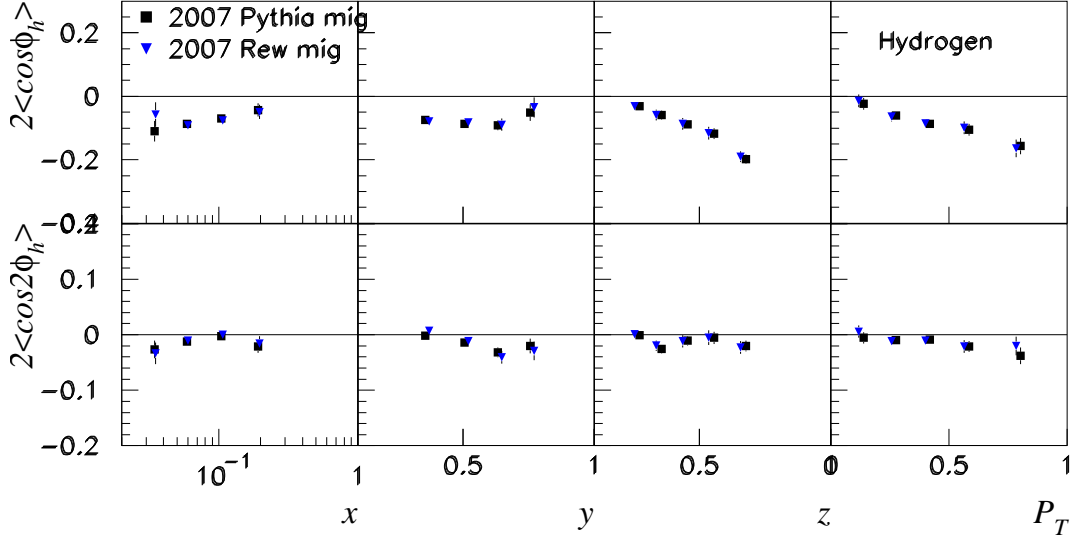


Figure 5.21: 2007 hydrogen π^+ moments unfolded with the standard migration matrix from Pythia (black squares) or the same matrix reweighted with the 38 parameter fit to the data (blue triangles).

5.4 MC model dependence tests

As shown in the last section, this analysis is dependent on MC to correct for the spectrometer acceptance and other effects. Tests designed to evaluate the influence of the physical model implemented in the MC on the extracted results are presented in this section.

5.4.1 Model dependence of the smearing matrix

The smearing matrix (Section 4.4.1) is designed to minimize its dependence on the physics model of the cross section implemented in the MC. Since it is a ratio of the reconstructed to Born-level yields, in the limit of infinitely small bins in all the variables on which the cross section depends (i.e. the 5-dimensional binning used here, but with infinitely small bins), the smearing matrix is completely model independent and depends only on the detector simulation.

In order to test the model dependence of the smearing matrix the 2007 hydrogen π^+ smearing matrix was weighted with the $\cos n\phi_h$ moments from the 4-dimensional parameterization (described in Section 4.4.7 and presented in Section 6.4) and applied to the data. This is compared to the data unfolded with the standard smearing matrix with no $\cos n\phi_h$ moments included and shown in Figure 5.21. As expected, the two results are compatible. The systematic error includes a contribution from the difference between the moments extracted with these two different smearing matrices.

5.4.2 Model dependence of the background vector

The background vector (Section 4.4.1) describes events which would have been excluded from the analysis in the absence of radiative effects and detector smearing. Unlike the smearing matrix, the background vector is completely model dependent. Luckily, as demonstrated by Figure 5.6, when the DIS normalization is modulated by a factor of 2, effectively changing the background vector by a factor of 2, the results hardly change.

To evaluate the model dependence of the results due to the background vector the 2007 hydrogen π^+ moments were extracted using two different background vectors: one from the standard Pythia and the other from the Pythia background weighted with the $\cos n\phi_h$ moments calculated with the 4-dimensional parameterization (described in Section 4.4.7 and presented in Section 6.4). The systematic error includes a contribution from the difference between the moments extracted with these two different background vectors.

5.4.3 Model dependence of the integration procedure

In order to interpret the results and compare them with other experiments and theory it is necessary to integrate over three kinematics variables and present the moments versus one dimension at a time (see Section 4.4.6). This requires weighting the moments with the Born cross section. As discussed in Section 4.4.6, the Born cross section is taken from Pythia, which introduces a model dependence on the cross section model implemented in Pythia. The Pythia production used (see Section 4.3.3) is tuned to HERMES kinematics and reasonably reproduces the HERMES multiplicities. However, to quantify the model dependence, an alternate MC generator, `gmcTRANS`, was used. `gmcTRANS` generates SIDIS events according to the CTEQ6 [25] extraction of f_1 and the Kretzer [26] extraction of D_1 . It includes intrinsic quark momenta p_T with non-flat z -dependence extracted from a fit to HERMES data. At the generator level the 4-dimensional parameterization (see Sections 4.4.7 and 6.4) of the $\cos n\phi_h$ moments was also included. The results are presented in Figure 5.22. The systematic error includes a contribution from the difference between the moments extracted with these different models of the unpolarized cross section.

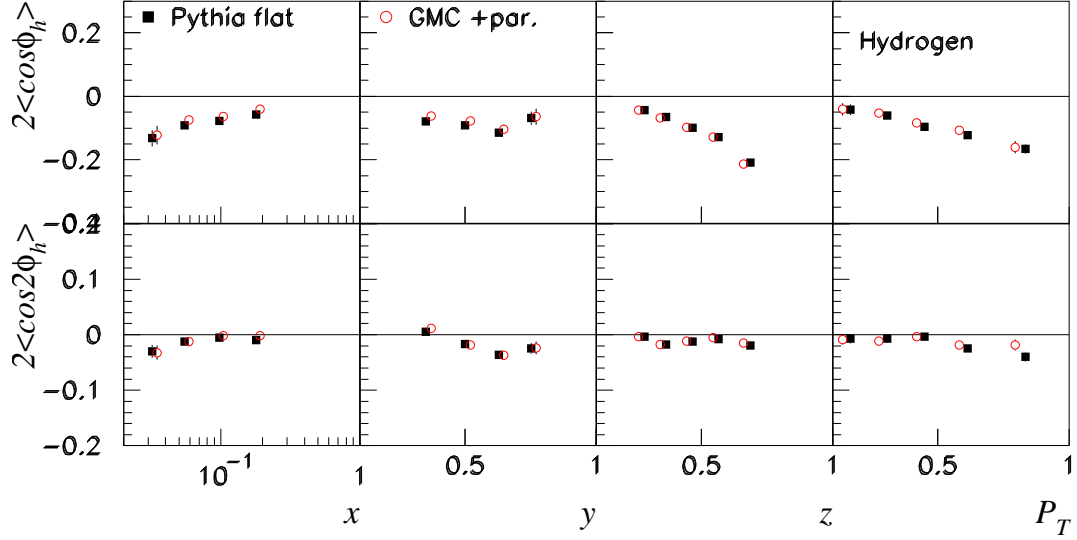


Figure 5.22: The hydrogen π^+ moments integrated with the standard cross section from Pythia (back squares) or the $\text{gmc}_{\text{TRANS}}$ cross section including the 38 parameter fit from data (red open circles).

5.5 MC self-test of full extraction procedure

In order to evaluate in a correlated way the influence of the various systematic uncertainties (identified in the previous sections) on the analysis procedure, a “MC self-test” was performed. A reconstructed Pythia MC production, weighted with the $\cos n\phi_h$ parameterization (see Sections 4.4.7 and 6.4) was treated like data and run through the Fold and Fit procedure. The results were then compared to the input model (the parameterization). Tracking code efficiency (Section 5.2.1) is taken into account since the reconstructed MC is run through the HERMES reconstruction code. Bin size effects (Section 5.3.2) are naturally taken into account since the reconstructed MC is binned in the same way as the data while the input model is smooth. The accuracy of the RICH unfolding (Section 5.2.2) is taken into account since the reconstructed MC includes a simulation of the RICH detector, EVT track identification, and event weights from the inverted center P-matrix. For integrated (i.e., 1-dimensional) plots, the contribution from bins where a measurement could not be made is also accounted for: the model was evaluated in all bins while the MC sample was integrated only over those bins included in the data integration. This test was also completed using each of the different $\cos n\phi_h$ parameterizations described in Section 4.4.7. The results are shown in Figures 5.23 and 5.24. The π^+ results obtained with different $\cos n\phi_h$ parameterizations are shown in Figures 5.25 to 5.27 and show very similar results to the 38 parameter function. The other results are also stable with respect to the parameterization chosen. A single systematic error that takes all these effects into account was evaluated by comparing the moments extracted from MC to those calculated from the input model.

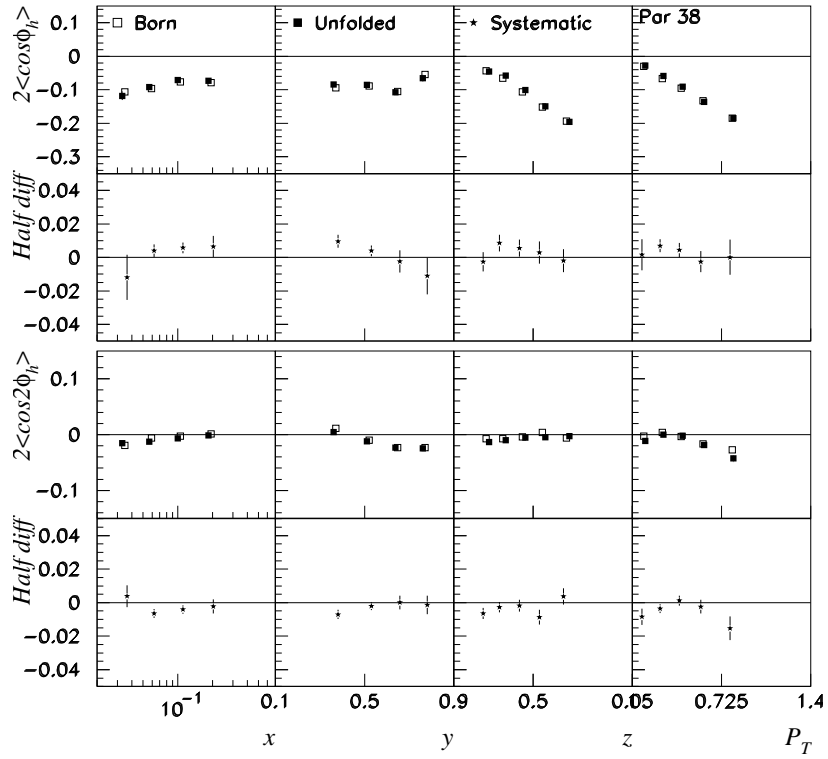


Figure 5.23: The π^+ Born-level moments input into the MC (open squares) from the 38 parameter function and moments extracted from the reconstructed MC (closed squares) for $\cos \phi_h$ (top row) and $\cos 2\phi_h$ (3^{rd} row) and the associated systematic errors (stars) calculated from the difference between the two.

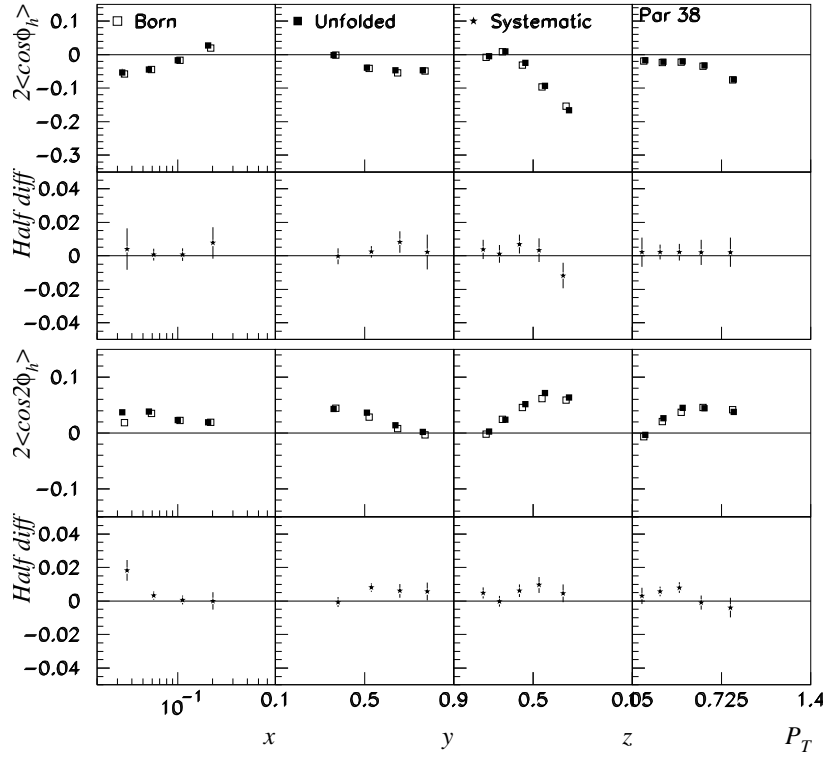


Figure 5.24: Like Figure 5.23 but for π^-

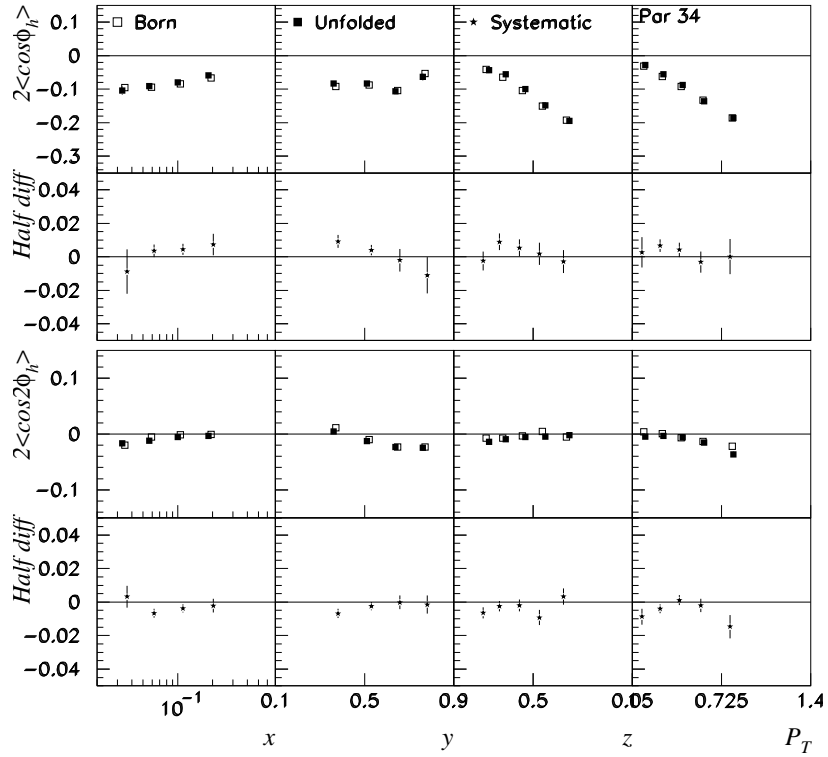


Figure 5.25: Like Figure 5.23 but for the 34 parameter function

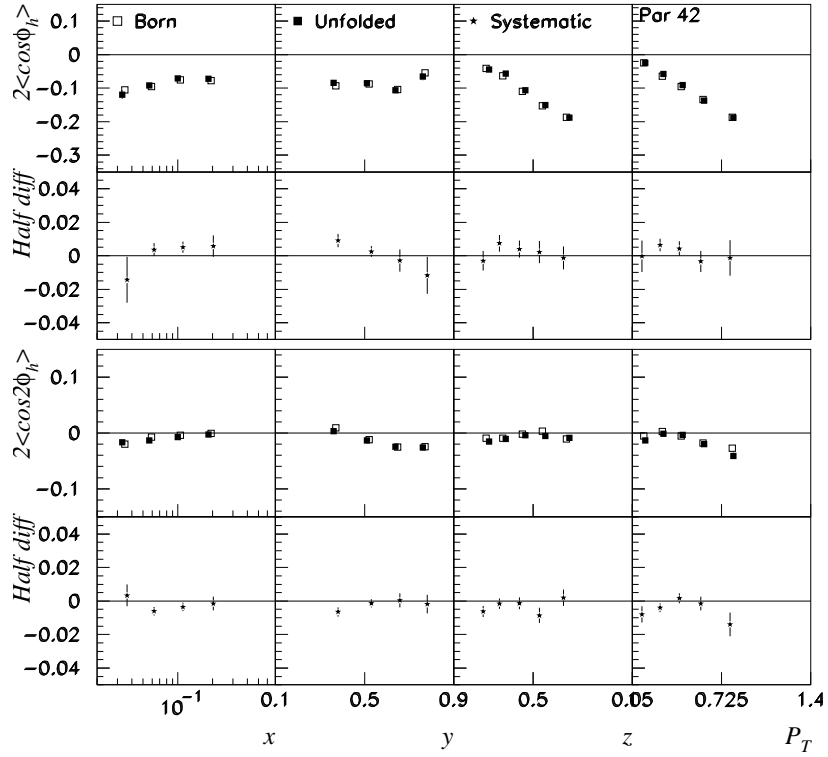


Figure 5.26: Like Figure 5.23 but for the 42 parameter function

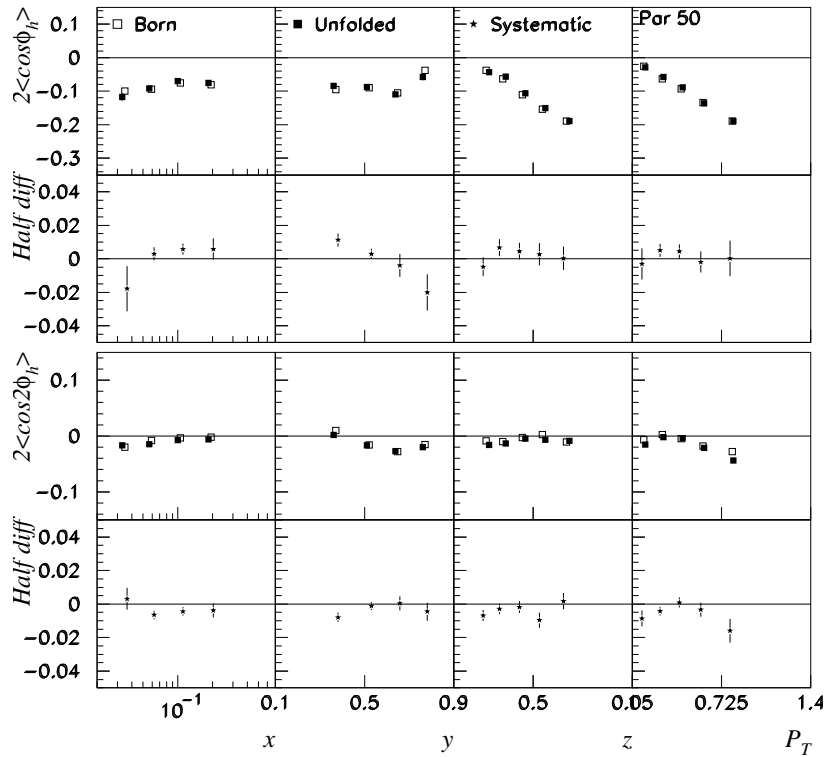


Figure 5.27: Like Figure 5.23 but for the 50 parameter function

5.6 Time dependence of the data

The results from the different data sets outlined in Table 4.1 are compared in Figures 5.28 to 5.31. The differences between the data sets are not consistent with purely statistical fluctuations, indicating that some small effects are not accounted for. These could include detector and beam misalignment or other inaccuracies in the the detector simulation, which are not corrected for with the unfolding procedure. In addition, since the 2000 data was analyzed with HRC and the rest of the data with HTC, any effects introduced by only one of these methods are incorporated in the year dependence. In particular, HRC does not take into account the known detector misalignment while HTC makes quality (probability) cuts which may not be exactly accounted for in the MC. The differences between the data sets is accounted for in the final systematic error, as described in the next section.

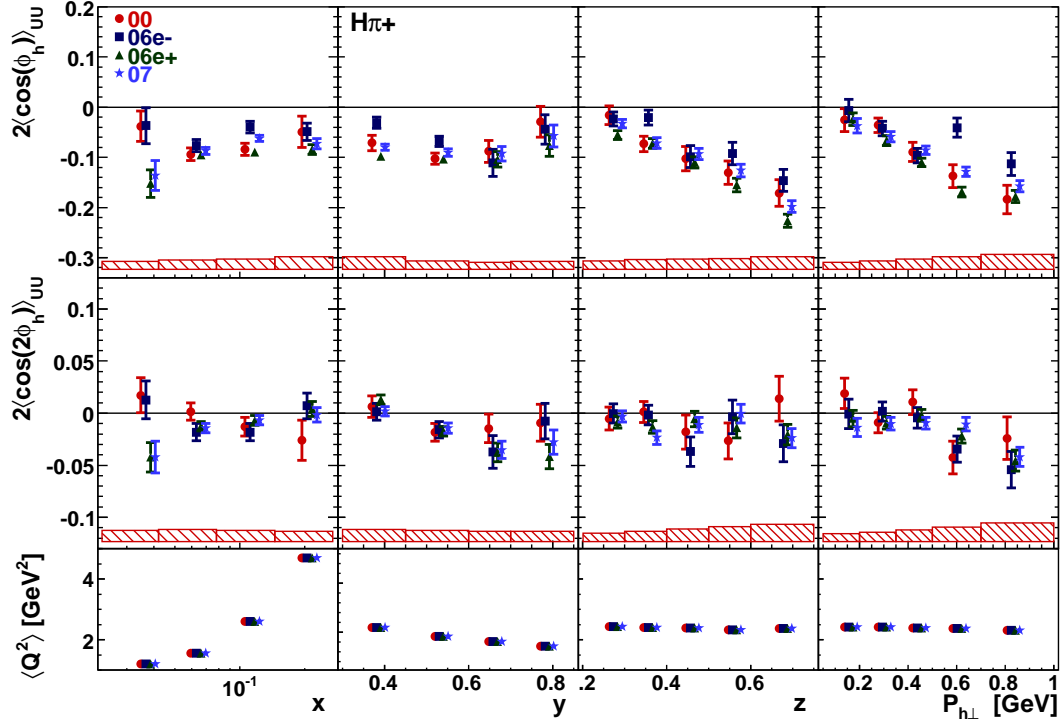


Figure 5.28: Comparison of four different data sets contributing to the hydrogen π^+ moments. The systematic error stemming from the variation between data sets is shown as a red band.

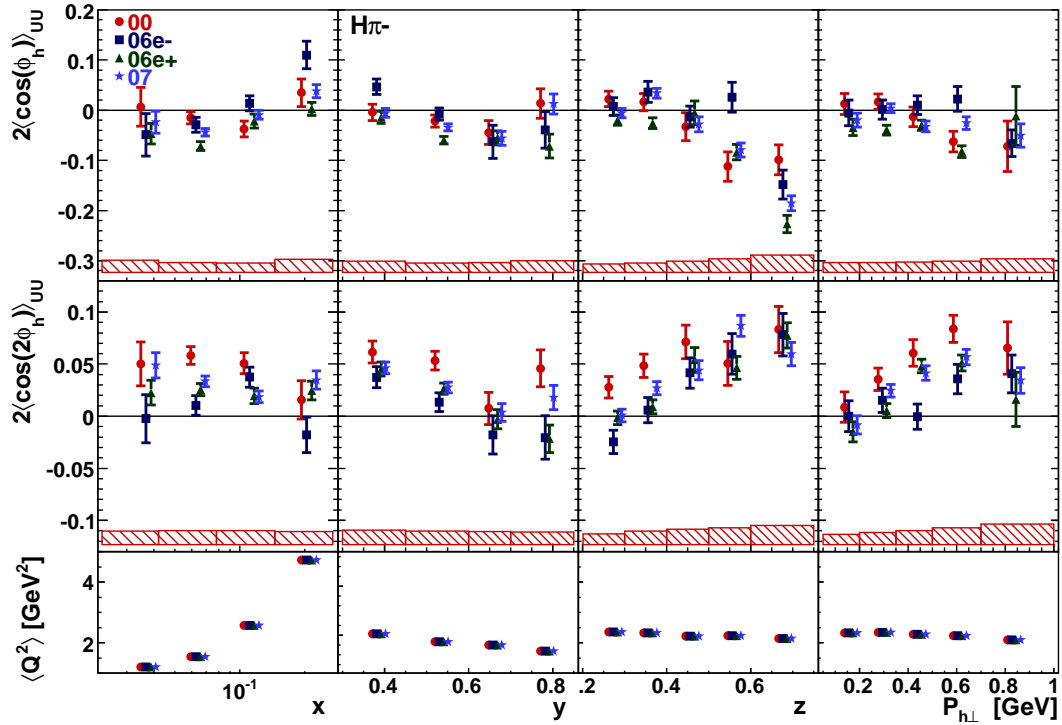


Figure 5.29: Comparison of four different data sets contributing to the hydrogen π^- moments. The systematic error stemming from the variation between data sets is shown as a red band.

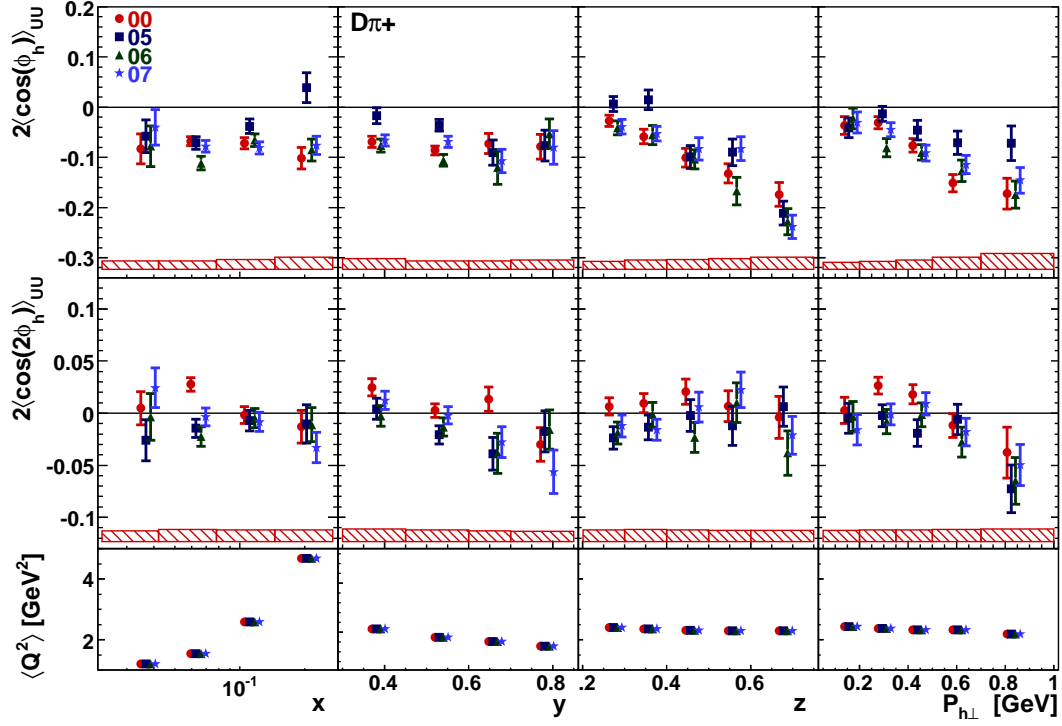


Figure 5.30: Comparison of four different data sets contributing to the deuteron π^+ moments. The systematic error stemming from the variation between data sets is shown as a red band.

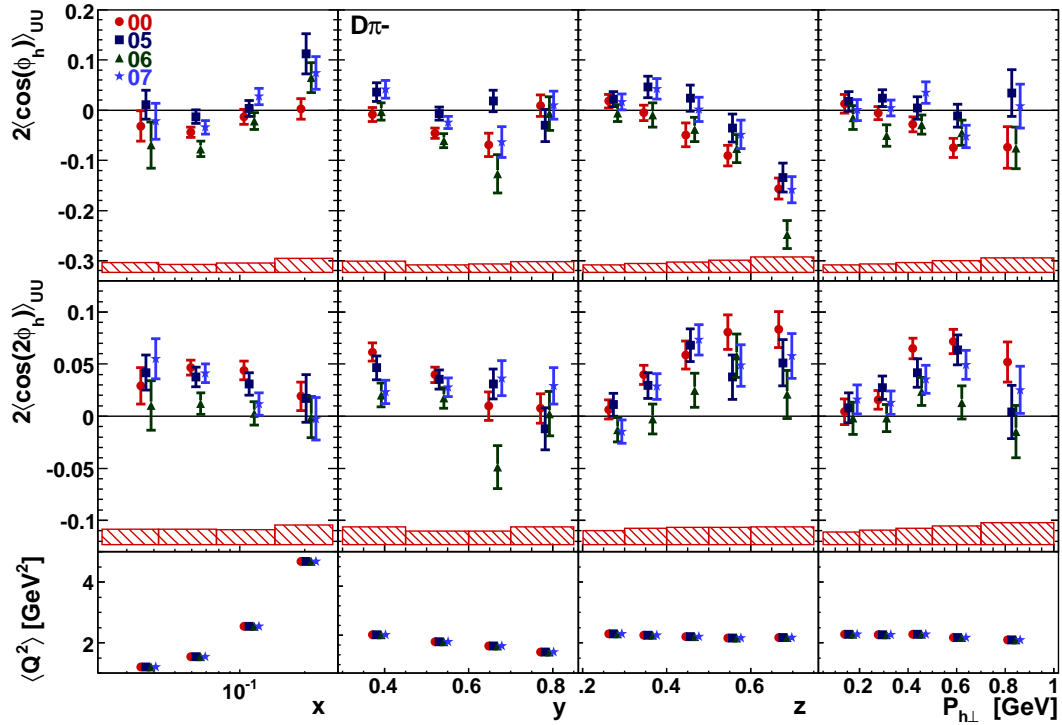


Figure 5.31: Comparison of four different data sets contributing to the deuteron π^- moments. The systematic error stemming from the variation between data sets is shown as a red band.

5.7 Systematic errors

The final systematic error includes the results from the following studies, all described in the previous sections: the MC self-test (Section 5.5), the time dependence of the data (Section 5.6), and the model dependence of: the smearing matrix (Section 5.4.1), the background subtraction (Section 5.4.2), and the cross section used for the integration (Section 5.4.3). The rest of the systematic studies either showed negligible impact on the results or are accounted for in the contributions enumerated above. Figure 5.32 provides a schematic diagram of the contributions to the final systematic uncertainty; the user may find it useful to consult the diagram while reading the text below.

For the MC self-test, the difference between the input model and the extracted moments was taken as the systematic error in each bin. For the time dependence, the moments from each data set were compared to the average (simultaneous fit) of the other three data sets and half the difference was taken in each bin. These differences were then *smoothed* to remove jumps due to normal statistical fluctuations. This was accomplished by fitting the half-differences to a four-dimensional linear function ($p_0 + p_1x + p_2y + p_3z + p_4P_{h\perp}$). In each bin the four fits (one for each data set) were evaluated and the largest of them (in absolute value) was taken as the systematic error in that bin. For the smearing matrix and background vector model dependence tests, half the difference between the results with different models was taken as the systematic error in each bin.

The final systematic error for the fully differential moments was computed as the quadrature sum of these four contributions. The final systematic for the integrated plots is more complicated. First, for the MC self-test, the systematic error in bins that were not included in the data integration was taken as the full value of the input model moment. This takes into account the effect on the data due to an incomplete integration. Each contribution to the systematic error was independently integrated over three kinematic variables (for example y , z , and $P_{h\perp}$). In addition, the model dependence of the integration was computed as half the difference between the results with different cross section models in the integration. The MC self-test and 3 model dependences¹ were each fit to a linear function in the remaining variable (for example $p_0 + p_1x$). Finally, the results of each contribution were added in quadrature. The separate contributions to the pion systematic are shown in Figure 5.33 (5.34) for positive (negative) pions from the hydrogen target.

¹The time dependence was already *smoothed* at the fully differential level and was thus not fit to a linear function again

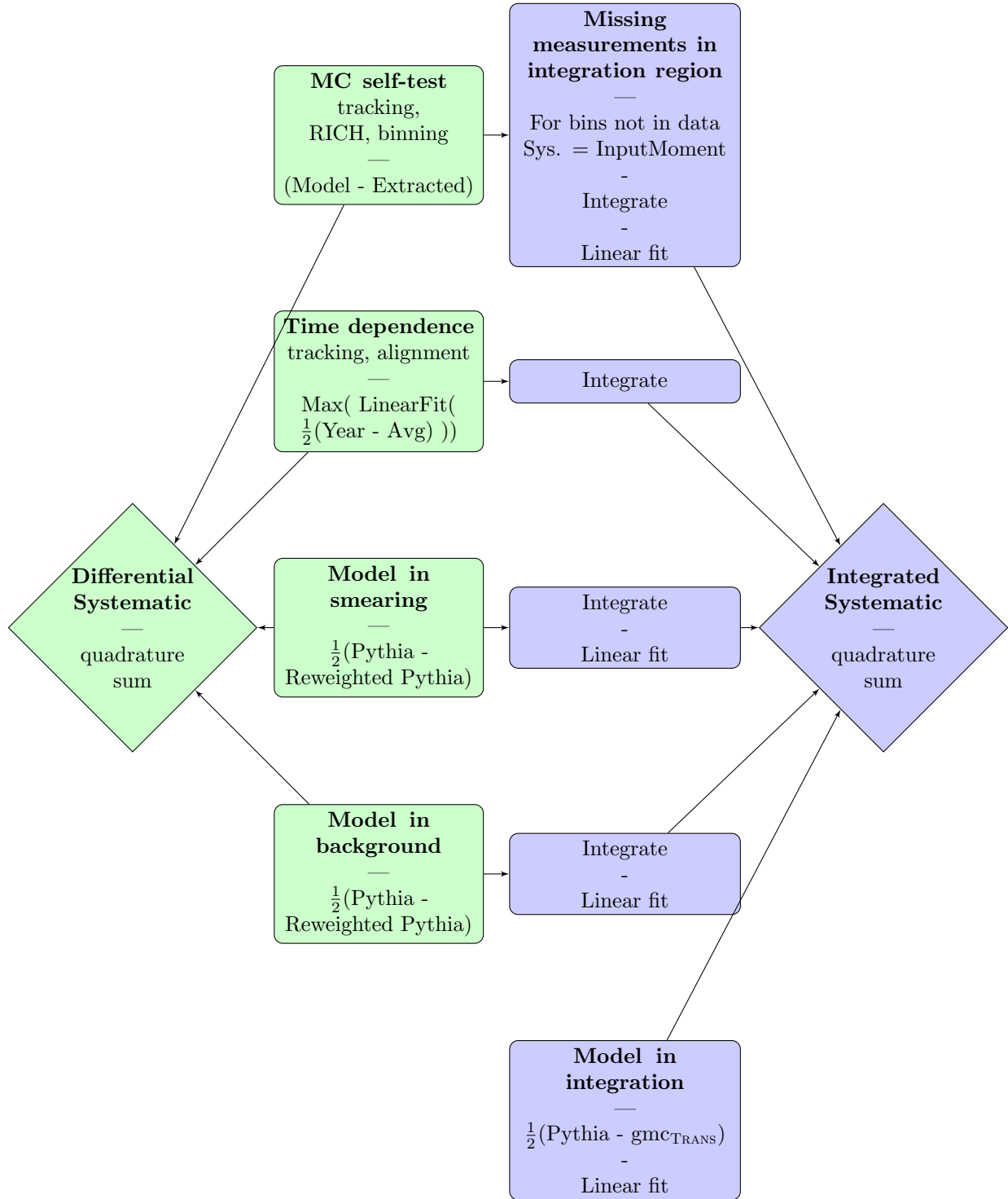


Figure 5.32: Procedure for calculating systematic errors. Four contribution were calculated at the fully differential level (green boxes) and added in quadrature to give the total systematic error of the fully differential results (green diamond). The four contributions were integrated (purple boxes) and contributed to the total systematic error of the integrated results, along with a fifth contribution from the model used in the integration. The were all added in quadrature to give the final systematic error for the integrated results (purple diamond).

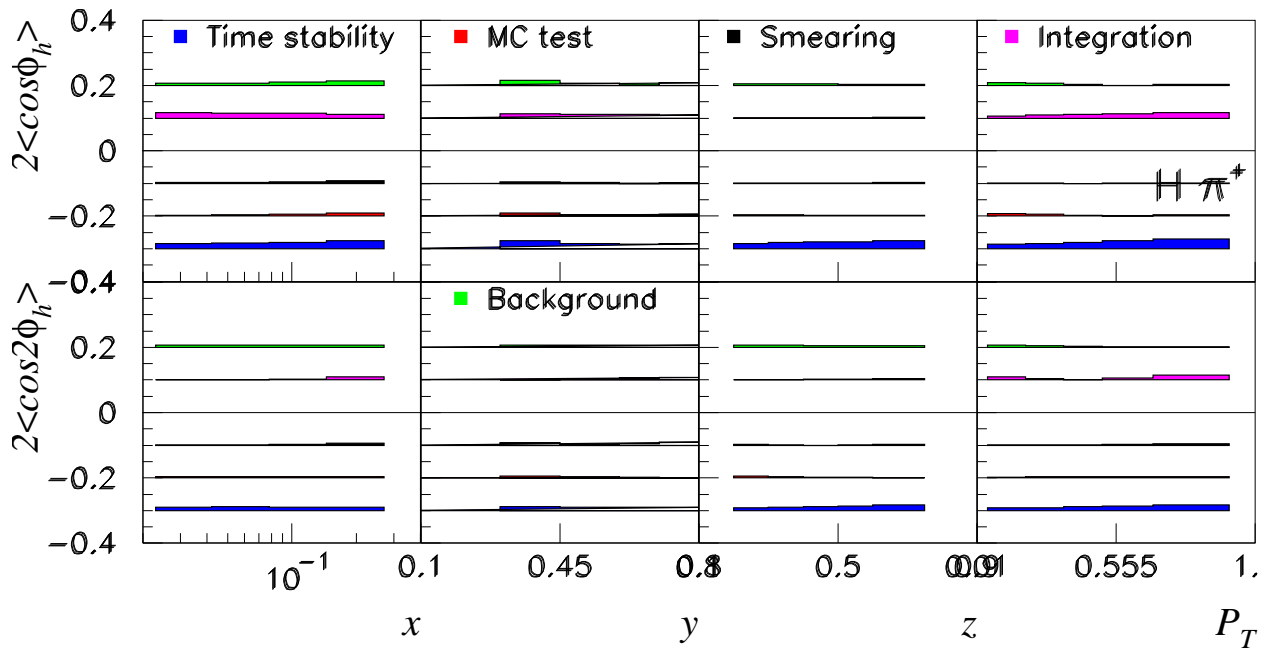


Figure 5.33: The five separate contributions to the systematic error for positive pions produced from a hydrogen target, calculated from: the MC self-test (red), the time dependence (blue), the model dependence of the smearing matrix (black), the model dependence of the background subtraction (green), and the model dependence of the integration (pink)

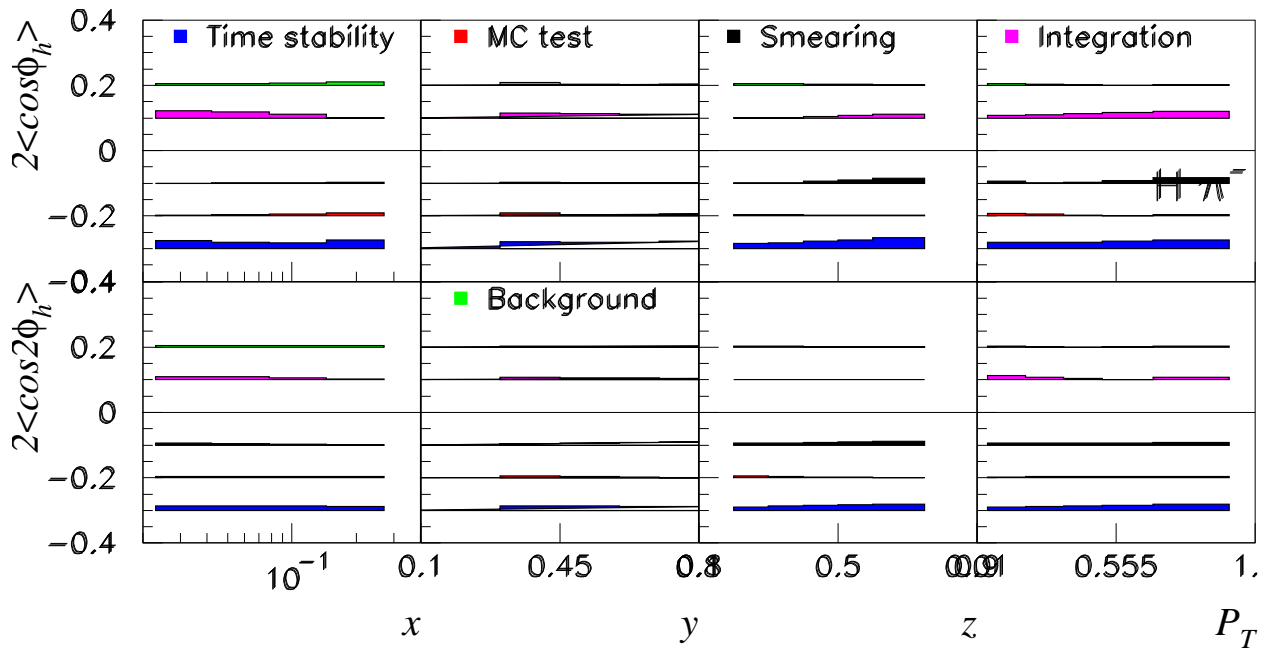


Figure 5.34: The same as Figure 5.33 except for negative pions.

Chapter 6

Results and interpretation

One of the main challenges of this analysis is its multi-dimensional nature. The detector acceptance and radiative effects require an elaborate correction procedure while the the $\langle \cos \phi_h \rangle_{UU}$ and $\langle \cos 2\phi_h \rangle_{UU}$ moments involve several terms, each of which vary in unknown and potentially correlated ways. Measurements must be corrected in five dimensions before fitting the ϕ_h -dependence. The final azimuthal moments in four dimensions are the final results and will be vital in constraining models. However, to gain a qualitative understanding of the data, and to compare to existing experimental and theoretical work, one-dimensional results can be very useful. As mentioned in Section 4.4.6, such one-dimensional results can be obtained by integrating the fully differential results. To properly compare the moments from different targets and hadron in a meaningful way, it is vital that comparisons are only made in identical kinematic ranges, being careful to take into account kinematic bins where a measurement is not possible due to the limited statistics of the data. In this chapter the integrated $\langle \cos \phi_h \rangle_{UU}$ and $\langle \cos 2\phi_h \rangle_{UU}$ moments for pions, kaons, and unidentified-hadrons are presented versus each kinematic variable: x , y , z , and $P_{h\perp}$. Some simple conclusions are drawn from these results. In addition a multi-dimensional parameterization of the moments is presented.

6.1 Pion results

The pion results are presented in the kinematic range

$$0.023 < x < 0.27$$

$$0.3 < y < 0.85$$

$$0.2 < z < 0.75$$

$$0.05 < P_{h\perp} < 1.$$

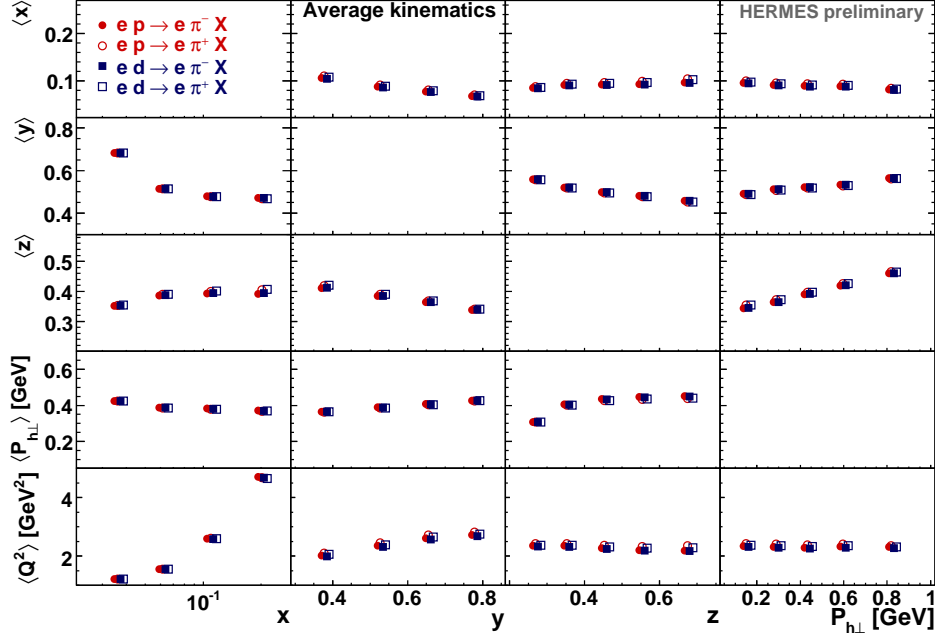


Figure 6.1: Average kinematics of the results presented in Figures 6.3 to 6.6.

Within this kinematic range there remain a few bins where a measurement is not possible due to statistics. For consistency, such bins are eliminated in the integration of all four measurements (positive and negative pions from hydrogen and deuterium targets). In practice this means that only bins where the statistics were sufficient to make a measurement of π^- produced from a deuterium target — the data set with the lowest statistics — are included in the integration. The average kinematics of each bin are shown in Figure 6.1 for positive and negative pions from hydrogen and deuterium targets.

The underlying four-dimensional binning of the data is shown schematically in Figure 6.2. Each small square represents one kinematic bin. Each column of subplots represents one z bin where left to right is low to high z . Each row of subplots represent one $P_{h\perp}$ bin, where bottom to top is low to high $P_{h\perp}$. Each subplot contains all of the x and y bins for a single z - $P_{h\perp}$ bin. The x binning runs from left to right on the x -axis of the subplot while the y binning runs from bottom to top along the y -axis of the subplot. Red squares mark where a measurement is not possible. Empty yellow squares represent bins where a measurement is not possible but the cross section is near-zero so including the bin or not in the integration makes no difference. Yellow squares with an X indicate bins where a measurement has been made. This is an interactive tool and in this screen shot only the integration range indicated above has been selected in the check boxes to the left. The un-selected region (those bins in Table 4.3 which are not included in the chosen integration range) is indicated by the white squares where again the X indicates bins where a measurement was possible. The integration region stated above has been chosen to maximize the kinematic range (yellow squares) while

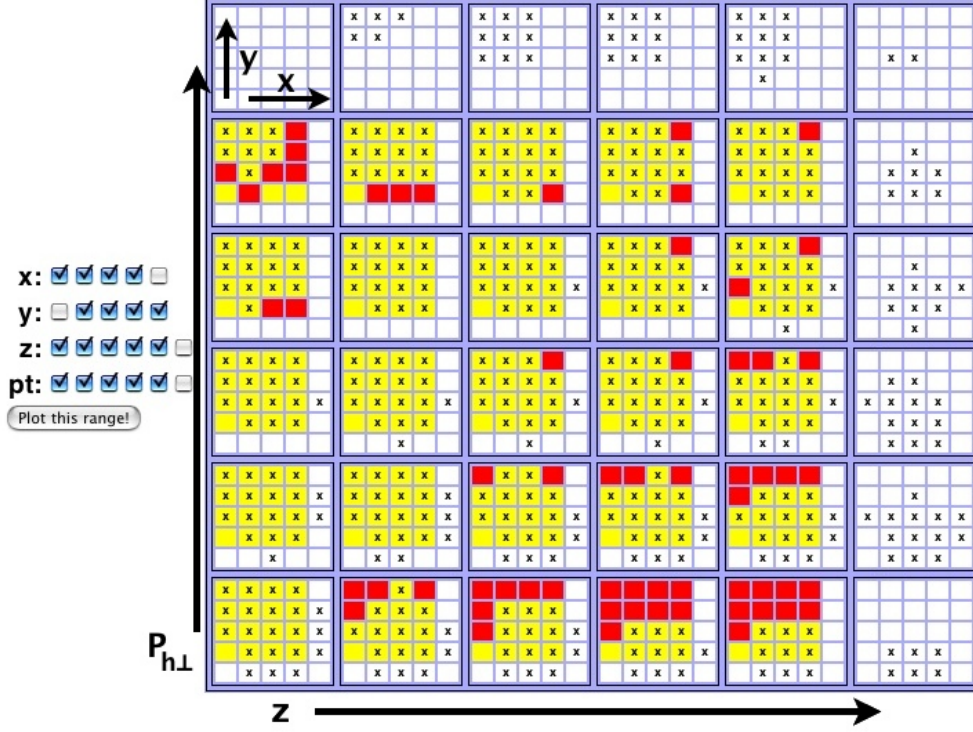


Figure 6.2: Graphical representation of the bins included in the integration in Figures 6.3 to 6.6. See text for details.

minimizing the number of bins where a measurement cannot be made (red squares).

The hydrogen and deuterium target results are compared in Figure 6.3. Both the $\cos \phi_h$ and $\cos 2\phi_h$ moments are nearly identical for the two targets. This unexpected finding is a dramatic constrain for models, as discussed in Chapter 8.

The π^+ and π^- moments are compared in Figure 6.4. To more clearly see the dependence of the structure functions, the structure function ratio is presented in Figure 6.5. The structure function ratio is defined by Equations 4.41 and 4.42 and is simply the moment divided by the relevant ϵ dependent factor, specifically:

$$\frac{F_{UU}^{\cos \phi_h}}{F_{UU,T}} = \frac{2\langle \cos \phi_h \rangle_{UU}}{\sqrt{2\epsilon(1+\epsilon)}} \equiv \frac{2\langle \cos \phi_h \rangle_{UU}}{k_1(y)} \quad (6.1)$$

$$\frac{F_{UU}^{\cos 2\phi_h}}{F_{UU,T}} = \frac{2\langle \cos 2\phi_h \rangle_{UU}}{\epsilon} \equiv \frac{2\langle \cos 2\phi_h \rangle_{UU}}{k_2(y)} \quad (6.2)$$

where the $k_n(y)$ functions have been defined and are used in the axis labels in the relevant figures throughout this chapter. This allows for a more direct observation of the kinematic dependence of the structure functions by removing known kinematic dependences. In addition it facilitates comparisons with other experiments at differing kinematics.

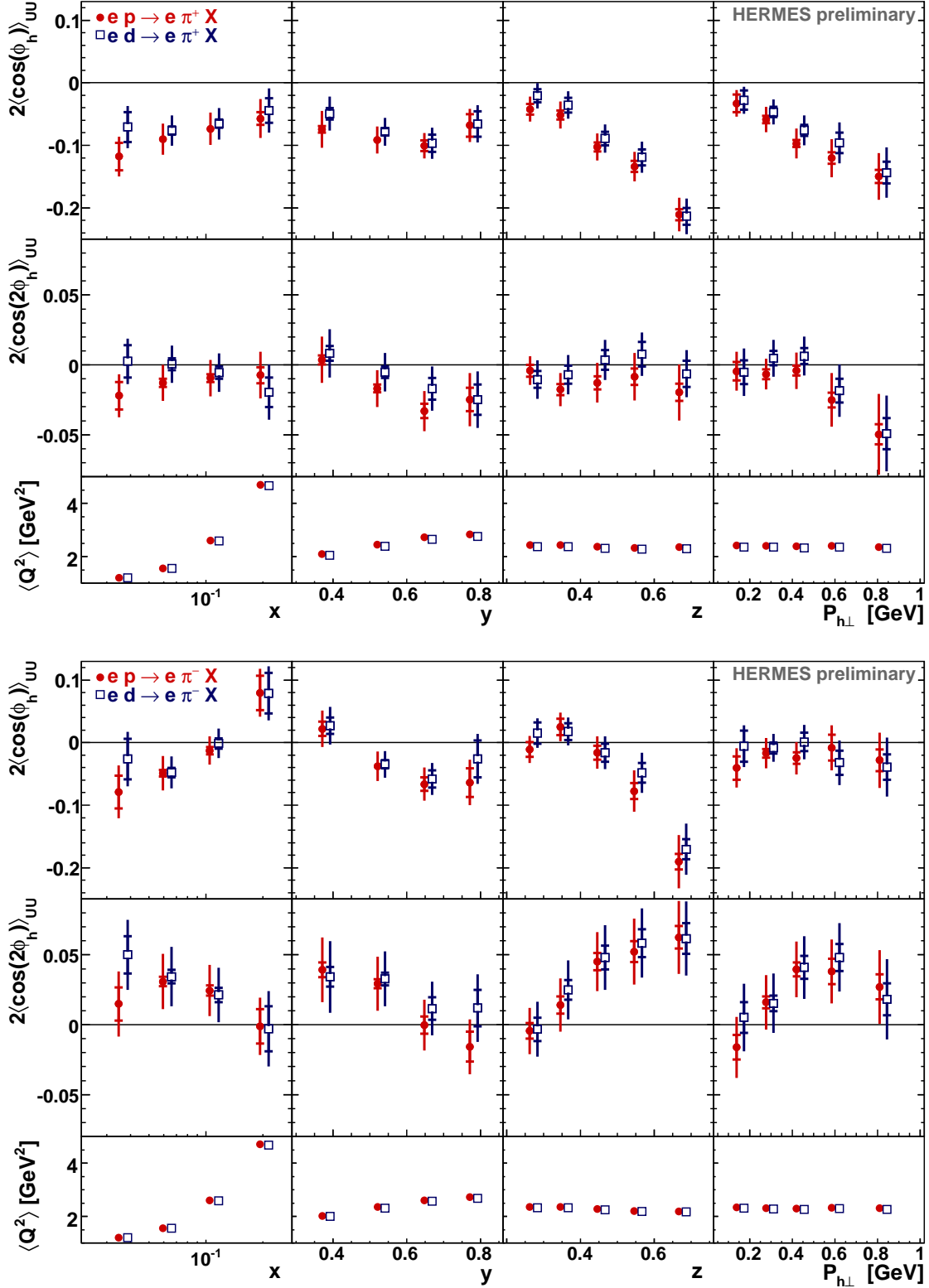


Figure 6.3: $\langle \cos \phi_h \rangle_{UU}$ (top row) and $\langle \cos 2\phi_h \rangle_{UU}$ (center row) for positive (upper plot) and negative (lower plot) pions produced on a hydrogen (red) or deuterium (blue) target versus one kinematic variable at a time. Inner error bars correspond to statistical error while outer error bars represent the total statistical and systematic error.

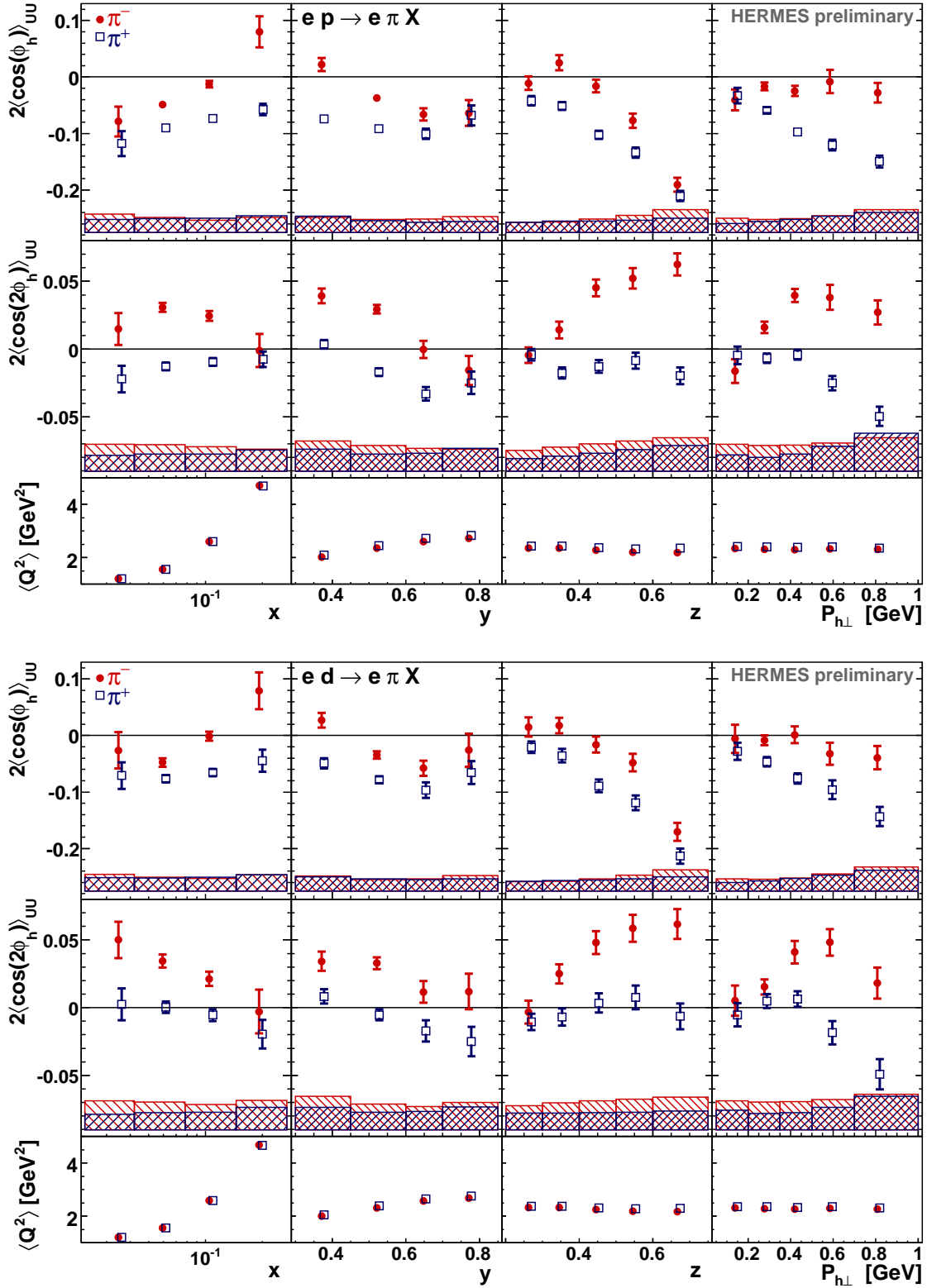


Figure 6.4: $\langle \cos \phi_h \rangle_{UU}$ (top row) and $\langle \cos 2\phi_h \rangle_{UU}$ (center row) for positive (blue) and negative (red) pions produced on a hydrogen (upper plot) or deuterium (lower plot) target versus one kinematic variable at a time. Error bars correspond to statistical error while error bands represent the systematic error.

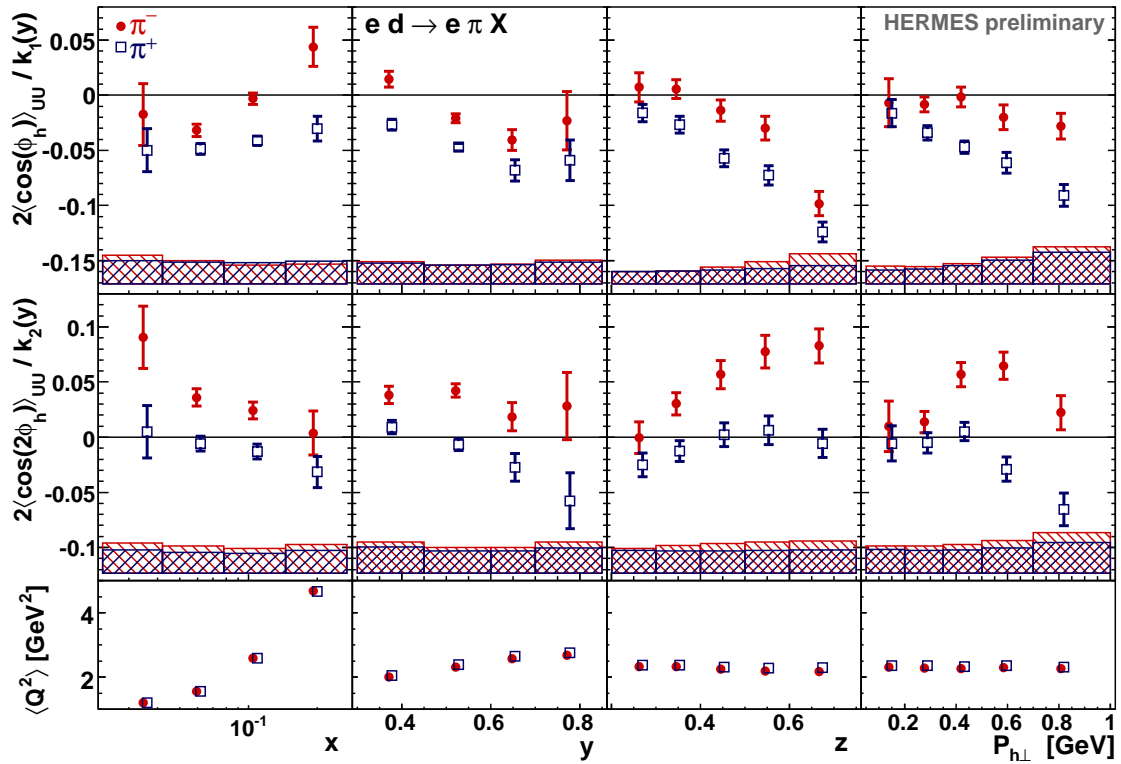
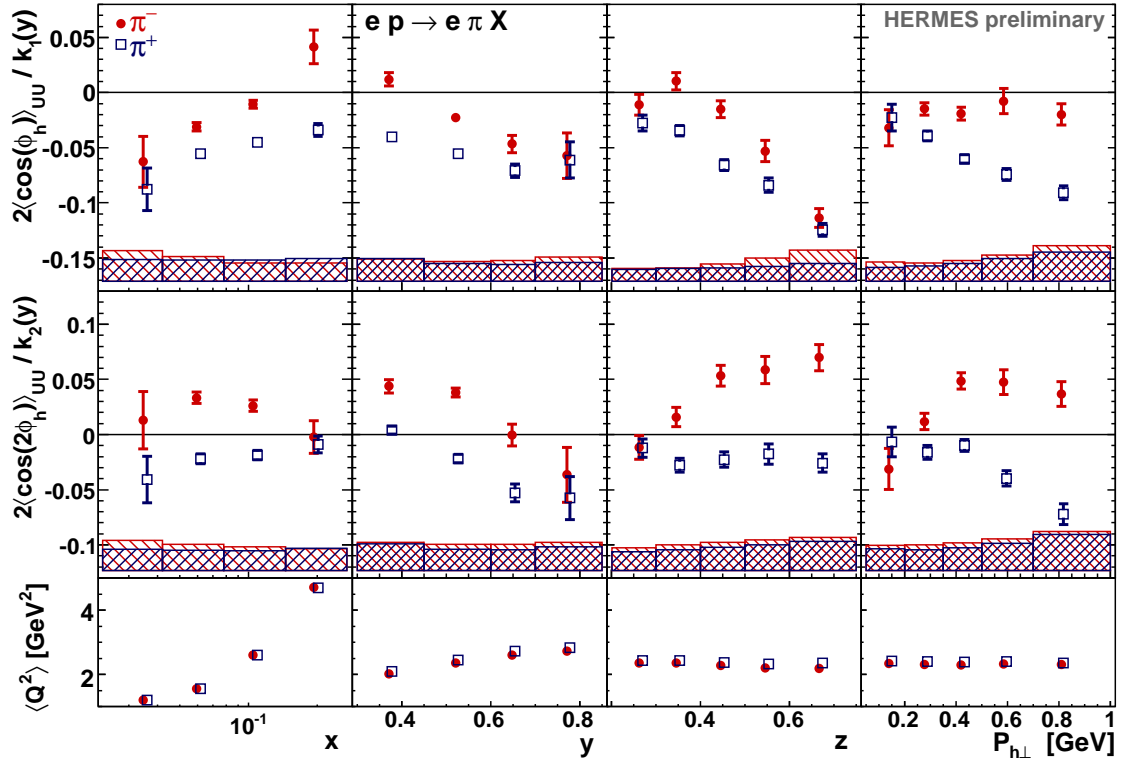


Figure 6.5: The same as Figure 6.4 but for the structure function ratios. See Equations 6.1 and 6.2.

Along with the similarity between the hydrogen and deuterium targets, one of the most striking characteristics of these data is the difference between the moments for positive and negative pions. As it is difficult to discern from Figure 6.4 if this difference is truly statistically significant the charge difference has been investigated in more detail. In Figure 6.4 the systematic errors for π^+ and π^- are overlaid to convey that they are correlated; detector misalignment, model dependence, binning effects, etc. should all effect both charges in the same way, leading to the same systematic effect on the moments for π^+ and π^- . The degree to which the systematics are correlated is difficult to determine directly. To overcome this in Figure 6.6 the difference between the π^+ and π^- moments is shown. The difference between the integrated moments is taken and the statistical error of the difference is computed from the diagonal elements of the covariance (exactly the error bars that are presented in Figure 6.4). The systematic errors are recalculated. Using the same contributions as described in Section 5.7 the difference is taken in all cases for the pion difference. For example, the systematic error from the MC self-test takes the difference between $(2\langle\cos\phi_h\rangle_{UU}^{\pi^-} - 2\langle\cos\phi_h\rangle_{UU}^{\pi^+})$ extracted from the reconstructed MC and $(2\langle\cos\phi_h\rangle_{UU}^{\pi^-} - 2\langle\cos\phi_h\rangle_{UU}^{\pi^+})$ from the input model. In this way a systematic shift in both charges is not included in the systematic error. From Figure 6.6 it is clear that the difference between the moments for negative and positive pions is statistically significant and positive over nearly the entire kinematic range of the measurement.

The most obvious features of both the $\cos\phi_h$ and $\cos 2\phi_h$ moments are the similarity between hydrogen and deuterium targets and the difference between π^+ and π^- . The consequences of these observations are most easily explained in the context of several models of the Cahn and Boer-Mulders effects presented in Chapter 8. The $\cos 2\phi_h$ pion difference for a hydrogen target is easily explained by the u quark dominance in the proton, paired with favored ($u \rightarrow \pi^+$) and disfavored ($u \rightarrow \pi^-$) Collins fragmentation functions of opposite signs (supported by data, see Section 7.2). The similarity between the hydrogen and deuterium targets indicates that, even in the absence of u quark dominance, the same effects persist, indicating the Boer-Mulders function for d quarks is similar to that of u quarks. The difference between π^+ and π^- along with the similarity between hydrogen and deuterium targets for the $\cos\phi_h$ moments, where the Boer-Mulders effect also contributes, could again be due to different signed Collins u and d and same signed Boer-Mulders u and d . In fact, the average difference in the moments as shown in Figure 6.6 is ~ 0.05 for both moments, possibly indicating the same mechanism in both cases. This argument assumes the Cahn effect is the same for π^+ and π^- , which is predicated on similar \mathbf{p}_T -dependence for u and d quarks. This is commonly assumed but there is no strong evidence for such a claim. Since the Cahn effect contributes to both the $\cos\phi_h$ and $\cos 2\phi_h$ moments (though at higher twist for $\cos 2\phi_h$) it could also induce or contribute to the difference in the moments seen between pion charges.

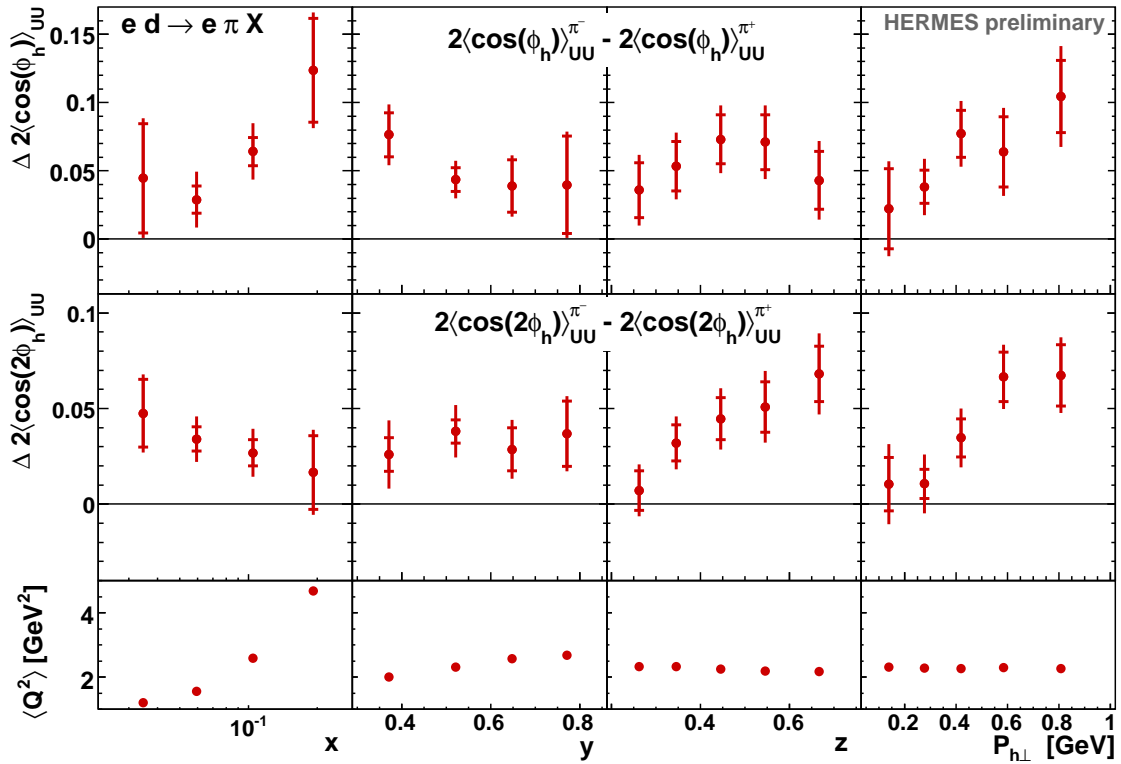
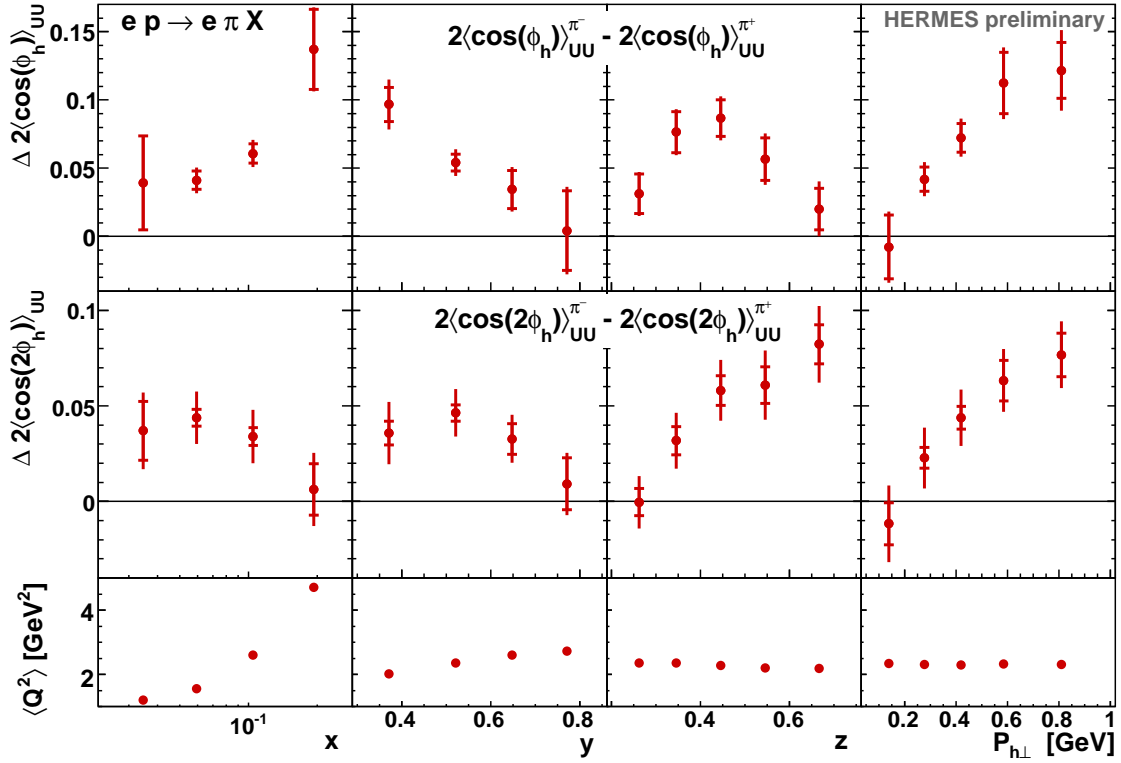


Figure 6.6: The difference between the negative and positive pion results. The inner error bars represent the statistical error on the difference between the integrated points in Figure 6.4 while the outer error bars represent the systematic error of the difference, taking into account the correlated systematic errors.

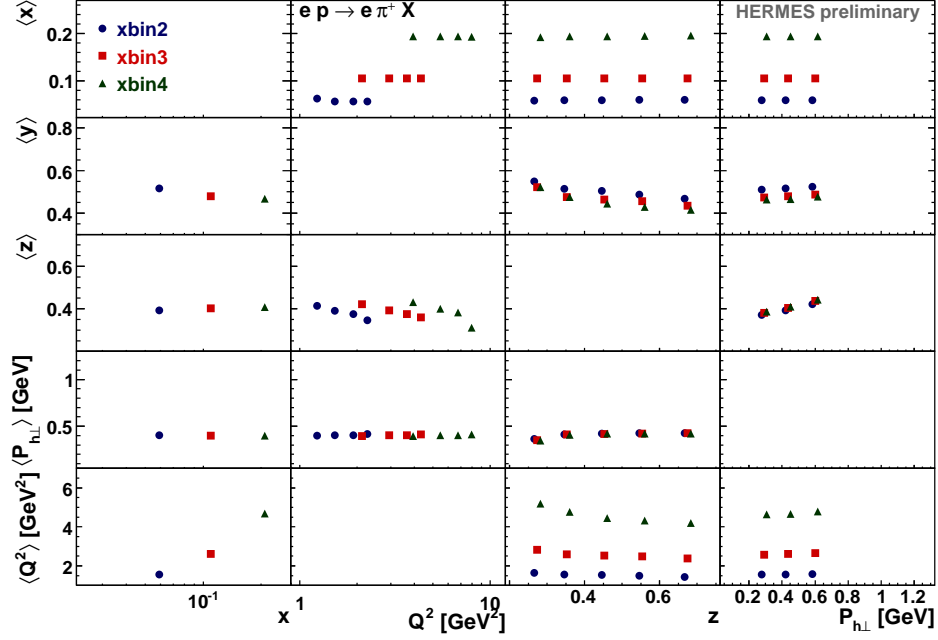


Figure 6.7: Average kinematic for the points presented in Figures 6.9 to 6.12.

6.1.1 Q^2 -dependence

The strong correlation between x and Q^2 , shown in Figure 4.2 and discussed in Section 4.2.3, makes it difficult to disentangle the x and Q^2 -dependence of the moments. The Q^2 -dependence is particularly interesting due to the known Q^2 dependence from the twist expansion. The Q^2 -dependence of the $\cos 2\phi_h$ moments, for example, may offer a way to disentangle the Boer-Mulders effect from the higher twist Cahn contribution.

To explore the Q^2 -dependence, the y -dependence is plotted at the average Q^2 in each bin. Further, the data is presented in three independent x bins. To minimize the integration over bins where a measurement was not possible a limited range in z and $P_{h\perp}$ was chosen. The kinematic range chosen is:

$$\begin{aligned}
 0.042 < x < 0.078 & & 0.078 < x < 0.145 & & 0.145 < x < 0.27 \\
 0.3 < y < 0.85 & & & & \\
 0.2 < z < 0.75 & & & & \\
 0.2 < P_{h\perp} < 0.7 & & & &
 \end{aligned}$$

The average kinematics for this region is shown in Figure 6.7. The region is shown graphically, for all three x bins, in Figure 6.8. The results are presented for the hydrogen (deuterium) target in Figure 6.9 (6.10). In addition, the structure function ratio (see Equations 6.1 and 6.2 and surrounding text) is presented for the

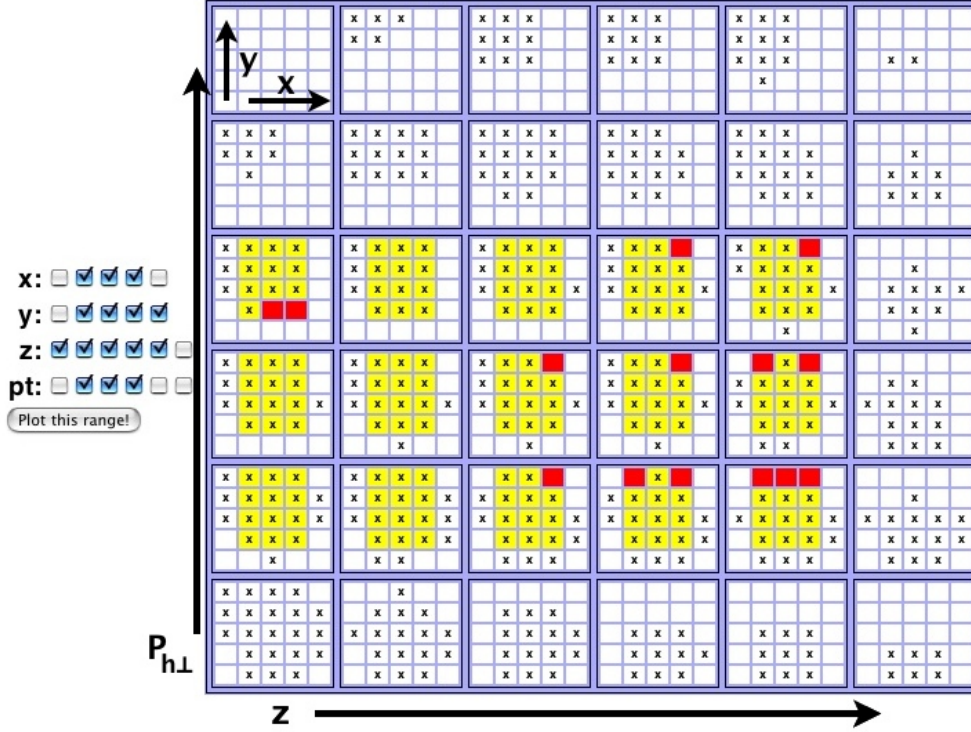


Figure 6.8: Graphical representation of the deuteron π^- bins included in Figures 6.9 to 6.12.

same kinematic range in Figure 6.11 (6.12).

The structure function ratios are useful to evaluate the Q^2 -dependence of the structure functions without the complication of the y dependent kinematic factor that is included in the moments. The $\pi^+ \cos 2\phi_h$ moments from the hydrogen target (the statistically largest data set, yielding the smallest statistical errors) show a Q^2 dependence. While the average z (Figure 6.7) changes somewhat from bin to bin, Figure 6.5 shows that in this range lower z , which corresponds to higher Q^2 (Figure 6.7) has a moment closer to zero. This is the opposite trend as seen in Figure 6.11. This is evidence of a true Q^2 -dependence and that the twist-4 Cahn effect term makes a negative contribution (at higher Q^2 the Cahn effect is suppressed, yielding more positive moments). In the other data sets a similar trend is seen but the limited statistics do not allow for a clean interpretation. The $\cos \phi_h$ results are also difficult to interpret within the limited statistics available; some hint of Q^2 -dependence is visible, possibly pointing to contributions from higher twist effects.

At the time of writing studies are being performed to study the Q^2 -dependence: using a parameterization that includes $1/Q$ terms, implementing a Q^2 binning after the unfolding but before the integration, and calculating the Q^2 -dependence of the pion charge difference. Before this work is complete it is difficult to reliably interpret these results.

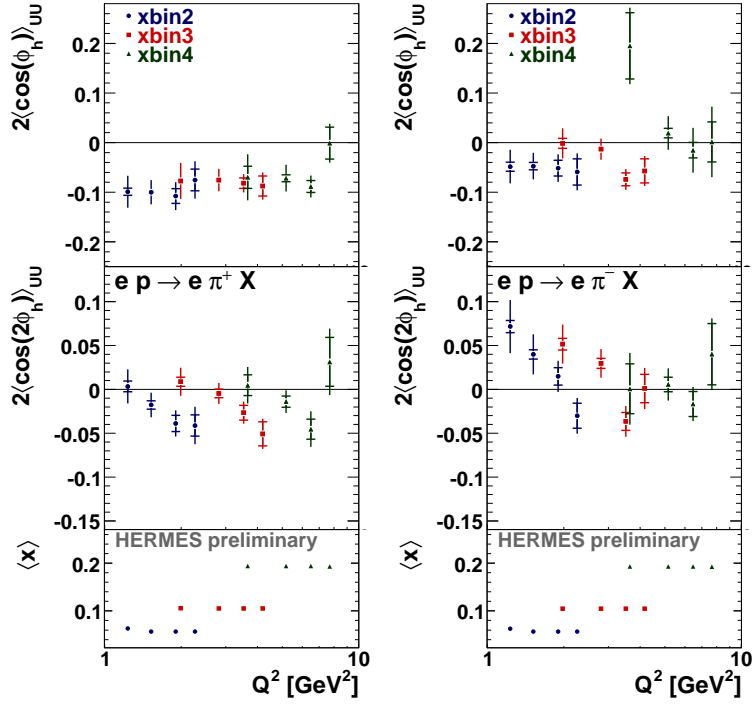


Figure 6.9: Q^2 -dependence of the moments in three x slices for π^+ (left) and π^- (right) on a hydrogen target.

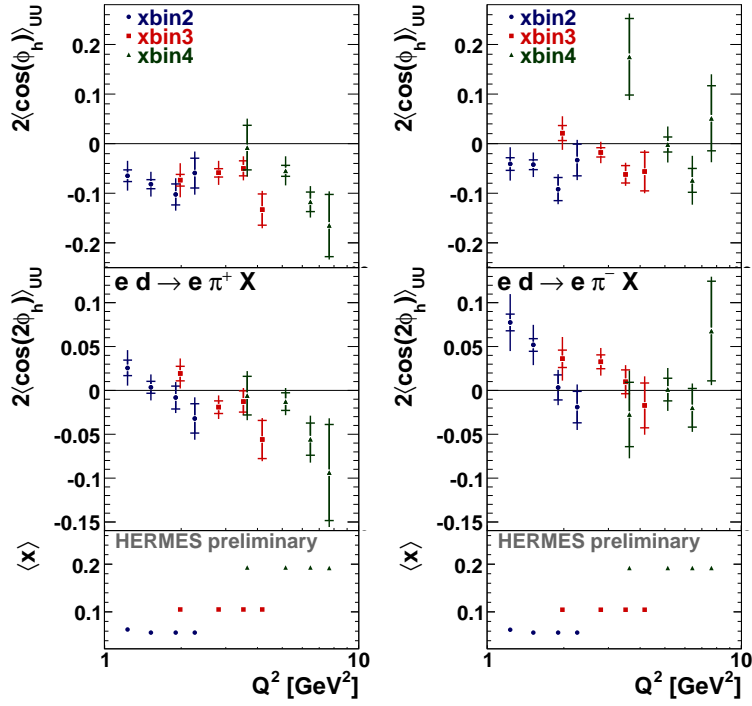


Figure 6.10: Q^2 -dependence of the moments in three x slices for π^+ (left) and π^- (right) on a deuterium target.

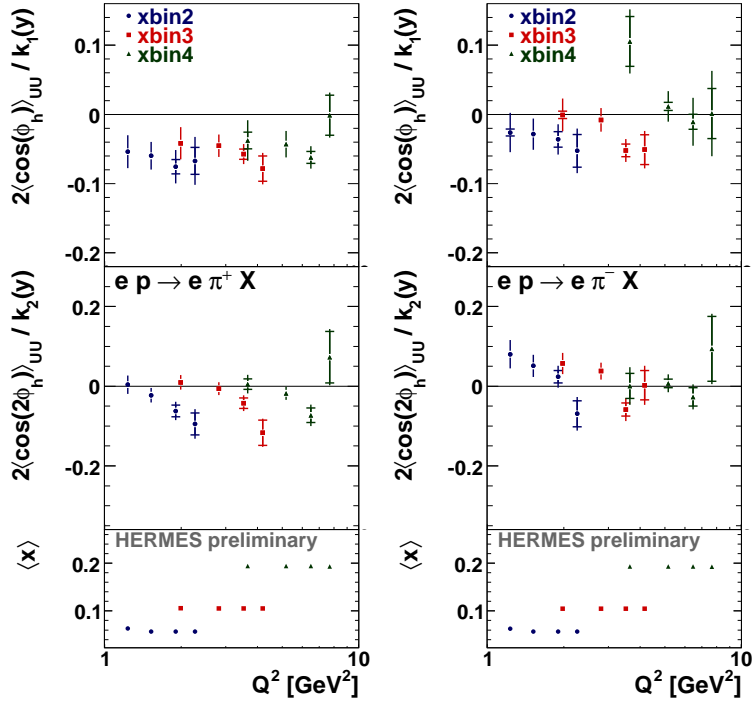


Figure 6.11: Q^2 -dependence of the structure function ratio in three x slices for π^+ (left) and π^- (right) on a hydrogen target.

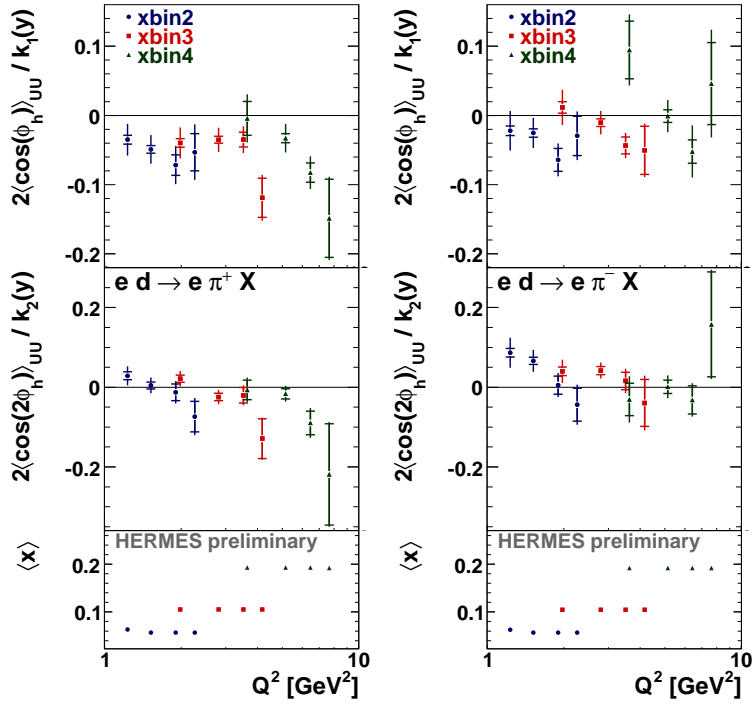


Figure 6.12: Q^2 -dependence of the structure function ratio in three x slices for π^+ (left) and π^- (right) on a deuterium target.

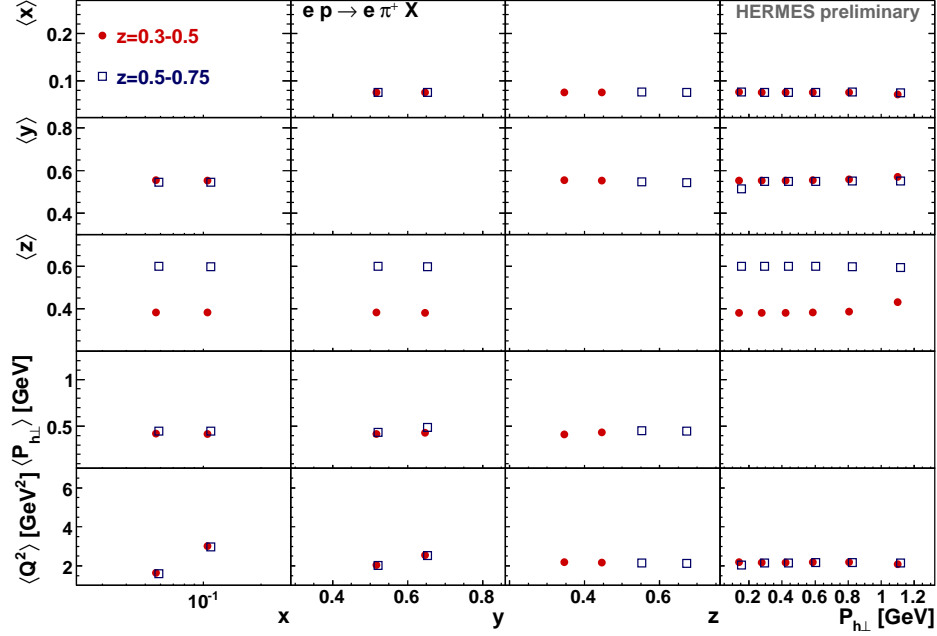


Figure 6.13: Average kinematics for the points presented in Figures 6.15 to 6.18.

6.1.2 $P_{h\perp}$ -dependence

The high $P_{h\perp}$ region ($P_{h\perp} > 1\text{GeV}$) is at the edge of the perturbative regime, where higher order (in α_s) pQCD effects are expected to begin to contribute [28]. The highest $P_{h\perp}$ point is also approaching the limit of the TMD-factorization regime (see Section 1.2.1) since $P_{h\perp} \sim Q^2$ ($\langle P_{h\perp} \rangle \sim 1.1\text{GeV}$ and $\langle Q^2 \rangle \sim 2\text{GeV}^2$). This region, which is not well understood theoretically, is interesting to study experimentally to search for evidence of a fundamental change in physics in the region $P_{h\perp} > 1\text{GeV}$.

To obtain full coverage in $P_{h\perp}$, a limited x and y range is considered. In addition, in an effort to de-convolute the z and $P_{h\perp}$ -dependence of the moments two z ranges are chosen. The kinematic ranges are:

$$0.042 < x < 0.145$$

$$0.45 < y < 0.7$$

$$0.3 < z < 0.5 \quad 0.5 < z < 0.75$$

$$0.05 < P_{h\perp} < 1.3$$

The average kinematics are given in Figures 6.13 and the region is shown graphically in Figure 6.14. The moments are presented in Figures 6.15 and 6.16 and the structure function ratios are presented in Figures 6.17 and 6.18. The $\cos \phi_h$ moments show a dependence on z , with larger z corresponding to larger

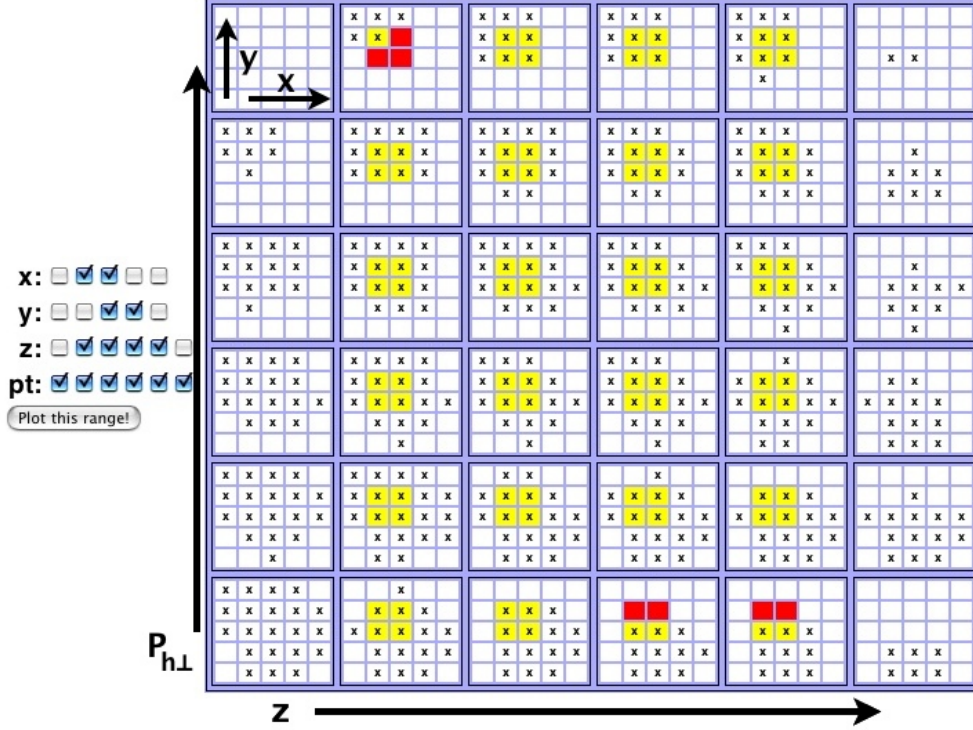


Figure 6.14: Graphical representation of the deuteron π^- bins included in Figures 6.15 to 6.18.

negative moments. This is expected since the Collin fragmentation function grows with z . In addition the positive pion moments grow negatively with $P_{h\perp}$. This is consistent with the Cahn effect where $P_{h\perp}$ originates directly from intrinsic \mathbf{p}_T such that high $P_{h\perp}$ corresponds to a large negative Cahn effect (see Section 1.2.2). In addition the Collins fragmentation function grows with \mathbf{k}_T , increasing the contribution from the Boer-Mulders effect at high $P_{h\perp}$. The negative pion moments are approximately constant in $P_{h\perp}$, indicating that the Boer-Mulders effect may have a contribution that cancels the $P_{h\perp}$ -dependence of the Cahn effect.

The $\cos 2\phi_h$ moments show no z -dependence within the sizable errors, which is unexpected due to the z -dependence of the Collins fragmentation function. The positive pion moments show a similar but less pronounced $P_{h\perp}$ -dependence as the $\cos \phi_h$ moments. The reduction is consistent with a positive (rather than negative for $\cos \phi_h$) and suppressed (twist-4 relative to the twist-2 Boer-Mulders effect) contribution from the Cahn effect. The negative pion $P_{h\perp}$ -dependence is less clear, again possibly indicating that the Boer-Mulders effect is dominant.

Within the available errors, neither the $\cos \phi_h$ or $\cos 2\phi_h$ moments show an obvious change in behavior above $P_{h\perp}$ of 1 GeV.

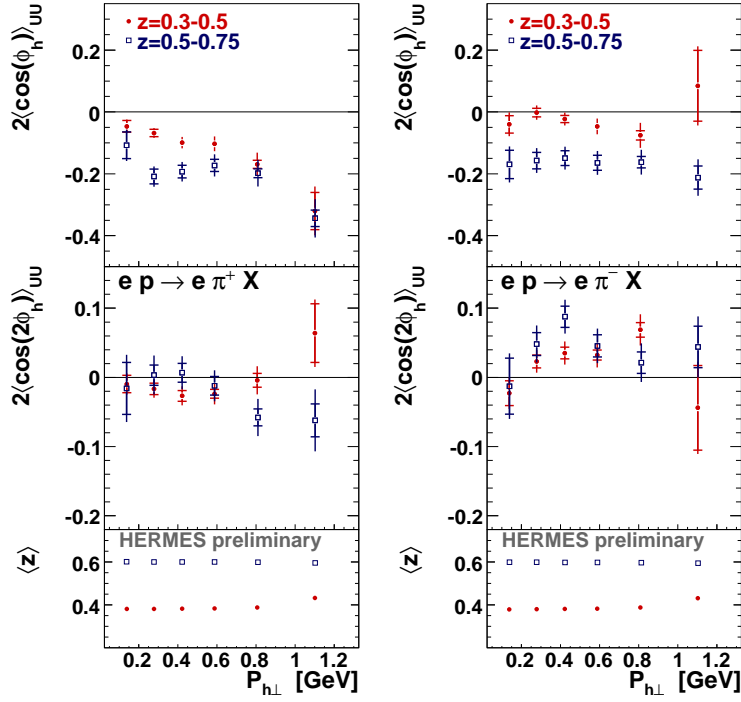


Figure 6.15: $P_{h\perp}$ -dependence of the moments in two z slices for π^+ (left) and π^- (right) on a hydrogen target.

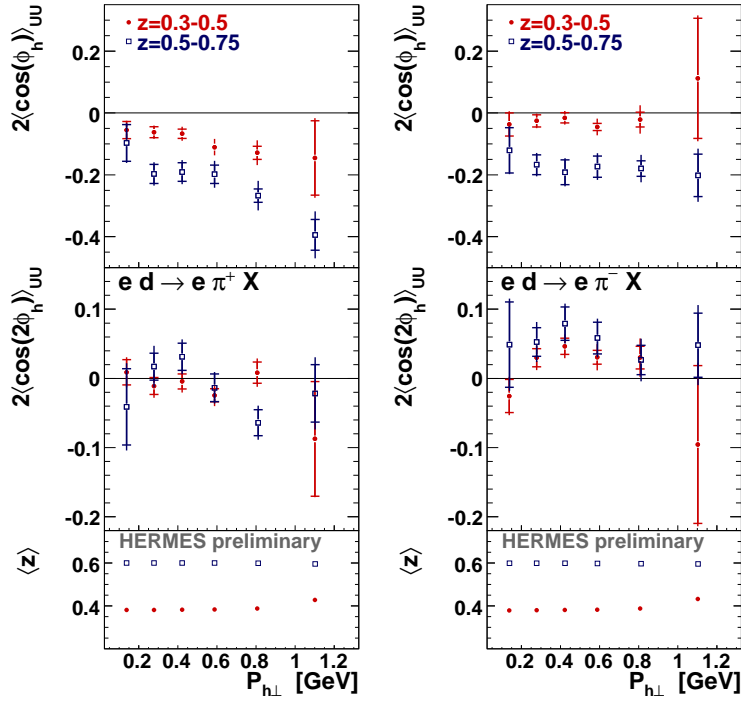


Figure 6.16: $P_{h\perp}$ -dependence of the moments in two z slices for π^+ (left) and π^- (right) on a deuterium target.

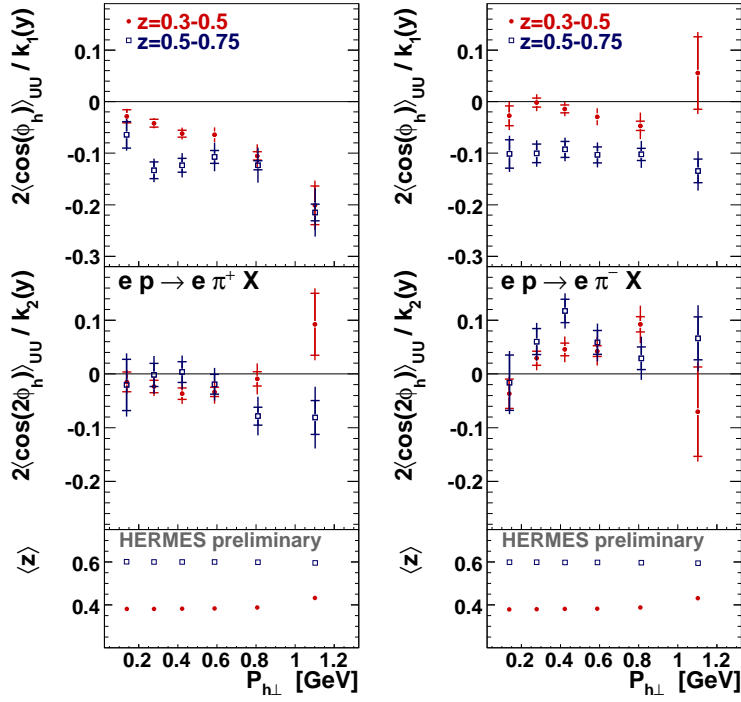


Figure 6.17: $P_{h\perp}$ -dependence of the structure function ratio in two z slices for π^+ (left) and π^- (right) on a hydrogen target

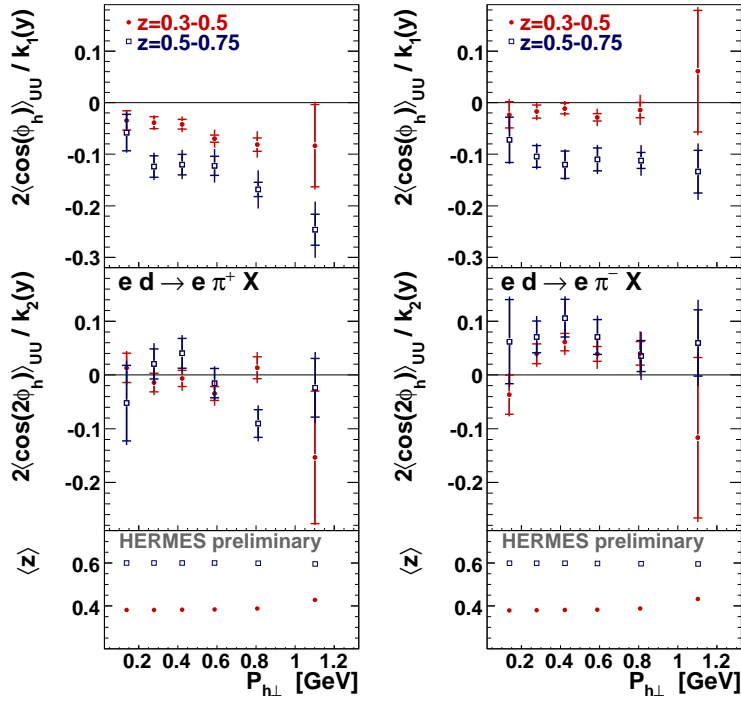


Figure 6.18: $P_{h\perp}$ -dependence of the structure function ratio in two z slices for π^+ (left) and π^- (right) on a deuterium target.

6.2 Hadron results

Almost all other existing measurements of $\langle \cos \phi_h \rangle_{UU}$ and $\langle \cos 2\phi_h \rangle_{UU}$ involved unidentified-hadrons (the only exception is the CLAS result for π^+ , see Section 7.1.1), while theoretical models only include pion production. Hadron samples are generally dominated by pions (at HERMES $\sim 72\%$ of the positive hadron are π^+ while $\sim 88\%$ of negative hadrons are π^-), making the comparison reasonable, but not precise. Here, for the first time, results for both pions and unidentified-hadrons are presented. This allows for a clear comparison with both other experimental results and theory. In addition, the deviation between the hadron and pion results can be taken as a rough systematic error on the results of other experiments when comparing them to theory predictions for pions. The results for both hadrons and pions are presented together in Figure 6.19 for the hydrogen target and Figure 6.20 for the deuterium target. For consistency, the hadron results are integrated over the same kinematic range as the pions, again excluding bins where a measurement is not made in all data sets.

Overall the hadron results are very similar to the pion results and thus lead to the same interpretation. Statistically, the most significant difference between the results is due to the kaon contribution. Preliminary results for kaons are presented and interpreted below.

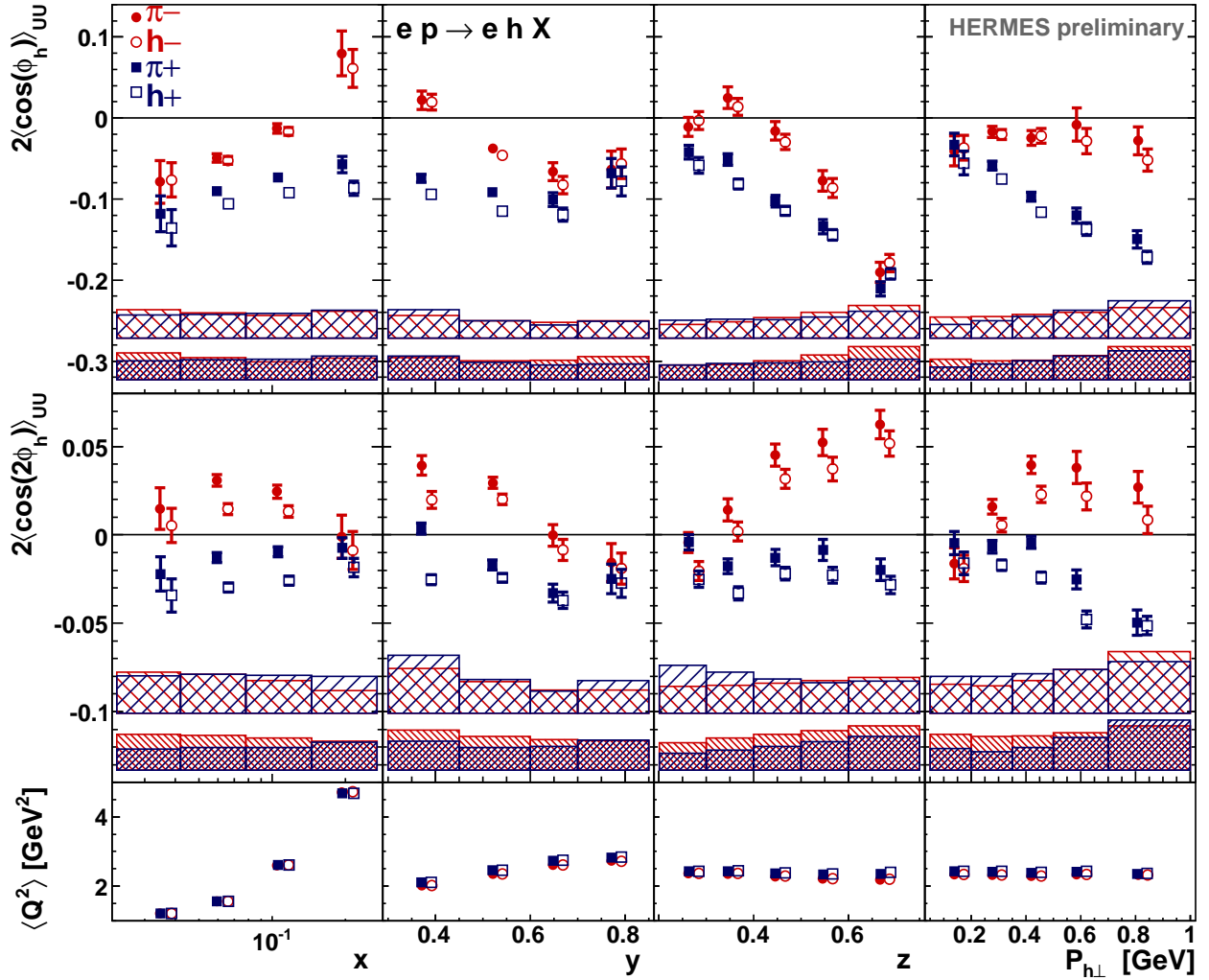


Figure 6.19: The $\langle \cos \phi_h \rangle_{UU}$ (top row) and $\langle \cos 2\phi_h \rangle_{UU}$ (middle row) moments for positive (blue) and negative (red) hadrons (open symbols) and identified pions (filled symbols) produced from a hydrogen target. The bands with closely spaced hatching show the systematic error for pions (the closed points) while bands with widely spaced hatching show the systematic error for hadrons (open points).

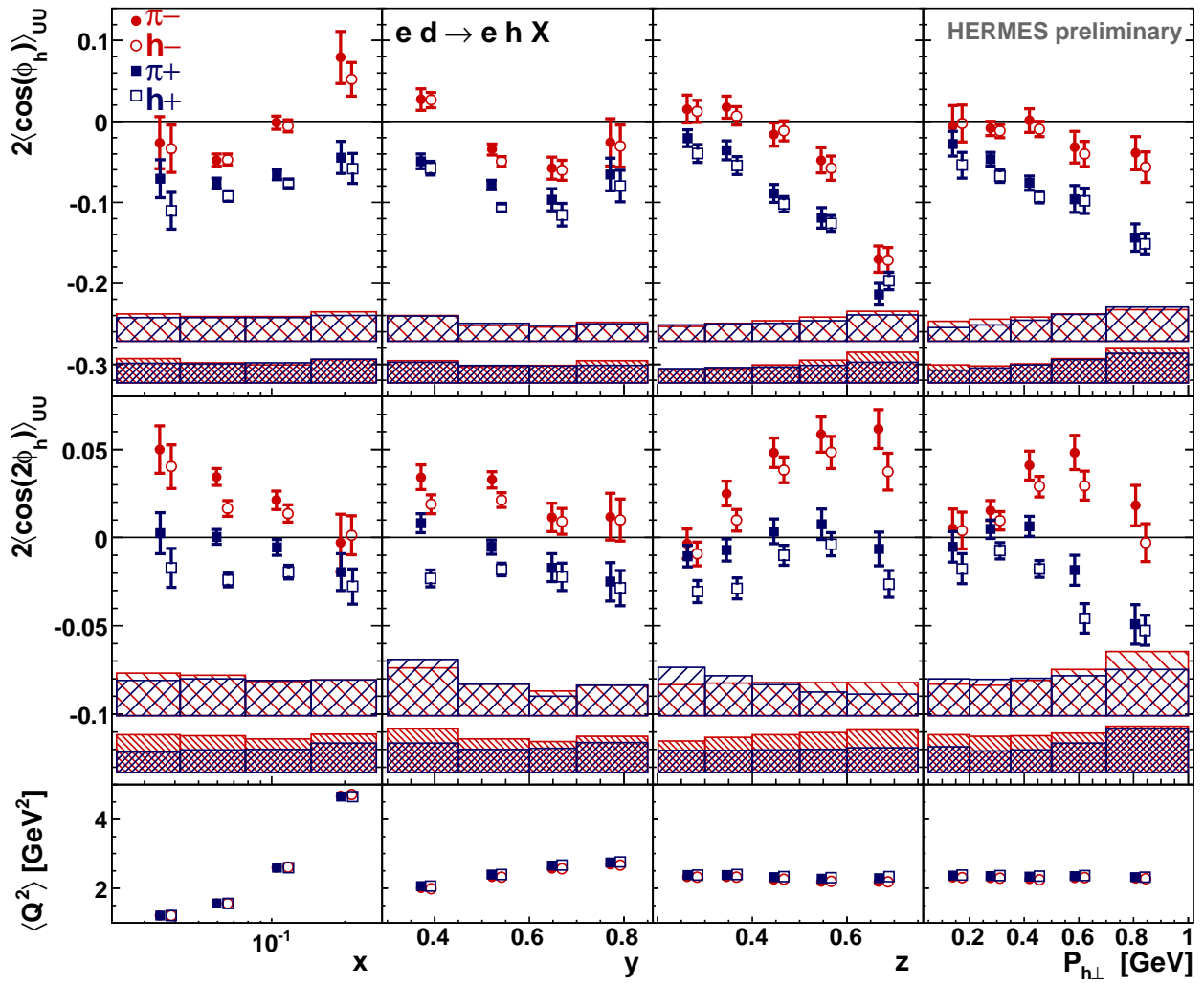


Figure 6.20: The same as Figure 6.19 but for a deuterium target

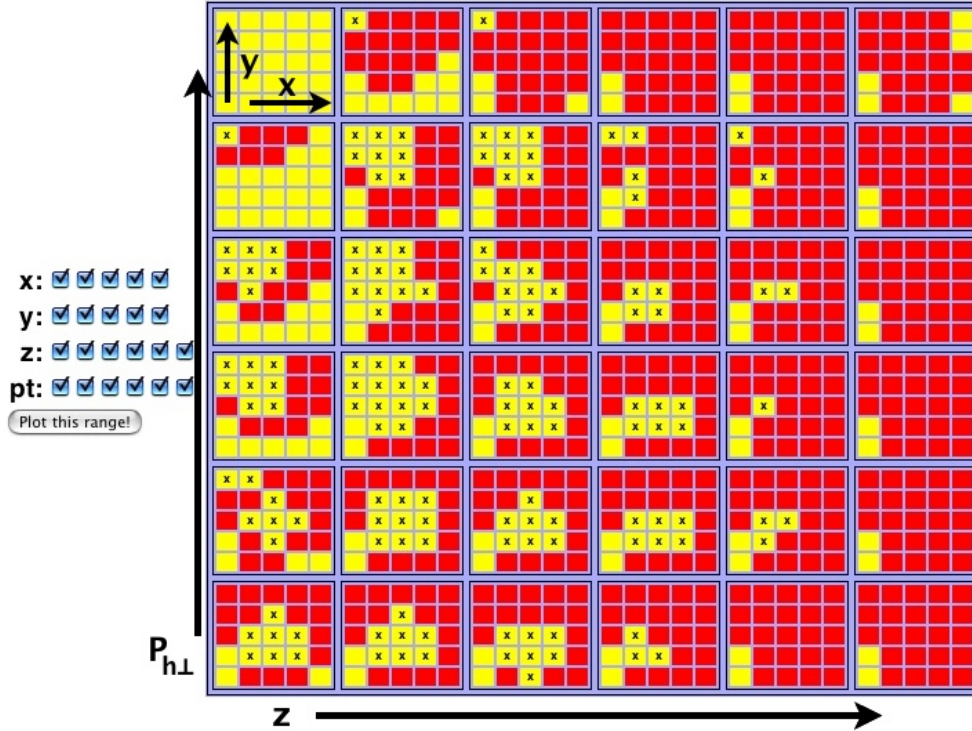


Figure 6.21: Graphical representation of the bins in the deuterium K^- data set.

6.3 Kaon results

Unlike the other results in this chapter, the kaon results have not been cross checked and no systematic error has been evaluated. This is because, due to the low kaon statistics, it is difficult to draw any strong conclusions from the kaon results and so they will (most probably) not be published. However, with the warning that the (unevaluated) systematic error on the kaons is expected to be larger than that for pions, the kaon results are presented here, compared to the pion results.¹

As has been stressed above, it is vital when making a comparison that the same integration region is used for all data sets. This is a particular challenge for the kaons where the statistics are very low. The problem is clearly seen in Figure 6.21 where the statistically accessible kinematic region for negative kaons from a deuterium target (the worst case) is shown. Like Figure 6.2 (see detailed description above), the kinematic region is shown where squares with yellow Xs indicate where a measurement has been made and red squares indicate where the statistic are too poor to make a measurement. Clearly only a small kinematic range is available with the HERMES deuterium K^- data set.

In order to properly compare pions and kaons, and kaons of different charges, a proper kinematic region

¹ The pion systematics are also not included in these figures as the systematic *in this kinematic range* has not been explicitly evaluated. The pion systematic in this range can be expected to be comparable or larger than that of Figure 6.4.

must be chosen. Two attempts are made to present interpretable kaon results. First a small kinematic region is chosen:

$$0.042 < x < 0.27$$

$$0.3 < y < 0.7$$

$$0.3 < z < 0.6$$

$$0.2 < P_{h\perp} < 0.7$$

Figure 6.22 shows this kinematic region for the positive and negative kaons from hydrogen and deuterium targets. As can be seen from these pictures, some unmeasured bins remain in the integration. Figure 6.22e shows the same region for negative pions where a measurement can be made in every bin included in the integration. The positive pions from a deuterium target and the pions from a hydrogen target are higher statistic samples and thus all have full coverage in this kinematic range. The pion and kaon moments in this integration range are presented in Figure 6.23.

Second, in Figure 6.24, every bin where a measurements could be made for every data set, that is, the bins where a measurement could be made for negative kaons on a deuterium target (Figure 6.21), were included in the integration. This has the advantage that each data set contains exactly the same kinematic region and that the maximum number of bins is included. The disadvantage is that each point in a given plot (for example, versus x) is integrated over a different range in the other three kinematic variables so the the general trend (in x) cannot be interpreted.

The $\cos \phi_h$ results show that K^- is similar to π^- while K^+ is significantly larger in magnitude than π^+ . This is exactly the opposite of what might be expected from the quark content and the typical assumption that sea quarks contribute negligibly to spin-dependent distributions. $K^+(u\bar{s})$ and $\pi^+(u\bar{d})$ share a valence u quark, but, the difference in the moments seems to indicate that the sea contribution is significant. $K^-(s\bar{u})$ has no valence content in common with the target while $\pi^-(d\bar{u})$ contains a valance d quark, making the similarity in their moments surprising. This may indicate a large contribution from \bar{u} or s quarks, although the similarity in the negative hadron moments could also be a conspiracy of competing contributions which result in similar moments within the large statistical and systematic uncertainties.

For the kaon $\cos 2\phi_h$ moments, unlike for pions, it is not clear that the moments are charge dependent, although the statistical error may obscure some difference. In addition, the moments are in general larger than the pion moments and negative. The charge dependence of the pion results is attributed to u quark dominance and differing signs for the Collins favored and disfavored fragmentations functions. This argument

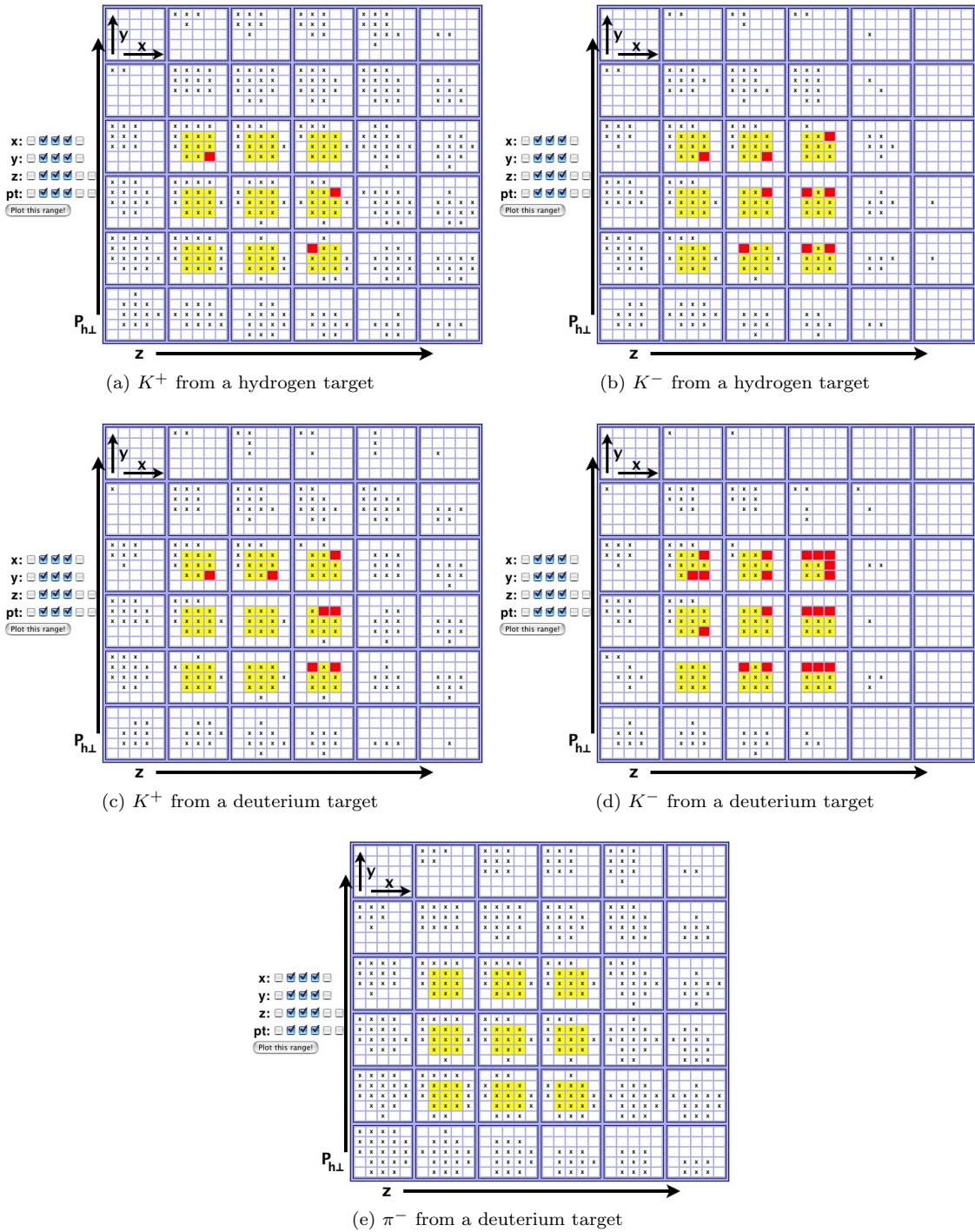


Figure 6.22: Graphical representation of the bins included in the integration of Figure 6.23. All pion results (not shown) have full coverage in the indicated kinematic region.

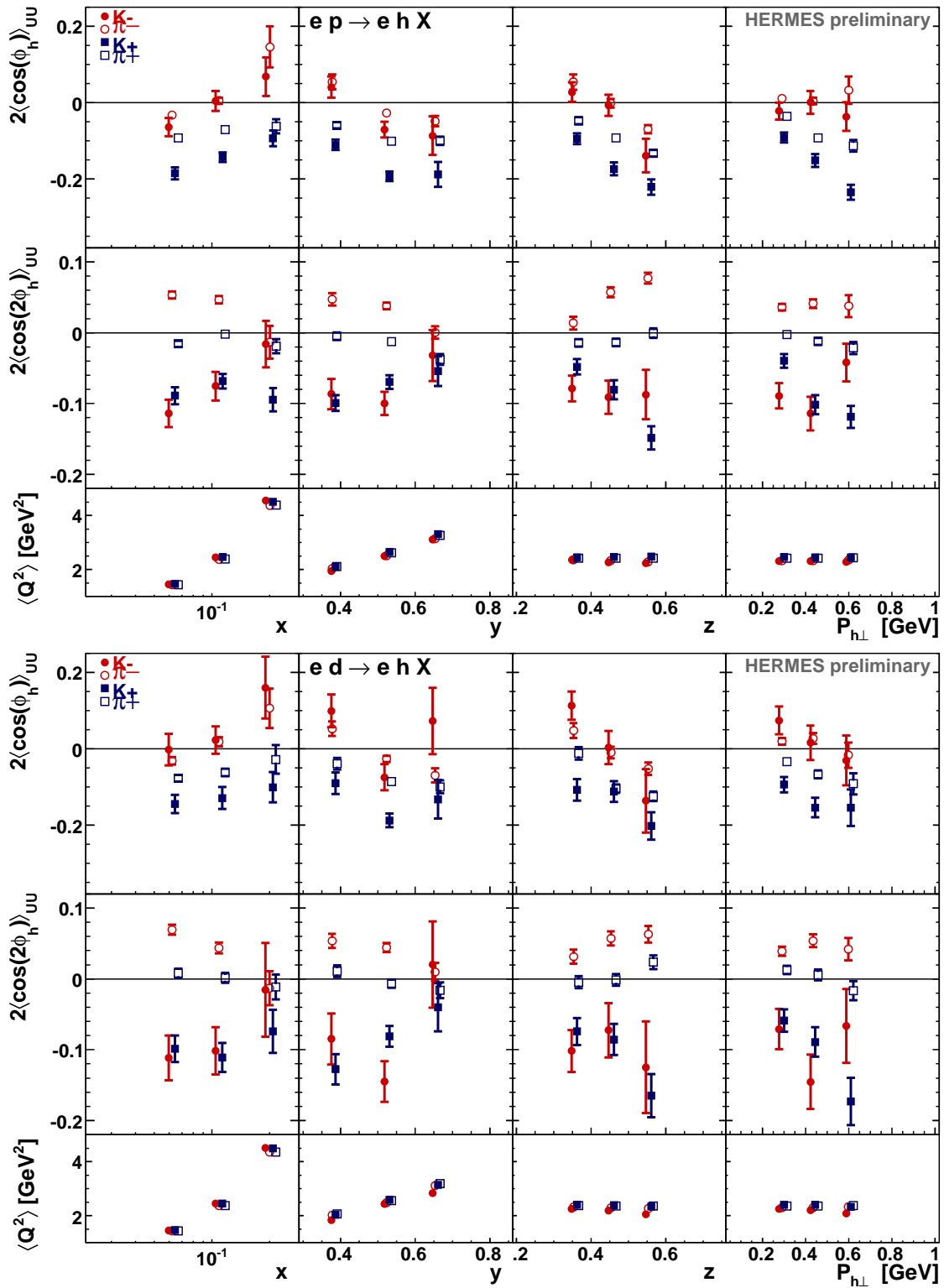


Figure 6.23: Comparison of the moments from pions and kaons on hydrogen (upper plot) and deuterium (lower plot) targets in the kinematic region shown in Figure 6.22

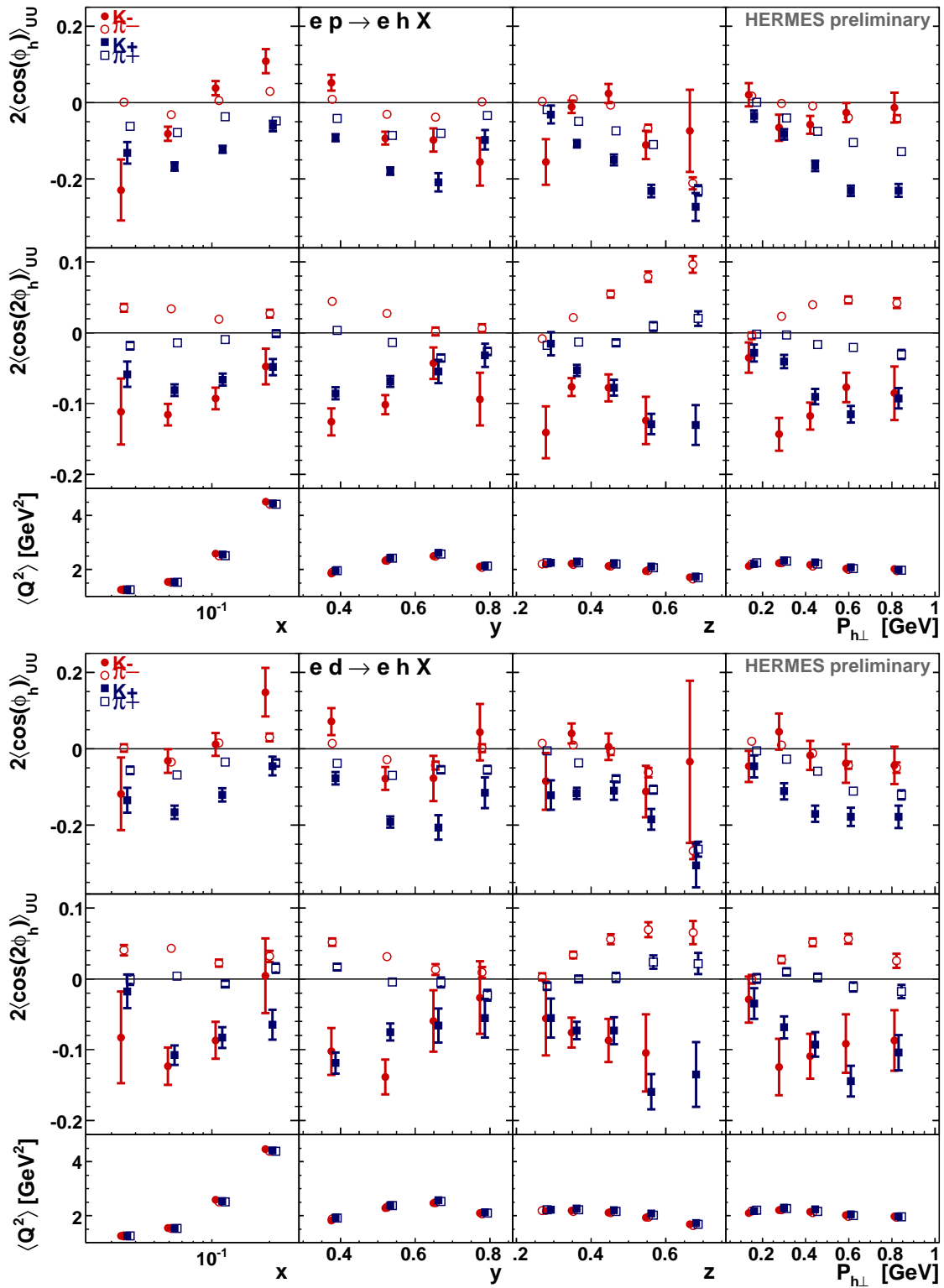


Figure 6.24: Comparison of the moments from pions and kaons on hydrogen (upper plot) and deuterium (lower plot) targets for an integration over all bins included in all data sets (see Figure 6.21)

should also apply to the kaons but is clearly not a sufficient description as it does not match the data.

Since $\cos\phi_h$ and $\cos 2\phi_h$ both receive contributions from the Boer-Mulders and Cahn effects a proper analysis of the results requires further experimental constraints on the Collins functions for kaon production from strange quarks and additional theoretical work to create models for kaons.

6.4 Four-dimensional fits to the results

As described in Section 4.4.7 the fully differential results were fit to a four-dimensional function of 34, 38, 42, or 50 parameters. The integrated parameterization of the results from the hydrogen target are shown in Figures 6.25 and 6.26 with the data superimposed.² For all parameterizations the reduced χ^2 is ~ 3 , showing no preference for any parameter set.

These parameterizations are used in the systematic studies discussed in Chapter 5, as well as in other HERMES analyses, as discussed in the next section.

6.4.1 Inclusion in other HERMES analyses

While a measurement of the $\cos n\phi_h$ moments is interesting in its own right, the azimuthal modulation of the unpolarized cross section is an important piece of input information for other analyses at HERMES. One example is the Δq (aka g_1 in Figure 1.4) analysis, which extracts flavor dependent polarized distribution functions. Here the unpolarized cross section, including its azimuthal modulations, enters in the denominator of the of the A_1 asymmetry, which corresponds to the σ_{UU} component of the cross section. To correct for this a multiplicative factor is estimated from MC which has been weighted with the azimuthal moments which are taken from the parameterization of the results presented here (Section 6.4). See Section 4.4 of reference [29] for details.

A second example is the multiplicity analysis, where the pion, kaon and (anti)proton SIDIS yields are extracted. This analysis applies an unfolding procedure like Equation 4.5. To correct for the azimuthal dependence which is not included in the MC generator, Born and reconstructed events are weighted according to their kinematics and the parameterization of Section 6.4. See reference [27].

² The fit is done in the fully differential binning, and then both the fit results and the data are independently integrated. Thus, the parameterization may not seem to have the best fit to the data points since the integrated over variables also constrain the fit.

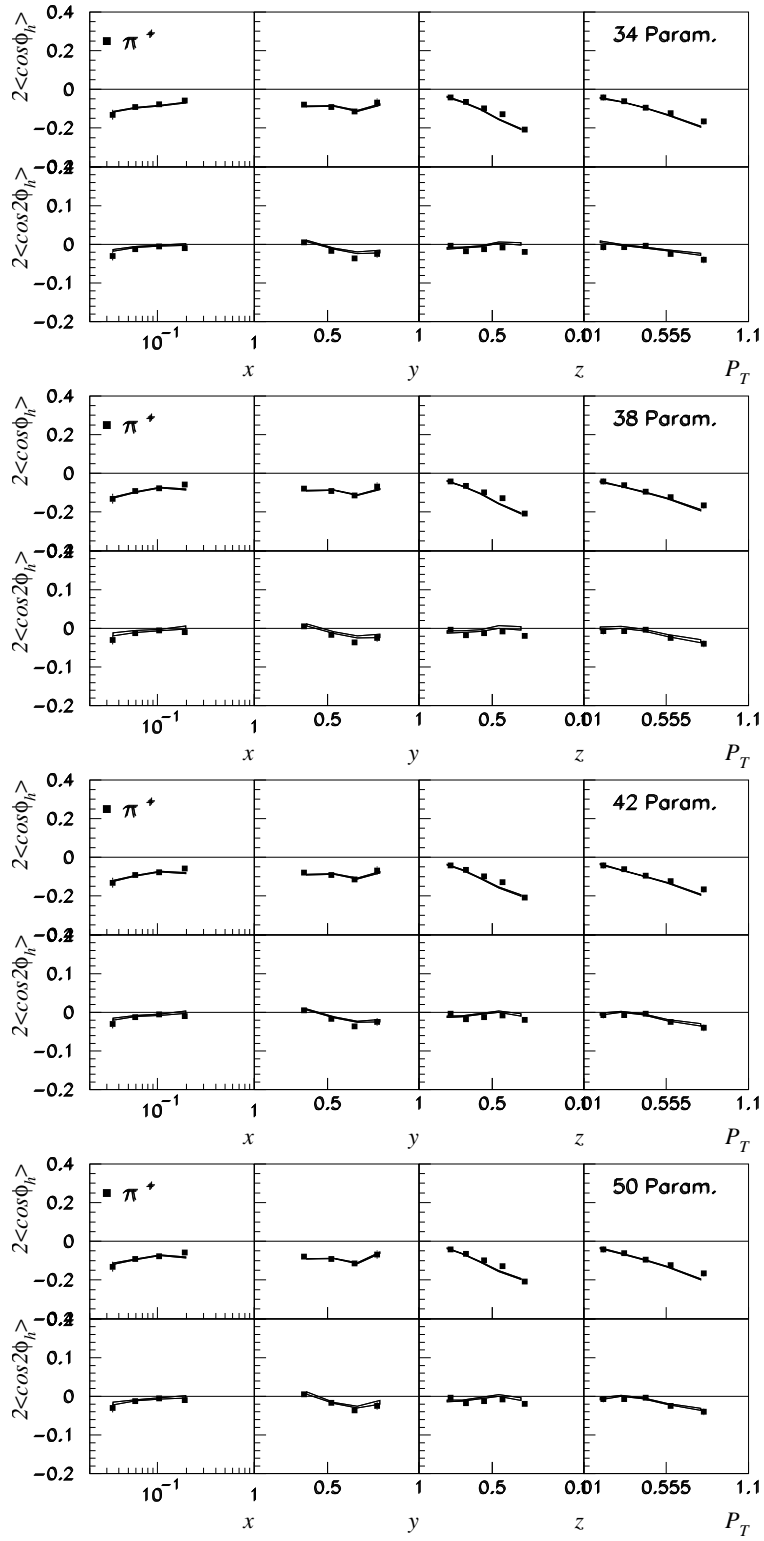


Figure 6.25: Parameterization of the hydrogen π^+ data with 34 (top), 38 (second row) 42 (third row) or 50 (bottom row) parameters.

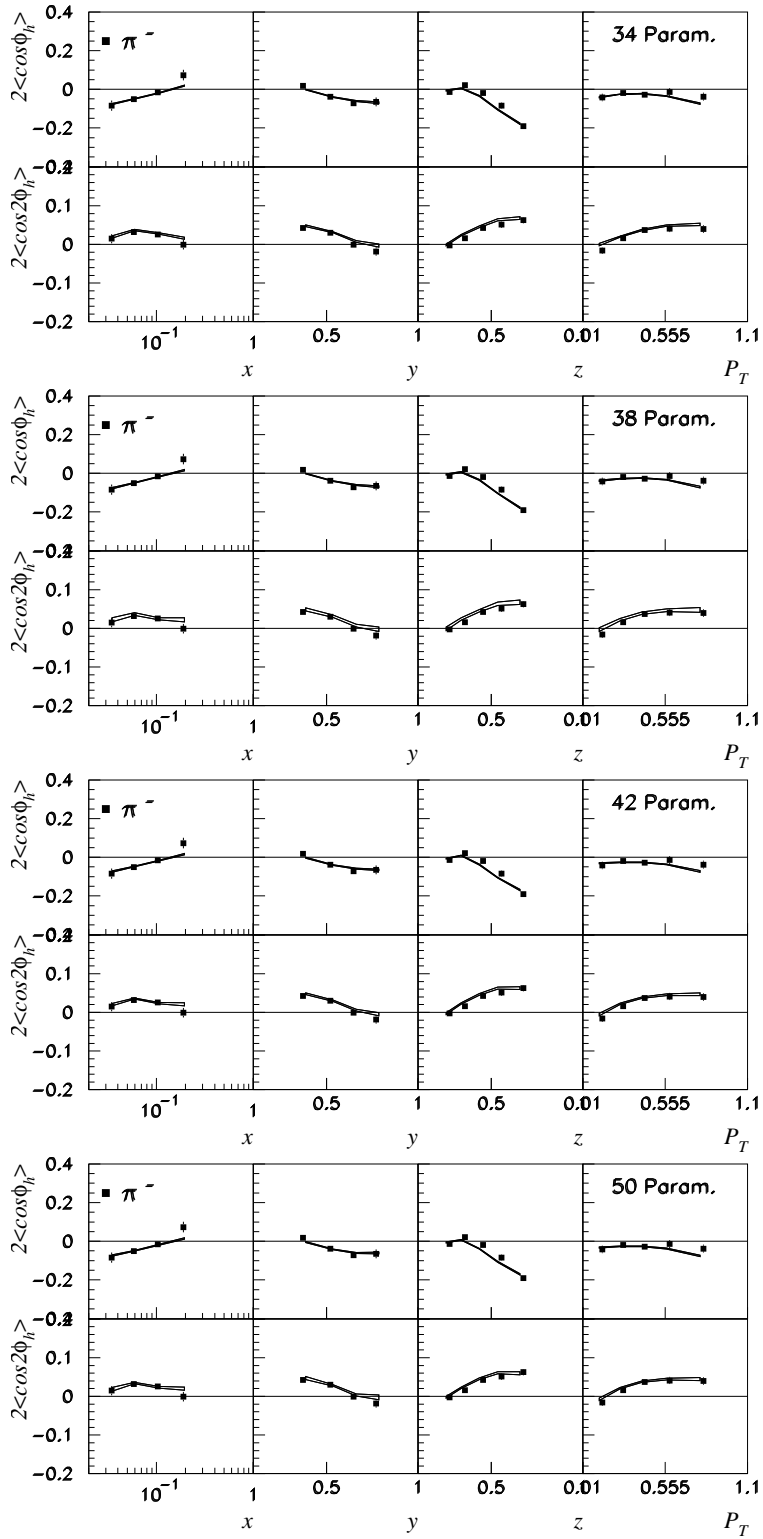


Figure 6.26: Parameterization of the hydrogen π^- data with 34 (top), 38 (second row) 42 (third row) or 50 (bottom row) parameters.

Chapter 7

Comparison with other experimental results

7.1 Other $\cos \phi_h$ and $\cos 2\phi_h$ measurements

Several measurements of $\cos \phi_h$ and $\cos 2\phi_h$ have been made over the past few decades, predominately in the early 1980s. The measurements made before 2008 are summarized here.

- Tao, C et al., Fermilab, 1980 [30]
 - charge-combined hadron production in muon-proton scattering
 - $\cos \phi_h$ slightly negative
 - $\cos 2\phi_h \sim 0$
- M. Derrick, et al., Fermilab, 1981 [31]
 - charge-combined hadron production in antineutrino-proton scattering
 - $\cos \phi_h \sim 0$
 - $\cos 2\phi_h \sim 0$
- BEBC Wide Band Neon Collaboration, CERN, 1982 [32]
 - charged pion production in neutrino scattering
 - $\pi^+ \cos \phi_h \sim 0$
 - $\pi^- \cos \phi_h$ slightly negative
- EMC, CERN, 1983 [33] , 1986 [34]
 - charge-combined hadron production in μp scattering
 - $\cos \phi_h \sim -0.1$
 - $\cos 2\phi_h$ slightly positive
 - comparison to models favors intrinsic quark momentum $\langle \mathbf{p}_T^2 \rangle \geq 0.19 \text{GeV}^2$

- E665, Fermilab, 1993 [35]
 - charge-combined hadron production in μp and μd scattering
 - $\cos \phi_h \sim -0.5$
 - comparison to models favors $\langle \mathbf{p}_T^2 \rangle \geq 0.25 \text{GeV}^2$
- ZEUS, DESY, 2000 [36], 2006 [37]
 - charge-combined hadron production in ep scattering (charged and neutral hadrons in [37])
 - $\cos \phi_h \sim -0.1$
 - $\cos 2\phi_h$ small and positive

These experiments cover a large kinematic range with ZEUS at the highest energy ($180 < Q^2 < 7220 \text{ GeV}^2$). The early experiments (before EMC) were of very low statistical precision and used primitive (if any) corrections for detector acceptance, smearing, and QED radiative effects. Since all of these measurements were in search of NLO pQCD generated azimuthal asymmetries they do not present results versus the kinematic variables of this work. In addition, with the exception of the BEBC results, only charge-combined measurements have been made. These obscure any Boer-Mulders contribution which is significantly different for positive and negative hadrons. However, a general trend is apparent: $\cos \phi_h$ is negative and $\cos 2\phi_h$ is smaller and positive. This is in general agreement with the HERMES results presented in the previous chapter.

The vigorous theoretical work in TMDs over the past decade has renewed interest in azimuthal asymmetries in unpolarized reactions, and two other experiments, in addition to HERMES, have made recent measurements.

7.1.1 CLAS results

The CLAS experiment at Jefferson Laboratory has recently published [38] their measurement of the azimuthal modulation of the SIDIS cross section for positive pions. Their results are presented in Figures 7.1 and 7.2. The vertical-axis labels on these plots denote the $\cos \phi_h$ and $\cos 2\phi_h$ moments with certain kinematic prefactors removed, as indicated by Equation 3 of Reference [38]:

$$2\langle \cos \phi_h \rangle_{UU} = 2 \left((2-y) \sqrt{\frac{1}{(1+\gamma^2)(1-y-\frac{1}{4}\gamma^2 y^2)}} \right) \frac{\mathcal{H}_3}{\mathcal{H}_2 + \epsilon \mathcal{H}_1} \quad (7.1)$$

$$2\langle \cos 2\phi_h \rangle_{UU} = 2 \left(\frac{1}{1+\gamma^2} \right) \frac{\mathcal{H}_4}{\mathcal{H}_2 + \epsilon \mathcal{H}_1} \quad (7.2)$$

To more easily compare the HERMES and CLAS results, the CLAS data have been multiplied by these kinematic factors and are presented, along with the HERMES data, in Figures 7.3 and 7.5. Only the CLAS points with the most similar kinematics are presented. The average kinematics of both experiments are presented in Figures 7.4 and 7.6.

The $P_{h\perp}$ -dependence of $\cos \phi_h$ shown in Figure 7.3 has the same shape in both the HERMES and CLAS results. The CLAS measurement is at much higher x and y (Figure 7.4) but the x and y -dependence observed at HERMES appears to be relatively flat (Figure 6.3). The $P_{h\perp}$ -dependence of the $\cos 2\phi_h$ measurements of HERMES and CLAS shown in Figure 7.3 are compatible, and compatible with zero. A possible exception to this is the highest $P_{h\perp}$ bin; however, in the highest z plot, the two experiments have the most similar z and the data points are compatible.

The z -dependence plots in Figure 7.5 unfortunately have very little overlap. The best cases are the $p_T^2 = 0.21$ and $p_T^2 = 0.34$ plots. The $\cos \phi_h$ results from CLAS show a shift to more positive moments in the central z region, which is not in agreement with the HERMES data. Again, the average x and y of each z bin varies, but the HERMES results give no indication that this should have a significant effect on the moments. The $\cos 2\phi_h$ results are again compatible between the experiments and compatible with zero.

Overall, the CLAS results provide a complementary data set that is not significantly at odds with the HERMES data. Further work to present the HERMES results integrated in the more limited z and $P_{h\perp}$ bins of the CLAS results could improve the agreement but would inflate the errors such that any agreement would lose significance.

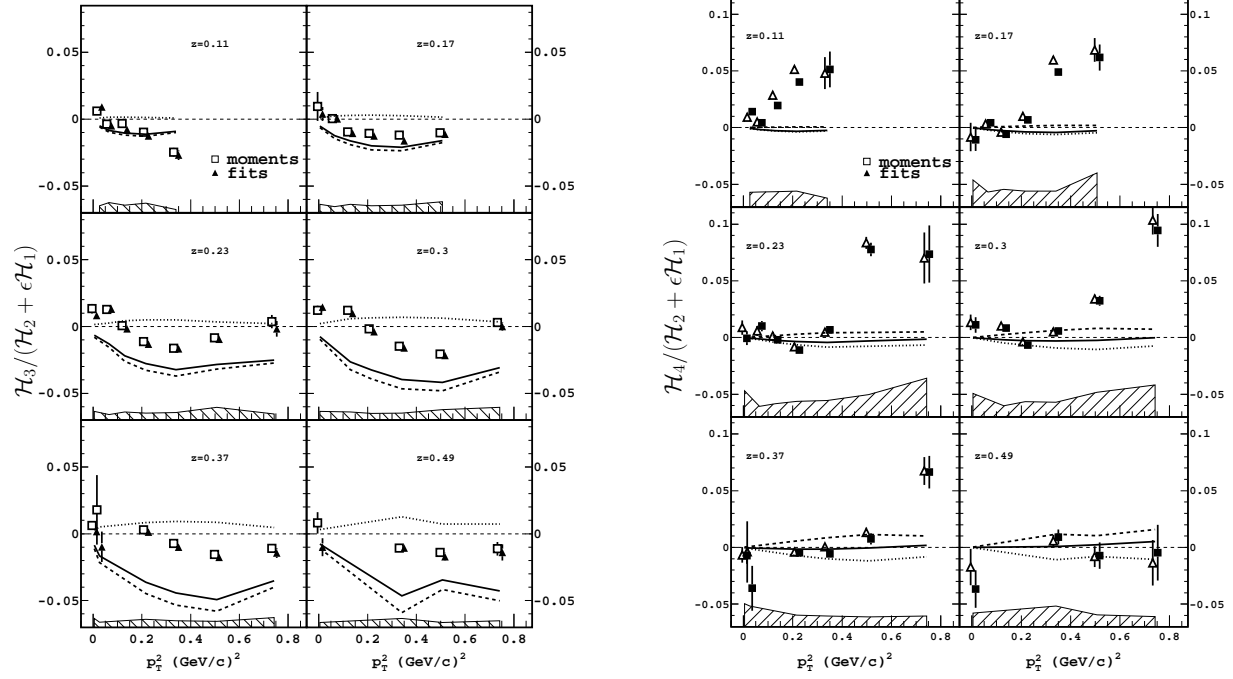


Figure 7.1: Figures 26 and 27 from [38]. Measurements which are related to the $\cos \phi_h$ (left) and $\cos 2\phi_h$ (right) moments are shown in bins of z versus $P_{h\perp}$.

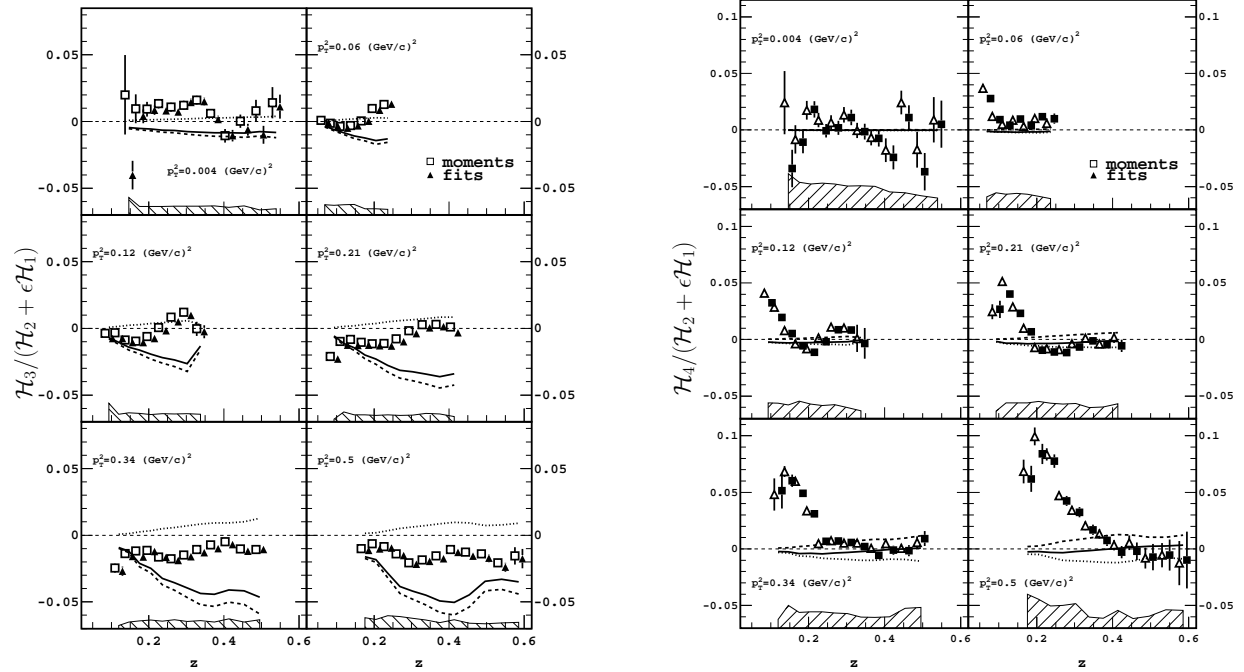


Figure 7.2: Figures 28 and 29 from [38]. Measurements which are related to the $\cos \phi_h$ (left) and $\cos 2\phi_h$ (right) moments are shown in bins of $P_{h\perp}$ versus z .

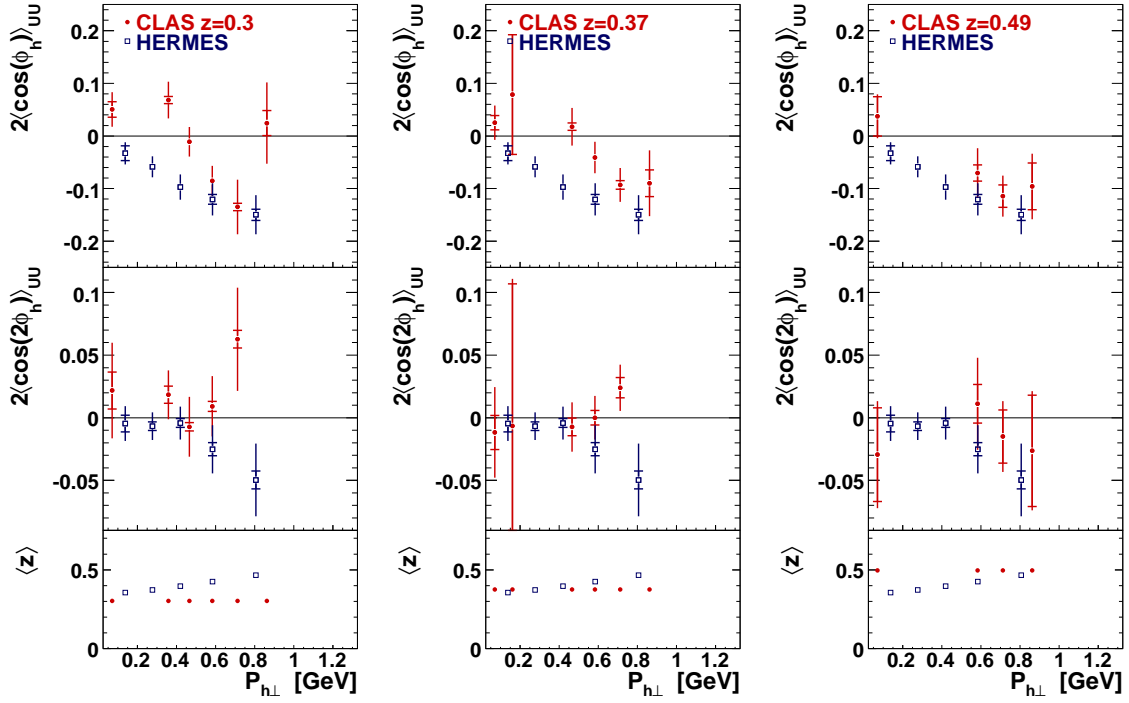


Figure 7.3: Comparison of HERMES results (in the integration range of Section 6.1) with CLAS results in different z bins (the HERMES results are the same in all cases).

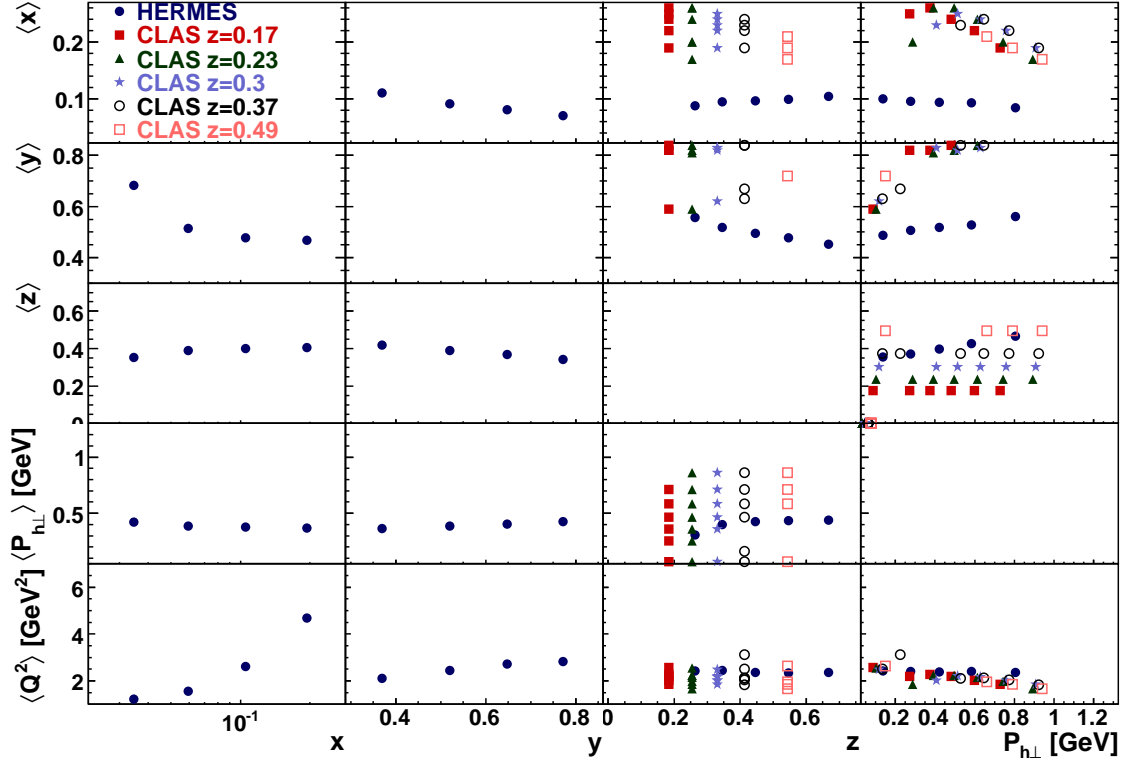


Figure 7.4: Average kinematics of HERMES and CLAS points presented in Figure 7.3.

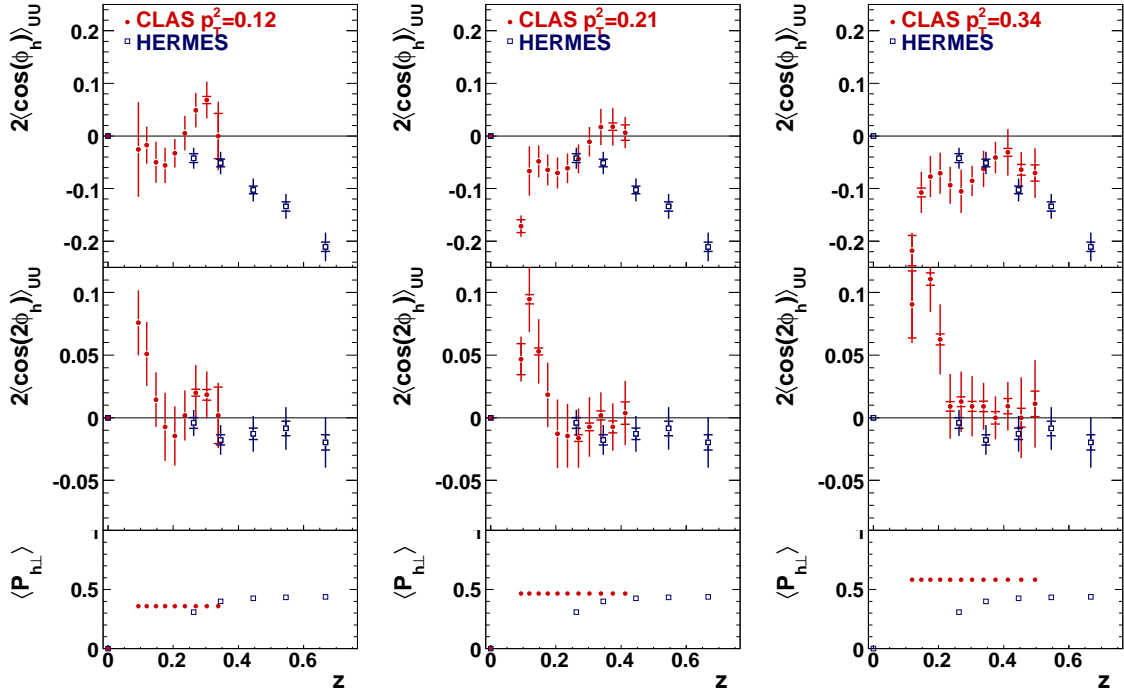


Figure 7.5: Comparison of HERMES results (in the integration range of Section 6.1) with CLAS results in different $P_{h\perp}$ bins (the HERMES results are the same in all cases).

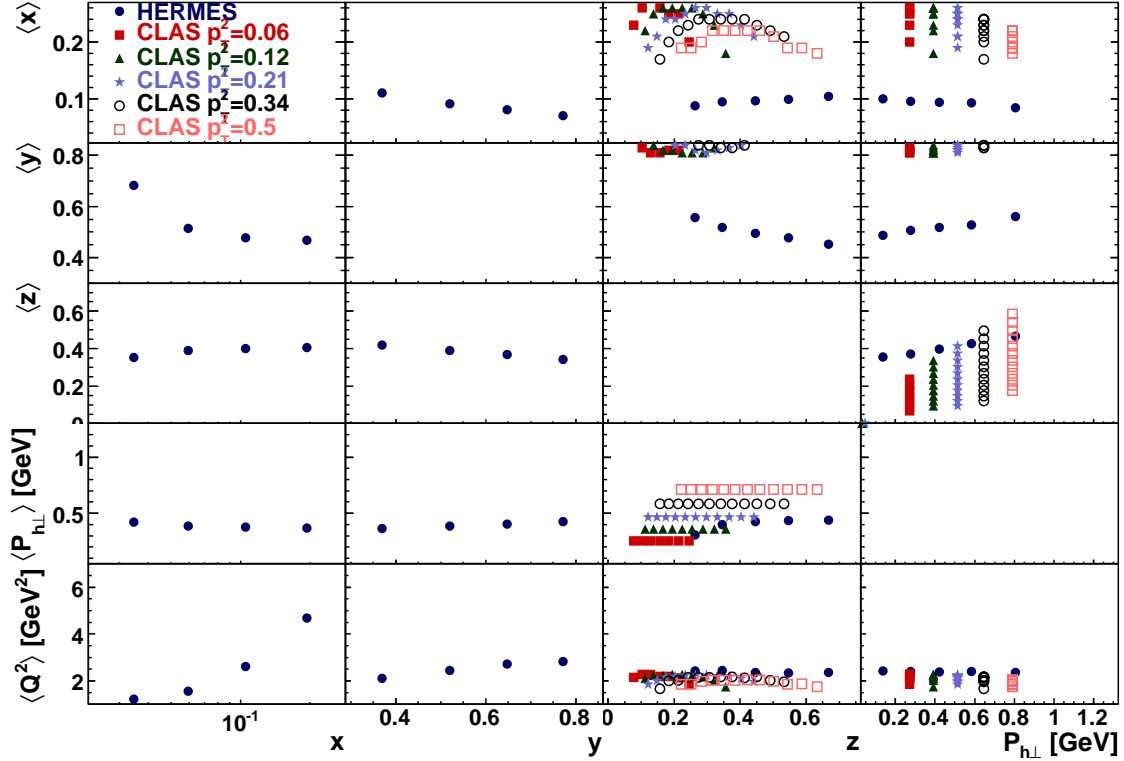


Figure 7.6: Average kinematics of HERMES and CLAS points presented in Figure 7.5.

7.1.2 COMPASS results

Positive and negative hadrons were measured by the COMPASS experiment in deep inelastic scattering of an incident muon beam from a ${}^6\text{LiD}$ target [39, 40]. The preliminary COMPASS results are shown in Figures 7.7 and 7.8. No attempt was made to correct for radiative or nuclear target effects and the acceptance was only corrected for with a simple ratio, taken from MC, in one kinematic dimension at a time (integrating over the rest). The systematic error quoted is due to the two different target configurations (longitudinally and transversely polarized targets and corresponding magnetic fields) and the uncertainty in the acceptance correction arising from the MC settings.

The COMPASS results are subject to the constraints

$$1\text{GeV}^2 < Q^2$$

$$0.1 < y < 0.9$$

$$0.2 < z < 0.85$$

$$0.1\text{GeV} < P_{h\perp} < 1.5\text{GeV},$$

which is somewhat wider than the HERMES kinematic range. The COMPASS results are best compared to the HERMES hadron results presented in Figure 6.20. The COMPASS $\cos\phi_h$ moments show a similar difference between positive and negative hadrons, but the results are systematically shifted to lower values than the HERMES measurements. This may be partially due to the contribution from the large moment in the highest $P_{h\perp}$ bin, which is not included in the HERMES kinematic range. However, the $P_{h\perp}$ dependent plots indicate a shift of similar size at all $P_{h\perp}$ values.

The $\cos 2\phi_h$ moments appear shifted up with respect to the HERMES measurement. This again may be partially due to the highest $P_{h\perp}$ bin. While the sign difference between the experiments for positive hadrons appears somewhat troubling both measurements are, strictly speaking, consistent with zero within their systematic errors.

The COMPASS and HERMES $\cos 2\phi_h$ results are discussed further in Section 8.2.2 where these COMPASS results along with preliminary HERMES results (for all hadrons, including only the 2000 to 2006 e^- data) were fit to determine a relative scale for the Boer-Mulders function relative to the Sivvers function. This work found that, taking into account the proper kinematics, the HERMES and COMPASS data sets are largely compatible. However, the COMPASS $P_{h\perp}$ -dependence is difficult to explain. See Section 8.2.2 for a more detailed discussion.

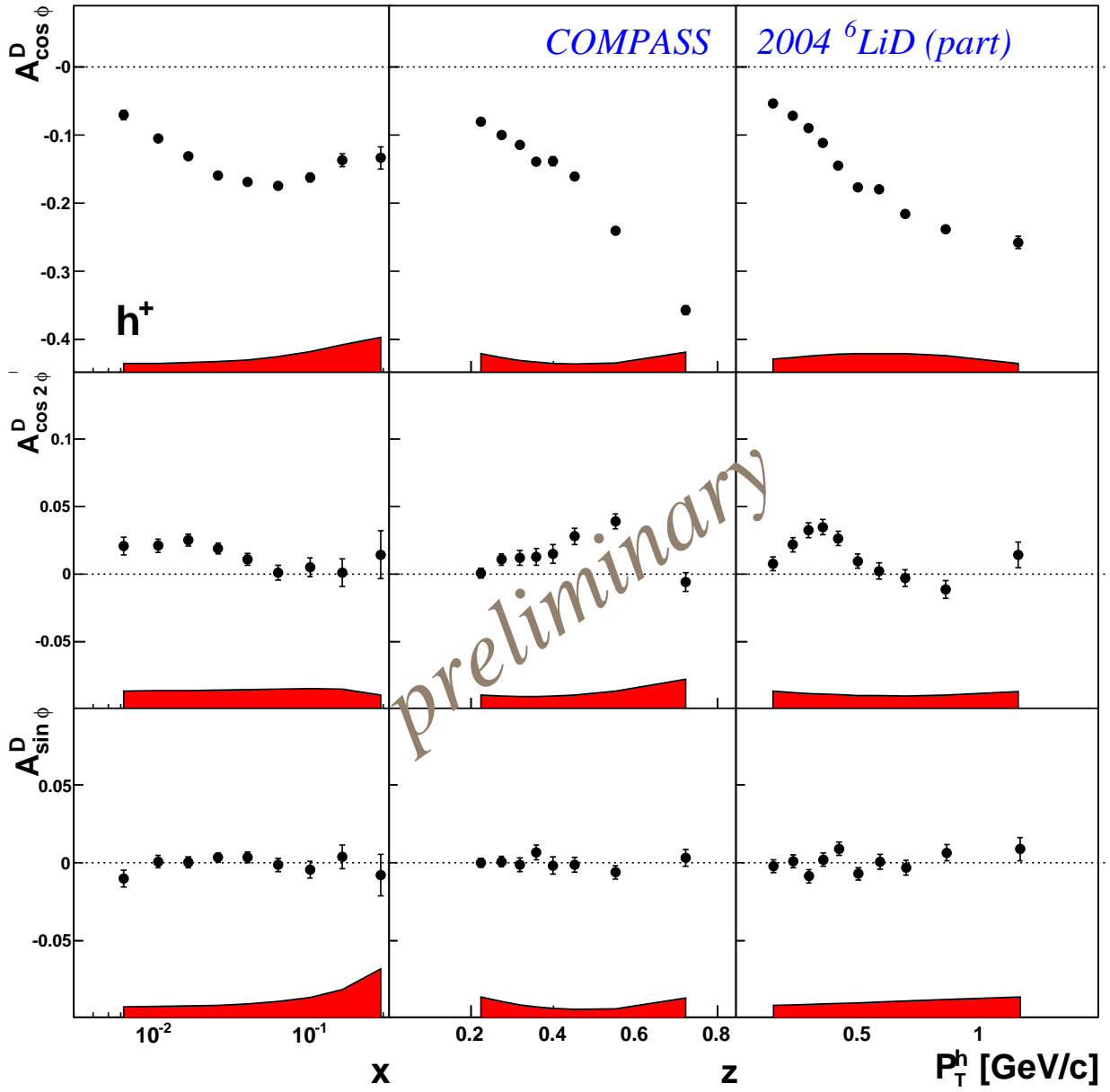


Figure 7.7: COMPASS results for positive hadrons

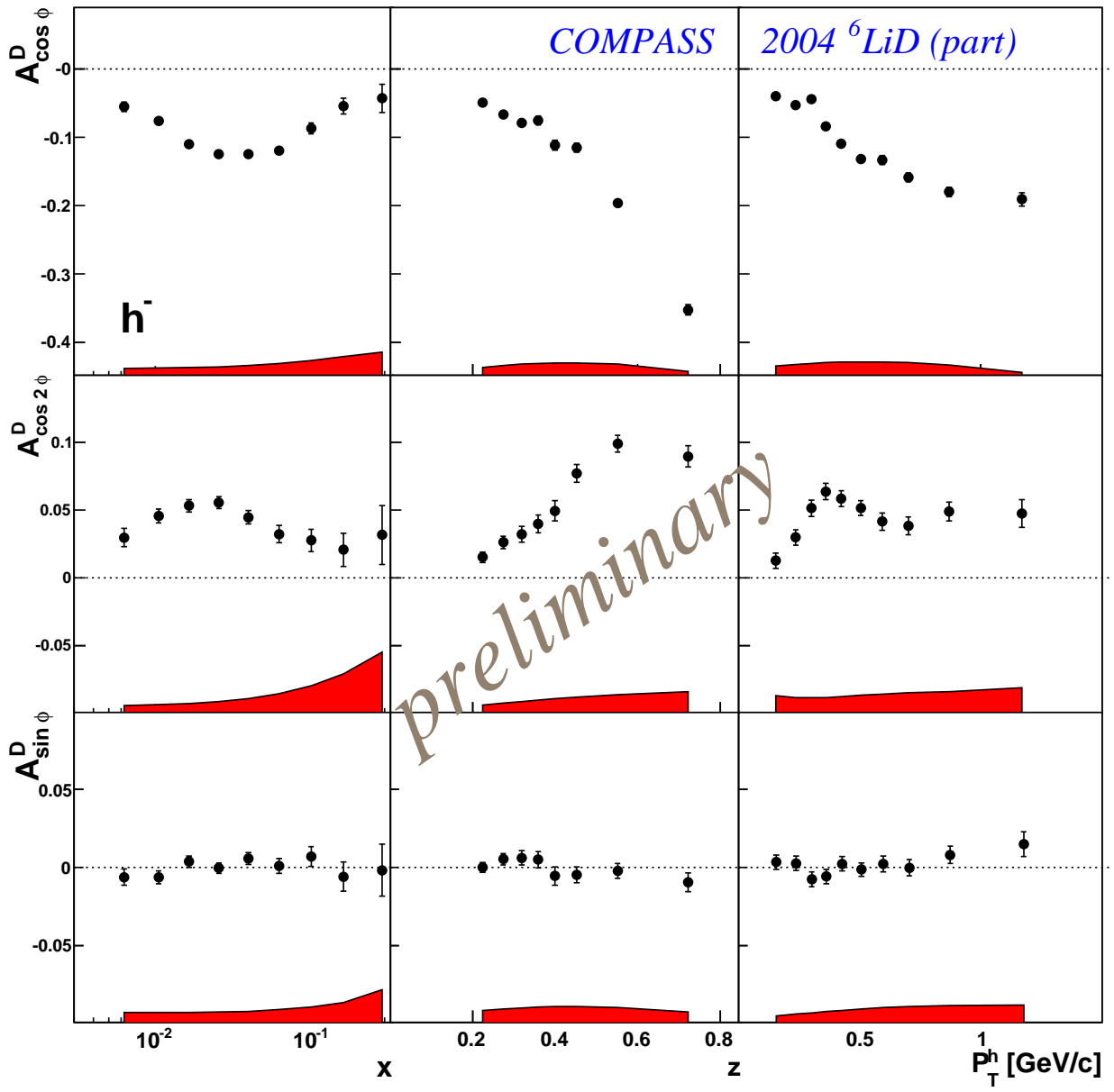


Figure 7.8: COMPASS results for negative hadrons

7.2 The Collins fragmentation function

Measurements sensitive to the Collins function have been published recently by the HERMES [6], COMPASS [7, 41] and Belle [42] collaborations. A global fit to these results was performed in [43] and is used as input in most model calculations of the Boer-Mulders effect.

7.3 Drell-Yan results

The Drell-Yan process is also sensitive to the Boer-Mulders function via a $\cos 2\phi$ modulation. The differential cross section is given by

$$\frac{1}{\sigma} \frac{d\sigma}{d\Omega} = \frac{3}{4\pi} \frac{1}{\lambda + 3} \left(1 + \lambda \cos^2 \theta + \mu \sin 2\theta \cos \phi + \frac{\nu}{2} \sin^2 \theta \cos 2\phi \right) \quad (7.3)$$

where θ and ϕ are the polar and azimuthal angles of the negative lepton in the dilepton rest frame, and λ , μ , and ν are azimuthally independent parameters measured by experiment. The Boer-Mulders function appears in the ν parameter of the Drell-Yan cross section and is different by a sign from that measured in SIDIS.

The ν parameter was measured by the NA10 collaboration [44, 45], the E615 collaboration [46, 47], and most recently by the E866/NuSea collaboration [48, 49]. While the ν parameter cannot be compared directly with SIDIS data, recent fits to the E866/NuSea data [50, 51] extract the Boer-Mulders function. This work is discussed in more detail in Section 8.2.3.

Future measurement of the Boer-Mulders function in Drell-Yan are planned at COMPASS ($\pi^- p \rightarrow \mu^+ \mu^-$, after 2011) and SEAQUEST, and may be feasible at J-PARC [51, 52], PANDA [51], PAX [51, 53], NICA [52], and RHIC [50, 52]. These experiments will provide vital additional information, at various energies, which will further constrain the Boer-Mulders function.

Chapter 8

Comparison to theory

The complex nature of the results presented in this thesis necessitate the use of phenomenological models to aid in interpretation. Several models are presented here.

8.1 $\cos \phi_h$ models

While new pre/post-dictions for the $\cos \phi_h$ moments are in progress only a single model is available at this time, which includes only the Cahn contribution.

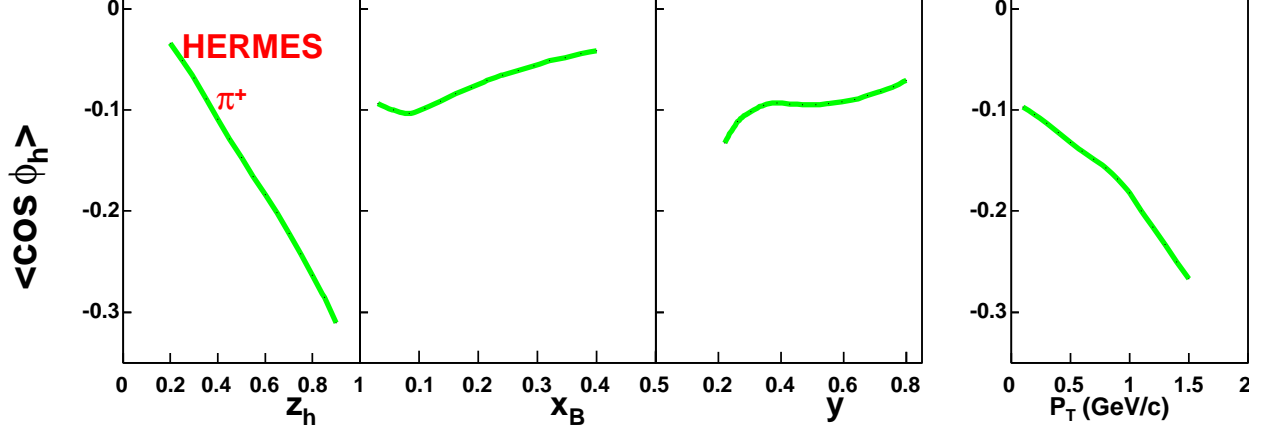


Figure 8.1: Prediction of the Cahn contribution to $\cos \phi_h$ at HERMES from Reference [54]

8.1.1 Anselmino et al.

In Reference [54] (and references therein) Anselmino et al. obtain estimates for $\langle k_{\perp}^2 \rangle$ and $\langle p_{\perp}^2 \rangle$ from a fit to existing data from the E665, EMC, and Zeus collaborations (see Section 7.1). Using these parameters they predicted the $\pi^+ \cos \phi_h$ amplitude due to the Cahn effect at HERMES kinematics for a hydrogen target. These predictions are shown in Figure 8.1. Note that $\langle \cos \phi_h \rangle_{UU}$, and not $2\langle \cos \phi_h \rangle_{UU}$ is shown; the moments must therefore be multiplied by two for comparison with the experimental results. Since the assumption is made that $\langle k_{\perp}^2 \rangle$ and $\langle p_{\perp}^2 \rangle$ are flavor independent a prediction for π^- would be identical to the π^+ moments presented in Figure 8.1.

While the general trends of a strong decrease with z and $P_{h\perp}$ and a slightly increase with x and y are similar to the dependences seen in the data (Figure 6.4, upper plot) the overall magnitude is much larger, reaching a maximum of -0.6 (for $2\langle \cos \phi_h \rangle_{UU}$) at high z compared to -0.2 in the data. In addition the data show an obvious charge dependence that is not present in the model. A likely explanation is the neglected Boer-Mulders contribution, which could also serve to make the overall results more positive. However, flavor dependence and kinematic dependence of $\langle k_{\perp}^2 \rangle$ and $\langle p_{\perp}^2 \rangle$ cannot be ruled out.

While the $\cos \phi_h$ model has not been updated since the release of the HERMES results, the Cahn contribution to $\cos 2\phi_h$ has been evaluated with a smaller average intrinsic quark momentum squared, $\langle k_{\perp}^2 \rangle$, in order to achieve better agreement with the HERMES data. The linear k_{\perp} -dependence of the Cahn contribution to $\cos \phi_h$ indicates that a smaller $\langle k_{\perp}^2 \rangle$ would also improve the agreement with data for the $\cos \phi_h$ prediction.

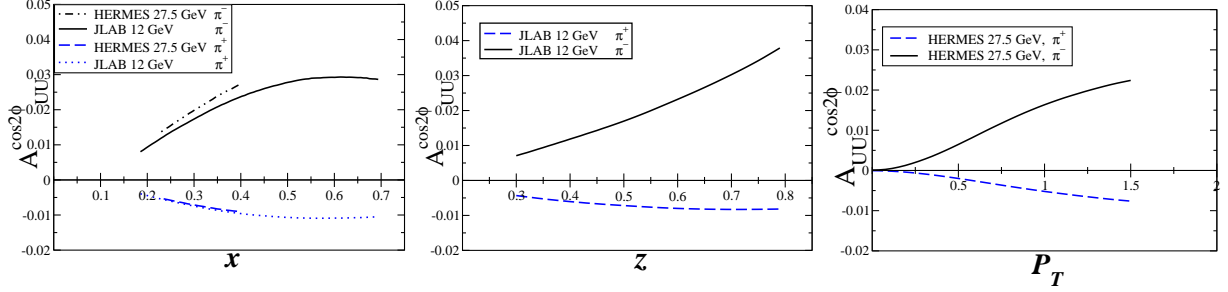


Figure 8.2: Prediction of the Boer-Mulders contribution to $\cos 2\phi_h$ at HERMES from Reference [55]

8.2 $\cos 2\phi_h$ models

Several models exist for the $\cos 2\phi_h$ results. Most include only the Boer-Mulders contribution while Section 8.2.2 presents a model that includes both the Boer-Mulders contribution and the Cahn twist-4 contribution.

8.2.1 Gamberg et al.

Gamberg et al. made predictions for the $\cos 2\phi_h$ moments of positive and negative pions from a hydrogen target with the diquark spectator model in Reference [55]. The authors calculate the Boer-Mulders function for u and d quarks and find that both flavors have a negative Boer-Mulders function. In conjunction with the Collins fragmentation function calculated in a spectator model in [56], they calculate the Boer-Mulders contribution to $\cos 2\phi_h$. The resulting predictions are shown in Figure 8.2. The asymmetries shown again differ by a factor of two from the experimental $2\langle \cos 2\phi_h \rangle_{UU}$ moments.

The general trends of the data are replicated by the model: the π^- results are positive while the π^+ results are smaller and negative. The shape of the model is also similar, however the drop in the data at high $P_{h\perp}$ and the moments' trend toward zero at high x are not apparent in the model. The magnitude of the model moments is roughly the same as the data although the x -dependence for π^- is slightly larger than the data. Overall this model does very well in describing the data, which is particularly impressive since most of the model parameters were fixed by comparison to the unpolarized distribution function f_1 with only a single additional parameter fixed by comparison to the T-odd Sivers function f_{1T}^\perp . The agreement between the model and data seem to indicate that the twist-4 Cahn contribution is small, though possibly significant in some kinematic regions.

Updated results that include the Cahn contribution and calculations for the deuterium target and $\cos \phi_h$ are expected soon.

8.2.2 Barone et al.

Predictions

The predictions of Reference [10] include contributions from the Boer-Mulders effect, the Cahn effect, and NLO QCD effects. The latter are found to be negligible in the HERMES kinematic regime.

The calculation of the Boer-Mulders effect makes use of the Collins fragmentation function extracted from data (including HERMES data) in Reference [43]. The Boer-Mulders function is parameterized as a constant factor times the Siverson distribution function, which is taken from a fit to HERMES and COMPASS single spin asymmetry data in Reference [57]. The proportionality constant is taken to be the ratio of the quark anomalous tensor magnetic moment κ_T^q to the anomalous magnetic moment κ^q . The former is taken from lattice calculations while the latter is taken from the measured proton and neutron anomalous magnetic moments. As for the $\cos\phi_h$ prediction presented above, $\langle k_\perp^2 \rangle$ and $\langle p_\perp^2 \rangle$ are taken from [58]. These assumptions generate Boer-Mulders functions that are negative for both u and d quarks, in agreement with the diquark spectator model presented in the previous section. The Cahn contribution is calculated from the GRV98 [59] unpolarized distribution function and Kretzer [26] unpolarized fragmentation function, both taken from fits to data.

The results of this prediction are shown in Figure 8.3. As before these should be multiplied by a factor of two for comparison with the data. In addition, P_T^{cut} is not the same as $P_{h\perp}$ and these distributions should not be compared. The π^- moments compare well with the data while the π^+ moments are slightly positive, compared to the slightly negative (though compatible with zero within the systematic uncertainty) moments seen in data. This may be due to too large of a contribution from the Cahn effect. This hypothesis is explored in the next section.

Fits

A follow up to the previous model, performed after the release of preliminary results from HERMES and COMPASS, is presented in [60]. As before most parameters are taken from data and the Boer-Mulders function is taken as a scaled Siverson function. However, in contrast to the original predictions, the experimental data is used to constrain this proportionality constant. Also included are updated fits to the Collins [61] and Siverson [14] functions. Two alternative values of $\langle k_\perp^2 \rangle$ and $\langle p_\perp^2 \rangle$ are used. *Fit 1* uses that of [58], as above. *Fit 2* uses values extracted from tuning MC to HERMES data, done by the HERMES collaboration. The latter, notably, has a smaller average quark transverse momentum in the nucleon, $\langle k_\perp^2 \rangle = 0.18\text{GeV}^2$, compared with $\langle k_\perp^2 \rangle = 0.25\text{GeV}^2$ from [58]. From the predictions shown above this should provide a small Cahn contribution, which would agree better with the data.

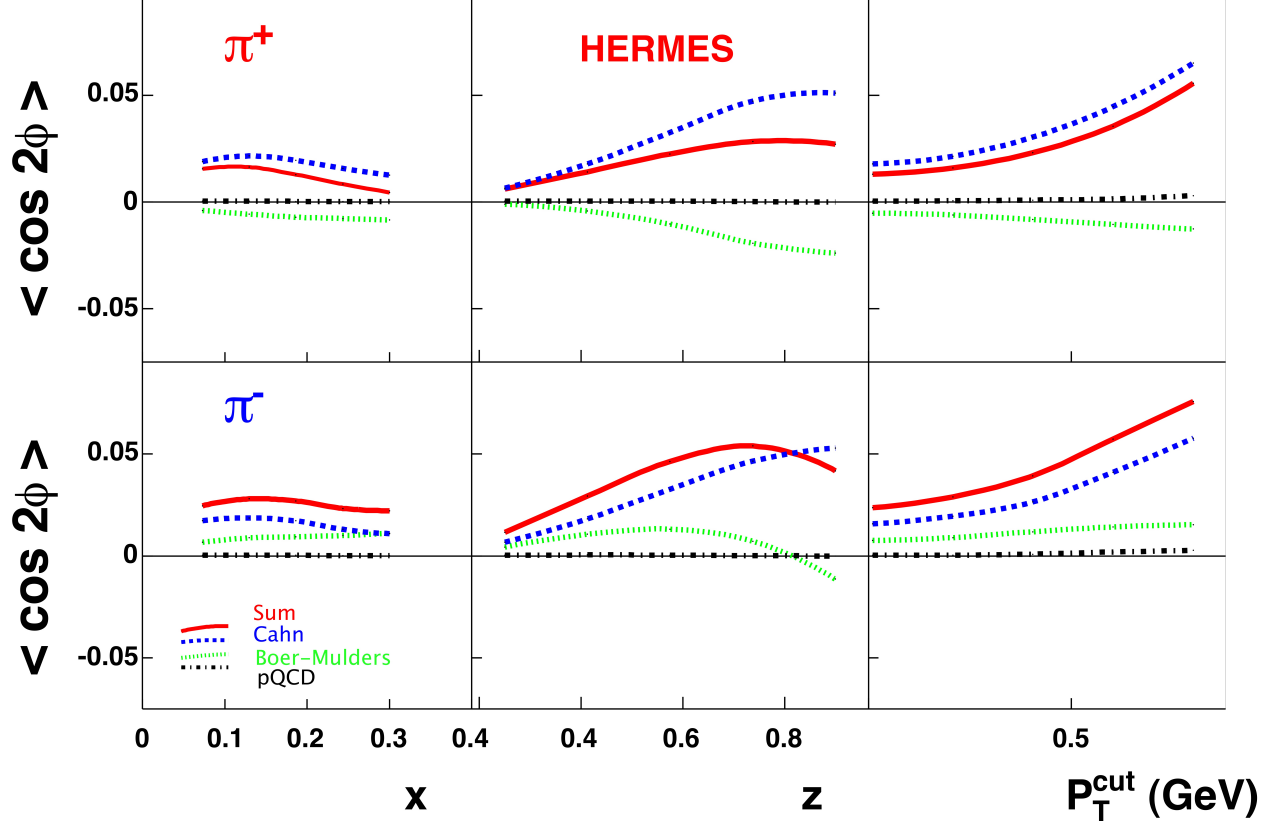


Figure 8.3: Prediction of $\cos 2\phi_h$ at HERMES from Reference [10]. The black dash-dot line is the pQCD contribution, the green dotted line is the Boer-Mulders effect, and the blue dotted line is the twist-4 Cahn effect. The red line is the sum of all contributions.

The results from Fit 1 and Fit 2 are presented in Figures 8.4 and 8.5 respectively, compared to the preliminary (including only the 2000 to 2006 e- data) HERMES hadron results.

The χ^2 per degree of freedom is 3.73 for Fit 1 and 2.41 for Fit 2. The better agreement with the HERMES data for Fit 2 is evident in the figures and seems to indicate that indeed a smaller $\langle k_{\perp}^2 \rangle$ is appropriate at HERMES kinematics. The model also nicely fits the COMPASS data, showing that the two measurements are not at odds. An exception is the COMPASS $P_{h\perp}$ -dependence, which is not included in the fit. The authors state that the COMPASS $P_{h\perp}$ data points are “clearly incompatible with the HERMES $P_{h\perp}$ data and have a counterintuitive behavior (it is infact difficult to envisage a transverse-momentum dependence of distribution and fragmentation functions able to describe them).”

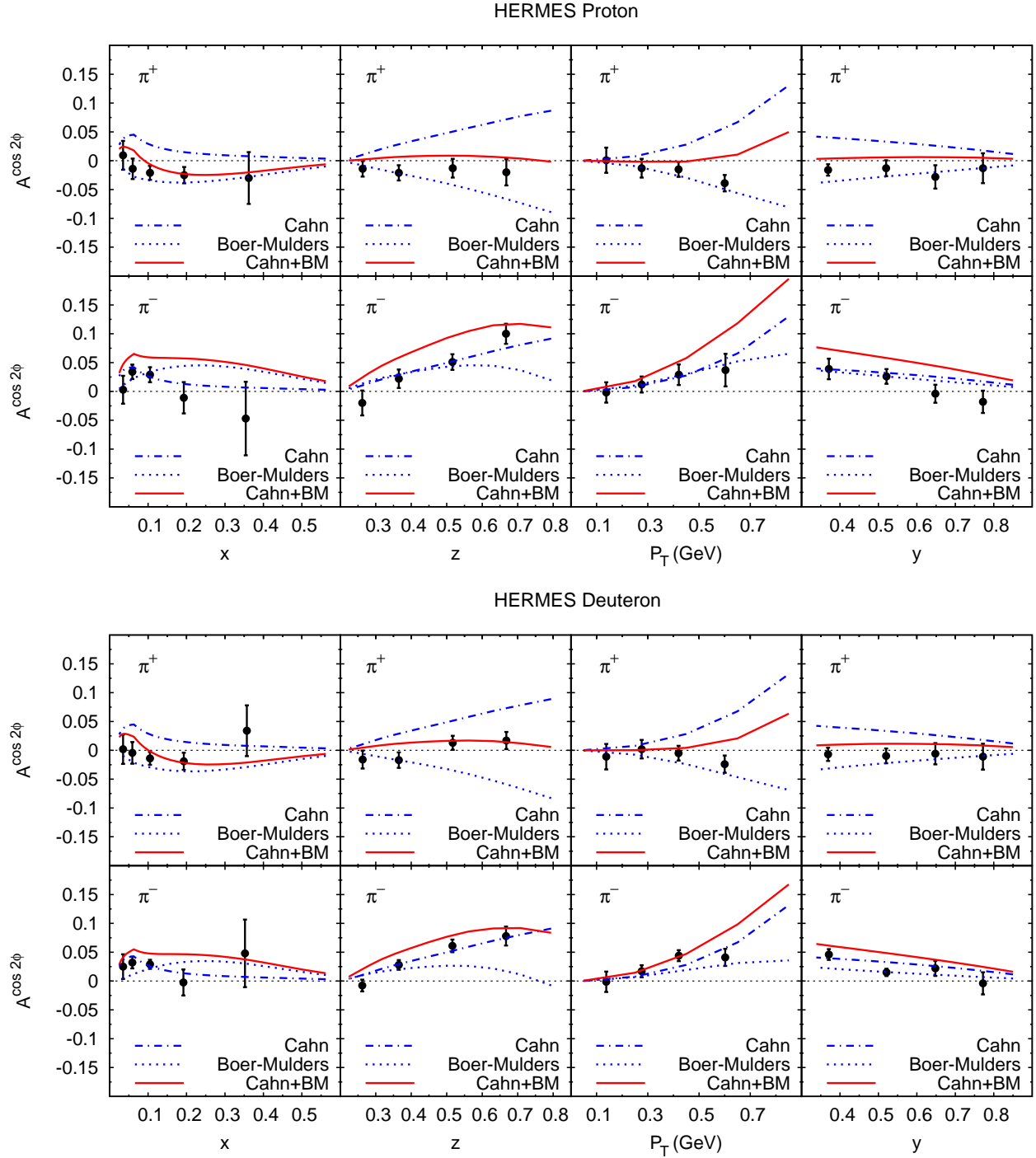


Figure 8.4: $\cos 2\phi_h$ at HERMES using parameters from Fit 1 from Reference [60] for hydrogen (top) and deuterium (bottom) targets.

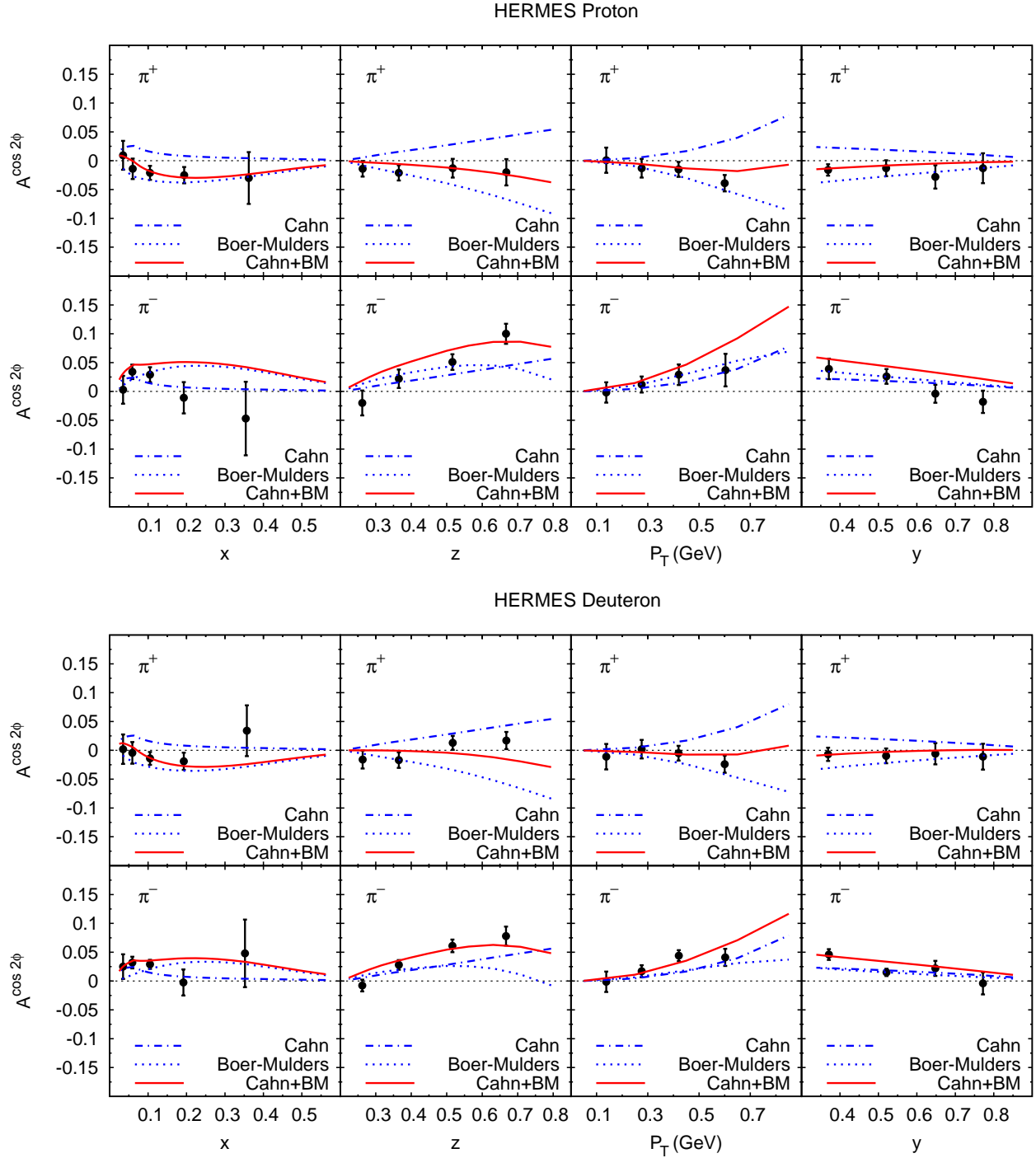


Figure 8.5: $\cos 2\phi_h$ at HERMES using parameters from Fit 2 from Reference [60] for hydrogen (top) and deuterium (bottom) targets.

8.2.3 Zhang et al.

In [62] another prediction of the Boer-Mulders contribution is made, this time using two fits to the NuSea/E866 Drell-Yan data (see Section 7.3). In [50] the u , d , \bar{u} and \bar{d} Boer-Mulders functions are extracted as modulated variations of the unpolarized distribution functions with the functional forms:

$$h_1^{\perp,u}(x) = \omega H_u x^c (1-x) f_1^u(x) \quad (8.1)$$

$$h_1^{\perp,d}(x) = \omega H_d x^c (1-x) f_1^d(x) \quad (8.2)$$

$$h_1^{\perp,\bar{u}}(x) = \frac{1}{\omega} H_{\bar{u}} x^c (1-x) f_1^{\bar{u}}(x) \quad (8.3)$$

$$h_1^{\perp,\bar{d}}(x) = \frac{1}{\omega} H_{\bar{d}} x^c (1-x) f_1^{\bar{d}}(x) \quad (8.4)$$

$$h_1^{\perp,q}(x, \mathbf{k}_T^2) = h_1^{\perp,q}(x) \frac{\exp(-\mathbf{k}_T^2/p_{bm}^2)}{\pi p_{bm}^2} \quad (8.5)$$

where c , H_q , and p_{bm}^2 are determined in the fit. The parameter ω is determined from unpolarized $p\bar{p}$ Drell-Yan data. The second parameter set is the same, but assumes that the scale factors H_u and H_d have opposite signs. Both fits achieve a χ^2 per degree of freedom of 0.79. The parameters determined for each fit are shown in Table 8.1. For both sets the unpolarized distribution functions are taken from the MRST fit [63] and $\langle k_{\perp}^2 \rangle = 0.25$, again taken from [58]. The SIDIS Boer-Mulders effect is then calculated from the Boer-Mulders function and the Collins fragmentation function, again taken from [43].

Table 8.1: Parameters determined in [50]

| Parameter | Set I | Set II |
|---------------|-------|--------|
| H_u | 3.99 | 4.44 |
| H_d | 3.83 | -2.97 |
| $H_{\bar{u}}$ | 0.91 | 4.68 |
| $H_{\bar{d}}$ | -0.96 | 4.98 |
| p_{cm}^2 | 0.161 | 0.165 |
| c | 0.45 | 0.82 |

The resulting prediction from both parameter sets is shown in Figure 8.6. Note that the plotted quantity is $\nu = \langle \cos 2\phi_h \rangle_{UU}$ and should again be multiplied by two compared to the experimental results. The two parameter sets give very similar results. This is somewhat surprising since not only does Set 2 have opposite signs for the u and d Boer-Mulders functions, it also has very large sea quark contributions $h_1^{\perp,\bar{u}}$ and $h_1^{\perp,\bar{d}}$.

Both sets overestimate the π^- moments, although Set 1 is slightly smaller. The π^- z -dependence does not go to zero at low z like the data. The model predicts π^+ moments largely consistent with zero, which mostly agrees with the data. However, the rise at low x is not evident in the data.

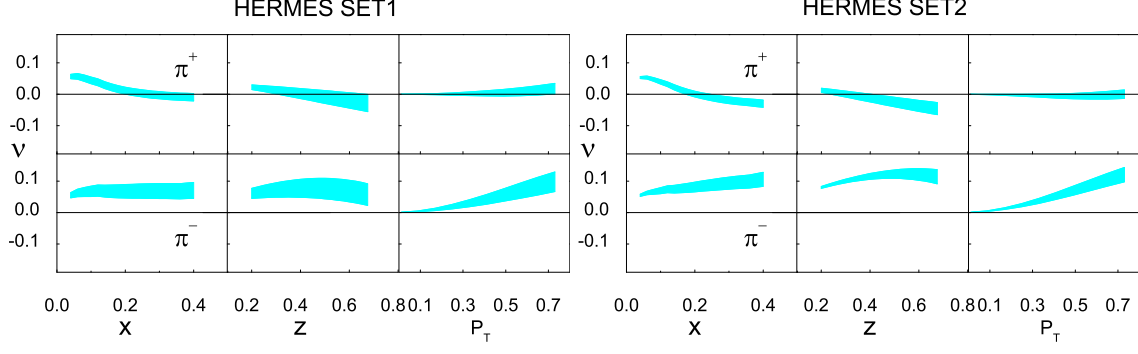


Figure 8.6: $\cos 2\phi_h$ at HERMES using parameters from Set 1 (left) and Set 2 (right) from Reference [62] for a hydrogen target

8.2.4 Evaluation of the model for a deuterium target

Unfortunately a prediction for the HERMES deuterium results was not made with the model in the previous section. In this section a calculation is performed to investigate what the fit parameters in Table 8.1 would predict for a deuterium target. In general the Boer-Mulders effect can be written as:

$$\langle \cos n\phi_h \rangle_{target}^h = \frac{\sum_q e_q h_{1,q}^\perp(x) H_{1,q \rightarrow h}^\perp(z)}{\sum_q e_q f_{1,q}(x) D_{1,q}(z)}. \quad (8.6)$$

The $\cos 2\phi_h$ moments are then:

$$\langle \cos n\phi_h \rangle_H^{\pi^+} \sim C \frac{4h_{1,u}^\perp + \eta_H h_{1,d}^\perp + 4\eta_H h_{1,\bar{u}}^\perp + h_{1,\bar{d}}^\perp}{4f_{1,u} + \eta f_{1,d} + 4\eta f_{1,\bar{u}} + f_{1,\bar{d}}} \quad (8.7)$$

$$\langle \cos n\phi_h \rangle_H^{\pi^-} \sim C \frac{4\eta_H h_{1,u}^\perp + h_{1,d}^\perp + 4h_{1,\bar{u}}^\perp + \eta_H h_{1,\bar{d}}^\perp}{4\eta f_{1,u} + f_{1,d} + 4f_{1,\bar{u}} + \eta f_{1,\bar{d}}} \quad (8.8)$$

$$\langle \cos n\phi_h \rangle_D^{\pi^+} \sim C \frac{(4 + \eta_H)(h_{1,u}^\perp + h_{1,d}^\perp) + (4\eta_H + 1)(h_{1,\bar{u}}^\perp + h_{1,\bar{d}}^\perp)}{(4 + \eta)(f_{1,u} + f_{1,d}) + (4\eta + 1)(f_{1,\bar{u}} + f_{1,\bar{d}})} \quad (8.9)$$

$$\langle \cos n\phi_h \rangle_D^{\pi^-} \sim C \frac{(4\eta_H + 1)(h_{1,u}^\perp + h_{1,d}^\perp) + (4 + \eta_H)(h_{1,\bar{u}}^\perp + h_{1,\bar{d}}^\perp)}{(4\eta + 1)(f_{1,u} + f_{1,d}) + (4 + \eta)(f_{1,\bar{u}} + f_{1,\bar{d}})} \quad (8.10)$$

where C involves the ratio of favored fragmentation functions $H_{1,fav}^\perp/D_{1,fav}$ and the η 's are the ratio of disfavored to favored fragmentation functions:

$$\eta \equiv \frac{D_{1,disfav}}{D_{1,fav}} \quad (8.11)$$

$$\eta_H \equiv \frac{H_{1,disfav}^\perp}{H_{1,fav}^\perp} \quad (8.12)$$

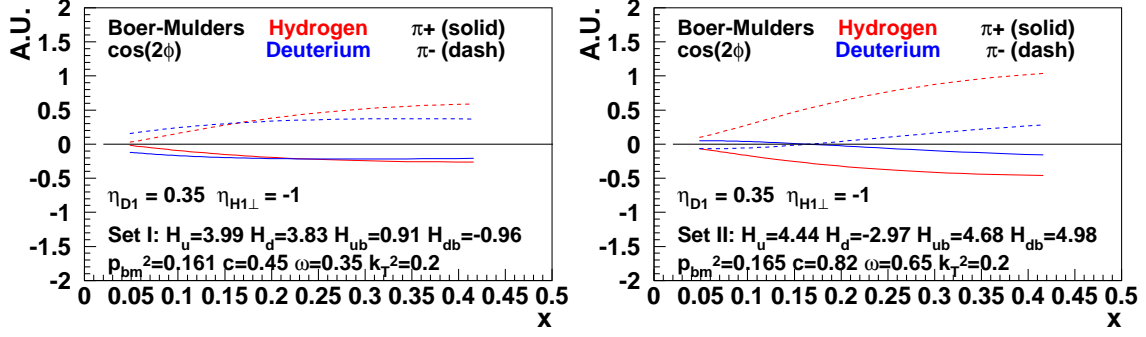


Figure 8.7: Results of the toy model using parameter Set I (left) and Set II (right) from [62] for hydrogen (red) and deuterium (blue) targets.

If η_H is taken as -1 , which is a good approximation to HERMES and BELLE results, and η is set to 0.35 , which is reasonable for HERMES kinematics, then only the distribution functions remain to be calculated. The unpolarized distribution functions f_1 are taken from CTEQ6L [64] while the Boer-Mulders function is calculated from f_1 and the parameterization presented in the previous section. The results are shown in Figure 8.7. Since the C factor is not evaluated the y-axis is in arbitrary units. The hydrogen results give similar shapes as in [62], indicating that this calculation is a reasonable approximation of the full model in [62]. The deuterium results are particularly interesting. For Set I, where the u and d quark Boer-Mulders functions are of the same sign, the hydrogen and deuterium results are very similar. This is reminiscent of the data where the two target give almost identical results. Set II on the other hand gives similar moments for hydrogen and near-zero moments for both pion charges on a deuterium target. This is decidedly not what is seen in the data. From this calculation it seems that the data strongly favor Set I, which is also in agreement with other models.

Perhaps as important as this observation is the fact that both pion charges for both hydrogen and deuterium targets are needed to clearly distinguish between models. This demonstrates the power of the HERMES data set and also the need for a complete set of predictions from all models.

Overall, the measurements of $\cos\phi_h$ and $\cos 2\phi_h$ presented in this thesis are in agreement with theoretical expectations and are well described by current models. The Boer-Mulders function is the same sign for u and d quarks, indicating that they both have their spin and orbital motion aligned. Further constraints of the models requires data of greater precision and kinematic range.

Chapter 9

Conclusions

This thesis has presented the $\cos \phi_h$ and $\cos 2\phi_h$ moments of the unpolarized SIDIS cross section for charged pions, kaons, and unidentified-hadrons on hydrogen and deuterium targets. Particular care was taken in extracting the moments. An improved hadron-type identification algorithm was presented and is now the primary particle identification software used at HERMES. An intricate analysis procedure was used to extract the moments in four kinematic dimensions and systematic errors were calculated. The results show that positive and negative pions have significantly different $\cos \phi_h$ and $\cos 2\phi_h$ moments while hydrogen and deuterium targets produce nearly identical modulations. From model calculations this seems to indicate that the Boer-Mulders function for u and d quarks are of the same sign. Model calculations for the Cahn contribution to $\cos \phi_h$ differ from the data, indicating that the Boer-Mulders contribution is significant. The Cahn contribution to $\cos 2\phi_h$ seems to be small, favoring a small intrinsic quark transverse momentum. Preliminary kaon results show that they have different trends than the pions but due to the low statistics it is difficult to draw any conclusions.

The complete data set presented provides a valuable constraint to models and still awaits a full response from the theory community.

Chapter 10

Poetry

My personal statement that helped me gain admittance to Illinois was in the form of a poem. I again exercised my poetic skills in my preliminary exam paper and presentation. Here, in the spirit of tradition, I include one last graduate school poem. While not my best work it does convey my sentiments on the final day of thesis writing.

Writing a thesis is a lot of hard work
You should warn your friends or they'll think you're a jerk
Because you won't call for days and days
since you are in such a craze.

While I have learned a lot
I'm feeling a bit distraught
There was much more I could have written
But with the thought of being DONE, I was bitten

So, while not completely exhaustive
You can be sure I am completely exhausted, so much so that I can't rhyme anymore
Thank you for reading all of this,
I hope you don't find me remiss.

References

- [1] the HERMES Collaboration and A. Airapetian. Search for a two-photon exchange contribution to inclusive deep-inelastic scattering. *Physics Letters B*, 682:351, 2010.
- [2] John C. Collins, Davison E. Soper, and George Sterman. Factorization of Hard Processes in QCD. *Adv. Ser. Direct. High Energy Phys.*, 5:1–91, 1988.
- [3] George Sterman, John Smith, John C. Collins, James Whitmore, Raymond Brock, Joey Huston, Jon Pumplin, Wu-Ki Tung, Hendrik Weerts, Chien-Peng Yuan, Stephen Kuhlmann, Sanjib Mishra, Jorge G. Morfín, Fredrick Olness, Joseph Owens, Jianwei Qiu, and Davison E. Soper. Handbook of perturbative qcd. *Rev. Mod. Phys.*, 67(1):157–248, Jan 1995.
- [4] Xiangdong Ji, Jian-Ping Ma, and Feng Yuan. Qcd factorization for semi-inclusive deep-inelastic scattering at low transverse momentum. *Physical Review D*, 71:034005, 2005.
- [5] A. Airapetian et al. Evidence for a single-spin azimuthal asymmetry in semi-inclusive pion electroproduction. *Phys. Rev. Lett.*, 84(18):4047–4051, May 2000.
- [6] A. Airapetian et al. Single-spin asymmetries in semi-inclusive deep-inelastic scattering on a transversely polarized hydrogen target. *Phys. Rev. Lett.*, 94:012002, 2005.
- [7] V. Yu. Alexakhin et al. First measurement of the transverse spin asymmetries of the deuteron in semi-inclusive deep inelastic scattering. *Phys. Rev. Lett.*, 94(20):202002, May 2005.
- [8] Stanley J. Brodsky, Dae Sung Hwang, and Ivan Schmidt. *Nucl. Phys.*, B642:344–356, 2002.
- [9] Alessandro Bacchetta et al. Semi-inclusive deep inelastic scattering at small transverse momentum. *JHEP*, 02:093, 2007.
- [10] Vincenzo Barone, Alexei Prokudin, and Bo-Qiang Ma. A systematic phenomenological study of the $\cos 2\phi$ asymmetry in unpolarized semi-inclusive DIS. *Phys. Rev.*, D78:045022, 2008.
- [11] Robert N. Cahn. Azimuthal Dependence in Leptoproduction: A Simple Parton Model Calculation. *Phys. Lett.*, B78:269, 1978.
- [12] R. N. Cahn. Critique of parton-model calculations of azimuthal dependence in leptoproduction. *Phys. Rev.*, D40:3107–3110, 1989.
- [13] Matthias Burkardt. Transverse deformation of parton distributions and transversity decomposition of angular momentum. *Phys. Rev.*, D72:094020, 2005.
- [14] M. Anselmino et al. Sivers Effect for Pion and Kaon Production in Semi- Inclusive Deep Inelastic Scattering. *Eur. Phys. J.*, A39:89–100, 2009.
- [15] N. Akopov, E. C. Aschenauer, K. Bailey, S. Bernreuther, N. Bianchi, G. P. Capitani, P. Carter, E. Cisbani, R. De Leo, E. De Sanctis, D. De Schepper, V. Djordjadze, B. W. Filippone, S. Frullani, F. Garibaldi, J. O. Hansen, B. Hommez, M. Iodice, H. E. Jackson, P. Jung, R. Kaiser, J. Kanetsaka, R. Kowalczyk, L. Lagamba, A. Maas, V. Muccifora, E. Nappi, K. Negodaeva, W. D. Nowak,

- T. O'Connor, T. G. O'Neill, D. H. Potterveld, D. Ryckbosch, Y. Sakemi, F. Sato, A. Schwind, T. A. Shibata, K. Suetsugu, E. Thomas, M. Tytgat, G. M. Urciuoli, K. Van de Kerckhove, R. Van de Vyver, S. Yoneyama, H. Zohrabian, and L. F. Zhang. The hermes dual-radiator ring imaging cherenkov detector. *Nuclear Instruments and Methods in Physics Research Section A: Accelerators, Spectrometers, Detectors and Associated Equipment*, 479(2-3):511 – 530, 2002.
- [16] Y. Miyachi T. Hasegawa. Estimation of RICH particle identification accuracy using decaying particles. */group01/richgrp/dPsys/pmatrix.v3.0/richsys.pdf*, 2005.
- [17] M. Tytgat. Particle identification with the hermes rich. *Nuclear Instruments and Methods in Physics Research Section A: Accelerators, Spectrometers, Detectors and Associated Equipment*, 433(1-2):286 – 288, 1999.
- [18] A. Maas. RPS - RICH PID Scheduler. *HERMES internal note 00-029*, 2000.
- [19] E. Cisbani D. Schepper R. Kaiser. Particle Identification with the HERMES RICH Detector: Description of the Different Approaches. *HERMES internal note 98-008*, 1998.
- [20] Torbjorn Sjöstrand et al. High-energy-physics event generation with pythia 6.1. *Comput. Phys. Commun.*, 135:238–259, 2001.
- [21] G. Ingelman, A. Edin, and J. Rathsman. Lepto 6.5 – a monte carlo generator for deep inelastic lepton-nucleon scattering. *Computer Physics Communications*, 101(1-2):108 – 134, 1997.
- [22] I. Akushevich, H. Böttcher, and D. Ryckbosch. Radgen 1.0: Monte carlo generator for radiative events in dis on polarized and unpolarized targets. 1998.
- [23] R. Brun, R. Hagelberg, M. Hansroul, and J. Lassalle. *CERN Report CERN-DD-78-2-REV*, 1978.
- [24] Z. Ye and E. C. Aschenauer. Misalignment effects on the beam-spin and beam-charge asymmetries in dvcs. *HERMES internal note 05-038*.
- [25] J. Pumplin, D. R. Stump, J. Huston, H. L. Lai, P. Nadolsky, and W. K. Tung. New generation of parton distributions with uncertainties from global qcd analysis, 2002.
- [26] S. Kretzer. Fragmentation functions from flavor-inclusive and flavor-tagged $e + e^-$ annihilations. *Phys. Rev. D*, 62(5):054001, Jul 2000.
- [27] the HERMESCollaboration and A. Airapetian. Charge and hadron type separated meson multiplicities at HERMES. *in preparation*.
- [28] Howard Georgi and H. David Politzer. Clean tests of quantum chromodynamics in μp scattering. *Phys. Rev. Lett.*, 40(1):3–6, Jan 1978.
- [29] Joshua George Rubin. Polarization, motion, and fragmentation: Exploring the role of quarks in the nucleon through semi-inclusive longitudinal spin asymmetries at HERMES. DESY-THESIS-2009-045.
- [30] C. Tao, R. G. Hicks, H. L. Anderson, N. E. Booth, W. R. Francis, B. A. Gordon, W. W. Kinnison, T. B. W. Kirk, W. A. Loomis, H. S. Matis, L. W. Mo, L. C. Myriantopoulos, F. M. Pipkin, J. Proudfoot, T. W. Quirk, A. L. Sessoms, W. D. Shambroom, A. Skuja, M. A. Staton, W. S. C. Williams, Richard Wilson, and S. C. Wright. Transverse momentum and angular distributions of hadrons in muon-proton scattering and tests of quantum chromodynamics. *Phys. Rev. Lett.*, 44(26):1726–1729, Jun 1980.
- [31] M. Derrick, P. Gregory, F. LoPinto, B. Musgrave, J. Schlereth, P. Schreiner, R. Singer, S. J. Barish, R. Brock, A. Engler, T. Kikuchi, R. W. Kraemer, F. Messing, B. J. Stacey, M. Tabak, V. E. Barnes, D. D. Carmony, E. Fernandez, A. F. Garfinkel, and A. T. Laasanen. Hadron-production mechanisms in antineutrino-proton charged-current interactions. *Phys. Rev. D*, 24(5):1071–1096, Sep 1981.
- [32] A. Vayaki. AZIMUTHAL ASYMMETRY OF HADRONS PRODUCED IN ANTI-NEUTRINOS REACTIONS. Contributed to 21st Int. Conf. on High Energy Physics, Paris, France, Jul 26-31, 1982.

- [33] J. J. Aubert et al. Measurement of hadronic azimuthal distributions in deep inelastic muon proton scattering. *Phys. Lett.*, B130:118, 1983.
- [34] M. Arneodo et al. Measurement of hadron azimuthal distributions in deep inelastic muon proton scattering. *Z. Phys.*, C34:277, 1987.
- [35] M. R. Adams et al. Perturbative QCD effects observed in 490-GeV deep inelastic muon scattering. *Phys. Rev.*, D48:5057–5066, 1993.
- [36] J. Breitweg et al. Measurement of azimuthal asymmetries in deep inelastic scattering. *Phys. Lett.*, B481:199–212, 2000.
- [37] S. Chekanov et al. Measurement of azimuthal asymmetries in neutral current deep inelastic scattering at HERA. *Eur. Phys. J.*, C51:289–299, 2007.
- [38] M. Osipenko et al. Measurement of unpolarized semi-inclusive pi+ electroproduction off the proton. *Phys. Rev.*, D80:032004, 2009.
- [39] W. Kafer and for the COMPASS Collaboration. Measurements of unpolarized azimuthal asymmetries at compass, 2008.
- [40] Andrea Bressan and for the COMPASS Collaboration. Azimuthal asymmetries in sidis off unpolarized targets at compass, 2009.
- [41] E. S. Ageev et al. A new measurement of the Collins and Sivers asymmetries on a transversely polarised deuteron target. *Nucl. Phys.*, B765:31–70, 2007.
- [42] K. Abe et al. Measurement of azimuthal asymmetries in inclusive production of hadron pairs in e+ e- annihilation at BELLE. *Phys. Rev. Lett.*, 96:232002, 2006.
- [43] M. Anselmino et al. Transversity and Collins functions from SIDIS and e+ e- data. *Phys. Rev.*, D75:054032, 2007.
- [44] S. Falciano et al. ANGULAR DISTRIBUTIONS OF MUON PAIRS PRODUCED BY 194-GeV/c NEGATIVE PIONS. *Z. Phys.*, C31:513, 1986.
- [45] M. Guanziroli et al. ANGULAR DISTRIBUTIONS OF MUON PAIRS PRODUCED BY NEGATIVE PIONS ON DEUTERIUM AND TUNGSTEN. *Z. Phys.*, C37:545, 1988.
- [46] J. S. Conway, C. E. Adolphsen, J. P. Alexander, K. J. Anderson, J. G. Heinrich, J. E. Pilcher, A. Possoz, E. I. Rosenberg, C. Biino, J. F. Greenhalgh, W. C. Louis, K. T. McDonald, S. Palestini, F. C. Shoemaker, and A. J. S. Smith. Experimental study of muon pairs produced by 252-gev pions on tungsten. *Phys. Rev. D*, 39(1):92, Jan 1989.
- [47] J. G. Heinrich, C. Biino, J. F. Greenhalgh, W. C. Louis, K. T. McDonald, S. Palestini, D. P. Russell, F. C. Shoemaker, A. J. S. Smith, C. E. Adolphsen, J. P. Alexander, K. J. Anderson, J. S. Conway, J. E. Pilcher, A. Possoz, and E. I. Rosenberg. Higher-twist effects in the reaction $\pi - n \rightarrow \mu + \mu - x$ at 253 gev/c. *Phys. Rev. D*, 44(7):1909–1932, Oct 1991.
- [48] L. Y. Zhu et al. Measurement of angular distributions of Drell-Yan dimuons in p + d interaction at 800-GeV/c. *Phys. Rev. Lett.*, 99:082301, 2007.
- [49] L. Y. Zhu et al. Measurement of Angular Distributions of Drell-Yan Dimuons in p + p Interactions at 800 GeV/c. *Phys. Rev. Lett.*, 102:182001, 2009.
- [50] Bing Zhang, Zhun Lu, Bo-Qiang Ma, and Ivan Schmidt. Extracting Boer-Mulders functions from p + D Drell-Yan processes. *Phys. Rev.*, D77:054011, 2008.
- [51] Zhun Lu and Ivan Schmidt. Updating Boer-Mulders functions from unpolarized pd and pp Drell-Yan data. *Phys. Rev.*, D81:034023, 2010.

- [52] A. Sissakian, O. Shevchenko, A. Nagaytsev, and O. Ivanov. Transversity, Boer-Mulders and Sivers distributions from Drell-Yan processes with pp , pD and DD collisions. *Eur. Phys. J.*, C59:659–673, 2009.
- [53] Vincenzo Barone, Zhun Lu, and Bo-Qiang Ma. The $\cos(2\phi)$ asymmetry of Drell-Yan and J/ψ production in unpolarized p anti- p scattering. *Eur. Phys. J.*, C49:967–971, 2007.
- [54] M. Anselmino, M. Boglione, A. Prokudin, and C. Turk. Semi-inclusive deep inelastic scattering processes from small to large $P(T)$. *Eur. Phys. J.*, A31:373–381, 2007.
- [55] Leonard P. Gamberg, Gary R. Goldstein, and Marc Schlegel. Transverse Quark Spin Effects and the Flavor Dependence of the Boer-Mulders Function. *Phys. Rev.*, D77:094016, 2008.
- [56] Alessandro Bacchetta, Leonard P. Gamberg, Gary R. Goldstein, and Asmita Mukherjee. Collins fragmentation function for pions and kaons in a spectator model. *Phys. Lett.*, B659:234–243, 2008.
- [57] M. Anselmino, M. Boglione, U. D’Alesio, A. Kotzinian, F. Murgia, and A. Prokudin. Extracting the sivers function from polarized semi-inclusive deep inelastic scattering data and making predictions. *Phys. Rev. D*, 72(9):094007, Nov 2005.
- [58] M. Anselmino et al. The role of Cahn and Sivers effects in deep inelastic scattering. *Phys. Rev.*, D71:074006, 2005.
- [59] M. Glück, E. Reya, and A. Vogt. *Eur. Phys. J.*, C5:461–470, 1998.
- [60] Vincenzo Barone, Stefano Melis, and Alexei Prokudin. The Boer-Mulders effect in unpolarized SIDIS: an analysis of the COMPASS and HERMES data on the $\cos 2\phi$ asymmetry. 2009.
- [61] M. Anselmino et al. Update on transversity and Collins functions from SIDIS and $e+e-$ data. *Nucl. Phys. Proc. Suppl.*, 191:98–107, 2009.
- [62] Bing Zhang, Zhun Lu, Bo-Qiang Ma, and Ivan Schmidt. $\cos 2\phi$ asymmetries in unpolarized semi-inclusive DIS. *Phys. Rev.*, D78:034035, 2008.
- [63] A. D. Martin, R. G. Roberts, W. J. Stirling, and R. S. Thorne. Nnlo global parton analysis. *Physics Letters B*, 531(3-4):216 – 224, 2002.
- [64] J. Pumplin et al. New generation of parton distributions with uncertainties from global QCD analysis. *JHEP*, 07:012, 2002.